FLOW PHYSICS OF FLUIDICALLY CONTROLLED ATTACHMENT IN SEPARATION CELLS

A Dissertation
Presented to
The Academic Faculty

by

Curtis James Peterson

In Partial Fulfillment
of the Requirements for the Degree
Doctorate of Philosophy in Mechanical Engineering

Georgia Institute of Technology
August 2022

FLOW PHYSICS OF FLUIDICALLY CONTROLLED ATTACHMENT IN SEPARATION CELLS

Approved by:

Professor Ari Glezer, Advisor
School of Mechanical Engineering
Georgia Institute of Technology

Professor Marc K. Smith
School of Mechanical Engineering
Georgia Institute of Technology

Professor Marilyn J. Smith
School of Aerospace Engineering
Georgia Institute of Technology

Dr. Bojan Vukasinovic
School of Mechanical Engineering
Georgia Institute of Technology

Professor Donald R. Webster
School of Civil and Environmental Engineering
Georgia Institute of Technology

Date Approved: [July 6, 2022]

Dedicated to my parents, Dr. and Mrs. Jim and Sue Peterson

ACKNOWLEDGEMENTS

This work was made possible by funding from the Boeing Corporation and the Georgia Tech Vertical Lift Research Center of Excellence (VLRCoE). I would like to thank my colleagues working on the computational efforts for this VLRCoE Task, Professor Marilyn Smith, Dr. Nicholson Koukpaizan, Aaron Crawford, and Dr. Daniel Heathcote, for their hard work, support, and guidance throughout these collaborative scientific efforts.

I would like to thank my research advisor, Professor Ari Glezer, who has taught me countless lessons during my time at Georgia Tech, which I will carry forward with me throughout my career. A special and heartfelt thank you to Dr. Bojan Vukasinovic for your continual advice and guidance over the years in and out of the research lab, your help made most of these experimental results possible. Thank you to my thesis committee: Professor Ari Glezer, Professor Marilyn J. Smith, Professor Marc K. Smith, Professor Donald R. Webster, and Dr. Bojan Vukasinovic for your time, patience, and assistance with this document.

This work would not have been possible without the help and support of both past and present members of the Fluid Mechanics Research Lab, who have assisted with everything from troubleshooting experimental equipment to Ph.D. qualifying exam preparation, your help and kindness have left a lasting impression and you have my profound gratitude. A special thank you to Dr. Svyatoslav Yorish, whose assistance with lab equipment, experimental construction, and design were invaluable.

Finally, thank you to my parents, brother, friends, and especially Alexa Sido, for your unending support, guidance, patience, encouragement and love, which were invaluable to completing my graduate school experience.

TABLE OF CONTENTS

LIST OF TABLES

LIST OF FIGURES

LIST OF SYMBOLS AND ABBREVIATIONS

A	Area of test section inlet
C_p	Compressible pressure coefficient
C_q	Mass flow rate coefficient
C_μ	Momentum coefficient
W, H, L	Test Section width, height, and length
ξ_x	Streamwise vorticity
ξ_z	Spanwise vorticity
c	Chord length of original VR-12 airfoil model used to create wind tunnel model
x^*	Streamwise distance of the local separation and reattachment location relative to the base flow separation location at $M_0 = 0.25$
L_x	Streamwise extent of closed separation domain
L_o	Streamwise extent of closed separation for the base flow at $M_0 = 0.25$
$\dot{m}$	Total mass flow rate through diverting duct geometry
$\dot{m}_0$	Unactuated flow total mass flow rate
$\dot{m}_1$	Mass flow rate through primary channel
$\dot{m}_2$	Mass flow rate through diverted (secondary) channel
$\Delta\dot{m}^*$	Relative increase in the total mass flow rate
M_0	Test section inlet Mach number
U^*	Scaled velocity component
η	Embedded shear layer scaling parameter
p	Static pressure
ρ	Density of air

Re	Reynolds number
$\overline{u'u'}$	Reynolds normal stress
$\overline{u'v'}$	Reynolds shear stress
U_0	Test section inlet velocity
U, V, W	Streamwise, cross-stream, and spanwise velocity component
U', U_n	Wall-tangential velocity component
V'	Wall-normal velocity component
γ	Specific heat ratio for air
W	Spanwise velocity component
Ω_{flux}	Non-dimensional vorticity flux
Γ	Circulation
$\Phi *$	Total circulation within reverse flow domain
Γ_1	Vortex detection scheme
TKE	Turbulent Kinetic Energy
TKE_{cell}	Turbulent Kinetic Energy within the reattachment cell

SUMMARY

The present investigations focus on the evolution of a separated boundary layer in an adverse pressure gradient over an inner surface of a diffuser duct and the mechanisms of its mitigation using spanwise-distributed fluidic actuation. The investigations place specific emphasis on the interactions between the separated boundary layer within a separation cell over a surface of a diffuser duct and a spanwise array of fluidically oscillating jets with the objective of understanding the actuation-induced changes in the base flow's structure and dynamics. It is shown that the base flow at the plane of symmetry is dominated by the formation of a wake-like structure that is characterized by a shear layer that separates between the diffuser's cross flow and a reversed flow layer near the surface. These effects are investigated in two diffuser configurations having significant differences in their inlet conditions: *i.* An open-end diffuser duct branching from a channel, and *ii.* A curved surface insert that forms a diffuser within a channel. The spanwise oscillating actuation jets are formed by modules that are integrated within and issue tangentially to the surface of the diffuser.

In the branched diffuser, the separated flow on the curved inlet surface blocks a significant fraction of the entrance area. Actuation of increasing strength upstream of separation migrates the onset of separation farther downstream while deflecting the cross-stream shear layer towards the surface and thereby alleviating the blockage of the reverse flow domain. The tangential actuation alters the structure of the shear layer and results in the formation and advection of larger-scale, lower-frequency vortical structures near the surface as the separation is delayed. The cross-stream scale of distributions of the wall-

tangential velocity at separation is significantly increased in the presence of the actuation as the separation is delayed into the diffuser's adverse pressure gradient. Despite alteration of the shear layer dynamics and increase in cross-stream scale of the velocity distributions, the time-averaged velocity distributions at the natural and delayed separation in the absence and presence of actuation, respectively, collapse when scaled by inherent characteristics of the shear layer (vorticity thickness and velocity deficit) displayed in the velocity distributions.

The formation of a separation cell in an adverse pressure gradient is investigated over a diverging convex surface insert (based on a VR-12 airfoil) that forms a diffuser within a channel with different inlet conditions. The separation cell is characterized by two surface-normal vortices that bound a central, nominally two-dimensional reverse flow region, with flow reattachment occurring downstream of the transition from the curved insert to the constant cross-section of the channel. The reverse flow along the sidewall is turned toward the central plane of symmetry and induces the orientation of the surface normal vortices to be CW on the left and CCW on the right. The separating base flow at the center plane over the insert model exhibits similar features to separation over the branching diffuser, and the flow evolution about streamwise positions of the time-averaged separation and reattachment are investigated in the absence and presence of actuation. Velocity distributions at separation and reattachment in the absence and presence of actuation collapse when scaled by the same parameters based on the shear layer (vorticity thickness and velocity deficit) formed in the adverse pressure gradient, which also collapse along with the velocity distributions at separation in the diffuser in the base and controlled flows, indicating similarity of the flow separation structure between the two configurations.

Surface oil flow visualization of the separation cell in the presence of jet actuation shows that the flow through the nominally 2-D central reverse flow region of the base flow becomes reattached, and that the surface-normal vortices remain in their original orientations, but are shifted downstream and towards the sidewalls. It is shown that the flow attachment mechanism is a consequence of the discrete jet actuation forming pairs of streamwise vorticity concentrations of opposing sense which impart a paired sense of downwash along the jet centerlines, and upwash between the neighboring jets. The presence of the discrete jet actuation divided the center part of the separation cell in the base flow into adjacent attached cell structures which are each bounded by the developed counter-rotating streamwise vorticity concentrations. The outboard jets couple to the surface-normal vortices of the base flow and are directed toward the center plane, which wraps the actuator flow into the vortices and intensifies them.

The associated sense of downwash and upwash developed by the actuators also effect the distributions of the turbulent kinetic energy (*TKE*) levels in the separation cell, which in the base flow are contained within the shear layer. The actuation redistributes the elevated *TKE* levels into arch-like structures centered in the induced upwash regions between adjacent jets, while the *TKE* levels are reduced along the centerline of the jets.

It is shown that separation cells formed in adverse pressure gradient are receptive to fluidic actuation via discrete arrays of fluidic oscillating jets that issue tangentially to the surface upstream of separation. Increasing actuation strength incrementally delays the separation in adverse pressure gradient along the surface bounded by the reverse flow domain by the manipulation of the flow dynamics in the vicinity of separation and creation of spanwise concentrations of streamwise vorticity which subdivide the separation cell in

the base flow into smaller spanwise-periodic reattachment cells which mitigate the adverse effects of reverse flow along the surface. By demonstrating the efficacy of active flow control to mitigate flow separation and its adverse effects while bringing new understanding to the mechanisms leading to the reattachment, such active flow control technologies could see their way to implementation within complex internal flow geometries susceptible to internal flow separation.

CHAPTER 1. INTRODUCTION

Internal and external aerodynamic flows subjected to significant adverse pressure gradients are highly susceptible to three-dimensional separation, resulting in flow instabilities (e.g. separated shear layers, complex wakes) and significant global losses in the case of internal flows. Active flow control (AFC) offers a potential solution for mitigating these adverse effects by delaying separation well into the imposed adverse pressure gradient or bypassing it altogether. This literature review will focus on the underlying characteristics of separated flows, active flow control technologies and structural effects due to such control strategies.

1.1 Literature Review

1.1.1 Flow Separation

The severe losses that are associated with internal flow separation have motivated numerous investigations of the fundamental aspects of these complex flows over the years in various geometries such as backward facing steps (Papadopoulos and Otugen, 1995), flow junctions (e.g., Ethier et al., 2000), curved ducts (Yang and Kuan, 2006), and convex banks (Blanckaert, 2015), to name a few.

In the presence of significant enough adverse pressure gradient conditions, boundary layers (BLs) are known to separate, typically forming a closed separation domain, where the downstream flow reattaches. Studies of a two-dimensional laminar separation bubble via time accurate numerical simulations by Pauley et al. (1990) determined that a strongly imposed adverse pressure gradient (APG) would cause the flow

to separate and shed vortices with regular frequency. The shedding Strouhal number was found to be independent of both the Reynolds number and pressure gradient. They determined that 'bursting' events of the laminar separation bubble observed in experiments occurred under the same conditions of the periodic shedding in the numerical results, and therefore, these 'bursting' events were simply the periodic shedding events averaged over time. The vortices being shed due to the separation were found to be formed by the instability within the detached separated shear layer.

Although laminar separation demonstrates an unsteadiness due to the shedding of vortices as suggested by the results of Pauley, Moin et al. (1990), turbulent separation has an inherent unsteadiness upstream of the separation, which directly alters the flow physics and structure at and through separation differently than that of laminar separation.

1.1.1.1 Structure of Turbulent Boundary Layers and Turbulent Separation

Early experiments on a separating turbulent boundary layer by Simpson et al. (1977) showed that the separated flow begins to behave like a free shear or mixing layer as the outer flow displays similarity of several terms including the $\overline{u_2}$. This separated region is characterized by a large-scale intermittent region and large-scale spanwise structures. Further, it was shown that the normal stresses contribute significantly to the overall momentum and turbulence energy equations near separation as approximately one-third of the turbulence energy production is directly attributed to these stresses. Later experiments by Simpson et al. (1981) further added that high turbulence levels (u' and v') exist within the backflow on the order of the steady freestream magnitude ($|U|$), but owing to the steady freestream, the near wall fluctuations are not a result of the flapping of the separating shear

layer, but due to the inherent turbulence in the separated flow. These conclusions led them in their second paper Simpson et al., 1981 to an updated model of a turbulent separation where the backflow is actually controlled locally by the outer flow near the separation, instead of the traditional view where it occurred from far downstream. The local formation of large coherent structures that then pass through the separation are actually the source of the intermittent backflow.

Studies of a highly unsteady turbulent boundary layer (TBL) formed on a flat plate by Kiya and Sasaki (1983) showed that the ensuing separation bubble not only shed vortices with regular frequency (like the findings by Pauley, Moin et al. (1990)), but that there was also a remnant of a large-scale unsteadiness inherent to the closed separation region. This large-scale unsteadiness was accompanied by a dynamic enlargement and shrinking of that domain, as well as a 'flapping' motion of the outer bounding shear layer. Their later work focused on the reverse flow near the reattachment zone of the bubble found that the separation bubble experiences the shrinkage and enlargement in connection with the low-frequency unsteadiness of the bubble and that the speed of the speed of shrinkage is much larger than the enlargement of the bubble (Kiya and Sasaki, 1985). The strength of the large-scale vortices in this region were found to be dependent on the phase of the low-frequency unsteadiness. They further developed a model that suggested the large-scale vortices in the reattaching zone are hairpin vortices with each end rotating in opposite directions such that the fluid between the ends if lifted up in between them.

In his later review of turbulent separation, Simpson (1989) again noted that turbulent separation has a significantly different underlying flow structure than that of a turbulent attached flow. Some of the defining characteristics are that the largest turbulent

stresses occur within the middle of the free shear layer due to occurrences of large-scale vortices, which have a complex and direct effect on the recirculation zone, specifically due to the large pressure fluctuations associated by the passing of these structures. Consequently, these vortices cause the separated flows to be highly unsteady. It was further noted that in the case of 2-D diffusers, once the flow has separated it would form a transitory stall regime, wherein the flow from the exit of the diffuser would entrain back into the reverse flow region, flow upstream within the separated shear layer, and eventually effect the upstream separating conditions such that the stall would then get washed back out of the diffuser. This process repeats as part of the inherent unsteadiness due to the turbulent separation.

Experiments by Elsberry et al. (2000) on a boundary layer maintained on the verge of separation demonstrated a nearly linear streamwise growth of the integral length scales. They noted, however, that the need to use different length scales to collapse the velocity and turbulence profiles is indicative of this BL being maintained in a non-equilibrium state. Further adding to this conclusion, was the observation that the incoming BL was extremely sensitive to the upstream flow conditions and any slight increase in adverse pressure gradient caused the BL to suddenly detach as it was maintained close to separating conditions. When considering equilibrium and non-equilibrium turbulent boundary layers (TBL), Castillo and George (2001) showed that when the pressure gradient parameter Λ is constant that most TBLs appear to be equilibrium similarity BLs. This is contrary to the previous beliefs that equilibrium flows are difficult to achieve experimentally. The pressure gradient parameter, then, has three distinct regimes associated with it defining adverse ($\Lambda > 0$), favorable ($\Lambda < 0$), and zero ($\Lambda = 0$), overall pressure gradient equilibrium

conditions. The structure of both non-equilibrium and equilibrium TBLs were described by the earlier studies of Perry and Marušić (1995) and Marušić and Perry (1995). They showed that two types (Type-A and Type-B) of eddies describe the energy containing motions within TBLs, and that the combination of the two types can model both equilibrium and non-equilibrium TBLs. Type-A eddies are defined as wall bound structures with vortex lines that reach down to the wall surface and take multiple forms, but are generally considered as 'horseshoe-shaped'. Being wall bound, these structures produce finite Reynolds stresses at the wall. Type-B eddies are considered as wake structures, with vortex lines that undulate in the spanwise direction, but do not reach the wall, as the Type-A structures do. Consequently, these wake structures produce zero Reynolds shear stress at the wall.

Of particular relevance to the current experiments is the TBL in the presence of an adverse pressure gradient. Experiments conducted by Dengel and Fernholz (1990) of a TBL in the vicinity of separation demonstrated that in an APG the TBL displays a decrease in the mean velocity gradient ($\partial\bar{u}/\partial y$) at the wall, which is accompanied by a reduction in the Reynolds stresses. Concurrently, however, the peak velocity gradient ($\partial\bar{u}/\partial y$), peak Reynolds stresses, and peak production locations then move away from the wall. More recently, experiments by Schatzman and Thomas (2017) concluded that flow physics of TBLs exposed to significant APG to cause an inflectional mean velocity profile are governed by the formation of an outer embedded shear layer. The outer flow features of the embedded shear layer are brought about by the inviscid instability of this outer inflection point. The authors note that separation is not a pre-requisite for the existence of the embedded shear layer, simply a significant enough APG. They showed that the TBL

turbulence intensity peak corresponded to the wall-normal locations of the outer inflection point within the shear layer. Due to the shear within this layer that produces clockwise, spanwise oriented vorticity, the outer, high-velocity side of the inflection point, corresponds to ejection events ($u' < 0,\ v' > 0$) within the TBL, while the underside is associated with sweep-type events ($u' > 0,\ v' < 0$). As the flow physics are clearly governed by this outer inflection point, they were able to create a scaling parameter based off of the vorticity thickness within the outer embedded shear layer. Later experiments on a ramp geometry to develop an APG by Simmons et al. (2018) showed an excellent collapse of the mean velocity profiles using the embedded shear layer scaling of Schatzman and Thomas (2017). They did not, however, show a direct collapse of the turbulence intensity profiles using the same scaling parameters. It was later suggested that they could achieve better collapse of the normal stress profiles by substituting in the wall-normal location of the peak intensities into the scaling parameter (Simmons et al., 2019). Other experiments of a decelerated boundary layer in an increasingly adverse pressure gradient over a body of revolution by Balantrapu et al. (2021) further demonstrated the ability to scale the BL by the embedded shear layer scaling of Schatzman and Thomas (2017), again providing evidence that the TBLs in significant adverse pressure gradient behave more like free-shear layers as the importance of the near wall turbulence lessens (i.e. the outer flow becomes dominant).

1.1.1.2 Separation Cells

Large separation domains, generally associated with post-stall aerodynamics, are highly three-dimensional, unsteady, and the separated flow naturally evolves into cellular structures, commonly referred to as stall cells (Weihs and Katz, 1983, and Schewe, 2001).

Such separation cells are characterized by their mushroom-like shape consisting of a reverse flow region bounded by two counter rotating vortices or foci (Winkelmann, 1981), which typically form on an airfoil from the reverse flow region traveling back upstream and then spreading outboard from the center to form the pair of surface vortices. Weihs and Katz (1983) suggest that the stall cells form due to an instability of the leading and

trailing-edge vortices and their observations showed that these cellular structures occur

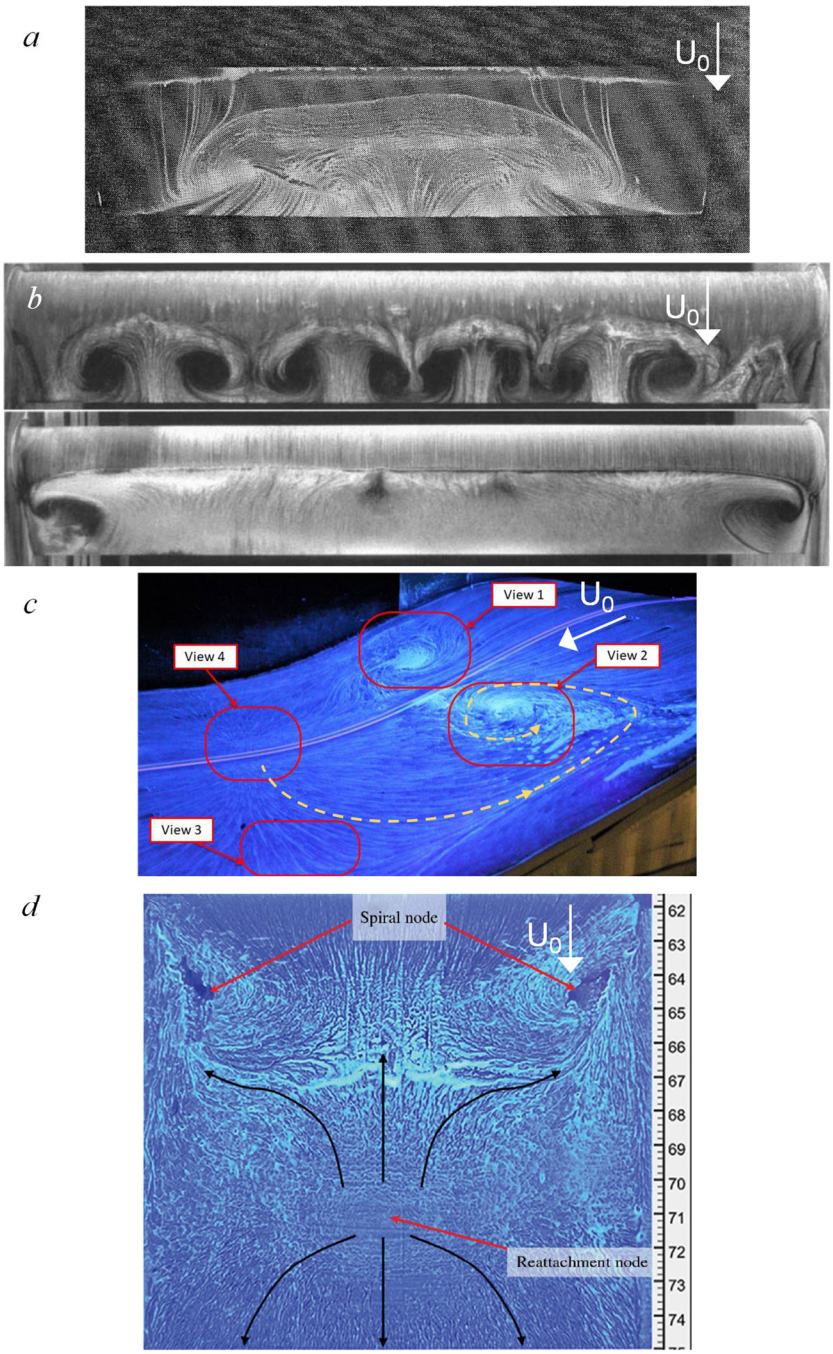

Figure 1.1. Examples of stall cell formation on airfoils (a and b) as well as their counterparts formed on internal flows over ramp-based geometries (c and d). The freestream direction (U_0) is indicated in each image by a white arrow. Images taken from Winkelmann (1982) (a), Schewe (2001) (b), Simmons et al. (2019) (c), and Koklu (2016) (d).

even on high aspect ratio planforms with the overall number of cells present being dependent on the aspect ratio, while the size of the individual cells seems to be independent of this parameter. Several examples of stall cells are given in Figure 1.1. A typical single cell formation on an airfoil is shown in Figure 1.1a, highlighting the central reverse flow region that fans out into the two counter rotating foci as the reverse flow meets the oncoming freestream flow over the airfoil. Stall cells are sensitive to the flow regime (i.e. Reynolds number), upstream conditions, and angle of attack in the case of airfoils, and as such, the formation of these structures are not limited to single cellular formations (Dell'Orso and Amitay, 2018). Such a pattern is indicated in Figure 1.1b which shows multiple cells forming on an airfoil (top), but at a different testing condition a single cell formation can span the entirety of the airfoil surface (bottom). Parametric studies by Dell'Orso and Amitay (2018) on a NACA 0015 airfoil indicated that the cells initially form above a critical Reynolds number where further changes in the Reynolds number and angle of attack lead to a variety of distinct surface patterns. Within these regimes, the number of cells present as well as their spanwise distribution (i.e. irregular spacing across the span) could be altered.

Experiments on the unsteady flow within stall cells and their pressure measurements by Yon and Katz (1998) showed two characteristic bands of high-frequency ($St \approx 0.15$) and large-amplitude low-frequency ($St \approx 0.04$) oscillations. The former is attributed to the wake instability, whereas the latter, large amplitudes are connected to the trailing-edge shear layers interacting with the model surface. They also noted that these frequencies were much lower than expected based on bluff body shedding, and that during tuft visualization the flow remained highly unsteady on the interior of the stall cells.

Rodríguez and Theofilis (2011) studied the global stability of separation cells and attributed their formation to amplifications of the laminar separation mode leading to a three-dimensional spanwise modulation of the separation that breaks down to form spanwise-periodic cells of separated flow regions in which the streamlines then organize around the typical counter-rotating foci. Investigations of separated flow on an 18% thick cambered airfoil designed for use on large scale wind turbines via stereoscopic particle image velocimetry (sPIV) by Manolesos and Voutsinas (2014) show that the surface-bound vortices in the separation cell are formed normal to the surface and quickly bend in the streamwise direction as they lift off the surface. As they lift off, they remain within the separated shear layer, above the reverse flow region, as they are convected downstream and eventually end up in the wake of the airfoil where their counter-rotation eventually pushes them up and away. They also demonstrated that the stall cells exhibited high concentrations of Reynolds stresses across the separated shear layer, which are indicative of fluctuations, specifically of the flapping nature of the shear layer (which were also shown in the prior findings of Yon and Katz (1998)). Investigations by Esfahani et al. (2018) examined the structural receptivity of a stall cell to active perturbations of varying frequency. They used plasma actuators at the leading edge to induce time-periodic perturbations on a separated flow over a VR-7 airfoil. The initial separation showed a nearly 3-D separation front, however, when actuated at three times the natural shedding frequency, the airfoil formed well-defined stall cells. They showed that further increases in the actuation Strouhal number stabilized the shape of the stall cells within a frequency band, above which the separating flow ceases to respond further to the actuation.

Stall or separation cells are designated as such because they were typically found forming on airfoils at (or near) stall conditions. However, similar patterns form in separated flows in internal geometries with imposed adverse pressure gradients (Figure 1.1c and d). Such separation conditions on ramp-like geometries form the familiar mushroom-like shape and counter rotating foci on the surface. One key distinction can be extracted, however, when examining the oil flow representations of Figure 1.1. The orientation of the counter-rotating foci is not always consistent between the airfoil (Figure 1.1 a and b) and ramp geometries (Figure 1.1c and d). The airfoils show the rotation of the surface bound vortices to rotate from the reverse flow and out to the sidewalls (clockwise on the right half of the cell in the images of Figure 1.1a and b), whereas the ramp geometries show the opposite (counter-clockwise on the right half of the cell in the images of Figure 1.1c and d). It is assumed the orientation is changed due to the presence of the side walls and the solid model surface in the ramp tests, where the oncoming flow over the airfoil extends past the stall cell.

1.1.2 Control of Separation (passive and active)

Nowadays, flow control effects a significant number of areas of aeronautical engineering performance such as external aerodynamic performance (e.g. drag and lift), internal flows (e.g. through propulsion systems and ductwork), acoustic characteristics, as well as turbulence transition and management (Joslin and Miller, 2009). Flow control techniques are categorized into either passive or active control strategies, where the former extract energy from the flow to effect changes, while the latter require external energy input that can typically be deployed as needed. Passive techniques such as the use of vortex generators (Mehta and Bradshaw, 1988, and Pauley and Eaton, 1988), do not require

external inputs and typically consist of mechanical surfaces that effect the flow. Active control requires an external input either via electrical power in the case of synthetic jets (Glezer and Amitay, 2002, Glezer, 2011, and Cattafesta III and Sheplak, 2011), or pressurized fluid in the case of fluidic oscillating jets (Cattafesta III and Sheplak, 2011, and Gregory and Tomac, 2013). In all instances of flow control the goal remains to reattach a separated flow, which is typically accomplished through the generation of vorticity (either stream- or span-wise) that re-energizes the boundary layer through entrainment of higher momentum fluid. The following subsections are focused on the review of a few types of actuators, but more importantly on the structural changes in the flow due to these methods.

1.1.2.1 Vortex Generators

Vortex generators (VGs) are small rectangular or wing-like vanes that are attached and extended from an aerodynamic surface to induce streamwise vortices that transfer momentum from the outer flow to the low-momentum region near the surface (Lin, 2002). The study by Pauley and Eaton (1988) discussed the characteristics of vortex pairs embedded in a turbulent boundary layer created by VGs oriented such that their common flow between vortex centers was directed away from (up) or towards (down) the surface. They demonstrated that in the areas where the induced secondary flow was towards the wall (down) the local boundary layer was thinned, whereas in areas when the induced flow was directed away from the wall the boundary layer was thickened. When directed with common flow up, the pair of vortices were carried away from the wall, but with common-flow down, the vortices remain wall bound and spread apart from each other as they progress downstream. As the vortices with common flow down remain wall-bound and

spread with downstream progression, consequently, they distort (i.e. thin) the boundary layer over the largest streamwise extent, implying that they would the ideal for separation control. It was further commented in this study that when multiple pairs of vortices are created, the neighboring pairs clearly influence the spreading of the vorticity in the streamwise direction (varying effects with common flow up or down), but did not increase the loss of vortex circulation.

When the common flow of the VGs are directed 'up', the vortices entrain and lift boundary layer fluid into them (Mehta and Bradshaw, 1988). The study by Mehta and Bradshaw (1988) showed that these vortices are convected downstream by the crossflow, but exhibit little 'wandering' or direct interaction between themselves once formed. The structural implications of VGs with common flow up, is that they form similar vortex pair orientations as that formed by steady jets in a crossflow (Kamotani and Greber, 1972, Fearn and Weston, 1974 , Fric and Roshko, 1994 and Mahesh, 2013). The study by Fric and Roshko (1994) showed that the vortical structures formed by a jet in crossflow do not originate from the shedding of the jet, but by the alteration of the vorticity that originates in the boundary layer of the near-wall (similar to the origination of the vortices by VGs) and as they convect downstream, sweep boundary layer fluid and vorticity into their base (into the upwash domain).

The formation of these longitudinal vortices by physical VGs has also been reconstructed by the use of pitched air-supplied vortex generator jets (Johnston and Nishi, 1990). The study by Johnston and Nishi (1990) showed that the formation of these longitudinal vortices of sufficient strength was able to reduce a large region of turbulent separated flow. They also showed that within their test parameters, arrays of counter

rotating vortex pairs gave way to large spanwise variations in the flow as not every vortex pair interacted together, and that when the jets pointed directly normal to the surface they had no effect on the separated region due to the lack of significant longitudinal vortex formation. They further postulated that in their case the extent of the separated region was more strongly affected by bringing the reattachment location upstream rather than pushing detachment downstream when considering the jet arrays intentionally forming pairs of counter rotating vortices.

1.1.2.2 Synthetic Jets

Synthetic jets (zero-net mass flux actuators) are formed through the intake and ejection of fluid through an orifice (commonly via piezoelectric materials), and this creates an inherent advantage of synthetic jets in that they use the working fluid of the system with which they are deployed (Glezer and Amitay, 2002). The expulsion of fluid from the orifice consequently forms vortex sheets that roll into isolated vortices as they are convected by the outer cross flow (Glezer and Amitay, 2002). As the synthetic jet actuators form discrete pulses based on their operational input (i.e. driving frequency) their operation can alter the cross flow in various ways. When the actuators are driven near the shedding frequency of the separated shear layer on an airfoil ($F^+ \sim O(1)$) the formation of discrete vortex structures creates an unsteady flow reattachment. However, in typical operation approximately one order of magnitude higher than the shedding frequency ($F^+ \sim O(10)$), the flow reattachment is not characterized by discrete vortical structures and is therefore a steadier process (Amitay and Glezer, 2006). Dandois et al. (2007) simulated the effects of synthetic jet forcing on a generic separated flow over a smooth ramp and found that there were two distinct modes of forcing that reduced the separation length: a vorticity dominated

mode at low operation frequencies, and an acoustic dominated mode at higher frequencies. They observed that in the lower frequency, vorticity dominated mode, the forcing is correlated to an increase in the turbulent kinetic energy as well as entrainment into the separation bubble. The three dimensional structure developed due to a synthetic jet operating at a significantly high actuation frequency to decouple it from the T-S waves in a crossflow was studied by Van Buren et al. (2016). They showed that the jet formed a localized recirculation region directly behind the jet orifice due to the suction and blowing cycles which induced a blockage of the cross flow by the expelled jet, but farther downstream, the jet formed two counter-rotating vortices with an associated upwash aligned with the center of the jet (again structurally similar to the VGs with common flow up and the steady jet in a cross flow discussed in Section 1.1.2.1). These counter-rotating vortices significantly increase the velocity within the boundary layer through entrainment of the outer surrounding flow, while the lifted low-momentum fluid along the center of the jet created a velocity deficit in the outer flow, implying that the decoupled operation of the synthetic jets would reattach a separated flow by re-energization of the boundary layer via these counter-rotating streamwise vortices.

1.1.2.3 Fluidic Oscillators

Fluidic oscillators convert a pressurized fluid supply to an oscillating jet through the internal interactions of a pair of supply streams in a chamber, which results in a sweeping jet capable of high exit velocities (Raghu, 2013). The oscillators are considered as feed-back free, wherein the supply jets interact directly to create the oscillations, or feedback type designs, which are built with internal feedback loops to create the oscillations (Raghu, 2013). Examples of such designs are shown in Figure 1.2. Fluidic

oscillators alter their oscillation frequency via the supplied pressure, or in turn the induced velocity ratio as the supplied pressure directly translates to output velocity (Raghu, 2013). Studies by Ostermann et al. (2019) of a fluidic oscillator issued into a crossflow show that it develops streamwise vortices outside of the boundary layer, which are then convected by the outer crossflow. The cross-flow penetration of the oscillating jet was found to be lower than that of a steady jet, while instead, affecting a much larger spanwise domain. They also showed that the penetration depth was dependent on the velocity ratio of the jet, but further that the deepest penetration occurred at the full deflections of the jet due to the dwelling time inherent in the fluidic oscillator operation. As the deflections of the jet are dependent on the velocity ratio, for small oscillations, they showed that the cross flow was able to adapt to all instantaneous realization of the deflecting jet and created a formation mechanism similar to that of a vortex-generating jet (see Mehta and Bradshaw, 1988, and Johnston and Nishi, 1990). For higher Strouhal numbers, the wake cannot adapt and consequently the crossflow only sees the jet at its larger dwelling times at full jet deflection, which creates a pseudo steady inclined jet at two angles (each deflection). Due to the oscillatory nature and formation of counter-rotating pairs of vortices the authors suggest the effectiveness of the oscillating jets on separation control or mixing stems from their creation of many streamwise vortices dependent on velocity ratio and deflection angle. Fundamentally, however, the flow fields are dependent on the Strouhal number of the operation of the jet, which incidentally, is entirely a function of the velocity ratio and not

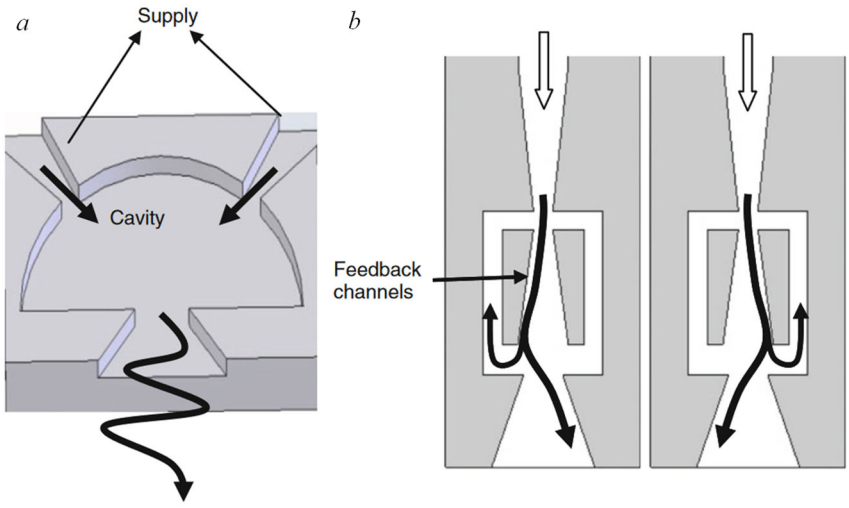

Figure 1.2. Schematics of feedback free (*a*) and feedback (b) fluidic oscillator designs. Images taken from Raghu (2013).

of the actuator size allowing for extrapolations of the flow field to other oscillator designs (Woszidlo et al., 2019 and Ostermann, Woszidlo et al., 2019). When the oscillation angle is skewed to the crossflow, as in the study by Ostermann et al. (2019), the formation of the vortices is clearly altered. At skew angle of 45^{o} only one dominant vortex is formed, while the penetration depth remains similar to the 90^{o} condition. Further when the jet is skewed such that the oscillation direction is parallel to the free stream, the jet operates similar to a steady jet, with larger penetration depth than the other skew angles due to the jet opposing some of the streamwise bulk flow during the oscillation.

For simulations of the fluidic oscillators used in the current experiments, as well as comparisons to experimental data (Chapter 4 and 5), please see the work by Koukpaizan (2020)

The effectiveness of fluidic oscillators compared to steady jets for separation control was assessed by Otto et al. (2018) on the NASA hump geometry. They

demonstrated that for a given jet spacing, fluidic oscillators (feedback type design) required lower momentum, mass, and energy coefficients to achieve similar control authority compared to steady jets. Conversely for a given input coefficient matched between the jet types, fluidic oscillators showed increased performance. The increased control of the fluidic oscillators was determined to stem from the increased organization of the separated flow into counter rotating vortex pairs as compared to the structure developed by the steady jets. The oscillating jets also demonstrated a reduction in the turbulent kinetic energy levels in the flow compared to that of steady jets, owing to the increased organization of the flow. Similarly, several different designs of fluidic oscillators were tested on the NASA hump model by Otto et al. (2019) to examine the effects of varying the internal geometry and exit angles of the oscillators. Despite the similar operational frequencies of the jets, they showed that the performance of the oscillators varied by design, indicating that the oscillation frequency is not a driving parameter for flow control. According to their studies the feedback free design performed worse overall compared to the feedback type designs. They showed further that the highest performing design (one of a feedback type) organized the flow into an array of counter-rotating vortices across the separated domain. More recent experiments by Koklu (2021) also examined the effectiveness of fluidic oscillators on the NASA hump compared to steady blowing, steady suction and synthetic jet actuators. They similarly found that fluidic oscillators demonstrated substantial control over the flow separation by increasing the upstream suction and downstream pressure recovery levels. Their unsteady pressure measurements taken near the oscillators showed the oscillation frequency of the jets, but also found that the oscillators do not cause vortex shedding associated with the separating bubble, which they attributed to the random oscillations of

the individual actuators within the array. They further found that when comparing actuators at similar momentum coefficients, the synthetic jet types actuators demonstrated less improvement, while the suction types and oscillators generated similar C_p distributions.

When deployed on a ramp-geometry, the experiments of Kim and Kim (2019) showed that the installation pitch angle of the fluidic oscillators relative to the outer moldline altered their overall effectiveness and was the most sensitive condition compared to the yaw or roll angles. They showed that a shallow pitch angle along the moldline surface ($\alpha = 20^{\circ}$ vs $\alpha = 90^{\circ}$ in their experiments) nearly doubled the overall effectiveness of the flow control. It was also shown that the spanwise deployed jets formed arrays of vorticity concentrations of opposing sense across the span, and demonstrated increased free stream velocity along the centerline of the jets' issuances. When compared to a single line array, the streamwise staggering of every other jet reduces the overall effectiveness.

The studies by Kim and Kim (2019) suggest that a reduced angle between a fluidic oscillator and the surface moldine where it is deployed increases the effectiveness compared to issuing directly normal to the crossflow. In the limit of this pitch angle, the fluidic oscillator will become a wall jet, with significant differences compared to the jets in crossflow discussed by Ostermann, Woszidlo et al. (2019). Studies of a wall-jet in the absence of crossflow by Matsuda et al. (1990) showed the development of counter-rotating vortices due to the jet. They suggest the wall-jet develops a similar shape to that of a horseshoe-like vortex with the legs tilting as the jet advects downstream, which in turn induces streamwise vorticity accounting for the lateral spreading of the jet in the downstream direction. A comprehensive study by Namgyal and Hall (2016) discusses the

varying characteristics and turbulent fluctuations inherent to the turbulent wall-jet. One observation they also made is the natural development of a counter-rotating vortex pair, and that the oriented pair evolves downstream such that the mean flow is drawn to the wall along the centreline and laterally outward as the jet progresses. They also showed the streamwise fluctuations had the largest impact on the Reynolds stresses throughout the jet due to the larger value of the average U velocity along the jet. The Reynolds shear stress ($\overline{uv}$) was found to be higher along the jet centerline at all downstream measurement locations, and was found to be a positive quantity which is commonly associated with separating shear layers.

1.1.3 Flow Control Applications and Performance Enhancement in Internal Flows

The fundamental conditions giving rise to separation and the ensuing flow physics as well as the technologies developed to control them (and ensuing structural changes) have been discussed in Sections 1.1.1-1.1.2. This subsection will discuss the application and flow physics effects of some control methods, and their ability to reduce separation and enhance performance in internal flows.

Studies of a separated internal flow by Nishi et al. (1998) demonstrated the ability of vortex generating jets (VGJ) to control the flow separation in a conical diffuser by assessing the overall internal losses. They reported that improvement in the pressure recovery coefficient C_p when the VGJ velocity ratio became greater than 1, and that for every VGJ arrangement there was a total increase in C_p with increasing velocity ratio. Since additional power was required to continually supply the jets and increase the recovery, another parameter was developed to assess the performance of the jets based on

the total energy conservation. They were able to show that the minimum losses occurred for VGJs with VR between 1.5 and 2 based on this parameter, and that further increases in VR cause the energy loss to increase rapidly. The study by Suzuki et al. (2004) considered flow separation in a two-dimensional diffuser and its control via periodic mass injection. They were able to show that the control reduced the size of the separation bubble, but had minimal effect on the local separation location. Their reduced order model also showed that the control alters the vortex formation and separation dynamics, leading to a reduction in the stagnation pressure loss even though the BL remained separated due to the more frequent shedding of the vortices (rather than the large-scale unsteadiness in the unforced diffuser separation). A study by Amitay et al. (2002) of internal separation in a two-dimensional diffuser with rectangular cross section showed that an array of synthetic jets can alter the streamwise extent of the separated domain. For $M < 0.2$ the flow became fully attached, whereas for $0.2 < M < 0.3$, the downstream reattachment of the separation moved upstream compared to the unactuated condition. Concomitantly with the reduced separation domain, the duct experienced a reduction in losses and an increased volume flow rate. Investigations of steady and unsteady slot blowing at the inlet of a compact rectangular offset duct ($M \approx 0.45$) conducted by Vaccaro et al. (2015) showed that steady blowing was able to reduce the separated domain and improve the overall losses by 1.7%. They also showed that unsteady forcing of the large slot jet had no improvement on the overall performance for St = 0.26, 0.59, which was attributed to the presence of a quasi-steady secondary corner flow structures. The steady actuation did, however, eliminate the shedding frequency found in the baseline separation field.

More recently, a study by Gartner and Amitay (2015) compared the effectiveness of sweeping, pulsed, and two-dimensional (slot) jet actuation on pressure recovery within a transonic rectangular diffuser duct and demonstrated that sweeping jets produced a larger pressure recovery at a mass flow ratio of 0.65% when compared to the other jets operated at a mass flow ratio of 1%. Experiments utilizing fluidic oscillators in a complex serpentine diffuser geometry by Burrows et al. (2021) showed that coupling fluidic actuation to the development of streamwise vortices can reduce distortion at the representative interface plane (AIP) of an engine by up to 60% at $M_{AIP} < 0.57$ using a mass flow rate ratio of $C_q < 0.5\%$. The actuation jets reduced the base flow separation domain by inducing vorticity concentrations of opposing sense on the outer edges of the actuator array, which incidentally modifies the surface vorticity layer to control the formation and evolution of streamwise vortices leading to the reduction in measured distortion.

1.2 Thesis Objectives and Overview

The present investigations focus on the key flow physics alterations to a nominally separated cross-flow in an adverse pressure gradient over a curved surface brought upon by the application of active flow control via a spanwise array of fluidic oscillating jets. The goals of the current research are to address the following:

1. Explore the structural and dynamic effects of spanwise fluidic actuator arrays on internal separation in an adverse pressure gradient within a diffuser.
2. Investigate the velocity field in spanwise and streamwise cross-stream planes upstream and downstream of separation in the base flow and in the presence of actuation.

3. Explore scalability of the flow field by the outer flow over separation in the absence and presence of actuation.
4. Assess the effectiveness of the actuation in the suppression of separation in a branched diffuser configuration.
5. Characterize the flow topology of a separation cell in an internal diffuser formed by a curved surface insert in a channel in the absence and presence of actuation.
6. Explore spanwise interactions between the actuation jets and the separation cell to characterize flow mechanisms that lead to attachment.
7. Investigate the effects of these interactions on the structure and turbulent characteristics of the separation domain at different spanwise actuation wavelengths.

Chapter 1 presents an overview of the relevant literature on the characteristics of turbulent separated flows and applications of flow control for the suppression of separation. The experimental setup of the present investigations is described in Chapter 2 including the wind tunnel facilities and the two test models for investigations of low separation in adverse pressure gradient in the presence and absence of fluidic control. The application of fluidic control for mitigation of the separation at the entrance of a branched diffuser with specific emphasis on structural changes of the separation that leads to reduction in losses and enables regulation of the mass flow rate fraction is discussed in Chapter 3.

The separation cell that is formed by separation in an adverse pressure gradient within a diffuser is the focus of Chapters 4 and 5. Chapter 4 focuses on the flow evolution along the center plane of the separation cell and comparison to the characteristics of the flow in Chapter 3. The three-dimensional characteristics of the separation cell in the base

flow and its receptivity to fluidic actuation at varying spanwise actuation wavelengths are investigated in Chapter 5 with emphasis on flow reattachment and its turbulent characteristics. Finally, the summary of the present investigations and the key findings and insight are presented in Chapter 6.

CHAPTER 2. EXPERIMENTAL METHODOLOGY

The experiments focusing on boundary layer separation and its control in an adverse pressure gradient were conducted in two stages in two separate wind tunnel facilities at Georgia Tech. In the first stage, separation was investigated within a duct diffuser test section pressure driven by an upstream blower, while in the second stage, separation was investigated over a curved surface within the test section of a transonic facility driven in suction by a downstream diffuser. The local structure of the separating flow and its control were investigated using planar and stereo particle image velocimetry. This chapter describes the wind tunnel facilities and diagnostic techniques.

2.1 Wind Tunnel Facilities

2.1.1 Pressure Driven Tunnel

The experiments described in Chapters 3 and 4 are conducted in a small, open-return, subsonic wind tunnel ($M_0 < 0.5$) that is driven by a computer-controlled 75 HP

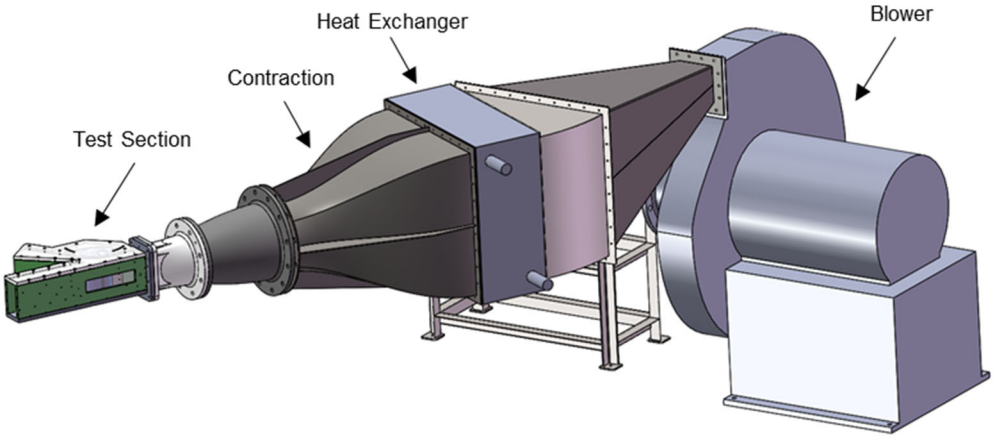

Figure 2.1. Subsonic, pressure driven wind tunnel, with blower, contraction, water-cooled radiator, and test section.

blower shown in Figure 2.1. The tunnel's test section is connected downstream of a settling section that comprises a low pressure drop chilled water heat exchanger along with a honeycomb block and screen followed by a contraction with contraction ratio 6.3:1. The test section forms a primary duct (primary channel dimensions: $L = 641$mm, $W = 2H$, H=76.2 mm) with a branched diffuser where each of the flow streams issues into the still ambient. The air streams are directed into the inlet of the diffuser using a curved deflector wall. The mass flow is measured at the inlet of the blower using a connected custom mass flow meter calibrated by Colorado Engineering Experiment Station Inc. (CEESI), which consists of an extended diameter-matched PVC tube with incorporated honeycomb elements and surface integrated static pressure ports connected to a 100 torr rated *MKS Baratron* pressure transducer to measure the pressure drop (and convert to mass flow) across the device.

2.1.2 Suction Driven Tunnel

The experiments described in Chapter 5 are conducted in an open-return, transonic ($M_0 < 0.75$), wind tunnel facility operated by suction using a downstream 200 HP blower as shown in Figure 2.2. The inlet section includes a bank of filters upstream of a plenum that includes screens and honeycomb upstream of a contraction (contraction ratio 44:1) that is connected to the test section (66 x 12.7 x 12.7 cm). The downstream end of the test section is connected to the blower through a diffuser. The blower exhausts the air through two overhead chilled water heat exchangers to control the exit air temperature. The tunnel enables better turbulence control than the pressure driven facility and the test section is designed to enable optical access for stereo PIV.

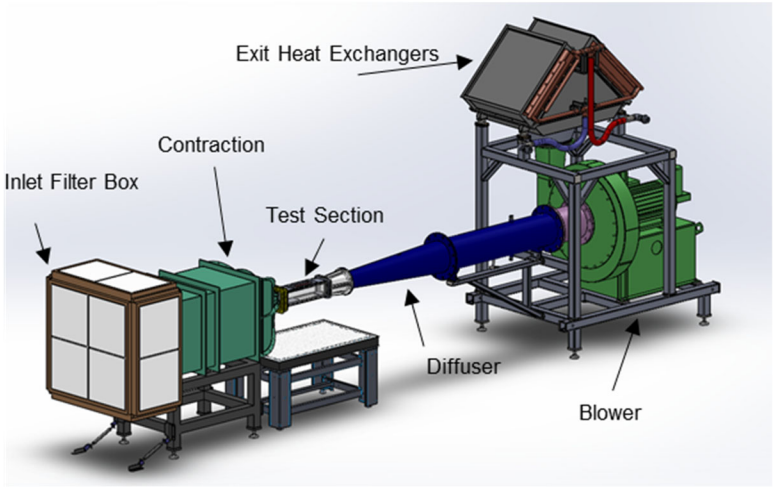

Figure 2.2. Suction operated transonic wind tunnel facility.

2.2 Test Sections

2.2.1 Diverging Diffuser in the Pressure Driven Tunnel

The modular diverging diverter was integrated into a constant cross section duct (measuring 76.2 mm high, 152.4 wide and 641mm long.) along a curved cylindrical surface having a radius of 152mm such that its upstream edge is 120 mm downstream from the duct's inlet as shown in Figure 2.3. The diffuser spans the entire width of the constant cross-section duct and its angle relative to the duct is adjustable along the cylindrical surface, by rotating the entire flow control module (purple component) shown in Figure 2.3a. In the present experiments, the diffuser is adjusted so that its upper and lower surfaces are at $\theta_1 = 45°$ and $\theta_2 = 60°$ relative to the centerline of the duct (cf. Figure 2.3b) so that the minimum distance between the lower branched wall and its upper surface in the diffuser section is 47.9 mm at the inlet (the throat of the diffuser section) and 122.7mm at the exit plane (while maintaining the same cross section width as the primary channel W = 152.4mm). The upper surface of the diffuser section transitions to the back to the

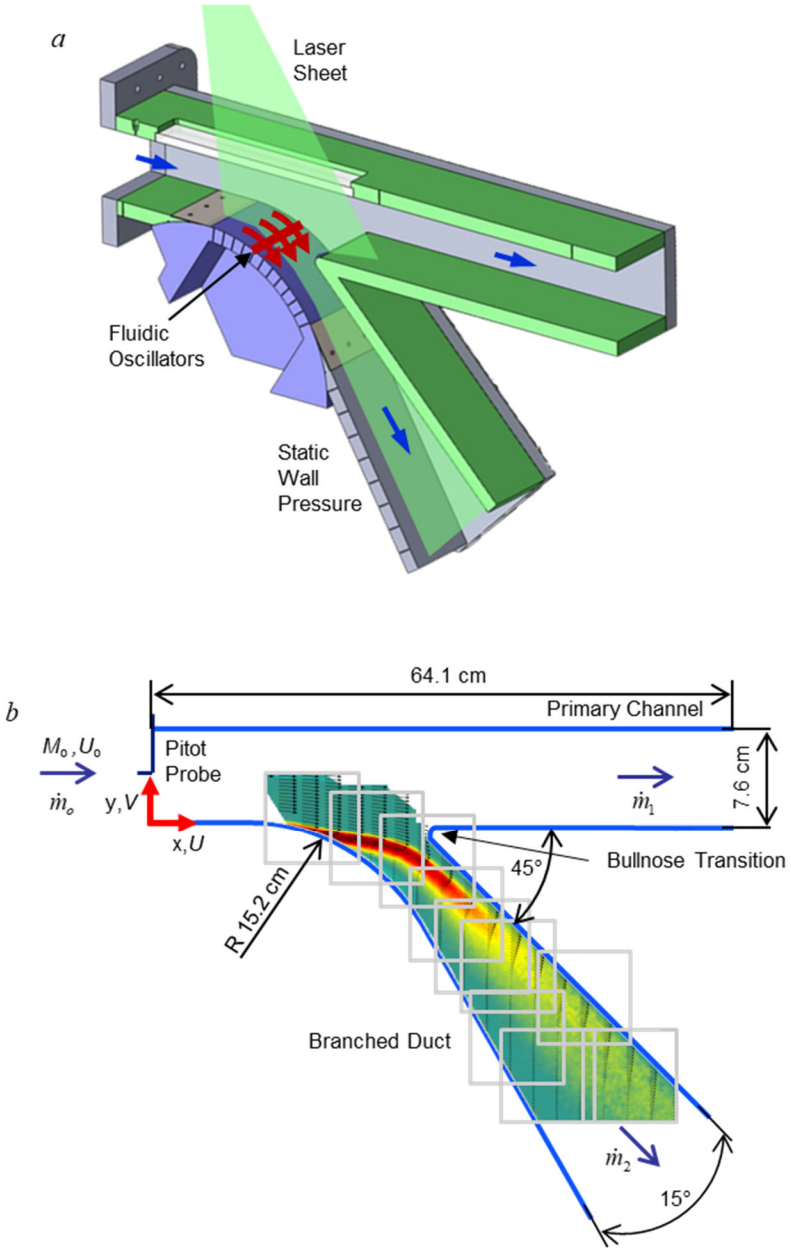

Figure 2.3. a) CAD model of the diffuser duct showing the cylindrical transition surface (R = 152.4mm) between the lower wall of the test section and the upstream surface of the diffuser's lower wall. The spanwise array of 23 fluidically oscillating actuation jets is marked on the transition surface; b) Side view of the test section showing the coordinate system and the relevant dimensions. The drawing also shows an overlaid sample composite PIV image of the spanwise vorticity in the base flow at $M_0 = 0.4$ diverted into the diffuser and partially overlapping PIV windows.

primary duct using a 12.7 mm diameter rounded bullnose fit (cf. Figure 2.3b). The lower

surface is equipped with surface static pressure ports at three distinct locations along the central plane: 1 port aligned at the entrance plane ($x = 0$), one cluster along the flow control module ($2.4 < x/H < 3.4$), and one downstream cluster ($3.76 < x/H < 4.76$). One sidewall is constructed of clear acrylic to allow optical access for particle image velocimetry. Flow separation at the upstream end of the diffuser's bottom surface is controlled using a spanwise array of fluidically oscillating jets that are integrated into the cylindrical transition surface (Figure 2.3a) such that they issue tangentially to the local surface using an overhang (discussed in Section 2.4). Since the jets are integrated into the (fixed) cylindrical surface, their streamwise position relative to the straight segment of the diffuser's bottom surface varies between $x = 120$ to 230 mm within the 60° arc travel of the cylindrical surface rotation. In the present experiments discussed in Chapter 3, the jet exit planes are located 152 mm downstream along the surface ($x/H \approx 1.6$) of the duct's inlet plane ($x = 0$), which was determined based on tufts visualization of the base flow separation location at $M_0 = 0.4$.

2.2.2 Test Section for Investigations of Separation Control on Curved Wall Insert

For detailed investigations of flow separation control on curved surfaces, a separate test section shown in Figure 2.4 was designed, constructed, and tested in both the pressure and suction driven tunnels (cf. Figure 2.1 and Figure 2.2). This test section comprises a constant cross-section duct measuring 127 mm wide, 127 mm high, and 660.4 mm long (W, H, L, respectively). As shown in Figure 2.4 one wall of the test section includes a 2-D modular insert based on a VR-12 airfoil that imposes an adverse pressure gradient to induce local flow separation. The insert models the suction surface of the VR-12 airfoil at an angle of attack $\alpha = 13^{o}$ with a chord of $c = 62.23$mm which is highlighted by the dashed

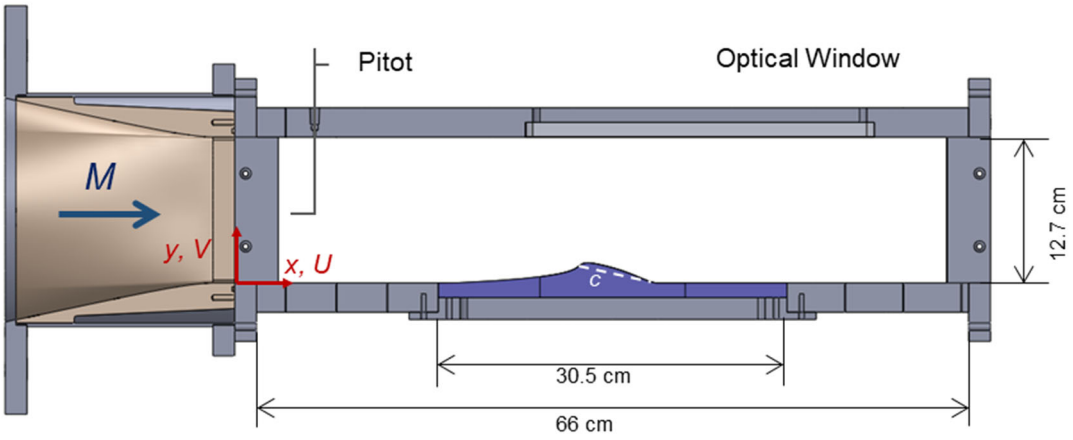

Figure 2.4. Test section geometry with global coordinate system and model showing chord length (c) for reference, as well as the inlet Pitot probe location.

line in Figure 2.4. A trip wire of diameter $0.007c$ is mounted at $x/c = 4.8$ ($0.05c$ upstream of the airfoil's leading edge) to ensure a Reynolds number independent flow separation location. The centerline ($z/c = 0$) is equipped with surface static pressure ports that span from the entrance ($x/c = 0.7$) to the end of the test section ($x/c = 10.2$), with the majority of the ports located along the aft of the insert model surface ($2.5 < x/c < 0.8$). The tunnel sidewalls are constructed using clear borosilicate glass to enable optical access for both planar and stereoscopic PIV, while the wall opposite the model insert has an inlaid glass floor to allow access for a laser sheet. Flow control is effected using integrated spanwise arrays of fluidically spanwise-oscillating jets (discussed in Section 2.4) that issue tangentially to the surface (cf. Section 2.4) of the model at $x/c = 5.10$.

A slim-profile Pitot probe is integrated into the test section at $x/c = 0.71$ downstream of the inlet plane ($x = 0$) for characterization of the oncoming flow Mach number, which is nominally set to $M_0 = 0.25$ (corresponding to a Reynolds number of $Re = 345{,}000$). This probe is paired with the wall static pressure in the same plane, and

this measured static pressure, along with the calculated Mach number at the test section inlet, are used as reference values for the flow characterization.

2.3 Diagnostics

2.3.1 Pressure Measurements

The inlet static and total pressures are measured using installed 1/16" pitot static probes centered (width and height) in the inlet plane and collocated with the first static surface pressure port in each test section ($x/H = 0$ in Figure 2.3 and $x/c = 0.7$ Figure 2.4). The static and total pressures are measured by dedicated *MKS Baratron* temperature compensated, differential pressure transducers connected to a National Instruments A/D data acquisition board (DAQ) and sampled at 200 Hz. The static pressures are measured using a 10 Torr (suction wind tunnel) or 100 (pressure driven wind tunnel) Torr rated model, while the total pressure is monitored via a 1000 Torr rated model in both wind tunnels. The transducers measure differential pressure (to ambient in the current experiments) and the inherent internal offsets are corrected by measuring the differential at ambient pressure conditions before operating the tunnels and the offset is subtracted to ensure a true zero reading when acquiring data during wind tunnel operations. The absolute ambient pressure is monitored separately with a Princo Fortin mercury barometer inside the lab. The *MKS Baratron* transducers output a linear voltage to pressure conversion from a 0-10 Volt range (0 to maximum stated pressure rating of each model: either 10, 100, or 1000 Torr) and have an error of 0.25% of the output voltage value (i.e. a reading of 5 V with a 10 Torr *Baratron* means an uncertainty of ±0.0125 V or ±0.0125 Torr).

Static pressure distributions along each of the two test sections (Section 2.2, Figure 2.3 and Figure 2.4) are measured using a dedicated PSI Netscanner system, having 5 scanner modules [range of 34.5 kPa (5 psi)]. The scanner takes 64 samples for each transducer (1 dedicated transducer per pressure port) and outputs the averaged values at a rate of approximately 3 Hz (not time-resolved). Typically, the mean static and total pressures are then based on 75 or 100 of such internal averages, creating a sample range over 25 to 33 seconds. The PSI system is quoted as having an accuracy of +/- 0.05% of full scale (corresponding to accuracy of +/- 17.25 Pa for these modules) for each individual measurement when the modules are re-zeroed to a known reference pressure (ambient in the current experiments) before use. This process is done before every use of the system. The PSI system is connected to the data acquisition computer using an ethernet connection.

The pressure coefficient C_p is computed using Equation 2.1:

$$C_p = \frac{2}{\gamma M_r^2}\left(\frac{p}{p_r} - 1\right) \tag{2.1}$$

where M_r is the reference Mach number calculated at the inlet of each test sections using the installed pitot probe and using Equation 2.2:

$$M = \sqrt{\frac{2}{\gamma - 1}\left(\left(\frac{p_t}{p_s}\right)^{\frac{\gamma-1}{\gamma}} - 1\right)} \tag{2.2}$$

The specific heat ratio for air (γ) is temperature corrected using thermocouples embedded into the individual test section inlet surfaces at the same streamwise locations as the pitot measurements ($x/H = 0$ in Figure 2.3 and $x/c = 0.7$ Figure 2.4). The reference pressure (p_r)

is the surface static pressure port collocated with the measurement plane of the individual pitot probes in each test section ($x/H = 0$ in Figure 2.3 and $x/c = 0.7$ Figure 2.4).

2.3.2 Mass Flow Measurements

The inlet mass flow rate ($\dot{m}_o$) in the diverter test section (cf. Figure 2.3) was measured using the custom calibrated CEESI mass flow meter discussed in Section 2.1.1. A secondary measurement of the inlet flow rate was also taken using the installed inlet pitot probe, which calculated the inlet Mach number, and assuming a bulk inlet flow at the test section entrance and calculating the air density from the installed thermocouple allowed for a secondary measure of the inlet mass flow rate ($\dot{m}_0$). Of interest is the ensuing split of the mass flow rate into the primary channel ($\dot{m}_1$) and the secondary branched duct ($\dot{m}_2$) and their changes with the application of the flow control. The mass flow rate fraction that is diverted into the secondary duct ($\dot{m}_2 = \dot{m}_0 - \dot{m}_1$) is computed using the mass flow rate at the exit plane of the primary duct ($\dot{m}_1$) estimated from measurements of the exit Mach number on a grid of 12 x 12 equally spaced points (Δy = 6.35 mm, Δz = 12.7 mm) at the exit plane (y-z) of the constant cross-section duct. The mass flow rate is determined from the total pressure measurements (via Netscanner System) at each grid point and the Mach number is calculated (Equation 2.2) using the lab static pressure, then the Mach number at each point gives an area averaged velocity and using the total exit area of the duct, and air density (using same inlet temperature) are used to determine the exit mass flow rate of the primary duct ($\dot{m}_1$).

2.3.3 Planar Particle Image Velocimetry

Planar PIV was used to measure cross-stream velocity components within the center planes of the diffuser (cf. Figure 2.3) and over the model insert (Figure 2.4). The flow was seeded with 1-5 μm fog particles (Rosco Vapour and Rosco 1700). The flow is illuminated using a single-cavity high-speed (up to 10kHz) ND:YLF laser (Photonics DM50-527-20D/4, 527 nm, 25mJ/pulse). The thickness of the laser sheet within the field of view is nominally set to 1.5 mm at its center on the surface of the test section. Planar measurement are taken using a high-speed 1024 x 1024 pixel camera (CCD FASTCAM-1024PCI) and a Nikkor 60 mm f/2.8 yielding a spatial resolution of 13 px/mm and a Nikkor 105 mm f/2.8 lens with a 2x teleconverter yielding spatial resolution up to 48 px/mm. The raw PIV images are acquired and processed using LaVision's DaVis software.

Within the diffuser (cf. Figure 2.3), the flow field was measured in multiple cross stream planes along the centreline using high-speed PIV as shown in Figure 2.3b and the CCD camera is translated using a computer controlled two-axis (*x*-y) traverse. Three separate sizes of PIV interrogation domains are used in the investigations in Chapter 3 (cf.

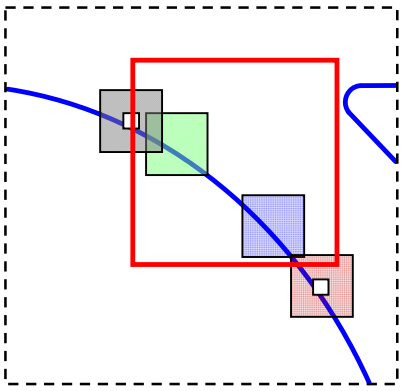

Figure 2.5. The planar PIV fields of view along the centerline of the entrance to the diffuser (cf. Figure 2.3b). One example of the larger field of view (0.95H x 0.95H, red square) is shown in reference to the four domains centered about the base and delayed flow separation locations (0.28H x 0.28H, shaded squares) and the two locations used for spectral analysis of the base and controlled flow (0.06H x 0.06H, white squares).

Figure 2.5). For the measurements described in Section 3.2, the largest domain (0.95H x 0.95H, 13 px/mm, cf. red square Figure 2.5 for size reference at the inlet to the secondary channel) is used to capture the entire flow field ($1 < x/H < 4.8$) through the secondary duct by taking measurements in 10 separate locations and creating a composite image of the entire flow field; such a composite image of the base flow is shown in Figure 2.3b using the large measurement domains. These data sets are taken at 200 Hz, and each measurement consists of 800 PIV image pairs. The second interrogation domain (0.28H x 0.28H, 48 px/mm) is used to zoom in to examine local features about the separation in the presence and absence of actuation. The four individual measurement domains are shown in Figure 2.5 as shaded rectangles in reference to the size of one single measurement window of the larger domain (0.95H x 0.95H), and are centered about $x/H = 1.56$, 1.80, 2.13, and 2.46 from left to right, respectively. The domains are centered about the time-averaged separation point, which is delayed and shifted downstream with increasing actuation levels. These data sets are also comprised of 800 images acquired at 200Hz. Finally, the smallest measurement domains (0.06H x 0.06H, 48 px/mm, white rectangles Figure 2.5) are used to examine the spectral content of the flow in two locations centered at $x/H = 1.56$ and 2.46. These data are acquired at 5 kHz and each set is an ensemble of 5000 images.

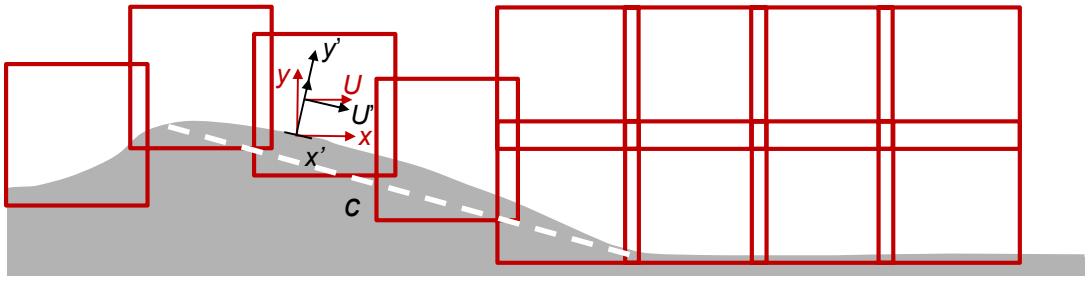

Figure 2.6. Side view of model geometry and zoomed-in view of twelve partially-overlapping individual PIV windows. The fixed global (x, y) and local wall-normal (x', y') coordinate systems are shown for reference.

Over the ramp insert (cf. Figure 2.4) the planar PIV measurements are acquired in 12 overlapping fields of view (0.31c x 0.31c, 52 px/mm) to create composite images of the flow spanning $4.6 < x/c < 6.7$. The locations of the fields of view and insert model are shown in Figure 2.6. Each ensemble was recorded at 200 Hz and included 1000 individual image pairs in each measurement location.

2.3.4 Spectral Analysis of the PIV Data

Spectral analysis of the flow is conducted using a field of view measuring 0.06H x 0.06H (cf. Figure 2.5) centered at $x/H = 1.56$ and 2.46 when the YLF laser is operated at 5 kHz. These highly resolved measurement domains (0.06H x 0.06H, 48 px/mm) yield a 20 x 20 grid with 250 μm resolution. This resolution produces 5 equally spaced velocity (U and V) time traces over the same span that a typical miniature hot-wire sensor (1.25 mm x 5 μm diameter) would produce a single measurement. Within each measurement domain, ten individual PIV data sets consisting of 5000 images were taken over 1 second intervals, and the individual velocity fluctuation spectra at each measurement point are averaged to suppress noise levels with a final spectral resolution of 1 Hz. The PIV spectra have a maximum bandwidth of 2.5 kHz

The spectral analysis of the PIV fields is conducted using a methodology developed by Peterson et al. (2020) to correct for inherent laser pulse timing fluctuations in single cavity lasers. At high repetition rates, single cavity lasers are known to have internal timing errors which results in the spacing between consecutive pulses (Δt) to be non-uniform throughout a PIV acquisition sequence. With non-uniform timing, the PIV images incorrectly calculate the velocity fields based on the measured particle motion due to the assumption of a uniform pulse spacing. The correction methodology involves monitoring the individual laser pulses to correct the measured velocity fields. To do so, the individual laser pulses are converted to TTL peaks using a custom circuit that reads the analog laser output via a Thorlabs DET10A-Si Detector photodiode and outputs digital TTL pulses corresponding to the individual pulse peaks, which are then recorded using a high-speed data logger. The pulse timings are used to correct the individual Δt for each frame within a recorded PIV acquisition sequence to ensure the correct velocity is calculated, and then the velocity time traces can be used to calculate the power spectra within the flow field. The PIV method for spectral decomposition is suitable for the current experiments due to the flow having significant magnitudes of both forward and reverse flow over which range could burn out a typical hot-wire probe. Furthermore, while the PIV spectral measurements enable spatial resolution within the flow field (0.06H x 0.06H), a hot wire probe would yield a single measurement point at a time. The spectral content of the PIV data was similar to corresponding hot wire measurements conducted of Peterson et. al. (2020), accounting for the response in the PIV seed particles.

2.3.5 Stereo PIV

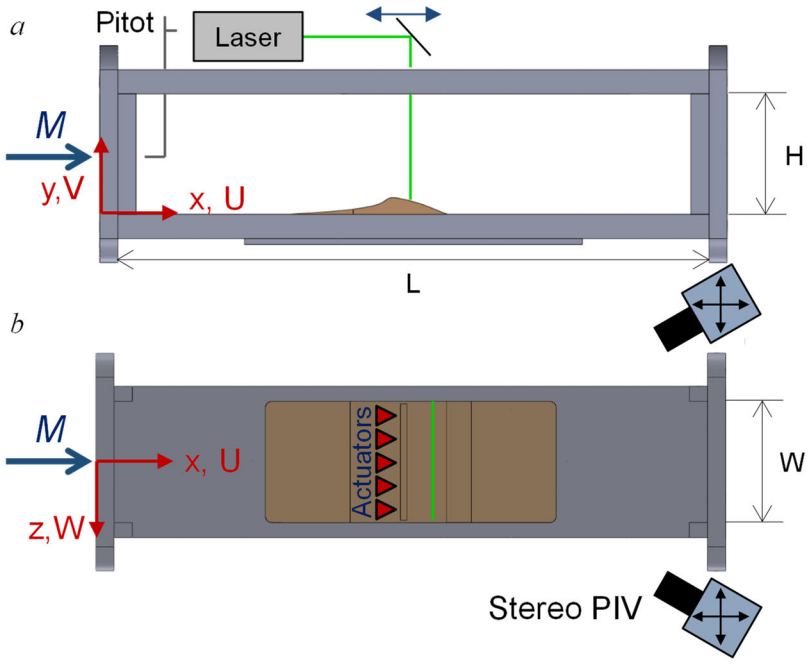

Figure 2.7. Side (a) and top (b) views of the test section described in Section 2.2.2 showing the stereo PIV camera locations (b only) and laser sheet. As shown, the cameras are traversed in the *x* and *z* directions (also can be traversed in *y*) via a 3-axis traverse. The global coordinate system (*x, y, z*), and upstream inlet pitot tube are shown for reference.

The three-dimensional flow features of the separated flow over the ramp insert was investigated in multiple streamwise-normal planes in several streamwise stations using stereo PIV. The optical setup and the laser sheet formed by a Nd:YAG laser (Quantel Evergreen 200, 532 nm, up to 0.2 J/pulse, max frequency 15 Hz) is shown in Figure 2.7. The CCD cameras (LaVision Imager sCMOS with Nikkor 105mm f/2.8 lenses and 2x teleconverters) are mounted on a 3-axis traversing system (*x, y, z*) and the laser is mounted on a separate traverse (*z*) that enables streamwise translation of the laser sheet along with the cameras (the cameras can also be moved in the spanwise direction). The cameras focal planes are angled approximately 35° relative to the laser sheet (Figure 2.7b), and are adjusted using a Scheimpflug adapter on each camera. The streamwise stations of the sPIV

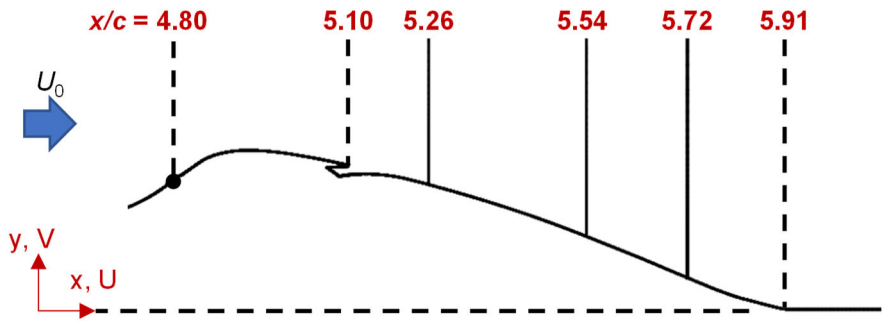

Figure 2.8. Side view of the moldline of a streamwise cross-section in the cross-stream *x-y* plane of the insert model in Section 2.2.2 showing the tripwire location at *x/c* = 4.80, the exit plane of the jet array at x/c = 5.10 and the location of the downstream edge of the insert at x/c = 5.90 marked by dashed lines. The streamwise locations of the spanwise sPIV measurements (*x/c* = 5.26, 5.54, and 5.72) are marked using solid lines. The global coordinate system is shown for reference (*x/c* = 0 at the inlet to the test section, and *y/c* = 0 on the test section wall).

planes (*x/c* = 5.26, 5.54, and 5.72) are shown in Figure 2.8 along with the moldline of a streamwise cross-section of the insert model in Section 2.2.2 in the cross-stream *x-y* plane showing a trip wire at *x/c* = 4.80 and orifice plane of the jet actuators (*x/c* = 5.1, Section 2.4). The sPIV measurements were acquired at 15 Hz, and each ensemble included 1000 individual realizations, with an interrogation domain -0.22 < z/c < 0.22 (97 px/mm). Three such interrogation domains are used to create composite views of the flow from the test section centerline (*z/c* = 0) to the sidewall (*z/c* = -1.02).

The various software setup parameters used for the planar and stereo PIV measurements described in Chapters 3, 4, and 5 respectively, were optimized during the setup time of the individual experiments including accounting for particle travel time through the laser sheet and the time delay between successive data frames (d*T*). The number of realizations used for the overall data acquisition were assessed based on

variations of the spatial RMS distributions for samples of varying durations to ensure saturation of RMS levels within the acquisition sequence.

2.3.6 PIV Error Analysis

A comparison between measurements using planar and stereo PIV is assessed using the time-averaged streamwise and cross-stream velocity components (U and V) in the centerplane $z/c = 0$ at $x/c = 5.52$ of the insert model in Figure 2.4. In the planar PIV U and

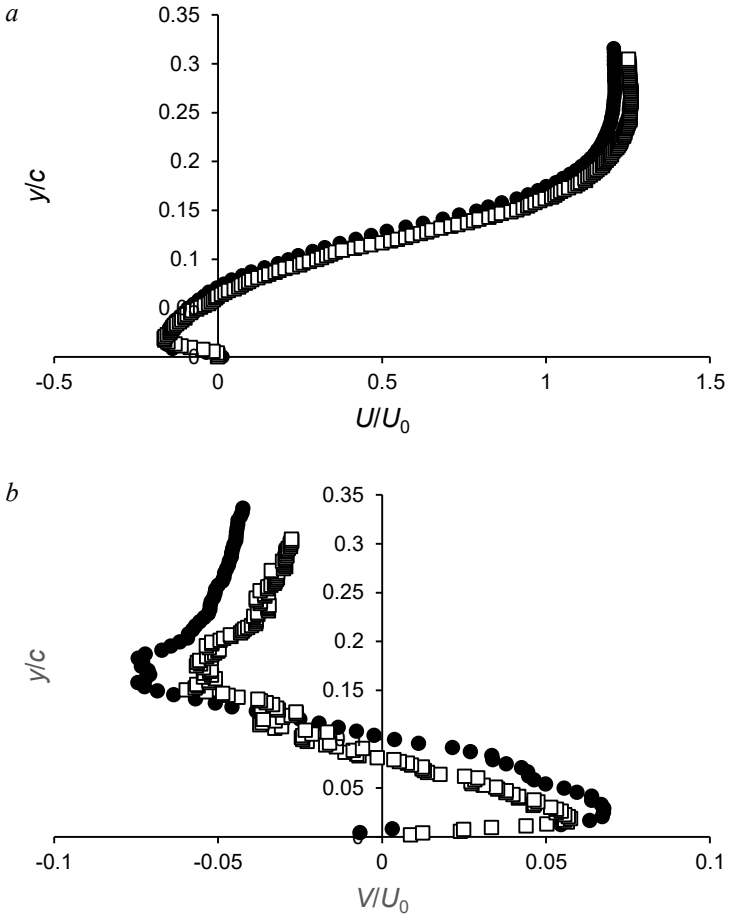

Figure 2.9. The time-averaged streamwise U (a) and cross-stream V (b) velocity components measured at $x/c = 5.52$, and $z/c = 0$ in the base flow at $M_0 = 0.25$ over the insert model (Section 2.2.1) using planar (●) and sPIV (□).

V are in the measurement plane, whereas in the sPIV orientation *U* is normal to the PIV plane while *V* and *W* are in the plane. The planar measurements do not resolve the spanwise velocity *W* and is expected to create variation between the two measurement approaches as any spanwise (*W*) motion of the fog particles is incorporated into the calculated *U* or *V*. The comparison between the *U* and *V* measured using planar and stereo PIV at the same streamwise ($x/c = 5.52$) and spanwise location ($z/c = 0$) are shown in Figure 2.9, where *y* is taken to be zero at the surface at that location. The streamwise velocity component (*U*) measured using sPIV is higher than the corresponding component measured using planar PIV and is shown to have agreement within 6% of the stereo value near the wall at $y/c = 0.013$, which decreases monotonically to within 3.5% near the outer flow at $y/c = 0.30$. The magnitude of the cross-stream component (*V*) is considerably lower than the streamwise velocity, and shows a larger discrepancy between the planar and stereo measurements throughout. It is noted that owing to the curved surface of the insert model, the outer freestream flow has a non-zero cross-stream component and is directed towards the model surface (i.e. negative *V*) as is traverses the aft portion of the model. The sPIV measurements are shown to have the same structural trend and zero crossing between the stereo and planar measurements, but the stereo shows lower magnitudes of the peak values of *V* at $y/c = 0.16$ near the wall and $y/c = 0.25$ in the outer flow, which have a discrepancy of 50% and 36% respectively between the stereo and planar measurements. This discrepancy is attributed to the orientation of the stereo planes relative to the flow. Since the planar measurements do not account for out of plane particle motion, such motion can bias the in-plane components (*U* and *V*). Since $V << U$ (in both measurements), out of

plane motion disproportionately affects V in the planar measurements, and therefore can account for the discrepancy with the stereo measurements.

PIV error stems from several sources including particle size, camera resolution, and regions of large velocity gradients, to name a few. The uncertainty levels of the present experiments (both PIV and sPIV) are calculated using the correlation statistics of the individual frames within the PIV acquisitions using the method of Wieneke (2015) and is calculated directly using the DaVis software. The corresponding nominal uncertainty

PIV Field of View	U/U_0	V/U_0	W/U_0
Diverter Duct (Large window, 13 px/mm, $M_0 = 0.4$)	± 0.007	± 0.007	N/A
Diverter Duct (Medium window, 48 px/mm, $M_0 = 0.4$)	± 0.006	± 0.004	N/A
Insert Model (Planar PIV, 52 px/mm, $M_0 = 0.25$)	± 0.008	± 0.008	N/A
Insert Model (Stereo PIV, 97 px/mm, $M_0 = 0.25$)	± 0.021	± 0.008	± 0.014

Table 1. PIV uncertainties.

values are reported in Table 1 in the free stream based on the average uncertainty of the base flow PIV sets.

2.4 Fluidic Based Flow Control

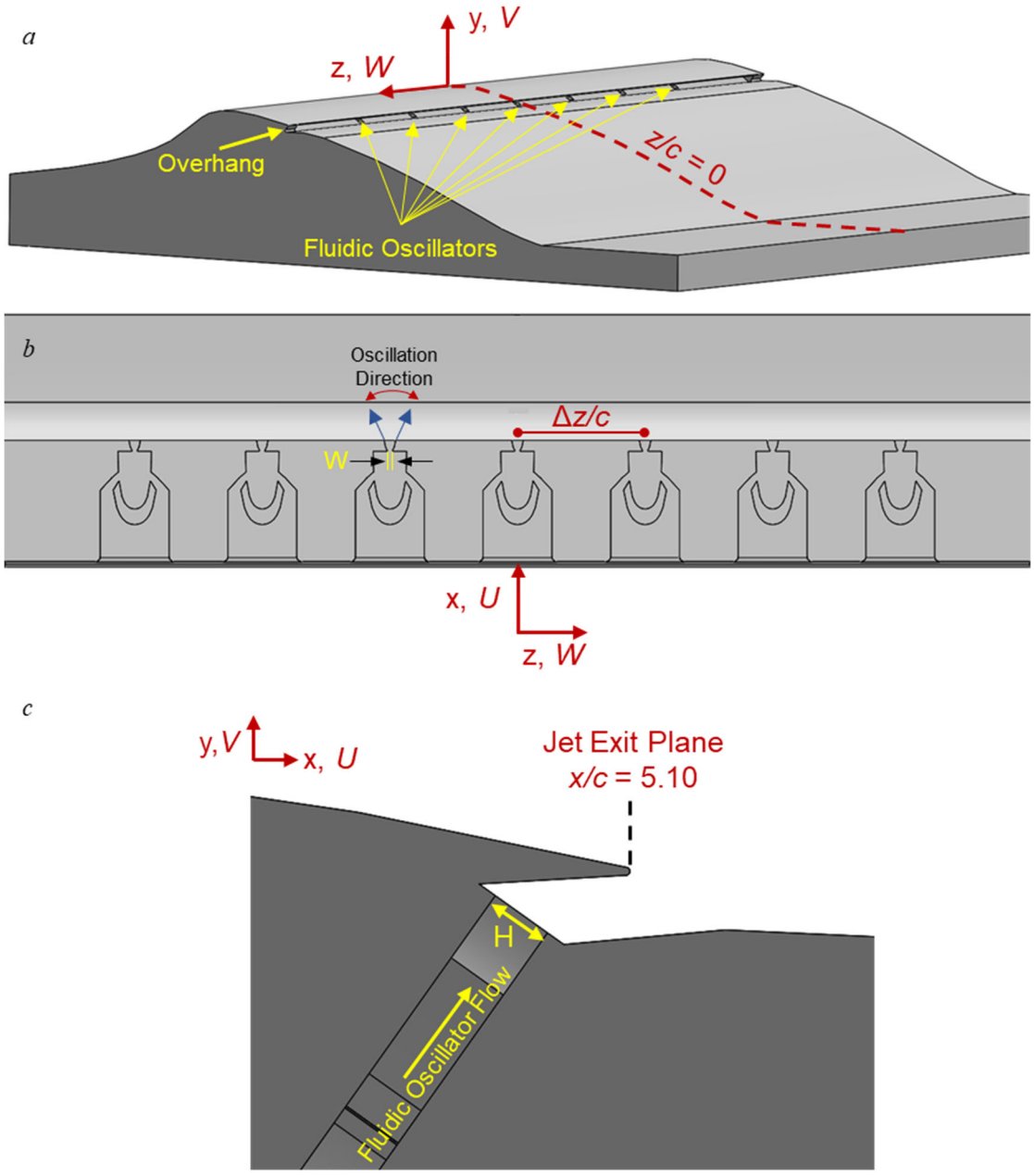

Figure 2.10. CAD of the insert model (a) showing the location of the jet overhang and spanwise fluidic oscillators, with a section cut under the overhang showing the spanwise jet array inlaid into the insert surface (b) and side profile showing the geometry of the "overhang" in reference to the jet exit plane at x/c = 5.10 (c). Global coordinate systems are marked for reference.

In the present investigations, flow control is effected using arrays of feedback-free fluidically oscillating jets that are embedded in the flow surfaces of the diffuser inlet (cf. Figure 2.3) and the insert model (Figure 2.4). Figure 2.10 shows the CAD model of the jets embedded within the surface of the insert model with jet spacing $\Delta z/c = 0.11$ as a representative installation of the oscillating jets for both the insert mode and diffuser inlet. As shown in Figure 2.10c, the jets issue tangentially to the local surfaces under an "overhang" that is nominally parallel to the local cross flow. A schematic diagram of a single jet is shown in Figure 2.11. Lateral oscillations of the output jet are effected by alternate attachment and separation of the flow within the two inlet conduits (A and B, Figure 2.11). The exit orifice of the oscillating jet is 0.5 mm wide in the spanwise direction and 1 mm high (normal to the direction of oscillation). Within the diffuser inlet (cf. Figure

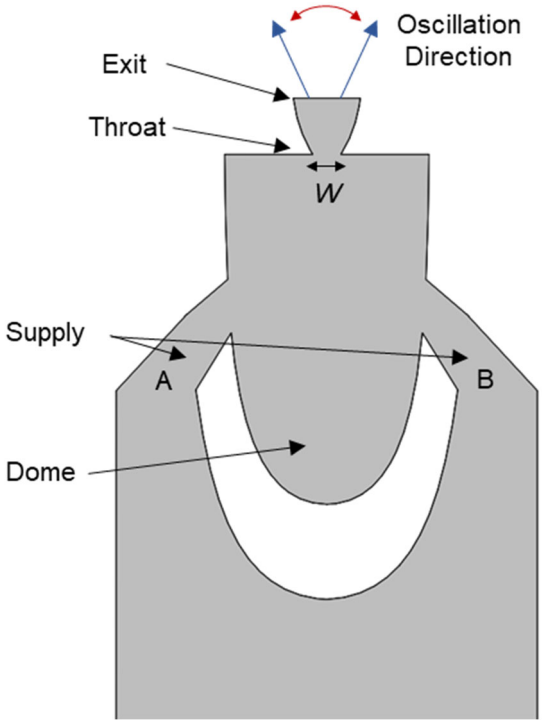

Figure 2.11. Fluidically oscillating jet module.

2.3), the model incorporates 23 jets (Figure 2.11) equally spaced at $\Delta 0.09H$ across the span with the middle jet centered at the midspan ($z = 0$). The experiments in Chapter 4 (insert model Figure 2.4) are conducted using an insert model with 17 discrete jets across the span with spacing $\Delta z/c = 0.11$, middle jet centered at $z = 0$, with jet exit plane $x/c = 5.10$. The experiments in Chapter 5 with the insert model utilize varying spacings and numbers of jets including a single jet model, the 17 jet model with spacing $\Delta z/c = 0.11$ ('1λ'), and two other models with different spacing: 7 jets ($\Delta z/c = 0.22$, '2λ') and 5 jets ($\Delta z/c = 0.33$, '3λ').

The actuation strength of the jets is characterized using the mass flow rate coefficient C_q

$$C_q = \frac{\dot{m}_{jets}}{\dot{m}_0} \tag{2.3}$$

where $\dot{m}_{jets}$ and $\dot{m}_0$ are the mass flow rates through the jets and the unactuated mass flow rate through the flow duct in which it is embedded, respectively, and the momentum coefficient C_μ

$$C_\mu = \frac{Thrust_{jet}}{\rho_\infty A_\infty V_\infty^2} \tag{2.4}$$

is the jet thrust normalized by the thrust of the cross flow (ρ_∞, V_∞) through the inlet reference area (A_∞). The investigations in the diffuser (Chapter 3) emphasized the jets' mass flow rate coefficient C_q while the investigations of the flow over the insert model (Chapters 4 and 5) utilized the momentum coefficient C_μ where the jet thrust is normalized by the momentum flux at $x = 0$, the inlet of the test section ($\rho_\infty, A_\infty, V_\infty^2$).

The jet thrust was measured directly on a benchtop test setup in quiescent ambient, using the test apparatus and procedure of Jhaveri et al. (2019). This setup measures the jet thrust directly using a six-axis load cell installed beneath a pressurized plenum that is connected to modules of fluidically oscillating jet arrays (the uncertainty of the force measurements was ±2 N in each direction). The mass flow rates of the jets are monitored using a thermal element flow meter (in the diffuser investigations: Aalborg 1000 SLPM uncertainty ± 15 SLPM; and in the insert model investigations: Aalborg 500 SLPM, uncertainty ± 7.5 SLPM and Aalborg 100 SLPM, uncertainty ± 1 SLPM). The oscillation frequency of the jet was measured using hot wire anemometry with a miniature sensor in which the sensing wire probe is 1.25mm long and 5 µm in diameter. The wire was placed 6 jet throat widths (6*W)* downstream of the exit plane and oriented normal to the oscillation direction. The anemometer output signal was sampled at 46 kHz for 60 seconds and the

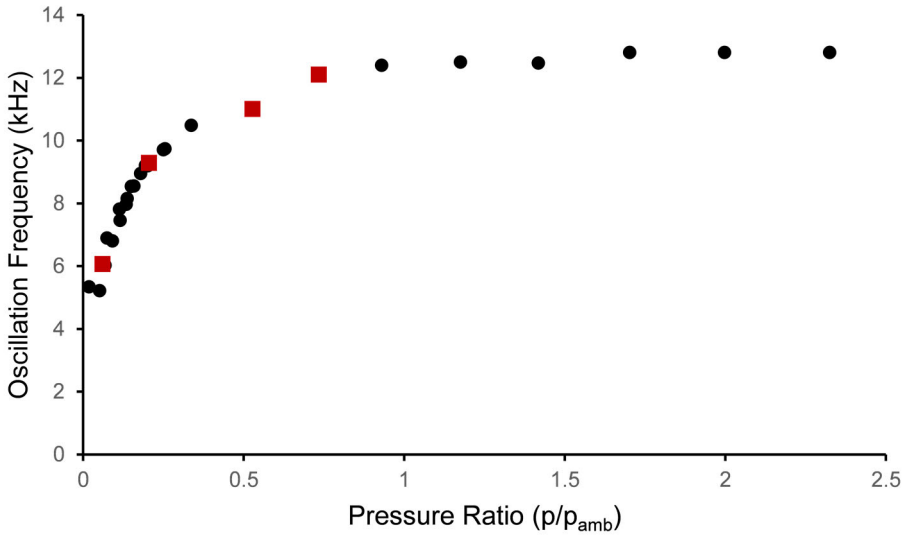

Figure 2.12. Variations of the fluidically oscillating jet frequency with the supply pressure ratio. Jet performance based on actuation levels used in Chapter 4 and 5 are marked (■).

resulting power spectra are subsampled and averaged such that the frequency resolution is 1 Hz. The variation of the oscillation frequency with varying supply pressure ratio (p/p_{atm}) is shown in Figure 2.12. These data show that the oscillation frequency responds rapidly to increasing pressure ratio, but begins to saturate to a maximum of 12 kHz near a pressure ratio of 1 indicating a choking effect within the jet. The operational conditions of the varying actuation strengths in the investigations in Chapter 4 and 5 are indicated by the red squares in Figure 2.12, and indicate the jets are becoming choked at the highest actuation strength C_μ utilized in the experiments.

The flow of the actuation jets for the varying spacing models (1λ, 2λ, 3λ) in the insert geometry (cf. Figure 2.4) is characterized by an *in-situ* measurement of the total pressure distribution across the span ($\Delta z/c = 0.004$) 4 jet throat widths ($4W$, cf. Figure 2.11) downstream of the jet exit plane ($z/c = 5.10$) in the absence of a cross flow and is shown in Figure 2.13. The jets are operated at the same input flow rate as the highest matched momentum coefficient in Chapter 4 and 5 ($C_{\mu,\text{ per jet}} = 0.12 \cdot 10^{-3}$). As the scan is done *in-*

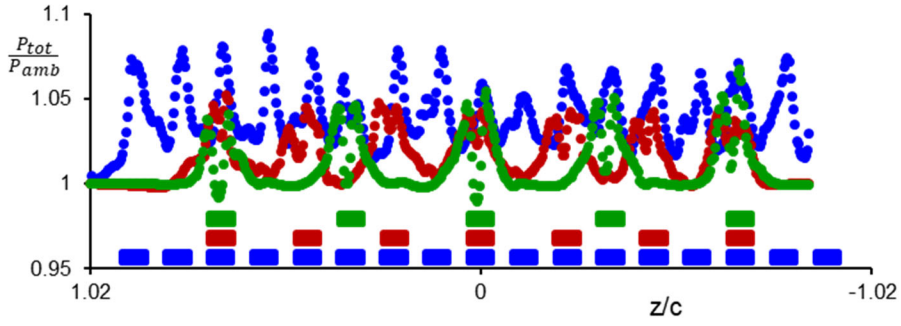

Figure 2.13. Spanwise variation of total pressure measured using a miniature total pressure tube across the actuation jets at $x/c = 5.1$: 1λ (●), 2λ (●), and 3λ (●) arrays in the absence of cross flow. The block schematic below shows the spanwise location of active jets for each array, marked by the corresponding color.

situ in the wind tunnel, the outer jet in the 1λ model (near z/c = -1.02, Figure 2.13) was unable to be resolved due to its proximity near the sidewall. While the total pressure distributions of individual jets within a given array are reasonably similar, there are differences between the distributions of jets from different arrays. As the jet spacing increases in the 2λ and 3λ arrays, the total pressure distributions exhibit nearly bimodal-like profiles that are characteristic of fluidically oscillating jets, whereas the jets of the 1λ array have a single peak about the jet's centerline and elevated total pressure between neighboring jets, indicating that the denser array results in spanwise interaction of neighboring jets. These interactions diminish significantly when the spacing between the neighboring jets increases

2.5 Comparison of the Test Section Streamwise Pressure in the Pressure and Suction Tunnels

The pressure distribution along the test section with the insert model (cf. Figure 2.4) were compared in both the pressure (cf. Figure 2.1) and suction (cf. Figure 2.2) driven wind tunnels. To assess the differences in the tunnel operation, the streamwise pressure distributions of the base flow measured at the nominal inlet Mach number $M_0 = 0.25$ are shown in Figure 2.14. The streamwise pressure distributions of the base flow is discussed in Chapter 4 along with the corresponding distribution in the presence of actuation and the discussion here is restricted to a comparison of tunnel operation. As discussed in Section 2.2.2, the pressure ports span $0.7 < x/c < 10.2$, but are concentrated along the insert between $2.5 < x/c < 8$, and the data in Figure 2.14 indicate that by and large the streamwise pressure distributions in both tunnels are nearly the same. In Figure 2.14, the pressure ports

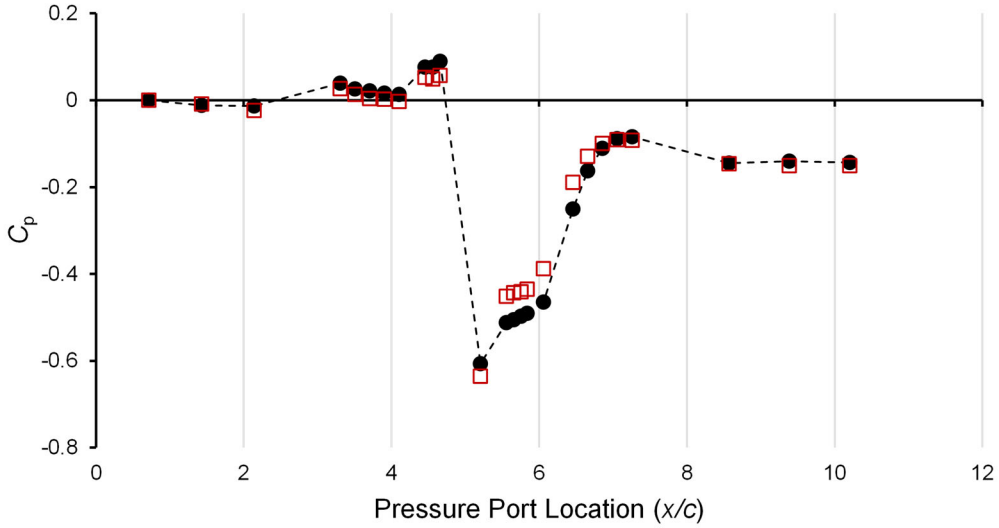

Figure 2.14. Streamwise pressure distribution (C_p) of the base flows in the test section (cf. Figure 2.4) in the suction (□) and pressure (●) driven tunnels at $M_0 = 0.25$.

for $2.5 < x/c < 4.6$ upstream, and $7.2 < x/c < 10.2$ downstream show that the inlet and outlet flow conditions match (indicating little or no change in overall pressure drop). However, these data also indicate that there are some subtle differences in the pressure distributions over the insert model itself ($4.6 < x/c < 7.2$). These pressure distributions show that in the suction wind tunnel a larger suction peak is induced at $x/c = 5.2$ (0.63 compared to 0.60 in the pressure tunnel). These data also show that the flow separation domain over the insert model ($5.2 < x/c < 6.2$) is somewhat smaller in the suction tunnel as is evidenced by the lower C_p values in this domain compared to the pressure tunnel, indicating some small differences in the evolution of the separation over the insert. The differences are attributed to the variations in the tunnel designs upstream of the test section inlets, that consequently effect the local separation conditions. The pressure driven tunnel (cf. Figure 2.1) has a shorter distance between the outlet of the blower to the inlet of the test section as well as the inline heat exchanger, which could propagate any frequency disturbance from the

turning of the individual blower blades. The pressure driven tunnel also has a slight bend in the flow path between the outlet of the blower and the contraction to the inlet of the test section due to the compact nature and space limitations of the tunnel design, while also terminating in a free-jet exit. The suction driven tunnel (cf. Figure 2.2) has a longer distance between the intake filter box and the test section inlet, and only has honeycomb and mesh screen upstream of the inlet. The suction tunnel has a straight intake path, and an extended downstream diffuser section past the end of the test section (instead of the free jet exit of the pressure tunnel) to the inlet of the blower.

CHAPTER 3. FLUIDIC BASED CONTROL OF SEPARATION IN A DIVERGING DIFFUSER

3.1 Overview

The experimental investigations in this chapter focus on characterization and mitigation of the inherent flow separation at the upstream edge of a diffuser duct that branches off a primary rectangular channel. Separation is manipulated using a spanwise array of fluidically oscillating jet actuators. The effect of actuation on the evolution of separation is assessed using its ability to reduce the total pressure losses throughout the test section developed due to the constriction of the separated flow at the entrance to the branched diffuser, and regulate the diverted mass flow rate from the primary channel into the secondary branched diffuser. Of particular interest are the underlying dynamic and structural features of the flow in the presence and absence of the actuation that are investigated using cross-stream velocity distributions within the diffuser by conditional averaging, spectral analysis, and decomposition methods.

3.2 The Flow Within the Diffuser in the Absence and Presence of Actuation

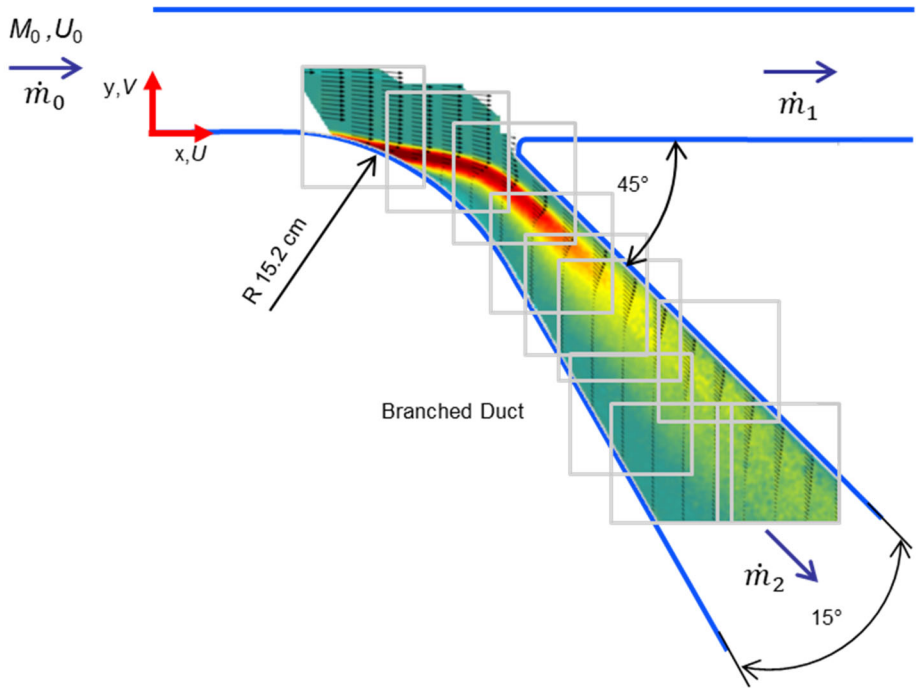

Figure 3.1. Side view of the diffuser duct showing an overlaid sample composite of PIV images (marked by the grey squares) of concentrations of spanwise vorticity in the base flow at $M_0 = 0.4$.

3.2.1 The Base Flow

The base flow through the diffuser duct was shown in Figure 2.3b and is reproduced in Figure 3.1 for reference. The base flow is depicted in PIV images of time-averaged spanwise vorticity ξ_z measured in the center plane. These images show the base flow separation at the inlet to the diffuser is driven from the main channel. Distributions of ξ_z at the center cross-stream plane of the diffuser at $M_0 = 0.1$, 0.2, 0.3, and 0.4 are shown in Figure 3.2a-d, respectively, overlaid with distributions of velocity vectors. As illustrated

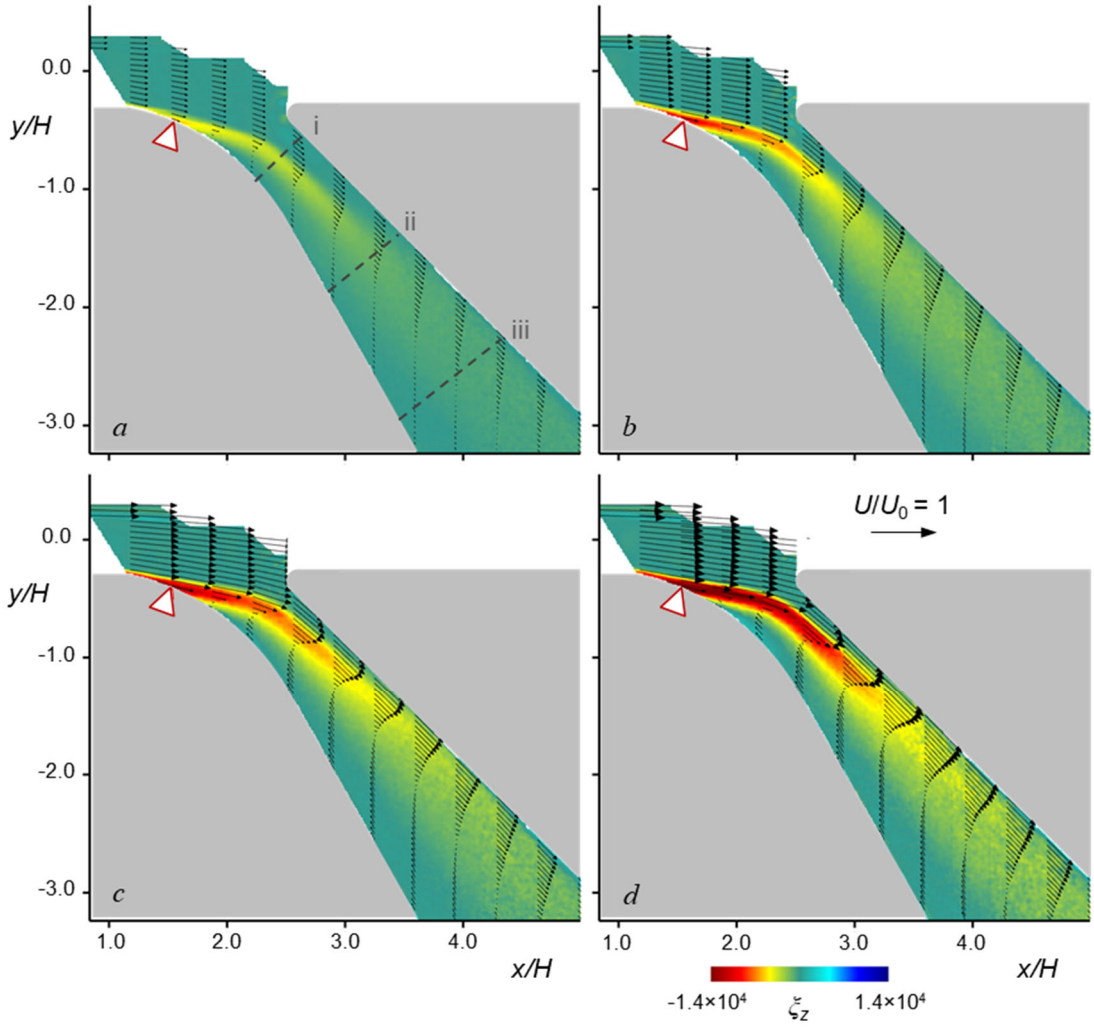

Figure 3.2. Color raster plots of the time-averaged spanwise vorticity overlaid with distributions of velocity vectors in the cross-stream y-x plane of the base flow at $M_0 = 0.1$ (a), 0.2 (b), 0.3 (c), and 0.4 (d). The locations of cross-stream velocity distributions that are discussed in connection with Figure 3.3 at $x/H = 2.1$, 2.7 and 3.3 are marked by dashed lines *i*-*iii* in (a). The reference vector is shown for $M_0 = 0.4$.

in Figure 3.1, each of the composite flow fields is assembled from ten partially overlapping views, such that the composite image covers the diffuser duct from its entrance to just upstream of its exit plane (the positions of the exit plane of the fluidic actuators is marked for reference). The base flow is marked by the formation of a CW vorticity layer that separates off the convex transition section ($x/H \approx 1.8$) as a result of an imposed adverse

pressure gradient. These data show that at all M_0 the separated vorticity layer follows the direction of the streamwise flow in the primary channel near the left side of the entrance to the diffuser and begins to deflect sharply into the diffuser duct within $2 < x/H < 3$. As M_0 increases, the vorticity layer bends closer to the top surface of the diffuser and the domain of the forward flow within the shear layer narrows and the velocity magnitude increases (a thin boundary layer forms on the surface). The flow into the diffuser duct is partially constricted by a reverse flow domain underneath the shear layer that increases in cross-stream extent with M_0 in the primary channel (in the reversed flow along the lower surface $U < 0$, $V > 0$). The flow into the diffuser remains confined between the upper surface and the separated domain along the lower surface all the way to the exit plane and the CW vorticity layer spreads in the cross-stream direction. The blockage induced by the massive separation leads to significant flow losses that affect the flow rate through the duct, indicating that suppression of this flow separation would not only enable regulation of the flow diverted into the diffuser ($\dot{m}_2$), but would also lead to an increase in the overall flow rate into the primary duct $\dot{m}_0$. The evolution of the vorticity layer with the underlying reverse flow indicates the flow is unsteady. These effects are captured by distributions of the total kinetic energy within the flow that are discussed in connection with Figure 3.10 below.

The effects of M_0 on cross-stream distributions of the time-averaged streamwise velocity component that is tangential to the lower wall in the diffuser, U_n, are shown in Figure 3.3 at $x/H = 2.1$, 2.7 and 3.3 (dashed line *i-iii* in Figure 3.2a). It should also be noted that these cross-stream velocity distributions reflect only the local velocity component that

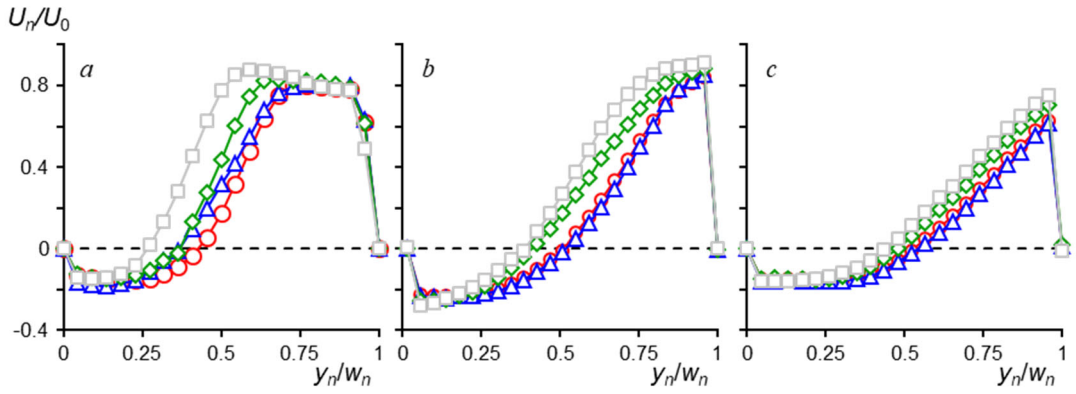

Figure 3.3. Cross-stream wall-tangential distributions of U_n across the height of the diffuser duct at $M_0 = 0.1$ (□), 0.2 (◊), 0.3 (Δ), and 0.4 (○), at $x/H = 2.10$ (a), 2.70 (b), and 3.36 (c).

is tangential to the lower surface and therefore the shape of the distribution is not indicative of the mass flow rate through the diffuser. The wall-tangential velocity is normalized by the corresponding inlet velocity of the primary channel at each M_0 and the cross-stream distance from the wall is normalized by the local width of the diffuser w_n. Just downstream from the diffuser inlet (Figure 3.3a) there is a clear increase in the cross-stream extent of the reverse flow region over the lower surface with increasing Mach number, which acts as a blockage to the forward flow. The obstruction of the inlet flow as measured by the cross-stream extent of $U_n < 0$, increases from about 25% at $M_0 = 0.1$ to more than 40% at $M_0 = 0.4$. It is also noted that the velocity of the flow that is drawn into the diffuser near its top surface has a nearly uniform magnitude of $U_n = 0.8U_0$. As the flow is advected along the diffuser (Figure 3.3b), these velocity distributions evolve under two competing effects, namely the increasing flow obstruction due to the growing separated flow domain along the lower surface that leads to acceleration of the "outer flow" near the top surface, and the divergence of the diffuser. Finally, the velocity distributions at $x/H = 3.36$ (Figure

3.3c) become more jointly similar for varying M_0, indicating that approximately 50% of the duct height is occupied by reverse flow independently of M_0. As can be seen in the color raster plots of the spanwise vorticity (Figure 3.2), the progression through stations *i-iii* in Figure 3.3 also exhibits the formation and growth of a cross-stream shear layer that is initially contained in the central region of the secondary duct, but expands as it is advected downstream towards the exit of diffuser.

The streamwise variation of the pressure along the lower surface of the diffuser is shown in Figure 3.4. The static pressure is measured within the domain $0 < x/H < 5$ (marked in Figure 3.4). The compressible pressure coefficient (Equation 2.1) over the lower surface of the diffuser is computed using the reference Mach number $M_r = M_0 = 0.2$, 0.3, and 0.4 and static pressure $p_r = p_1$ that are measured at the inlet plane ($x/H = 0$). The collapse of these pressure distributions onto a single trace indicates a similarity between

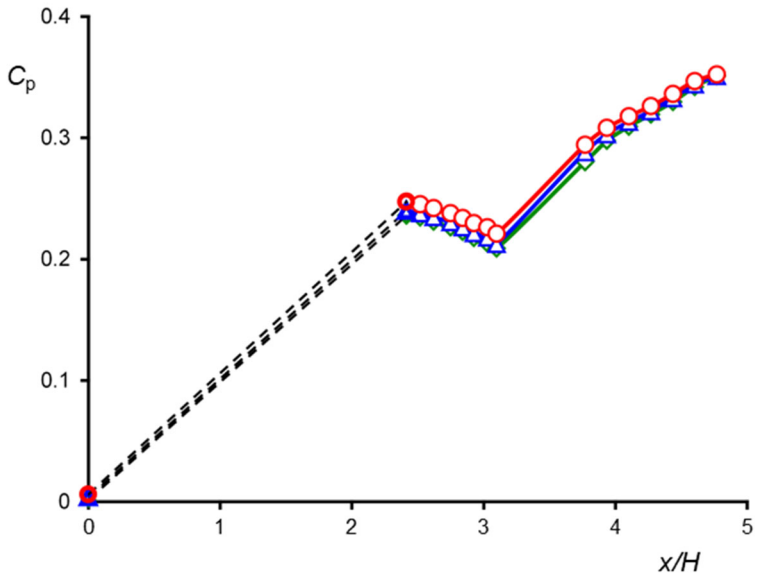

Figure 3.4. Streamwise variation of static pressure distributions along the lower surface of the diffuser for the base flow at $M_0 = 0.2$ (◊), 0.3 (Δ), and 0.4 (○).

the effects of the different inlet Mach numbers tested, as indicated by the topological similarity of the spanwise vorticity distributions in Figure 3.2. The cluster of pressure ports within $2.4 < x/H < 3.4$ indicates a favorable pressure gradient that appears to be associated with the streamwise acceleration of the flow between the recirculation domain and the upper surface. Farther downstream, the contraction effect of the separation diminishes and the pressure ports within the domain $3.76 < x/H < 4.76$ are effected by the divergence of the diffuser which imposes a significant adverse pressure gradient on the cross flow as reflected by the monotonic streamwise increase in the pressure in Figure 3.4, and is indicative of pressure losses within the diffuser. It appears that the change in sign of the streamwise rate of change of the pressure at $x/H = 3.4$ is indicative of the transition between these two domains.

3.2.2 The Controlled Flow

As noted in § 3.1, the present investigations focus on alleviation of the adverse effects of flow separation at the inlet to the diffuser and thereby its adverse effects on the mass flow rate of the diverted flow into the diffuser. The flow is reattached using a spanwise array of actuation wall jets that are placed upstream of the diffuser's inlet section, and, as shown in Chapters 4 and 5, the jets segment the separation domain along the span of the diffuser into smaller-scale cells that entrain fluid from the core flow and thereby deflect the core flow towards the diffuser's wall to overcome the adverse pressure gradient. The global effectiveness of the flow control approach in diverting the oncoming flow into the diffuser duct is illustrated in Figure 3.5 using time-averaged composites of velocity and

vorticity fields assembled from separate views in PIV measurements (cf. Figure 2.3b). These plots are shown in three columns corresponding to M_0 = 0.2 (left), 0.3 (center), and 0.4 (right). The data for the base flow were already discussed in connection with Figure 3.2, but are included here as well for reference. The fluidic actuation is measured using

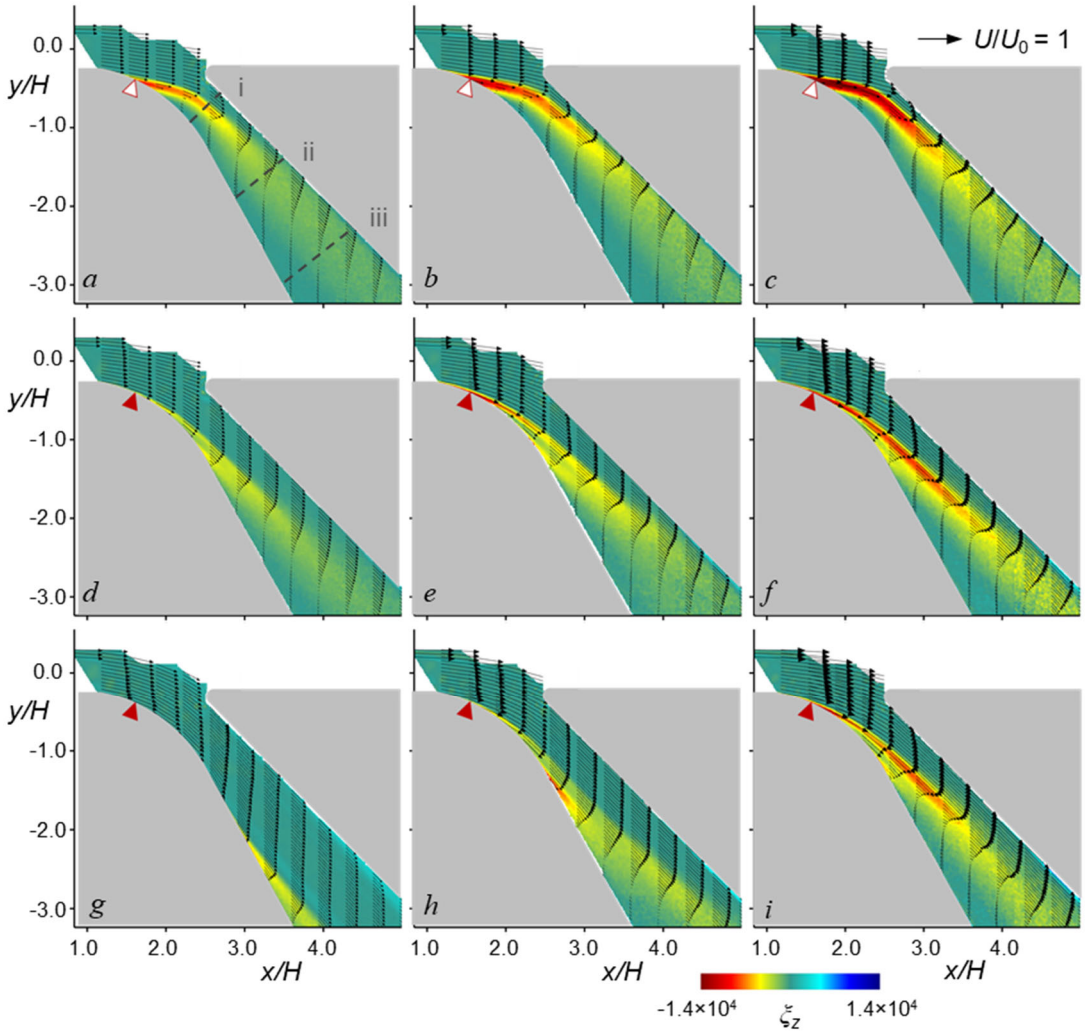

Figure 3.5. Color raster plots of the time-averaged spanwise vorticity overlaid with cross-stream distributions of time-averaged velocity vectors in the diffuser's cross-stream center plane $z/H = 0$. The columns include data at: M_0 = 0.2 (left), 0.3 (center), and 0.4 (right) for the base flow (a-c), in the presence of actuation at C_q = 0.008 (d-f), and at the maximum attainable respective C_q (for fixed actuation mass flow rate $\dot{m}_{jets}$ = 0.018 kg/sec) for each M_0: = 0.019 (g), 0.013 (h), and 0.01 (i). Reference vector is shown on the upper right for M_0 = 0.4.

the mass flow coefficient C_q, which is taken to be the ratio of the mass flow rate through the entrance to the primary channel and the mass flow rate of the actuation jets so that for a fixed C_q, the mass flow rate to the jets is increased with increasing M_0. The most salient flow feature in the presence of actuation is partial flow attachment downstream from the inlet at $C_q = 0.008$ in Figure 3.5d-f and the alleviation of the blockage imposed by the separation in the corresponding baseline flows in Figure 3.2. In fact, these data indicate that for the same C_q, the global features of the flow at each inlet Mach number are similar. These data show that the partial flow attachment to the bottom surface is accompanied by bending of the cross-stream shear layer towards the bottom surface and indicates that diminution in blockage at the diffuser's inlet leads to a reduction in losses. While the downstream migration of separation appears to be similar for the fixed C_q, at these M_0 the extent of the deflection of the separated shear layer towards the bottom surface diminishes somewhat with increasing M_0. The images in Figure 3.5g-i show the effect of the actuation at the maximum available actuation mass flow rate ($\dot{m}_{jets} = 0.018$ kg/sec) in the present investigations at each Mach number. At this $\dot{m}_{jets}$, C_q effectively decreases with increasing M_0. At $M_0 = 0.2$, and the highest actuation level $C_q = 0.019$ (Figure 3.5g) the flow becomes attached through the majority of the lower surface of the diffuser ($x/H = 3.5$). As M_0 increases the separation moves upstream to $x/H \approx 3$ and 2.7 in Figure 3.5h ($C_q = 0.013$) and Figure 3.5i ($C_q = 0.01$), respectively, and the cross-stream shear layer occupies a larger fraction of the diffuser's cross-section indicating that the actuation cannot overcome the adverse pressure gradient.

Cross-stream distributions of the time-averaged velocity component tangent to the lower wall in the presence of actuation measured at $C_q = 0.008$ at $x/H = 2.10$, 2.70, and

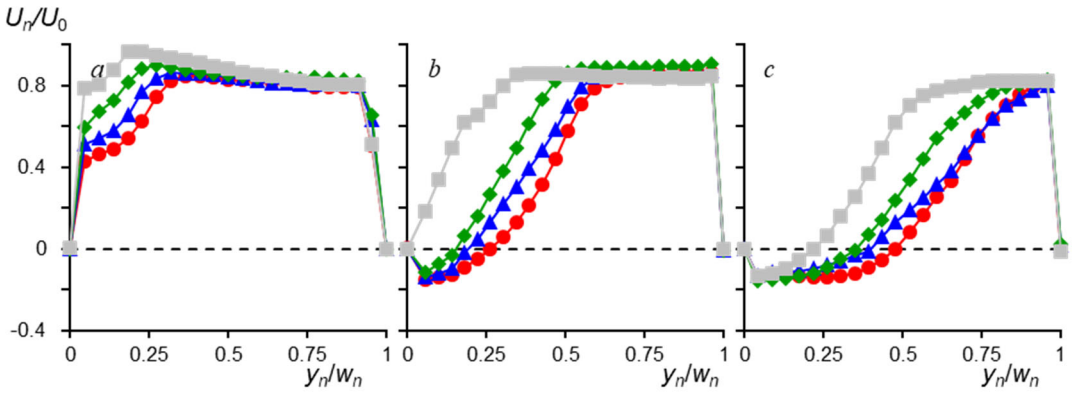

Figure 3.6. Time-averaged cross-stream wall tangential distributions of U_n across the height of the diffuser duct at x/H = 2.10 (a), 2.70 (b), and 3.36 (c) measured at C_q = 0.008 and M_0 = 0.1 (■), 0.2 (♦), 0.3 (▲), and 0.4 (●).

3.36 (cf. Figure 3.5a) are shown in Figure 3.6a-c, respectively. Although not shown in Figure 3.5, the cross-stream distributions of U_n for M_0 = 0.1 at C_q = 0.008 are also included in Figure 3.6. These data show that in the presence of the actuation, the flow downstream of the diffuser's inlet (x/H = 2.10, Figure 3.6a) is attached (i.e. no reversed flow) for all M_0, with a nearly-uniform velocity $U_n \approx 0.8U_0$ within the domain $0.25 < y_n/w_n < 0.92$. Although it is noted that the distribution indicates an inner velocity deficit ($0 < y_n/w_n < 0.25$) owing to the turning near the flow at the inlet. Further downstream x/H = 2.70 (Figure 3.6b), the velocity distributions indicate that despite the actuation, the flow is weakly separated within $0 < y_n/w_n < 0.25$ for $M_0 > 0.1$, and the uniform flow domain where $U_n \approx 0.85U_0$ is confined to $0.5 < y_n/w_n < 0.95$. By x/H = 3.36 (Figure 3.6c), the shear flow above the reversed flow domain ($0 < y_n/w_n < 0.5$) reaches the upper surface of the diffuser.

The effects of the actuation on flow separation and ensuing losses are further explored through measurements of distributions of the static pressure along the centerline

of the diffuser's lower surface for nine equal increments of C_q (up to 0.019, 0.013, and 0.01 for M_0 = 0.2, 0.3, and 0.4, respectively) up to the maximum available actuation mass flow rate (Figure 3.7). The range of C_q at each M_0 is marked in Figure 3.7 and is also indicated

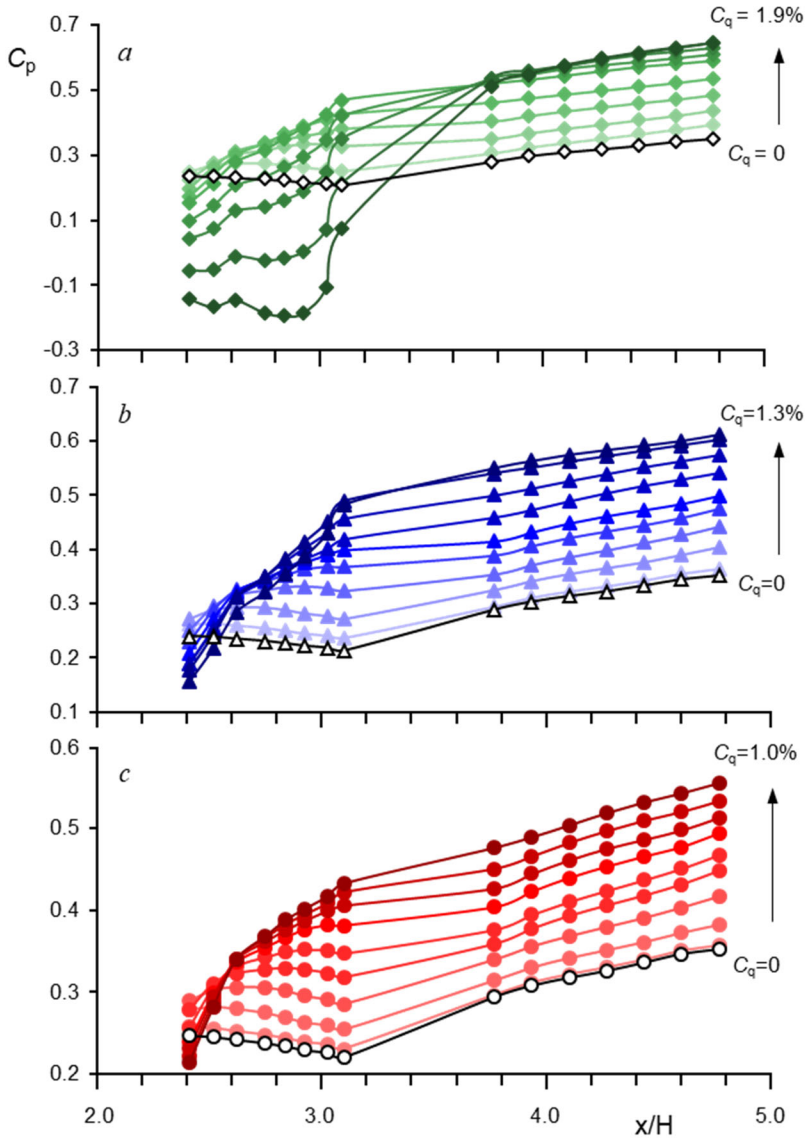

Figure 3.7. Streamwise distributions of the static pressure along the centerline of the lower surface of the diffuser in the absence and presence of actuation (open and closed symbols, respectively) at M_0 = 0.2 (a), 0.3 (b), and 0.4 (c). At each M_0, the distributions are shown at nine equal increments of C_q (up to 0.019, 0.013, and 0.01 for M_0 = 0.2, 0.3, and 0.4, respectively) where the range of C_q is marked on the right-hand side of each plot and is also denoted by the color intensity.

by increased color intensity (the pressure distribution in the base flow is also shown for reference using open symbols). It is noted that due to the variation of the pressure range with M_0, the scale of C_p in Figure 3.7a-c changes with M. As noted in connection with Figure 3.4, the upstream cluster of pressure ports ($2.4 < x/H < 3.1$) serves as an indicator of the separation. In the presence of actuation at $M_0 = 0.2$ (Figure 3.7a), the actuation delays separation even at the lowest level of C_q (0.0021) as indicated by the change in the slope of C_p, and the flow is fully attached for $0.0021 < C_q < 0.01$, and further increases in the actuation level ($0.013 < C_q < 0.019$) lead to significant suction peaks up to $C_p = -0.19$ at $x/H = 2.8$. As M_0 is increased to 0.3 (Figure 3.7b), the effect of the actuation on upstream separation is diminished, and separation is marked by a favorable pressure gradient as a result of acceleration of the inlet flow over the separated domain that diminishes with increasing C_q as the flow becomes attached over the inlet's transition surface ($2.4 < x/H < 3.4$) for $C_q > 0.007$. By comparison to $M_0 = 0.3$, the presence of actuation at $M_0 = 0.4$ (Figure 3.7c) exhibits an even more gradual streamwise migration of the separation location with increasing C_q, and the flow appears to be attached over the inlet transition surface ($2.4 < x/H < 3.4$) for $C_q > 0.009$ as evidenced by the smoothly transitioned adverse pressure gradient throughout $2.4 < x/H < 3.4$. Similar to the discussion in connection with Figure 3.4, the downstream cluster of pressure ports ($3.76 < x/H < 4.76$) reflects the flow losses in the diffuser. The pressure distributions there are affected by the increase in the cross section (and the adverse pressure gradient) that are coupled with the effects of actuation on the flow conditions near the inlet. As shown in Figure 3.7a, at $M_0 = 0.2$, the effects of the actuation on upstream separation are accompanied by an increase with C_q in the magnitude of C_p downstream, which is

indicative of an overall reduction in duct flow losses. The reduction in the rate of the increase in C_p with C_q for $3.76 < x/H < 4.76$ at $C_q > 0.013$ is the result of the attachment along most of the diffuser (cf. Figure 3.5g). Similarly, at $M_0 = 0.3$ (Figure 3.7b) a decrease in the flow losses is marked by a streamwise increase in the C_p at each location in the domain $3.76 < x/H < 4.76$, with reduction in the rate of the increase in C_p with C_q for $C_q > 0.011$ indicating that full reattachment through the diffuser may be achieved at $C_q > 0.013$. At $M_0 = 0.4$ (Figure 3.7c), the rate of increase of the magnitude of the pressure levels with C_q for $x/H > 3.76$ does not appear to change significantly with increasing C_q even at $C_q = .01$, which is commensurate with separation even in the presence of actuation (cf. Figure 3.5i).

The delay of separation at the inlet to the diffuser with increasing actuation level alters the global flow at $x/H > 2.4$ (c.f. Figure 3.5) and consequently effects the diffuser's inlet conditions. The constriction of the inlet flow is a primary source of losses in the

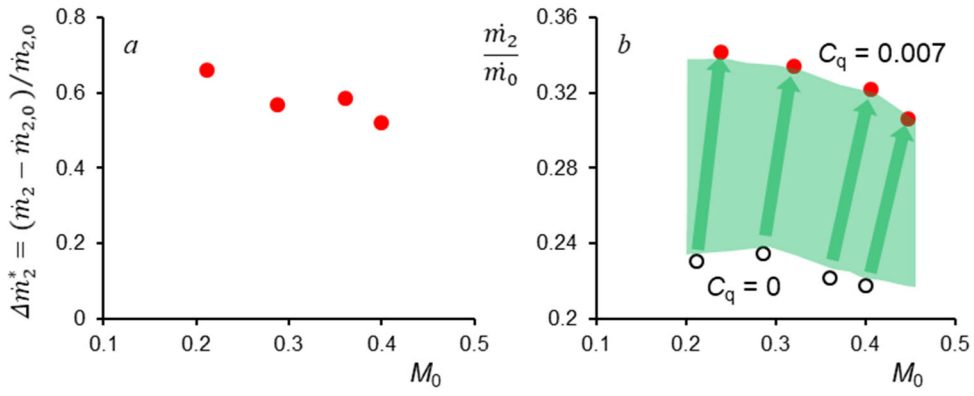

Figure 3.8. a) Variation with M_0 of the relative mass flow rate increment through the diffuser for $C_q = 0.007$, and b) Ratio of the diffuser's mass flow rate $\dot{m}_2$ to the total inlet mass flow rate $\dot{m}_0$ at $C_q = 0$ (○) and 0.007 (●).

diffuser and can restrict the overall mass flow rate ($\dot{m}_0$) and the mass flow into the diffuser ($\dot{m}_2$). To explore the effects on the mass flow rate split by delaying separation, the incremental increase in the mass flow rate relative to the base flow in the diffuser $\dot{m}_2 - \dot{m}_{2,0}$ is normalized by the mass flow rate of the base flow and shown for a fixed C_q = 0.007 for varying M_0 is shown in Figure 3.8a. These data exhibit a significant increase in the fraction of the mass flow into the diffuser over the entire range of M_0. For example, at M_0 = 0.4 the flow rate through the diffuser increases by more than 50% with C_q = 0.007. The ratio between the mass flow rate within the diffuser ($\dot{m}_2$) and the mass flow rate into the main channel ($\dot{m}_0$) for varying inlet M_0 is shown in Figure 3.8b for the base flow and in the presence of actuation with C_q = 0.007 where the arrows show the transition from the base flow at some M_0 to the presence of actuation. These data show that the increased flow rate into the diffuser is accompanied by an increase in the M_0 due to the reduction in losses. These data also show that for a given actuation level the effectiveness of the actuation in diverting flow into the diffuser decreases slightly with increasing M_0. In fact, the data in Figure 3.8a and b indicate that by controlling the extent of separation, the actuation can be used for on-demand regulation of the flow rate through the diffuser.

The green-highlighted area in Figure 3.8b may be thought of as a measure of the control authority and the corresponding actuation effectiveness in terms of the relative increase in the total mass flow rate $\Delta\dot{m}^* = (\dot{m} - \dot{m}_0)/\dot{m}_0$ for M_0 = 0.2, 0.3, and 0.4 (and their associated base flow $\dot{m}_0$), where at varying levels of C_q within the available range of actuation is shown in Figure 3.9. These data show that for each M_0 there is a range over which $\Delta\dot{m}^*$ varies nearly linearly with increasing C_q, and for C_q < 0.005, the curves for the different M_0 nearly collapse showing that in this regime $\Delta\dot{m}^*$ increases by up to 7%

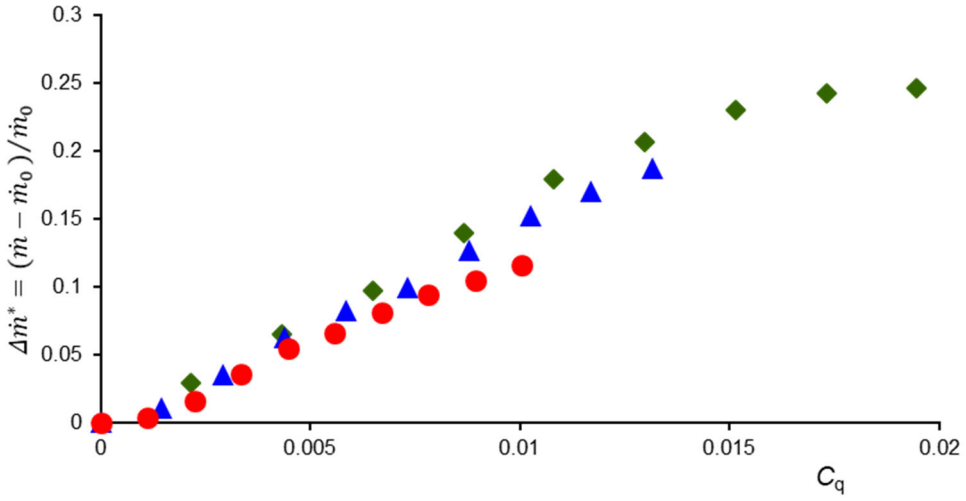

Figure 3.9. Variation with C_q of the relative increase in the total mass flow rate through the channel at $M_0 = 0.2$ (♦), 0.3 (▲), and 0.4 (●).

regardless of the base flow Mach number. As the actuation strength increases, the data for $M_0 = 0.2$ shows that the rate of increase in $\Delta\dot{m}^*$ diminishes and saturates for $C_q > 0.015$, for which the reattached flow extended along most of the lower surface of the diffuser (c.f. Figure 3.5g). At the saturation level $C_q > 0.015$, the increase in $\Delta\dot{m}^*$is approximately 25% compared to the base flow. The slight spreading of the three curves after the nearly linear, collapsed region, is reminiscent of the slight variation in the structure of the flow for fixed C_q and increased M_0 shown by the cross-stream distributions of U_n in Figure 3.6. Although the data for $M_0 = 0.3$ and 0.4 in Figure 3.9 do not display the same saturation effect as for $M_0 = 0.2$, it is expected that higher C_q would result in similar effect since these flows would have similar structures as shown in Figure 3.5d-f. Another important feature of the data in Figure 3.9 is that it allows direct comparison of the fraction of the actuation mass flow rate to the increase in mass flow rate through the duct system, and can be considered the 'cost' to increase the overall mass flow rate. Since C_q is defined as the ratio of the mass flow rate

through the jets $\dot{m}_{jets}$ to the unactuated mass flow rate $\dot{m}_0$, it can be inferred from Figure 3.9, for example, that supplying only 0.5% of the base flow mass flow rate to the jets results in an increase of the inlet mass flow rate of 7% (14 times the effect of the jet supply mass flow rate) regardless on inlet M_0. At $M_0 = 0.2$, it is shown that a supply of only 2% of the unactuated mass flow rate results in 25% increase in overall flow rate, a 12.5x overall increase in effect for small input supply. Finally, the data in Figure 3.9 also indicate that the migration of separation over the inlet to the diffuser is indeed the primary source of the reduction in losses so increased actuation level does not lead to significant continual improvement in the inlet mass flow rate.

3.3 Flow Dynamics and Structure About Local Flow Separation

While § 3.2 focused on migration of separation at the entrance of a branched diffuser and the associated changes in flow losses and mass flow rate, in §3.3 attention is diverted to the dynamics of the flow within the separation domain in the absence and presence of the fluidic actuation. In §3.3.1 the effects of the actuation on the evolution of separation is investigated within a given field of view, while in §3.3.2 the evolution of separation along the diffuser is followed with high spatial resolution.

3.3.1 Large Scale Dynamics

The flow structure about the border between separated and attached flow in the absence and presence of actuation is investigated using distributions of the turbulent kinetic energy $TKE = \frac{1}{2}(\overline{u'u'} + \overline{v'v'})$. Figure 3.10 shows color raster plots of the *TKE* ($M_0 = 0.4$)

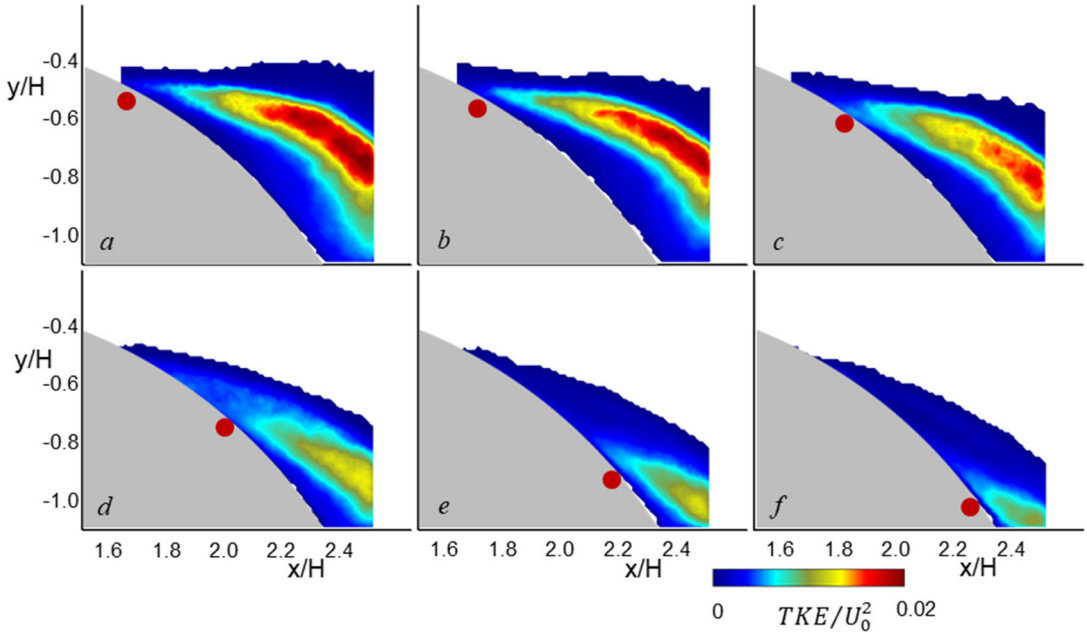

Figure 3.10 Color raster plots of the turbulent kinetic energy in the base flow (a), and with actuation at $C_q = 0.001$ (b), 0.002 (c). 0.003 (d), 0.004 (e), and 0.005 (f) for $M_0 = 0.4$.

at increasing actuation levels up to $C_q = 0.005$ so that the streamwise migration of the onset of separation is within the same field of view. The *TKE* in the base flow (Figure 3.10a) marks the formation of the shear layer above the recirculation domain (cf. Figure 3.2d) at the entrance to the diffuser and is marked by a peak in the intensity away from the surface, that marks the formation and advection of large scale vortical structures and mixing within the shear layer. The location of separation is inferred from distributions of the *U* velocity component (not shown) indicating reverse flow near the surface, and is marked at $x/H \approx 1.6$, 1.7, 1.8, 2.0, 2.2, and 2.3 in Figure 3.10 a-e, respectively. In the presence of actuation (Figure 3.10b-f) the location of separation migrates downstream, but it is still contained within this measurement domain. The actuation leads to a diminution in the rate of streamwise increase in *TKE* levels within the shear layer and to bending of the layer towards the surface and thereby intensification of the *TKE* levels near the wall downstream

of separation. The reduction in *TKE* within the shear layer is attributed to the dissipative, high-frequency actuation (Vukasinovic et al., 2010). It is also noted that the increase in *TKE* in the separated domain near the surface is also commensurate with overcoming the adverse pressure gradient that is imposed by the diffuser flow.

The flow dynamics in the presence and absence of actuation are further investigated using proper orthogonal decomposition (POD, e.g. Sirovich, 1987 and Berkooz et al., 1993) to extract modes of the instantaneous flow. The POD methodology is outlined in Appendix A.1. PIV measurements are first taken over a field of view (c.f. Figure 2.5) that captures the evolution of the separated base flow within the diffuser ($1.56 < x/H < 2.52$, $-0.14 < y/H < -1.10$) and for reference as shown schematically in Figure 3.11a (large square). The smaller domains are used for measurements in the vicinity of separation as discussed in more detail below. To illustrate the modal composition of the base flow at $M_0 = 0.4$, the first five POD modes are shown in Figure 3.11b-f in terms of the composite modal velocity fields that are captured based on 45% of the total energy in the flow, along with corresponding color raster plots of the spanwise vorticity (the point of separation is marked on the surface for reference). These modal based vorticity distributions may be thought of as 'suboptimal' (Glezer et al., 1989) since they are not based directly on POD modes of the vorticity fields. The most energetic mode (Figure 3.11b) represents a dual layer of CW (top) and CCW (bottom) concentrations of opposite sense vorticity perturbations that are commensurate with the time-averaged shear layer. The second mode (Figure 3.11c) has two lobes of opposite sense anti-symmetric vorticity with a streamwise gap centered at $y/H = -0.6$, $x/H = 2.3$ that is located downstream relative to the separation. In the third mode (Figure 3.11d), the two opposite sense vorticity concentrations in the

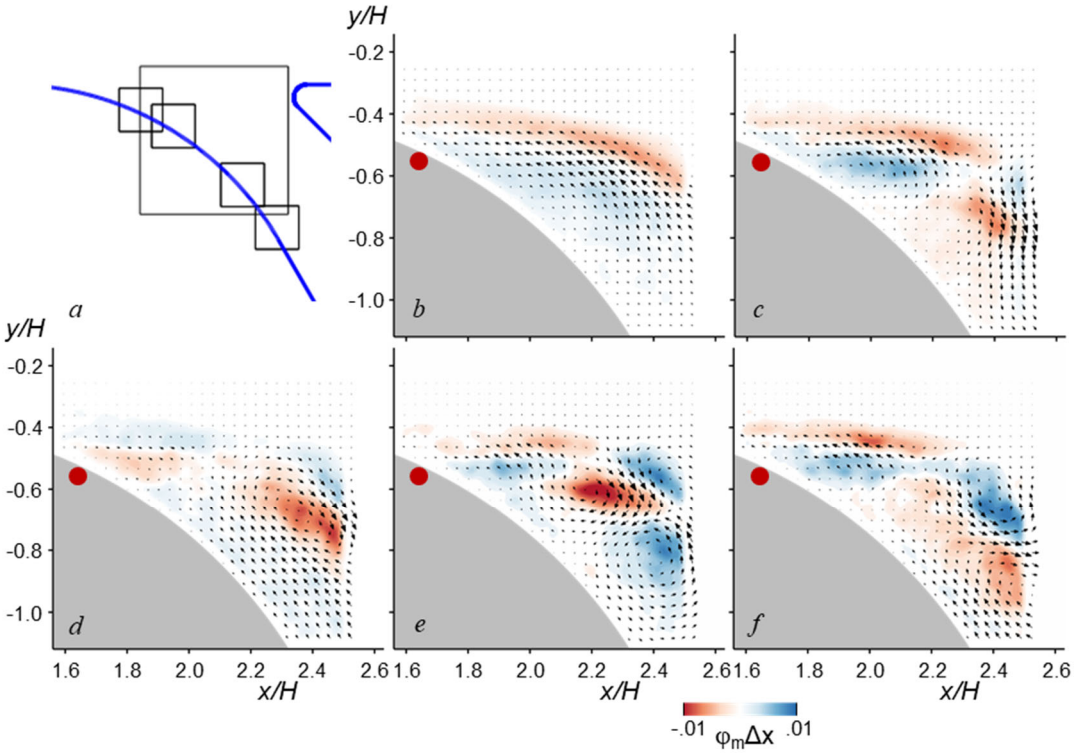

Figure 3.11. Global and individual PIV measurement domains within the diffuser (a). The first five dominant velocity POD modes in the base flow are shown using velocity vectors that are overlaid on top of color raster plots of their vorticity distributions φ_m, m = 1 (b), 2 (c), 3 (d), 4 (e), 5 (f) at $M_0 = 0.4$.

downstream lobe ($2.2 < x/H < 2.5$) are stronger, indicating the evolution of a coherent vortex formation and separated flow underneath the concentrations. The following mode (Figure 3.11e) includes another concentration of CCW vorticity at the downstream end of the field of view indicating the evolution of the separated domain and breakdown to multiple coherent vortical structures (which is continued further in Figure 3.11f).

The corresponding first four POD modes in the presence of actuation at $C_q = 0.002$ and 0.005 are shown in Figure 3.12e-l for $M_0 = 0.4$, and the corresponding locations of separation are marked for reference. The first four modes of the base flow are repeated in Figure 3.12a-d, respectively, and the corresponding modes at $C_q = 0.002$ and 0.005 are

shown in Figure 3.12e-h and i-l, respectively. In all cases, the first mode (Figure 3.12 a, e, i) shows a similar dual vorticity layer perturbation of the outer shear layer, which is displaced downstream and moved closer to the surface with the streamwise migration of separation in the presence of actuation (note the intensification of the CCW (blue) concentration in Figure 3.12i). Mode 2 (Figure 3.12 b, f, j) is altered in the presence of actuation and the gap between the two anti-symmetric modes disappears as the separation migrates downstream and the CCW (blue) concentration migrates closer to the surface marked by the dashed lines (also shown to be just downstream of the migrated separation in all cases). A different effect on the underlying structure, however, is visible in the third

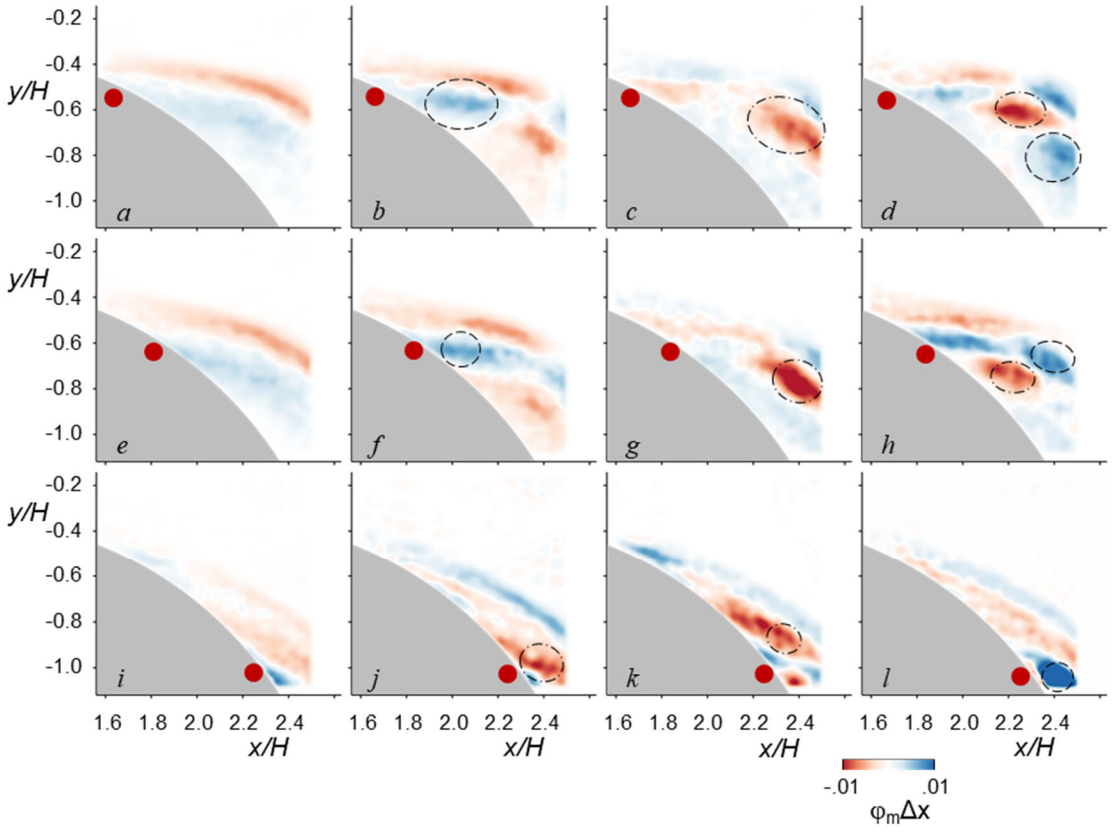

Figure 3.12. The first four dominant POD modes at $M_0 = 0.4$, φ_m, m = 1 (a,e,i), 2 (b,f,j), 3 (c,g,k), and 4 (d,h,l) for the base flow (a–d) and in the presence of actuation with $C_q = 0.2\%$ (e–h) and 0.5% (i–l).

mode (Figure 3.12c, g, k), which exhibits a 'free' CW vorticity concentration in the base flow (Figure 3.12c) that is advected downstream and towards the surface at $C_q = 0.002$ (Figure 3.12g) and eventually becomes surface-bound at $C_q = 0.005$ (Figure 3.12k). The two free vorticity concentrations in the fourth mode of the base flow (Figure 3.12d) are first split into a surface bound and free concentration at $C_q = 0.002$ (Figure 3.12h) and with further increasing actuation to $C_q = 0.005$ (Figure 3.12l) only one single, strong, surface bound vorticity concentration remains in the field of view. The dominant modes in Figure 3.12 show that with migration of separation in the presence of actuation, the vorticity concentrations are aligned along the flow boundary and the 'free' concentrations within the shear layer above the separated domain evolve into surface-bound vorticity concentrations that are associated with enhanced momentum transfer to the wall region.

The POD analysis not only examines the modal structure of the flow, but can also be used to reconstruct the flow using an energy (or modal) basis to exclude small scale perturbations in the fields while retaining global structural details associated with the advection of large coherent vortices. With the exclusion of the higher order, small-scale motions, further analysis can be conducted on instantaneous flow features such as vortex detection schemes. The distinct vortical motions in the presence of the actuation discussed in connection to the modal structures in Figure 3.12 are further investigated using such a vortex detection scheme applied to the POD-reconstructed velocity fields from the 20 highest order modes. The tracking and identification of coherent vortical structures is performed using the Γ_1 Criterion (e.g. Graftieaux et al., 2001 and Huang and Green, 2015) that searches the velocity fields for rotational motions such as a vortex core. A threshold

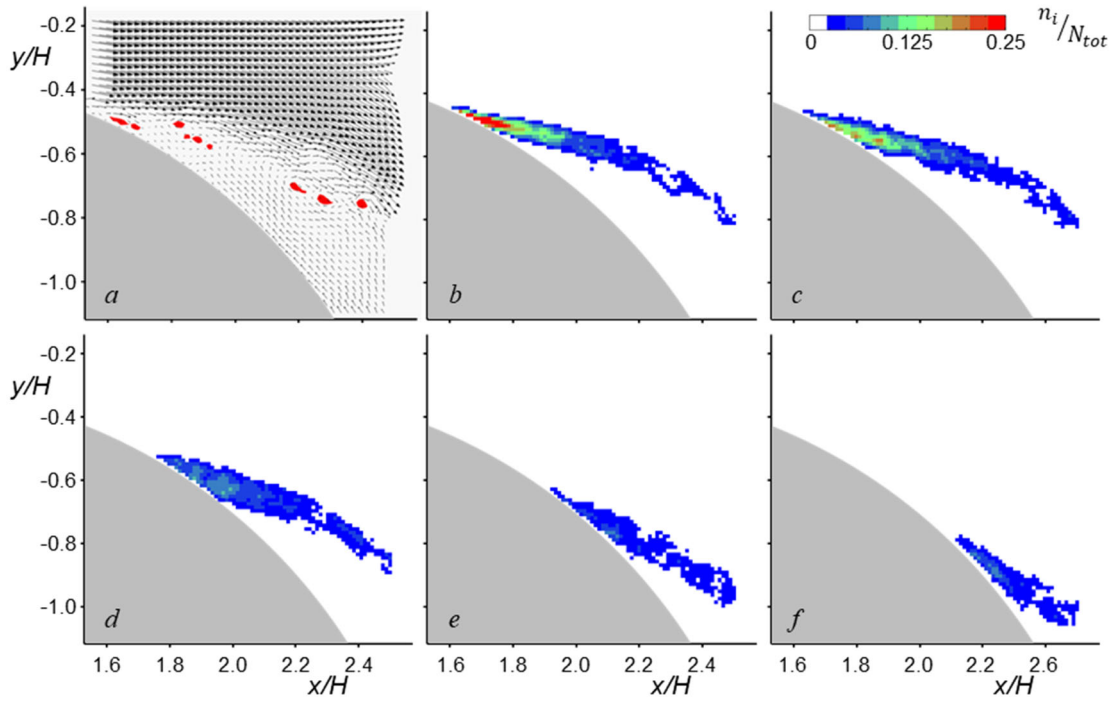

Figure 3.13. a) Illustration of threshold procedure based on Γ_1 vortex detection criterion in a reconstructed instantaneous velocity field. Spatial distributions of vortex detection counts n_i for $M_0 = 0.4$ in the base flow (b) and in the presence of actuation at $C_q = 0.001$ (c), 0.002 (d), 0.003 (e), and 0.004 (f).

applied to distributions of the Γ_1 fields yields levels that correspond to a coherent vortex core. Figure 3.13a shows the application of this criterion to an instantaneous POD-reconstructed velocity field of the base flow ($M_0 = 0.4$) in which the Γ_1 structures are shown in red. The vortex detection scheme is applied to reconstructed velocity fields in the base flow and in the presence of actuation and the vortex detections are spatially binned throughout the measurement domain for the acquired PIV data (800 frames). The normalized vortex counts n_i in the base and controlled flows ($C_q = 0.001$, 0.002, 0.003, and 0.004) are shown in Figure 3.13b-f. The base flow (Figure 3.13b) is marked by a thin layer of vortices that follows the evolution of the shear layer over the separated domain, and

exhibits a high count of vortex detections near the surface just past the location of separation ($x/H \approx 1.6$, c.f. Figure 3.5c). In the presence of actuation (Figure 3.13c-f), the number of detection counts is reduced compared to the base flow and the concentrations of vortices are drawn towards the surface with increasing level of actuation. Drawing the vortices towards the surface supports the conclusions of the mode analysis of Figure 3.12, which showed that increasing actuation levels turned outer 'free' vortices into wall-bound vortices. As the separation migrates due to the actuation, the vortex populations of the incipient shear layer varies with C_q in Figure 3.13, clearly indicating that not only does the separated vorticity layer become deflected towards the surface with increasing C_q but the ensuing dynamics and structure of separation and therefore of the flow farther downstream are significantly altered in the presence of actuation.

A supplemental analysis of the velocity fields in Figure 3.13 is conducted to assess the effects of the actuation on the circulation (Γ) fields within the incipient separated flow because the Γ_1 criteria does not differentiate between vortices of different strengths, and only serves to locate these structures. The circulation at a given grid point is computed using the two velocity components in the reconstructed instantaneous velocity field over its eight neighboring points and the circulation is spatially binned for three equally spaced ranges based on the maximum circulation levels in the base flow: 'low-' ($0.5\times10^3 < -\Gamma < 1.2\times10^3$), 'mid-' ($1.4\times10^3 < -\Gamma < 2.2\times10^3$) and 'high-' ($2.3\times10^3 < -\Gamma < 3.1\times10^3$). Typically, the vortices were found to have CW orientation giving them negative circulation values in the global coordinate system, hence they are reported as $-\Gamma$. The resulting spatial distributions of the three circulation levels are shown in Figure 3.14 for the base flow (Figure 3.14a - c) and in the presence of actuation at $C_q = 0.002$ (Figure 3.14d - f) and 0.004

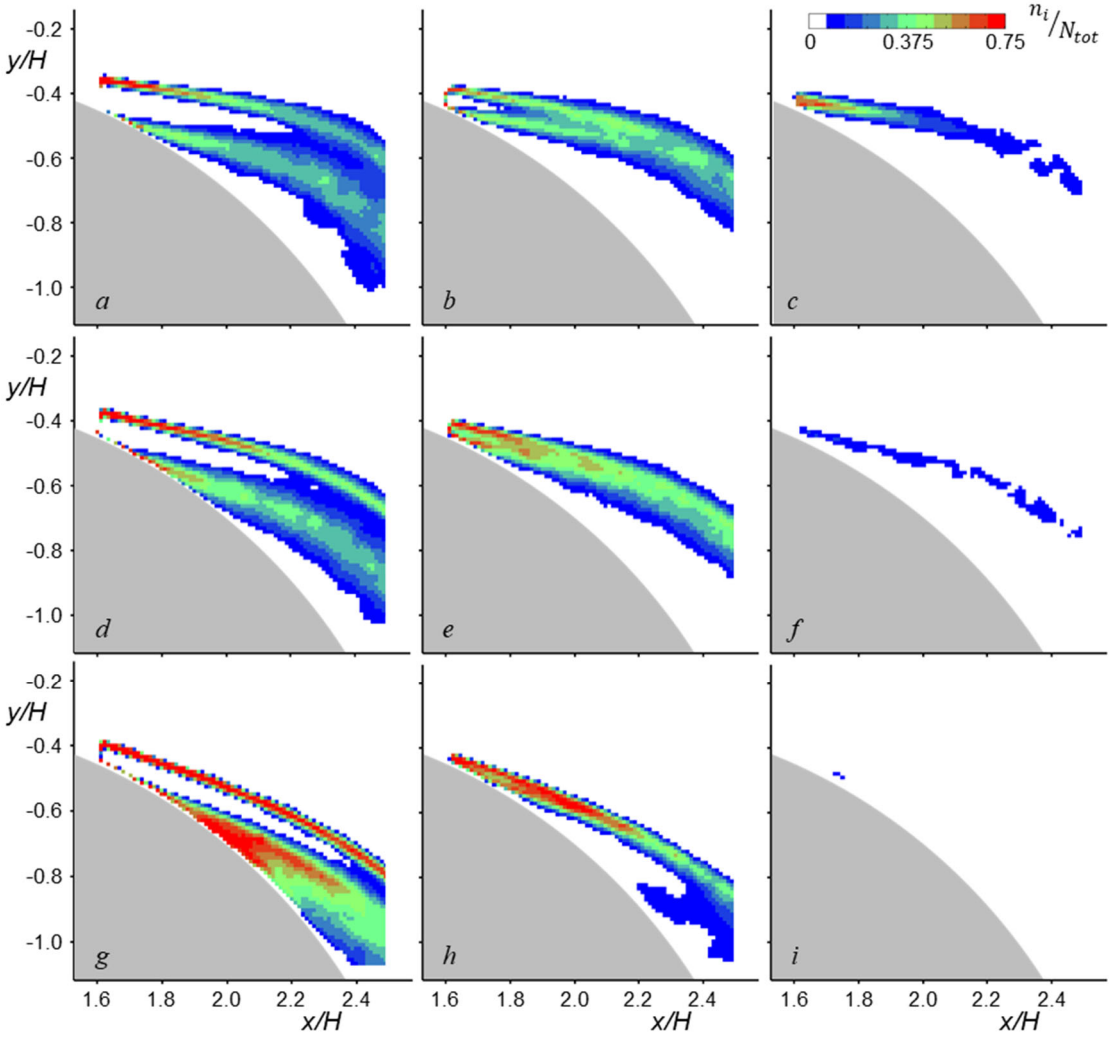

Figure 3.14 Spatial distribution of the count n_i at circulation levels - $\Gamma^* = 0.5$ - 1.2×10^{-3} ('low-', a, d, g), 1.4 - 2.2×10^{-3} ('mid-', b, e, h), and 2.3 - 3.1×10^{-3} ('high-', c, f, i) for the base flow (a–c), and with $C_q = 0.002$ (d–f), and 0.004 (g–i) at $M_0 = 0.4$.

(Figure 3.14g - i). The base flow (Figure 3.14a) exhibits a broad spread of the 'low-level' circulation in the streamwise direction, which appears to stem from two distinct sources: *i*. An upper region ($y/H > -0.4$) affected by the upstream flow, and *ii*. A lower domain along the lower edge of the shear layer. A similar split is also seen in the medium-level circulation levels in Figure 3.14b, which does not spread noticeably downstream, and

appears contained in the shear layer over the separation domain. Finally, the high levels of circulation in Figure 3.14c originate at the separation point and seem to decay as the flow is advected downstream. Actuation at $C_q = 0.002$ (Figure 3.14d-f) appears to intensify the lower level circulation (Figure 3.14d), without significantly altering their overall spatial distribution. It does, however, significantly suppress signatures of regions with high circulation values as shown in Figure 3.14f. With increased actuation at $C_q = 0.004$ (Figure 3.14g-i), the signatures of the lower circulation band are significantly enhanced, with a larger intensified region that is bound to the surface that is not present in the base flow or with the lower actuation level. The medium level circulation (Figure 3.14h) is also enhanced, but is confined to a smaller region than in the base flow or with actuation at $C_q = 0.002$, while the highest circulation range (Figure 3.14i) is almost entirely suppressed. These data show that, in principle, the actuation suppresses higher levels of circulation while intensifying lower circulation levels in the flow, further demonstrating how the actuation modifies the underlying flow dynamics and formation of vortical structures.

3.3.2 Local Flow Characteristics

This section focuses on details of the separation dynamics using high-resolution PIV measurements where the measurement domain is centered about the separation point and measure $0.28H$ x $0.28H$ (cf. Figure 2.5, and Figure 3.11a). The evolution of the flow about local separation in the absence and presence of actuation ($C_q = 0.002$, 0.005, and

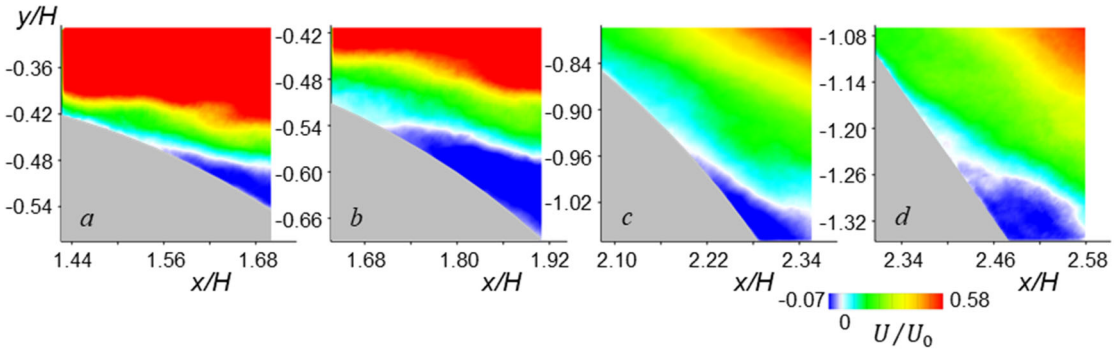

Figure 3.15. Color raster plots of the streamwise velocity component (U) for flow fields centered about local mean separation at $M_0 = 0.4$ for the base flow (a) and with $C_q = 0.002$ (b), 0.005 (c), and 0.008% (d).

0.008 for $M_0 = 0.4$) is illustrated in Figure 3.15 using distributions of the instantaneous streamwise velocity component U in which a white contour $U = 0$ corresponds to the boundary of the reversed flow domain. Separation in the base flow (Figure 3.15a) is at the most upstream location and also experiences the lowest adverse pressure gradient as was shown in the pressure measurements (cf. Figure 3.7c) since the base flow separates upstream of the first cluster of pressure ports between $2.4 < x/H < 3.1$, which showed that initially the flow experiences a favorable streamwise pressure gradient within the reverse flow domain. Delaying separation with increasing actuation strength changes the slope of the pressure gradient and the flow along the surface experiences the increasing adverse pressure gradient within the diffuser. Since the separation occurs close to the entrance plane, the boundary layer upstream of separation is relatively thin compared to the controlled flow (Figure 3.15b-d). As the local separation migrates downstream in Figure 3.15 from b to d with increasing actuation level, the increase in adverse pressure gradient (cf. Figure 3.7c) leads to thicker boundary layer upstream of separation and consequently to cross-stream spreading of the shear layer that bounds the reversed flow domain. The

most amplified vortical structures of a free planar shear layer scale with the local characteristic momentum thickness at separation (e.g. Ho and Huerre, 1984), in the presence of actuation the vortical structures in the separated flow are expected to become progressively larger owing to the increase in the cross-stream extent of the boundary layer shown in Figure 3.15. This is consistent with the discussion of Figure 3.13 which showed that the number of detected vortices immediately downstream from the separation decreases with increasing C_q and the concomitant increase in the lower band of circulation indicate larger characteristic scale of vortices within the shear layer.

The unsteadiness of the base flow about the local separation for $M_0 = 0.4$ is assessed from families of velocity profiles along the surface in local wall-normal coordinates for the time-averaged and instantaneous flow fields. An example of the time-averaged flow velocity profiles in local wall-normal coordinates is shown in Figure 3.16a, in which the reversed flow ($U' < 0$) is colored in red. Corresponding profiles in the instantaneous flow field are shown in Figure 3.16b, in which the separation point is upstream from its mean

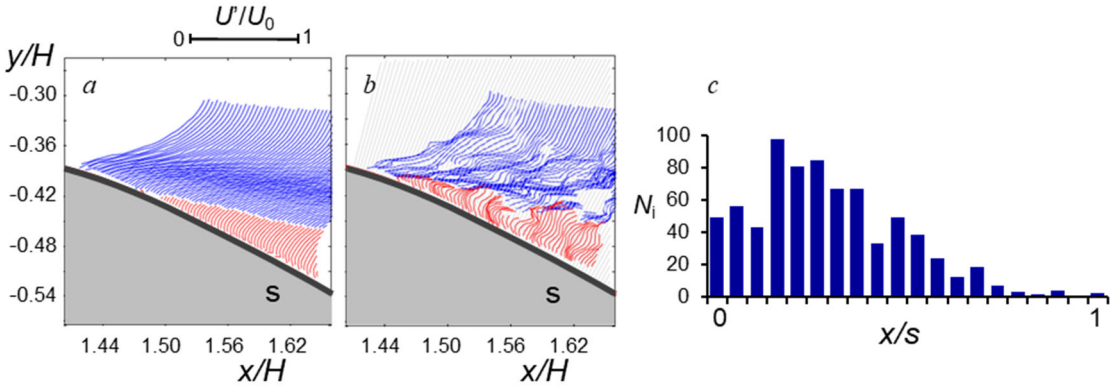

Figure 3.16. Time-averaged (a) and instantaneous (b) velocity profiles in the base flow at $M_0 = 0.4$ (the reversed flow is colored in red). The corresponding histogram of the locations of flow separation along the surface is shown in (c).

location. Using these families of instantaneous velocity profiles, the separation location along the surface is tracked along the field of view to form a histogram during the entire PIV acquisition sequence as shown in Figure 3.16c (based on 20 subdivisions of the surface within the field of view, each about 1 mm wide). The spatial distribution of separation locations in Figure 3.16c clearly shows that the natural separation traverses the entire streamwise extent along the wall, although rarely stretching to the farthest downstream location. The histogram also shows that the flow clearly exhibits a preferred separation location that coincides with the mean location in Figure 3.16a at about one-third of the streamwise extent. The separation binning also creates the basis for a conditional averaging of the flow field based on the local separation location, which can be applied in the absence and presence of actuation. This conditional averaging is shown in Figure 3.17 at three locations of incipient separation along the PIV field of view, (an upstream, central, and downstream) in which the instantaneous distributions and their resulting conditionally-averaged distributions of wall-normal velocity profiles of the flow are drawn using open

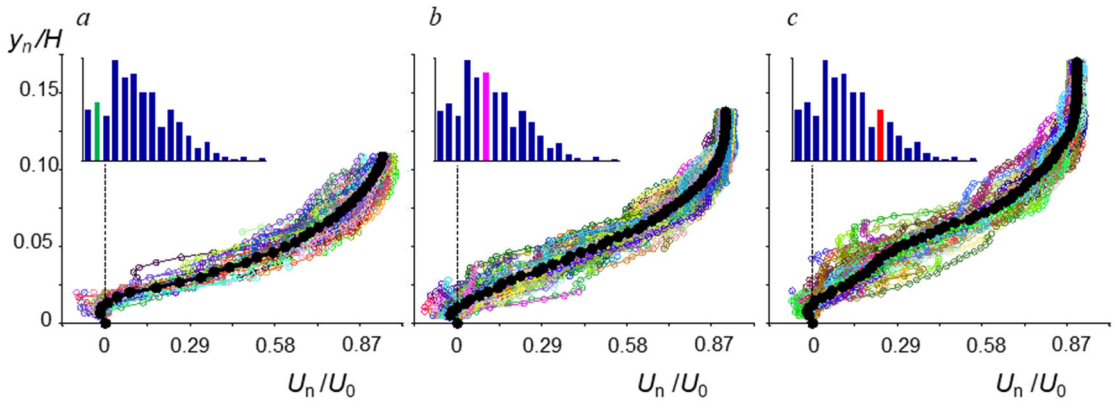

Figure 3.17. Wall-tangential velocity profiles conditionally averaged for separation upstream (a), near (b), and downstream (c) of the time-averaged separation in the base flow. The instantaneous and conditionally-averaged profiles are marked by open and solid symbols, respectively. Inset plots highlight the streamwise bin position.

and solid symbols, respectively. Figure 3.17a-c show respective profiles along with the corresponding location of the data in the histogram (in the inset) upstream, near the most probable separation location, and when the flow remains attached beyond the midpoint of the view (Figure 3.17c). Each of these distributions captures the flow as it reverses its direction above the surface within one PIV acquisition sequence. Furthermore, within these three bins the conditionally averaged velocity profiles exhibit the expected cross-stream extension of the velocity profiles which progresses as the separation moves downstream.

Similar to the analysis of the base flow in connection with Figure 3.15, the statistics of the separation location in the controlled flow is extracted from profiles of the instantaneous wall-tangential velocity at $C_q = 0.008$. The ensemble averaged profiles along the surface are shown in Figure 3.18a, (the reverse flow is colored in red), which shows that the time-averaged separation location is just beyond the mid-point of the flow field. An example of the instantaneous velocity field is shown in Figure 3.18b in which, the instantaneous separation is migrated upstream of the mean location. The histogram of

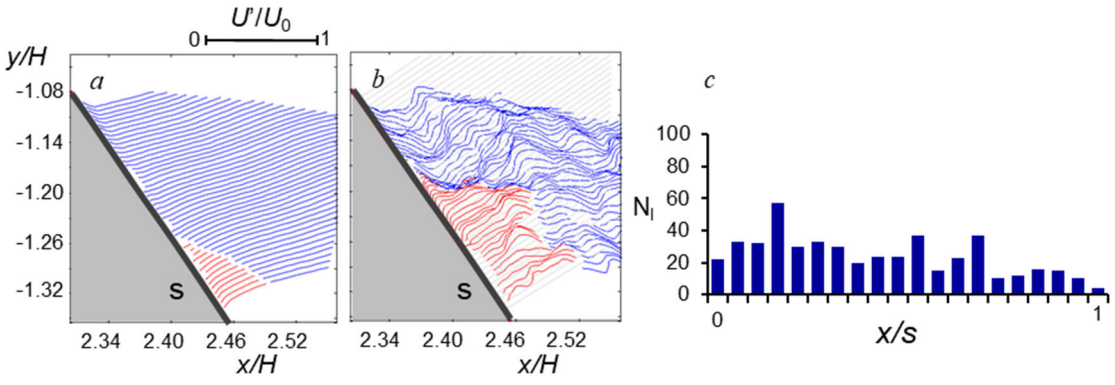

Figure 3.18. As in Figure 3.16 in the presence of actuation at $C_q = 0.008$.

separation locations along the surface are shown in Figure 3.18c. Similar to the histogram of the base flow (Figure 3.16c), in the presence of actuation the instantaneous separation location (Figure 3.18c) traverses the entire streamwise domain along the surface. However, in contrast to the base flow, the histogram of the controlled flow is relatively featureless and does not show a clear preferred location that coincides with the time-averaged position in Figure 3.18a. This histogram suggests that the streamwise movement of the local separation intensifies in the actuated flow, which is commensurate with the increase in the local *TKE* about the location of separation as suggested in Figure 3.10.

As illustrated in connection with Figure 3.17 in the base flow, the histograms of the separation location in the actuated flow (Figure 3.18) can be used for conditional averaging of the streamwise extent of the local separation. This conditional averaging not only allows for the examination of the separation centered velocity profiles as in Figure 3.17, but also extends the analysis to examine the evolution of the wall-tangential velocity profiles through the separation process along the discretized surface locations. This evolution of the cross-stream velocity distributions through separation is shown in Figure 3.19 for three locations of the conditionally averaged separation location (as in Figure 3.17) in the base flow (*a*) and in the presence of actuation at $C_q = 0.008$ (*b*) for $M_0 = 0.4$. The conditionally averaged locations of separation based on the histograms in Figures 3.16 and 3.18 are selected to be the most probable locations (blue profiles) at $x/H = 1.5$ and 2.4 for the base and controlled flows, respectively, and instances where the conditional separation occurs 4 mm upstream (green profiles) and downstream (red profiles) along the surface, and all the profiles in Figure 3.19a and b are plotted respectively centered at the conditionally-averaged separation location with two equidistant velocity profiles upstream and

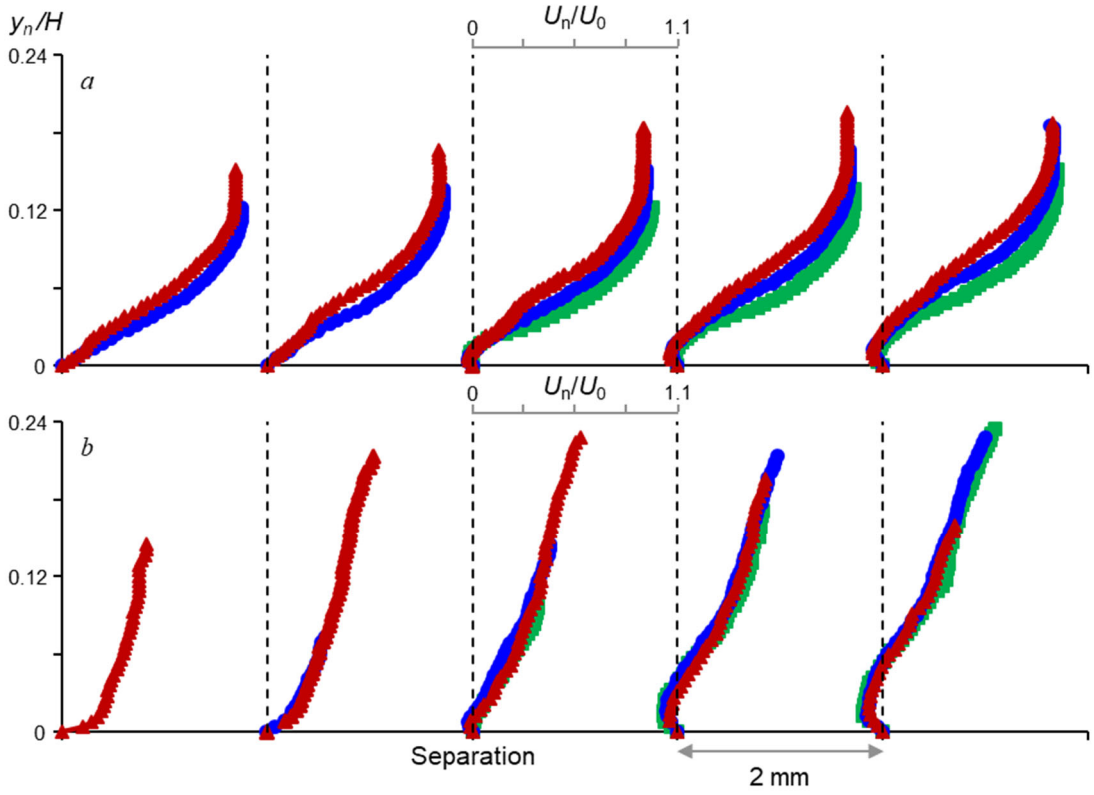

Figure 3.19. Conditionally-averaged wall-tangential velocity profiles U_n in the base flow (a) and in the presence of actuation at $C_q = 0.008$ (b). The profiles in (a) and (b) are plotted respectively at the time-averaged location of and with two equidistant profiles immediately upstream and downstream of separation (spaced 2 mm along the surface). Conditional averaging in (a) and (b) is based on the histograms of Figures 3.16 and 3.18 where the most probable separation location (●) is at $x/H = 1.5$ and 2.4 for the base and controlled flows, respectively, with two other instances where the conditional separation location occurs 4 mm upstream (■) and downstream (▲).

downstream spaced 2 mm along the surface in the fields of view shown in Figures 3.16 and 3.18. These conditionally-averaged velocity profiles capture the progression of separation as the flow passes from immediately upstream, through and then downstream of the conditional location of separation. The cross-stream extent of the base flow profiles (Figure 3.19a) is fully captured within the field of view, and shows the streamwise increase in cross-stream spreading of the boundary layer (i.e. from green to red in Figure 3.19a). The progression of the flow through local separation in the presence of actuation in Figure

3.19b shows that unlike the base flow, the cross-stream scale of the boundary layer in the controlled flow is extended beyond the top edge of the present field of view of these high-resolution measurements. This cross-stream spreading shows that in the presence of actuation the cross-stream scale of the shear layer that bounds the separated domain from above indicates that a similar increase in the scale of the shear layer vortices that is commensurate with the earlier analysis(c.f. Figure 3.13 and Figure 3.14) that showed that the actuation reduces the overall vortex count while increasing their scale. The formation of these larger scale vortices in the presence of actuation also explains the increase in the unsteadiness of the location of separation (Simpson, Chew et al., 1981 and Simpson, Chew et al., 1981). Furthermore, another important aspect of the actuation is the collapse of the velocity profiles, unlike the profiles of the base flow, which do not exhibit a similar increase in the cross-stream scale as the separation moves downstream within the field of view.

Conditionally averaged analysis of spatial distributions of turbulent kinetic energy within the global field of view (0.95*H* x 0.95*H*, Figure 2.5) is shown in Figures 3.20a and d using color raster plots of time-averaged *TKE* in the absence and presence of actuation (C_q = 0.008), respectively. These distributions of the *TKE* are closely aligned with the vorticity distributions in Figure 3.5. Once the flow separates and the bounding shear layer forms, enhanced entrainment and mixing increases the levels of turbulent kinetic energy. More details of local *TKE* distributions in the bae and actuated flows are obtained from *TKE* distributions that are extracted from high-resolution PIV measurements (0.28*H x* 0.28*H*, Figure 2.5) within the domains marked by white squares in Figure 3.20a and d in which flow separation is located close to the middle of the streamwise domain

($x/H \approx 1.56$ and 2.4 in Figures 3.16a and 3.18a, respectively). These high-resolution vies are shown in Figure 3.20b and e. The base flow in Figure 3.20b is marked by an uninterrupted *TKE* layer above the surface, which only begins to intensify as the free shear layer forms past separation (also shown in Figure 3.10a). Similar TKE evolution past separation is evident in the presence of actuation (Figure 3.20e), although the cross-stream expanse of the TKE is much larger corresponding to the increase in the cross stream scale of the shear layer (cf. Figure 3.19b). Additionally, these data show that the *TKE* levels about separation are higher in the presence of actuation compared to the base flow. If the

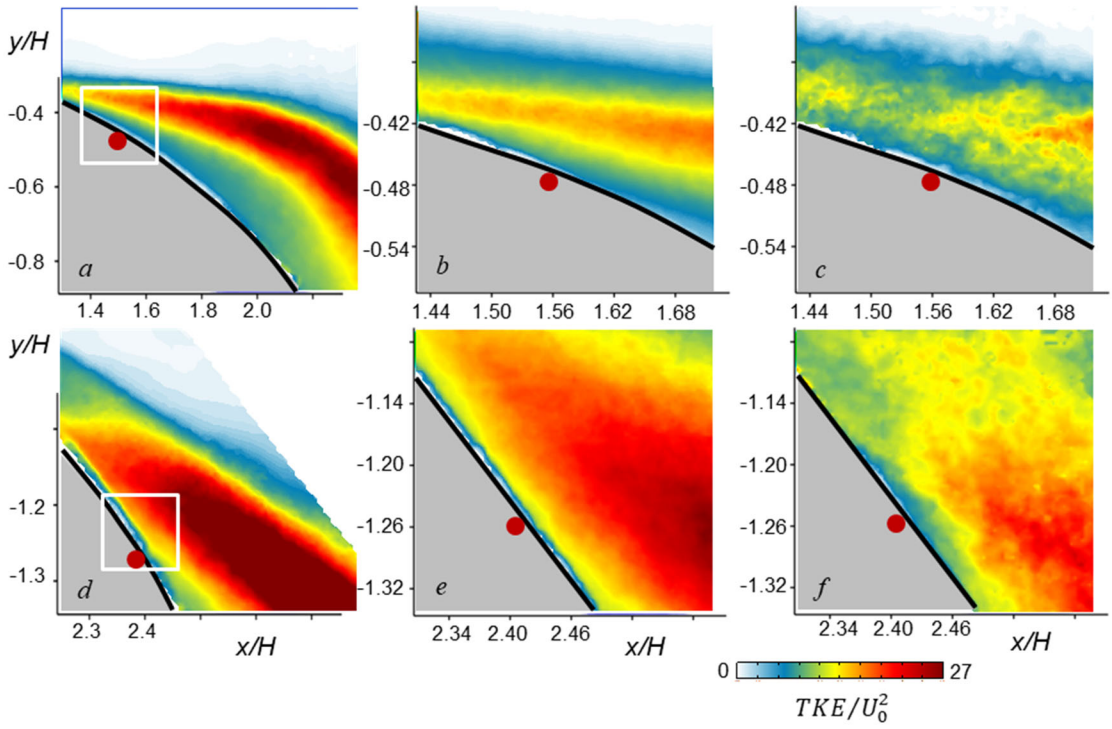

Figure 3.20. Color raster plots of distributions of the time-averaged turbulent kinetic energy in the base flow (*a-c*) and in the presence of actuation at $C_q = 0.008$ (*d-f*) using the global (0.95*H* x 0.95*H*, *a*, *d*) and local (0.28*H* x 0.28*H, b* and *e* and marked by white squares in *a* and *d*) fields of view. Figures 3.20 *c, f* show conditionally-averaged *TKE* for the median bin of the separation histograms in Figures 3.16c and 3.18c.

TKE is conditionally averaged based on a bin near the time-averaged separation from the histograms in Figure 3.16c and Figure 3.18c, details of the pseudo-instantaneous features of the *TKE* distributions (that are not lost by time-averaging) are visible in Figures 3.20c and f. The enhanced *TKE* beyond the separation locations is more clearly delineated from the *TKE* distribution upstream. The conditional averages also indicate that the *TKE* levels at the separation point (and immediately downstream from it) are overall higher in the presence of actuation (Figure 3.20f) than in the base flow (Figure 3.20c). In both the base (Figure 3.20c) and controlled flows (Figure 3.20f) the *TKE* is intensified immediately past separation (nearly the streamwise center of the fields of view), however, in the controlled flow the *TKE* is intensified within a larger cross-stream extent. The increase in the *TKE* beyond the separation is attributed to the instability of the boundary layer due to cross-stream stretching of the outer shear layer in the adverse pressure gradient and reduced shear at the wall.

To further explore the dynamics about local separation, the PIV window is set to $0.06H$ x $0.06H$ (Figure 2.5) and is centered about the time-averaged separation point in the base flow and in the presence of actuation (at $C_q = 0.008$, $M_0 = 0.4$), and the PIV images are acquired at 5 kHz (cf. Section 2.3.4). This highly-resolved measurement domain yields approximately five equally-spaced velocity time traces over the same span as would be typically covered by a 1.25 mm wide miniature hot-wire sensor. The sizes and locations of these miniature PIV measurement domains are marked by dashed squares on the color raster plots of the ensemble averaged *TKE* in Figure 3.21a and b for the base flow and in the presence of actuation, respectively. As discussed in Section 2.3.4 and reported by Peterson, Vukasinovic et al. (2020), the enhanced PIV acquisition rate is used for spectral

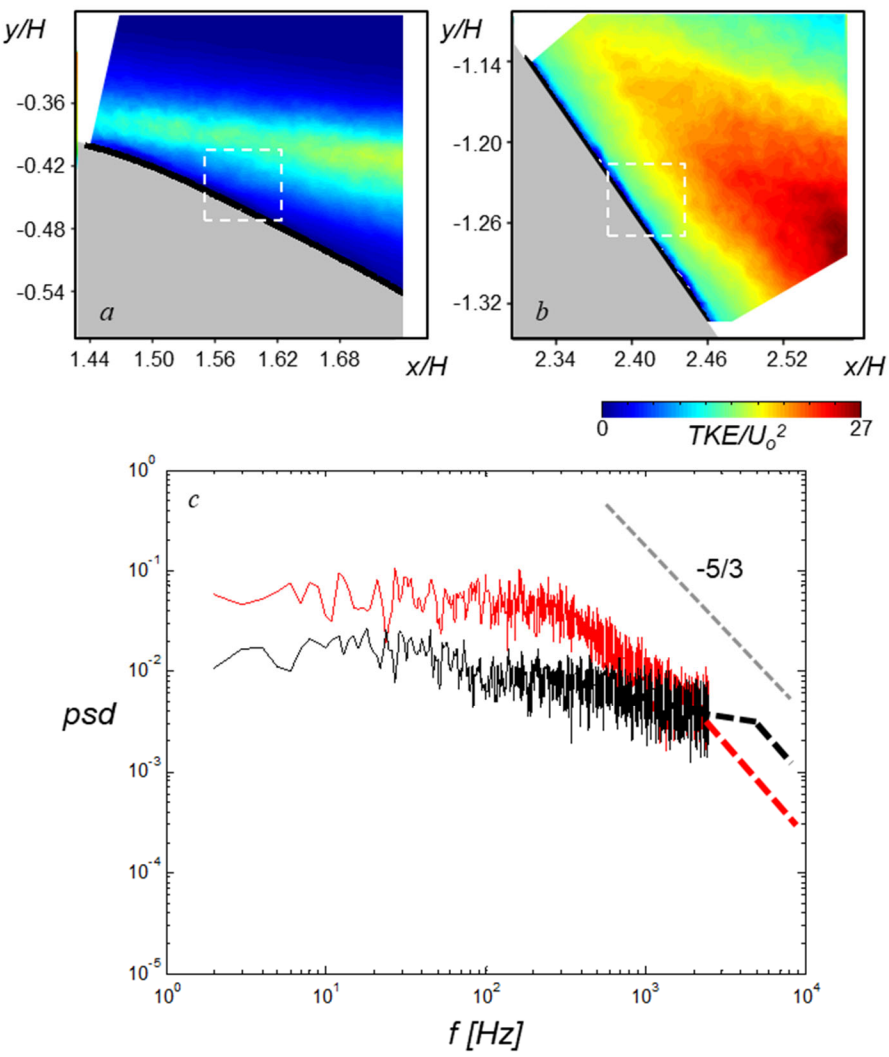

Figure 3.21. Color raster plots of *TKE* in the base flow (*a*) and in the presence of actuation at $C_q = 0.008$ (*b*) at $M_0 = 0.4$. Figure 3.21c shows power spectra of velocity fluctuations measured within the dashed windows in *a* (—) and *b* (—).

analysis of the flow. Ten sets of PIV data are acquired over one second intervals, and the individual velocity fluctuation spectra at each measurement point are averaged and the resulting power spectra are shown in Figure 3.21c. These data show that the spectral content of the individual velocity fluctuations within these measurement domains are similar to each other, due to the small scale of the measurement region. Therefore, only a

single characteristic spectrum in each flow is shown in Figure 3.21c. Although the frequency bandwidth (2.5 kHz) is not sufficient to capture all relevant scales of the velocity fluctuations, it is sufficient to capture a range of energy-bearing motions. While the energy-bearing scales of the base flow stretch over the entire range of the resolved scales, in the presence of actuation, part of the inertial subrange (close to -5/3 slope) is contained within the resolved frequencies. These spectra show that there is a significant increase in large-scale motions in the presence of actuation compared to the base flow, since the power in the lower frequencies is higher, in agreement with the earlier analysis (cf. Figure 3.13 and 3.14) that indicated that the actuation amplifies the formation and advection of large-scale vortices. These data also show that the presence of actuation leads to earlier transfer of energy to the smaller scales within the inertial subrange. These spectra also indicate the presence of a crossover at higher frequencies beyond which the energy content of the small scales in the base flow is higher than in the actuated flow, as emphasized by the dashed extensions of the measured power spectra in Figure 3.21c.

The spectral analysis of Figure 3.21c showed that the fluidic control augments the lower frequencies and large-scale motions within the flow, indicating the presence of larger scale motions near the local separation. This analysis does not, however, assess the local structure at the separation. The four dominant POD modes assessed in Figure 3.12 showed that low levels of control significantly altered the outer flow, but the larger fields of view did not center and focus on the local separation as it is delayed with increasing C_q. The underlying separation flow structures in the base flow and in the presence of actuation are compared using the underlying POD of the flows' first 6 vorticity modes for $C_q = 0.002$, 0.005, and 0.008 at $M_0 = 0.4$, that are shown in Figure 3.22. A striking feature here is the

similarity of the higher order modes, despite the differences observed in the turbulent kinetic energy (cf. Figure 3.20) and the spectral energy distribution (Figure 3.21c), which suggested that the migration of separation had significant alteration of the energy composition of the flows. All modes of the actuated flow (Figure 3.22 row II-III) are tilted and stretched versions of the base flow modes, indicating essentially the same dominant structure of flow perturbations near the mean separation in the presence or absence of actuation.

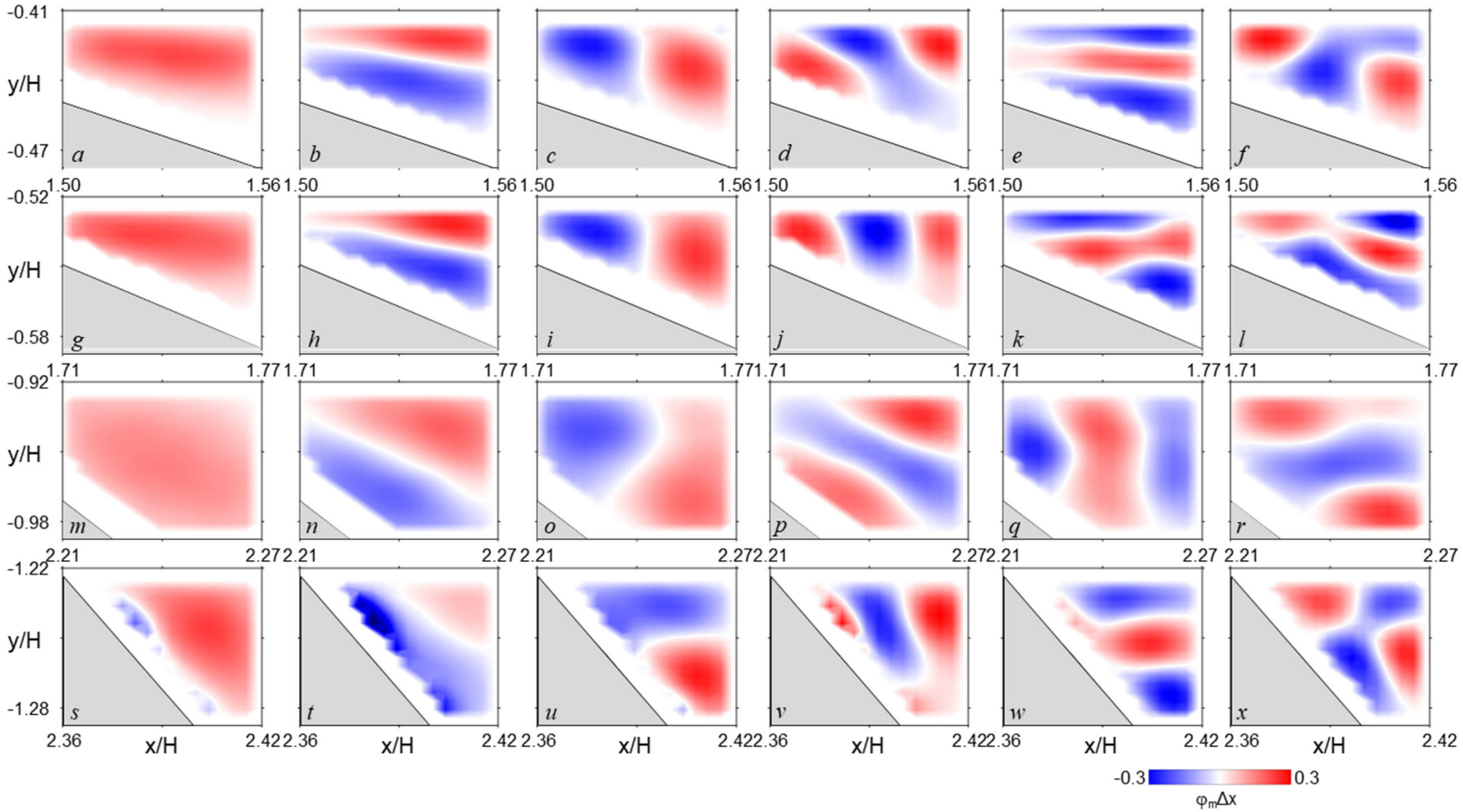

Figure 3.22. The first six vorticity POD modes (from left to right) for the base flow (a–f) and in the presence of actuation at C_q = 0.002 (g–l), 0.005 (m–r), and 0.008 (s–x) at M_0 = 0.4.

This modal similarity implies an underlying structural commonality between the base and actuated flows at separation despite the significant near-wall effects of the fluidically oscillating jets. Considering the differences between the time-averaged global vorticity fields (cf. Figure 3.5), it is remarkable that the changes in separation between the absence and presence of actuation have underlying structural similarities. To highlight just how different these flow fields are, especially near local separation, several profiles of the ensemble averaged wall-tangential velocity profiles are extracted about the mean local separation point (x/H = 1.56 and 2.4, x/s = 0), and that include two equally-spaced (2 mm along the surface) profiles upstream and downstream from the central separation profile (similar to the conditionally averaged profiles in Figure 3.19) for the base and actuated flows at C_q = 0.008 as shown in Figure 3.23. Both velocity profiles indicate a dominant shear-layer-like structure even upstream from separation, which is characteristic of

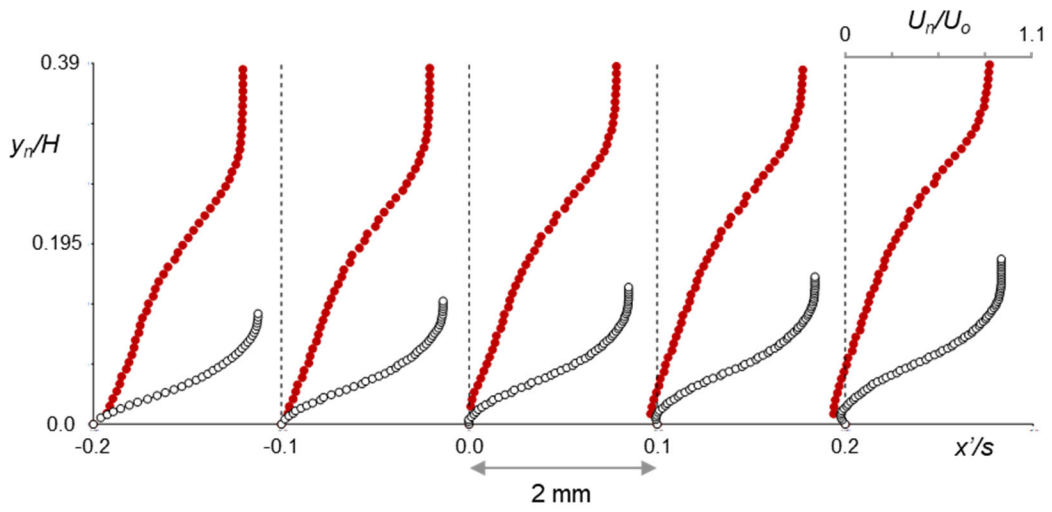

Figure 3.23. Time-averaged wall-tangential velocity profiles in the base flow (○) and in the actuated flow at C_q = 0.008 (●) centered at local separation (x/H = 1.56 and 2.4, in the absence and presence of actuation, respectively) with corresponding profiles upstream and downstream of separation at M_0 = 0.4.

boundary layers in an adverse pressure gradient (Elsberry et al. 2000). As noted in connection with Figure 3.19, the velocity profiles in the controlled flow extend significantly farther away from the surface as the flow overcomes the adverse pressure gradient, having almost a threefold characteristic scale compared to the base flow.

Finally, the work of Elsberry, Loeffler et al. (2000) asserted that the effects of the wall layer of a turbulent boundary layer in an adverse pressure gradient are significantly diminished as the shear stress at the wall vanishes approaching. More recently Schatzman and Thomas (2017) proposed scaling of such boundary layer flow in an adverse pressure gradient that, instead of traditional boundary layer wall-scaling, utilizes parameters based on the outer shear layer using the vorticity thickness and velocity deficit at the inflection point of the outer shear layer. They demonstrated excellent scaling of their and similar data from other investigations. They showed that the proposed scaling is applicable to different flows undergoing separation in an adverse pressure gradient that develops an embedded shear layer away from the wall, identified by a linear cross-stream growth region in the velocity profile, with the inflection point (*IP*) defined as the mid-point of this linear region. The scaling parameters are based on the length scale, which is the embedded shear

$$\delta_\zeta = (U'_e - U')_{IP}/(dU'/dy)_{IP} \quad 3.1$$

$$U'_d = (U'_e - U')_{IP} \quad 3.2$$

$$\eta = (y' - y'_{IP})/\delta_\zeta \quad 3.3$$

$$U^* = (U'_e - U')/U'_d \quad 3.4$$

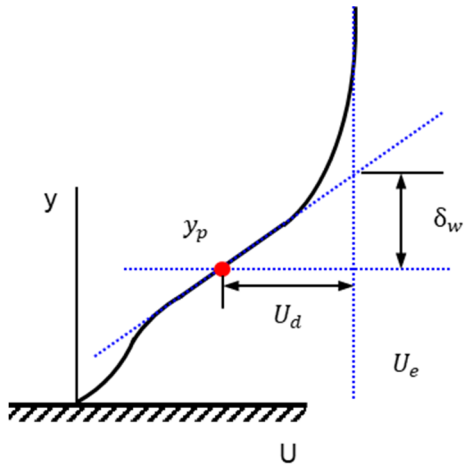

Figure 3.24. Schematic representation of the outer embedded shear layer scaling parameters of Schatzman and Thomas (2017).

layer vorticity thickness δ_ζ,and the velocity scale, which is the velocity deficit U'_d between the apparent free stream velocity (U'_e) and the velocity at the inflection point (U'). These scaling parameters are shown in Equations 3.1 to 3.2, which are then used to determine the similarity variables for the length (η) and velocity (U^*) in Equation 3.3 and 3.4, respectively. In Equations 3.1-3.4 the subscript *IP* designates the velocity or wall-normal distance at the inflection point in the embedded shear layer. The scaling parameters are shown schematically in Figure 3.24 using a representative velocity profile that includes an outer embedded shear layer. The ensemble averaged wall-tangential velocity distributions at separation for the base flow and in the presence of actuation that are markedly different as the actuated flow re-separates at different adverse pressure gradients due to the delay of the separation in the diffuser duct are scaled by the outer shear layer parameters and shown in Figure 3.25. These velocity distributions show remarkable collapse onto a single shear-layer-like distribution and only deviate somewhat near the surface (negative η), owing to the breakdown in the scaling by the outer flow parameters. It should be noted that the

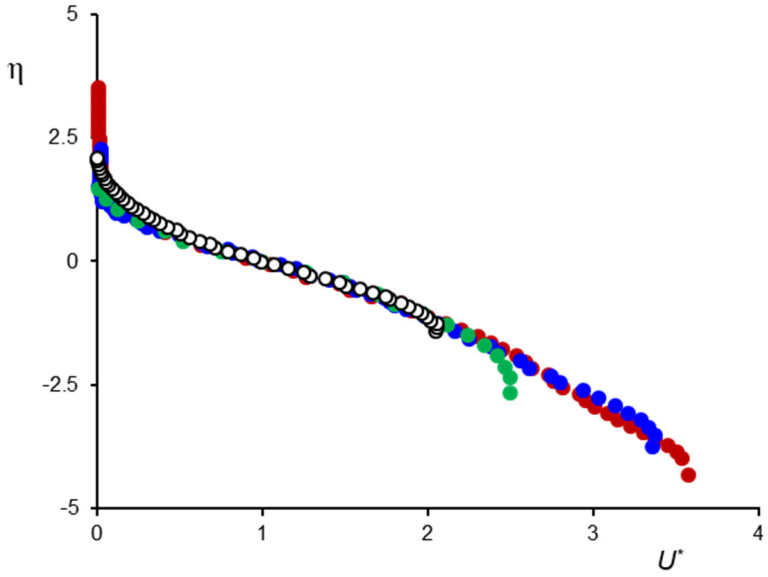

Figure 3.25. Time-averaged scaled velocity distributions at local separation of the base flow (○) and in the presence of actuation at C_q = 0.002 (●), 0.005 (●), and 0.008 (●) for M_0 = 0.4.

scaling in the actuated flow deviates from the scaled profile farther away from the surface than in the base flow. The collapse implies that the flow near separation is governed by the outer flow.

CHAPTER 4. CONTROL OF A CLOSED SEPARATION DOMAIN OVER A CURVED SURFACE

4.1 Overview

The results of Chapter 3 showed that an array of fluidic oscillators can delay internal flow separation into an adverse pressure gradient within a diffuser duct by altering the underlying flow dynamics in the near wall region. This chapter describes an investigation of the flow topology within a closed separation domain (i.e. a separation cell) that forms in the presence of an adverse pressure gradient on a wall-mounted insert within a test section of a pressure driven wind tunnel (cf. Section 2.1.1) and the control of separation using a spanwise array of fluidically oscillating jets. The confined flow domain upstream of the model forms a contraction region through the model's apex and is followed by a diffuser region downstream that effects an adverse pressure gradient until the insert merges with the test section's wall. The flow structure within the plane of symmetry ($z/c = 0$) of the separation domain is investigated in the absence and presence of separation using planar PIV and surface pressure measurements.

4.2 The Base Flow

The topology of the separation in the base flow over the model insert (cf. Chapter 2) was captured using surface oil flow visualization. This separation forms a closed separation cell (cf. Chapter 1) whose main features are shown in Figure 4.1 ($M_0 = 0.25$). The model was chosen to have a reference length $c = 62.23$ mm (cf. Chapter 2) based on the original VR-12 airfoil model, and the global coordinate system is set such that the

streamwise direction $x = 0$ at the inlet to the test section and the spanwise coordinate $z = 0$ is centered between the test section sidewalls ($z/c = \pm 1.02$). This image shows the surface of the insert model between the exit plane of the spanwise array of actuation jets at $x/c = 5.10$ (cf. Figure 2.8) and beyond the downstream end of the insert merging with the

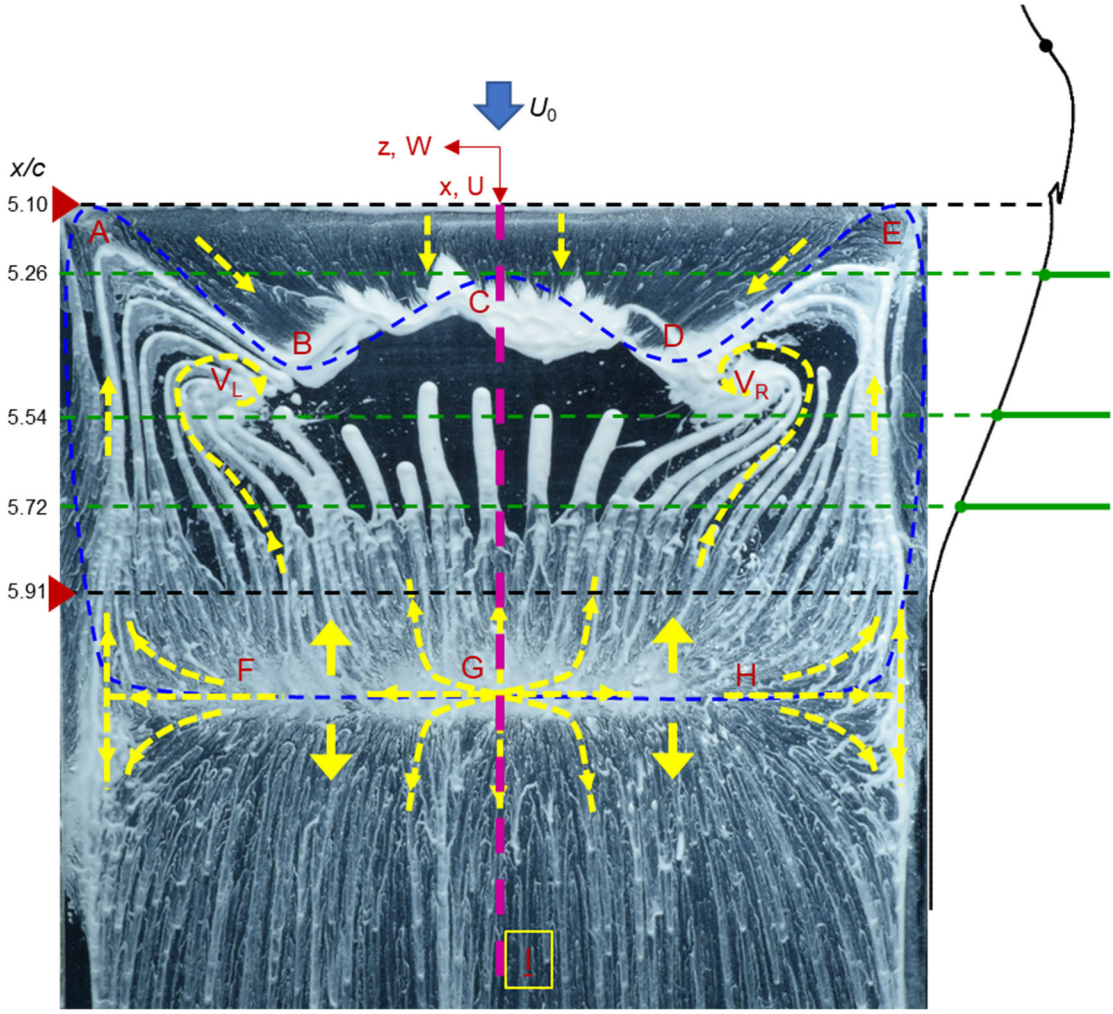

Figure 4.1. Surface oil flow visualization of the separation cell in the base flow ($M_0 = 0.25$, the flow is from top to bottom) along with a side view of the surface of the model's cross-stream section (cf. Chapter 2). The upper edge of the image is aligned with the exit plane of the jet actuator array at $x/c = 5.10$ (marked by ▶). The downstream edge of the insert model is at $x/c = 5.91$ (marked by ▶). The streamwise positions of the centerline of the spanwise y-z PIV planes ($z/c = 0$) is marked by the vertical dashed line C-G-I.

test section wall (x/c = 5.91) and spanning the entire width of the test section. The spanwise planar PIV in the following Chapter is conducted along the centerline (z/c = 0) marked by the vertical dashed line in Figure 4.1 (connecting points C-G-I) and the streamwise locations (x/c = 5.26, 5.54, and 5.72) of the stereo PIV conducted in Chapter 5 are also marked in Figure 4.1 for reference. The direction of the oil streaks are indicated by the yellow dashed lines and arrows in Figure 4.1. A further detailed discussion of the surface topology is discussed in Chapter 5, but a shortened summary is included here to contextualize the ensuing centerline results. The base flow forms a separation cell (cf. Section 1.1.1.2) that is characterized by an upstream separation front (marked A-B-C-D-E) as is evidenced by the accumulated oil (B-C-D) and the streamwise flow upstream of the separation front. The flow reattaches downstream at the reattachment node (marked G) and the topology shows lateral flow that connects to two saddle points near the sidewalls (F and H) and defines a line (F-G-H) which separates the upstream reverse flow and downstream reattached flow. The inner domain of the separation cell (marked by surrounding line connecting A-B-C-D-E-H-G-F) is characterized by two surface bound vortices marked V_L and V_R with CW and CCW orientations, respectively. The reverse flow along the sidewalls from F to A and H to E are turned towards the centerline after reaching the jet exit plane (A and E) as they approach the attached streamwise oriented flow from upstream and form the undulating upstream separation front (A-B-C-D-E), which in turn gives the CW and CCW orientations of the surface vortices. These vortices induce spanwise motions on the outer spans (between A and B and between D and E) within the reverse flow emanating from the reattachment (F-G-H). The central domain (spanning between B and D and bounded between the separation front A-B-C-D-E and the

reattachment F-G-H), however, shows nominally two-dimensional flow emanating upstream from the reattachment line (F-G-H), as evidenced by the parallel oil streaks reaching upstream along the central span (between B and D). Clearly the flow emulates a nominally two-dimensional flow closer to the reattachment (F-G-H) as the upstream separation front (A-B-C-D-E) is undulating across the span due to the presence of the surface vortices within the separation cell. Never the less, the separation cell is shown to be symmetric about the center plane ($z/c = 0$), and along the centerline of the separation front (marked C), there is little evidence of spanwise motion as the oil streaks between the jet exit plane at $x/c = 5.91$ and the separation front are directed nominally in the positive x (downstream) direction. The results of the current Chapter focus on the evolution of the flow along this nominally 2-D central plane.

The evolution of the flow over the curved surface insert is investigated using planar PIV in the y-x plane at $z/c = 0$ ($M_0 = 0.25$). As noted in Section 2.3.3 (Figure 2.6), multiple high-resolution, partially overlapping PIV fields are acquired at 200 Hz and the time-averaged flow is computed within each of these domains using an ensemble of 1,000 images. It is noted that here and elsewhere in this thesis, vorticity distributions are interchangeably referred to as *vorticity concentrations* since the time-averaged fields represent accumulations of multiple instantaneous vorticity strands. The time-averaged domains are subsequently combined to create composite views as shown in Figure 4.2 using color raster plots of spanwise vorticity concentrations overlaid with cross-stream distributions of velocity vectors (Figure 4.2a) and the turbulent kinetic energy ($TKE = \left(\overline{u'^2} + \overline{v'^2}\right)/2$, Figure 4.2b) (the outline of the model's surface shows the exit orifice of the actuation jets cf. Section 2.4). Due to the contraction of the test section

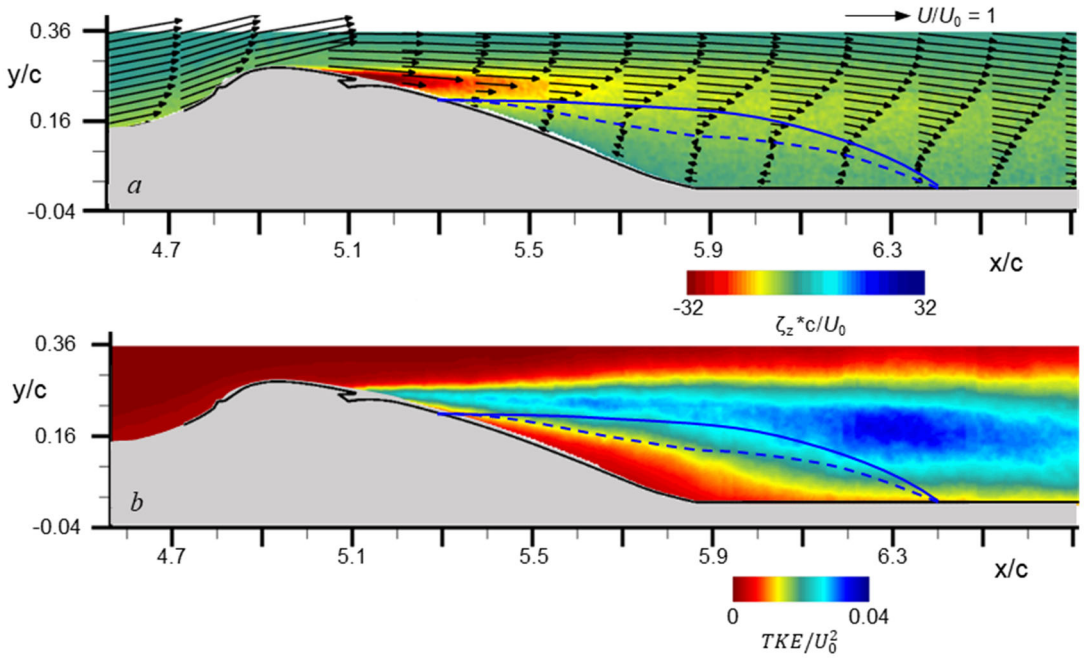

Figure 4.2. Color raster plots of the time-averaged spanwise vorticity with overlaid cross-stream distributions of vectors of the time averaged-velocity (a) and the turbulent kinetic energy (b) in the base flow at $M_0 = 0.25$. The outline of the model's surface is shown using a black line.

upstream of the model's apex, the flow upstream of the apex ($x/c < 5$) accelerates as is evidenced by the increased magnitude of the velocity vectors over the apex of the model. The flow over the model changes direction over its apex ($x/c = 5$) and the cross-stream velocity component (V) changes from positive to negative for $x/c > 5$, as the increase in the cross-sectional area results in a diffuser effect and consequently the apparent free-stream velocity (for $y/c > 0.2$ above the vorticity layer in Figure 4.2a) decreases along the x direction along the aft of the insert model ($5 < x/c < 5.91$). The wall boundary layer in Figure 4.2a separates at approximately $x/c \approx 5.2$, based on the where the streamwise flow (U) near the surface is reversed. The surface measurements are limited by laser reflections, and the ensuing separation location is determined within the resolved PIV data near the

surface. The flow downstream of the apex of the model ($x/c > 5$) is marked by the formation of a wake-like domain that is characterized by the formation of a cross-stream shear layer, flow separation, and reversed flow along the surface within $5.2 < x/c < 6.4$ that is part of a (time-averaged) closed recirculation domain (as was shown in the oil flow visualization in Figure 4.1). The wake domain deficit has a maximum cross-stream width based on the location of where $U = 0$ away from the surface as the indication between a switch from reverse flow to positive streamwise oriented flow of $y/c \approx 0.31$ at $x/c = 5.91$ and as shown in Figure 4.2a, the cross-stream concentrations of spanwise vorticity persist through the downstream end of the PIV composite view, well past the downstream end of the model's curvature at $x/c = 5.91$ and reattachment of the separated flow at $x/c = 6.4$. As shown by the velocity deficit in the vectors, the overall reverse flow is relatively shallow and a schematic of the bound of the reverse flow region is shown in Figure 4.2 in two ways: 1) a dashed inner line that follows the contour of $U = 0$ to highlight the bound of the reverse flow and forward flow region and 2) a solid outer line which is defined by the location away from the surface that the volume flow rate of the time-averaged reverse flow region ($U < 0$) is balanced by the forward flow region ($U > 0$) above the reverse flow. The narrow region between the dashed and solid lines indicate the region that, in the time-averaged sense, would be entrained from the outer forward flow into the reverse flow region (see schematic in Figure 4.3a). The formation of the shear layer (Figure 4.2a) associated with the wake structure is accompanied by increasing levels of turbulent kinetic energy in the flow (Figure 4.2b). The increased *TKE* levels that accompany the cross-stream concentrations of the spanwise vorticity peak in the streamwise direction at $x/c \approx 6.3$,

which is associated with the cross-stream stretching of the flow over the surface and

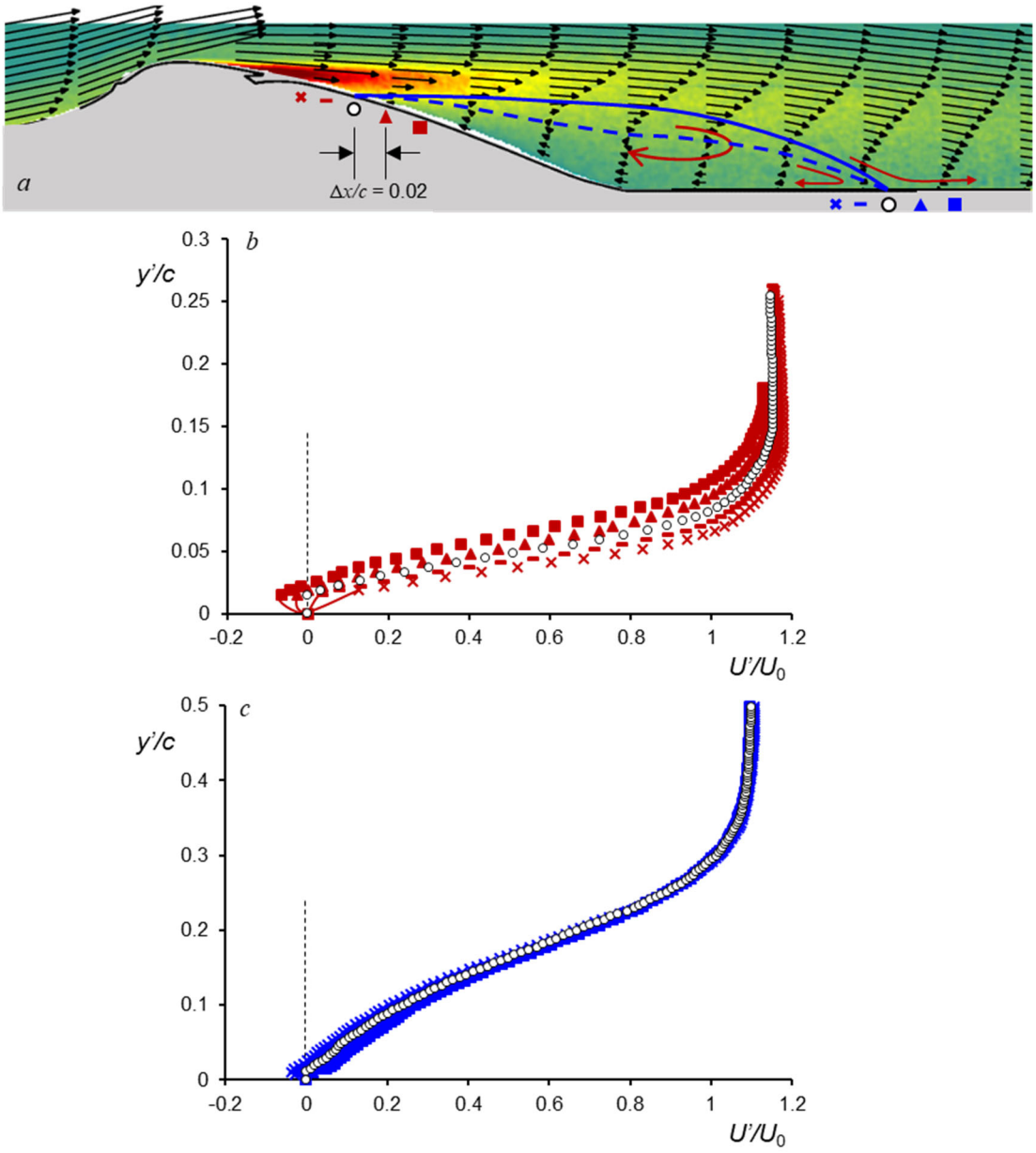

Figure 4.3. a) The composite PIV data of Figure 4.2 ($M_0 = 0.25$) where the streamwise positions of separation and reattachment ($x/c = 5.2$ and 6.4, respectively) are each marked by (○) and two equally spaced ($\Delta x/c = 0.025$) streamwise positions upstream and downstream of each of the locations of **separation** and **reattachment** are marked by (×), (-), (▲) and (■). b) and c) Time-averaged cross stream distributions of the surface-tangential velocity component U' about **separation** [in b, $x/c =$ (×) 5.17, (-) 5.19, (○) 5.22, (▲) 5.24, and (■) 5.27] and **reattachment** [in c, $x/c =$ (×) 6.33, (-) 6.35, (○) 6.38, (▲) 6.40, and (■) 6.43].

ostensibly strong cross-stream mixing.

The features of the flow upstream and downstream of the surface separation and reattachment are investigated using cross-stream distributions of the time-averaged velocity component that is locally tangential to the surface (U'), which is computed by determining the local surface tangent and normal directions as unit vectors and then interpolating the x-y gridded data from the PIV in Figure 4.2 onto a wall-normal projected line with same grid spacing ($\Delta y'/c = 0.004$) and then converting the global velocity components U and V into wall-tangential components U' and V' based on the dot product with the wall-tangential unit vector. The ensuing velocity distributions centered at the local separation and reattachment are marked by the open symbols in Figure 4.3 in which the PIV image of the spanwise vorticity from Figure 4.2 is reproduced for reference (along with a schematic of the bounding regions). The velocity distributions are extracted at two equally spaced ($\Delta x/c = 0.025$, ~1.6 mm) streamwise positions upstream and downstream of the locations of separation and reattachment. Each of the corresponding five velocity distributions are plotted in local wall normal coordinates (y'/c) and offset such that the local surface height is set to $y' = 0$, and are shown in Figure 4.3b and c. The symbols on the surface of the model in Figure 4.3a schematically indicate the position of the cross-stream distributions, but are not scaled in this view (recall the overall reference chord length $c = 62.23$ mm and the velocity distributions are extracted $\Delta x/c = 0.025$ surrounding the separation and reattachment). The velocity distributions evolving through separation in Figure 4.3b comprise three cross-stream domains: near-wall in which (typically $y/c < 0.025$), shear domain which is characterized by a nearly-linear velocity distribution containing concentrations of CW spanwise vorticity (typically $0.025 < y/c < 0.1$), and an

outer domain in which the velocity distribution within the core flow of the diffuser becomes nearly invariant with elevation (note that in the local wall-normal coordinates the direction of the resultant outer velocity changes along the model). As the flow evolves through separation ($5.17 < x/c < 5.27$), U' within the near wall region (e.g. $y'/c < 0.025$) progresses from positive to negative from attached to separated flow exhibiting zero shear at separation ($x/c = 5.22$), to having a thin reversed flow layer within $y'/c < 0.02$ at $x/c = 5.27$ (about 15% of the wall-normal extent of the shear layer where the reversed flow displaces the outer, forward flow). The concentrations of CW vorticity that are advected downstream of the model's apex appear to spread in the cross-stream flow by vertical advection by the wall-normal velocity component along the model. Owing to the cross-stream diffusion, the velocity of the outer (core) flow diminishes by about 3% through the short evolution through the separation from $U'/U_0 = 1.15$ to 1.12 at $x/c = 5.17$ and 5.27, respectively. The changes of the cross-stream velocity distributions through reattachment at $x/c = 6.38$ (Figure 4.3c) are rather benign and the profiles nearly collapse for $y'/c > 0.1$. The most salient aspect of these distributions is that their cross-stream width is nearly three-fold larger than the width of the corresponding cross-stream distributions at separation attesting to the cross-stream spreading of the near-wall flow at the apex. In common with the distributions at separation, the distributions at the attachment also comprise the same cross-stream domains, but with different cross-stream widths. The near-wall domain ($y'/c < 0.1$) is nearly 5 times wider than the corresponding domain at separation ($y'/c < 0.02$) and occupies about 5% of the wall-normal extent before reaching the local core speed of the diffuser (nominally $U'/U_0 = 1.10$). The linear shear domains, $0.1 < y'/c < 0.26$, appear to collapse despite the variation in their streamwise locations.

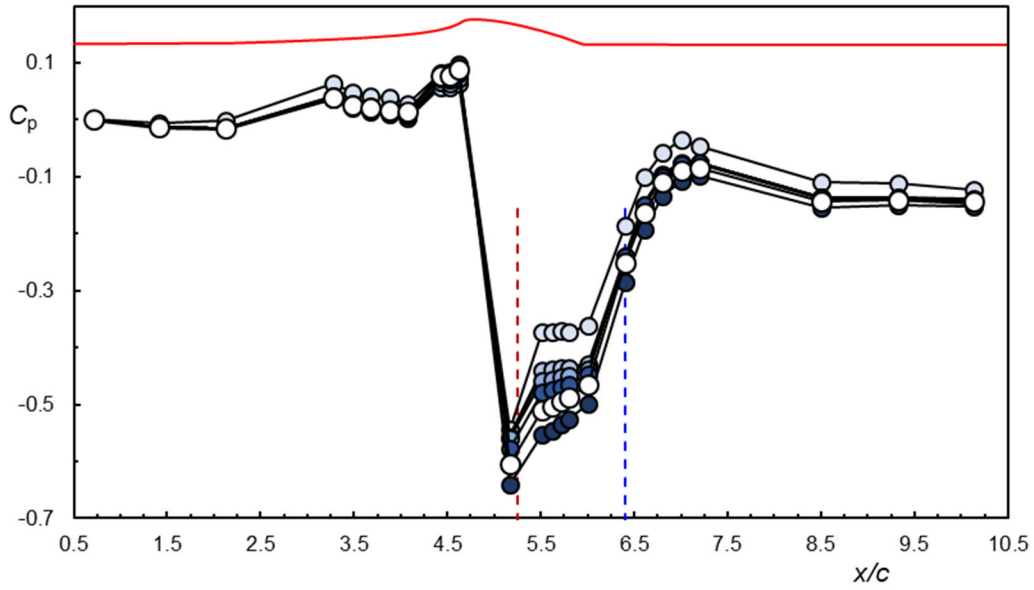

Figure 4.4. Streamwise distributions of the static pressure coefficient C_p along the centerline $z/c = 0$ of the test surface in Figure 2.4 at $M_0 = 0.8$ (●), 0.12, (●), 0.15, (●), 0.2 (●), 0.25 (○), and 0.31(●). The upstream separation ($x/c = 5.2$) and downstream reattachment ($x/c = 6.4$) points are shown as red and blue dashed lines, respectively, for reference.

The evolution of the flow along the centerline of the test surface in Figure 2.4 is assessed from streamwise distributions of the static pressure coefficient C_p (Equation 2.1) shown in Figure 4.4 for a range of inlet Mach number ($M_0 = 0.8$, 0.12, 0.15, 0.2, 0.25, and 0.31) where C_p is referenced to the inlet static pressure (i.e. $C_p = 0$ at $x/c = 0$). A schematic of the model situated within the wind tunnel is included for reference. The streamwise locations of flow separation and reattachment $M_0 = 0.25$ are marked in Figure 4.4 for reference using dashed lines. These data show that the variation of C_p upstream of the insert model ($x/c < 4.5$) is nearly invariant with M_0. The favorable pressure gradient induced by the downstream contraction over the insert model is evident by an initial decrease in C_p from 0 to -0.012 for $0.7 < x/c < 2$ along the constant cross-section segment

of the wind tunnel. The pressure then increases to 0.04 at $x/c = 3.28$ as the upstream portion of the insert model begins ($x/c = 2.85$) and as the upstream section ($2.85 < x/c < 5$) forms a contraction region, there is a negative pressure gradient between $3.28 < x/c < 4.6$ with decreased (increasingly favorable) slope compared to the constant cross-section portion of the wind tunnel upstream of the model ($x/c < 2.85$). Despite the favorable pressure gradient, the C_p increases and peaks at 0.08 at $x/c = 4.62$ as the flow reaches the front stagnation point at $x/c = 4.85$ at the leading edge of the airfoil that forms the top surface of the insert model (cf. Figure 2.8). As the flow progresses over the apex of the model ($x/c = 5$) the streamwise pressure gradient has a significant change in the magnitude of its slope as the C_p drops from 0.08 at $x/c = 4.62$ to -0.6 at $x/c = 5.16$, as the flow locally accelerates over the apex of the model causing the local suction peak due to the upstream favorable pressure gradient and curvature of the model, with slight changes in the magnitudes due to variations in inlet M_0. Downstream of the apex of the model, the separation domain ($5.2 < x/c < 6.4$), determined from the reverse flow near the surface in Figure 4.4, is associated with a change in sign of the pressure gradient from favorable to adverse as indicated by the positive slope in C_p values for $5.2 < x/c < 6.4$. The magnitude of the adverse pressure gradient within the separated domain increases with M_0, which is presumed to be a sign of a separation domain with decreased cross-stream (y) extent (cf. Figure 4.3a) which augments the diffuser effect beyond the apex of the model ($x/c > 5$) due to the reduced blockage of the separating shear layer, which is shown in Figure 4.2a. Once the flow reattaches ($x/c = 6.4$), C_p becomes nearly independent of M_0, and as the flow redevelops along the constant cross-sectional area downstream of the insert model ($x/c > 5.91$) there are signs of pressure recovery between $6.4 < x/c < 7.2$ as C_p increases

from about -0.24 at x/c = 6.4, peaking at -0.09 at x/c = 7, and then decreases to -0.08 at x/c = 7.2 to adjust to the overall favorable pressure gradient through the wind tunnel. Once the flow has reattached and progressed along the constant cross-section portion of the wind tunnel downstream of the model, the C_p values downstream ($8.5 < x/c < 10.12$) are nearly invariant with M_0, and demonstrate an overall pressure drop through the test section of ΔC_p = -0.14.

4.3 The Controlled Flow

The primary changes in the base flow over the insert model in the presence of actuation are depicted in Figure 4.5 using surface oil visualization. As shown in Chapter 2.2.2, actuation is applied using a spanwise array of fluidically oscillating jets that issue tangentially to the surface, and the momentum coefficient per jet is $C_{\mu,\,\text{per jet}} = 0.12 \cdot 10^{-3}$ and $M_0 = 0.25$ in the oil flow visualization in Figure 4.5, shown from the jet exit plane at x/c = 5.10 and extending downstream beyond the model moldline (x/c = 5.91). The stereo PIV locations at x/c = 5.26, 5.54, and 5.72 (cf. Chapter 5) are shown again for reference along with a side profile of the model surface, and a further detailed description of the topology of the actuated flow is discussed in Chapter 5. It is evident that the actuation at $C_{\mu,\,\text{per jet}} = 0.12 \cdot 10^{-3}$ shown in Figure 4.5 reattaches the flow, as there is no evidence of reverse oil streaks across the central span (B-C-D), which in the base flow (cf. Figure 4.1) comprised a majority of the central span of the test section. It is further noted that the reattachment appears to result from two competing effects: 1) the streamwise orientation of the issuance of the jets which moves the prior undulating separation line downstream (cf. Figure 4.1), and 2) an upstream migration of the prior reattachment node which shown to be downstream of the end of the model surface at x/c = 5.91 (cf. Figure 4.1). These two

competing effects seemingly merge along the line B-C-D in Figure 4.5, which shows an accumulation of oil as the effects of the jet array begins the wean, and downstream of this line shows a return to streamwise oriented oil streaks (C-I). The two side saddle points connected to the central reattachment node discussed in the base flow (cf. Figure 4.1), remain in relatively the same location (F and G) near the sidewalls, but are shown to be inclined toward line B-C-D, providing further evidence that the reattachment line shifts

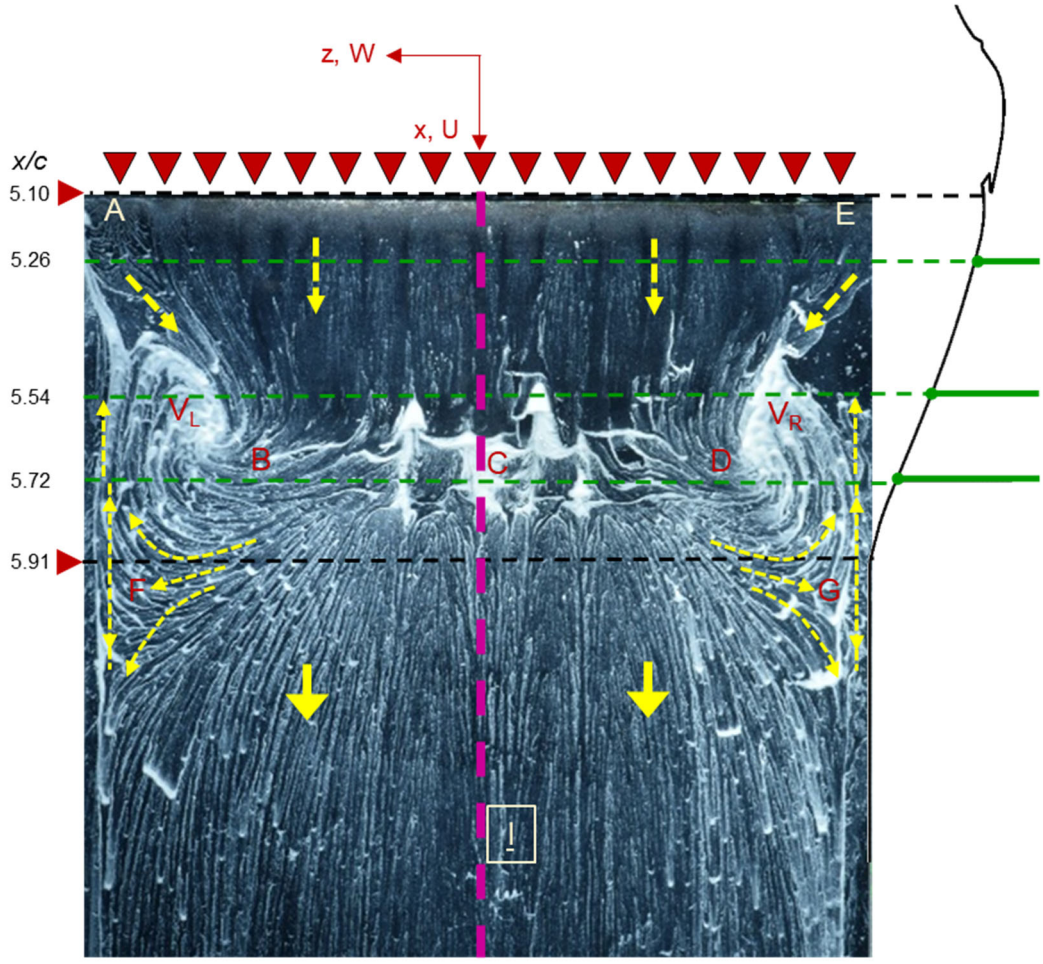

Figure 4.5. Oil flow visualization of the actuated flow ($C_{\mu,\text{ per jet}} = 0.12 \cdot 10^{-3}$, $M_0 = 0.25$, and the freestream (U_0) from top to bottom) aligned with a streamwise profile of the model insert section. The upper edge of the image is aligned with the exit plane of the actuation array at $x/c = 5.10$ (▶). The downstream edge of the model is marked $x/c = 5.91$ (▶), and the centerplane ($z/c = 0$) is marked by the vertical dashed line (C-I).

upstream. The two surface bound vortices present in the base flow (cf. Figure 4.1), remain in the actuated flow (V_R and V_L, with CCW and CW orientations, respectively), but are shifted downstream and towards the sidewalls, while retaining their orientation from the base flow, due to the presence of the jets which widen the nominally 2-D area through the central region spanning from B-D.

The effects of the jet array actuation was investigated by incrementally increasing the actuation level (the jet's momentum coefficient) $C_\mu = 0.36 \cdot 10^{-3}$, $0.96 \cdot 10^{-3}$, $1.5 \cdot 10^{-3}$ and $2.1 \cdot 10^{-3}$ (or $C_{\mu, jet} = 0.02 \cdot 10^{-3}$, $0.05 \cdot 10^{-3}$, $0.08 \cdot 10^{-3}$, and $0.12 \cdot 10^{-3}$). The effect of actuation level is investigated using planar PIV measurements within the cross-stream plane of Figure 4.2a and the corresponding composites of the concentrations of spanwise vorticity superposed with cross-stream distributions of velocity vectors at multiple streamwise locations along the centerline are shown in Figure 4.6. The base flow data from Figure 4.2 is repeated for reference in Figure 4.6a. At the lowest actuation level ($C_{\mu, jet} = 0.02 \cdot 10^{-3}$, Figure 4.6b) the actuation appears to slightly increase the cross-stream extent of the wake domain discussed in connection with Figure 4.2 by deflecting the apex shear layer away from the surface at the exit plane of the jets at $x/c = 5.10$, which is upstream of the separation in the base flow at $x/c \approx 5.2$ in Figure 4.6a. This small deflection of the shear layer is apparent in the increased width of the wake domain from $y/c \approx 0.31$ at the downstream end of the model curvature ($x/c = 5.91$) to $y/c \approx 0.35$, while delaying the reattachment farther downstream to $x/c \approx 6.5$ (compared to $x/c = 6.4$ in the base flow Figure 4.6a). When C_μ is increased to $0.05 \cdot 10^{-3}$ (Figure 4.6c) the formation of separation and reversed flow domain is delayed and the reattachment moves farther upstream such that their corresponding locations move to $x/c = 5.58$ and 6.2, respectively, and the maximum

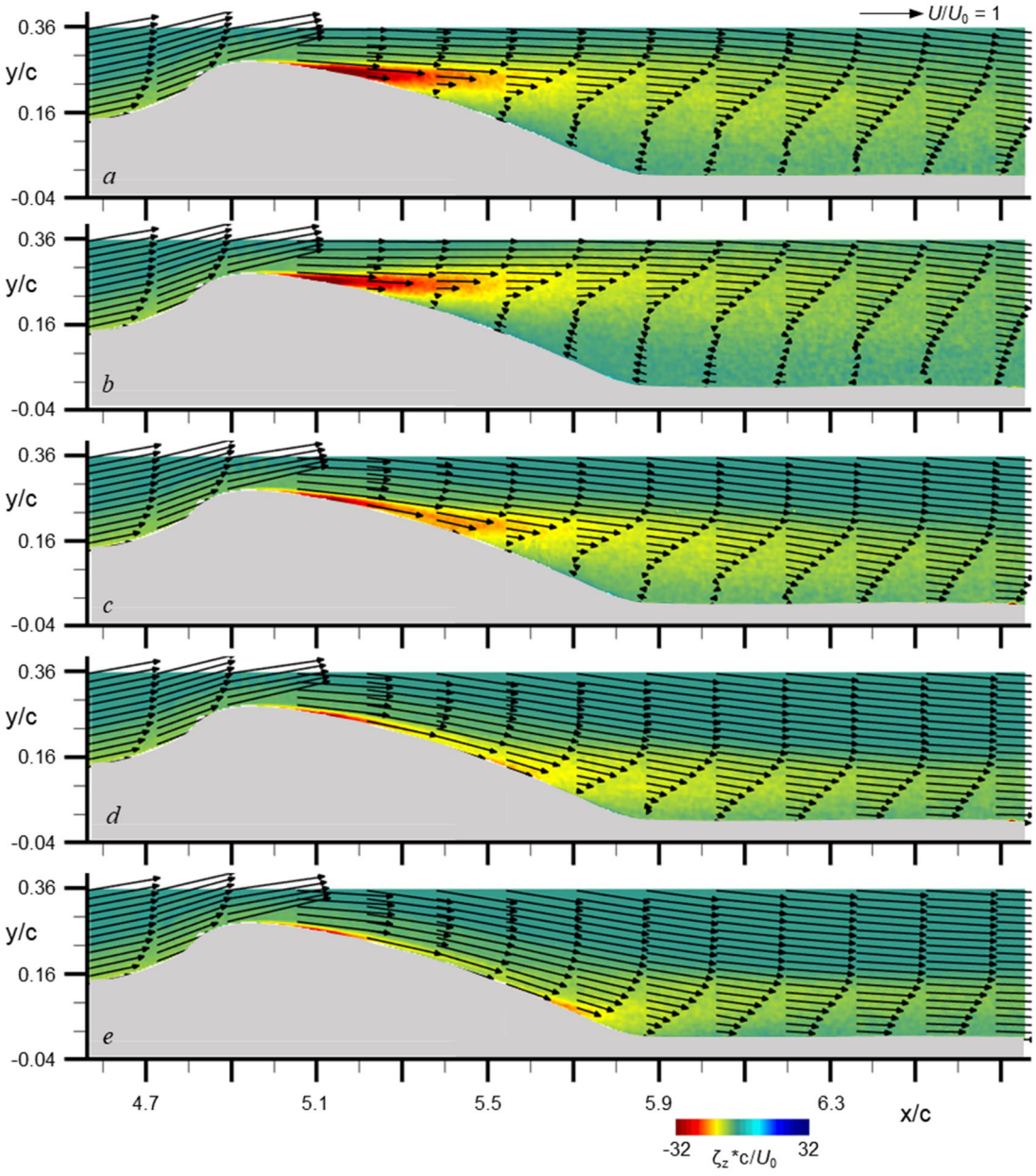

Figure 4.6. Color raster plots of the mean spanwise vorticity with overlaid mean velocity vectors at $M_0 = 0.25$ and for the jet momentum coefficient $C_{\mu, jet} \cdot 10^3 = 0$ (a), 0.02 (b), 0.05 (c), 0.08 (d) and 0.12 (e).

cross-stream height of the wake structure behind the insert model decreases to $y/c \approx 0.23$ at $x/c = 5.91$, compared to $y/c \approx 0.31$ in the absence of actuation. As the actuation level is increased further ($C_{\mu, jet} = 0.08 \cdot 10^{-3}$, Figure 4.6d), reversed flow is detected within the

domain $5.78 < x/c < 6.03$, and the maximum height of the wake decreases to decreases to $y/c \approx 0.18$ at $x/c = 5.91$. Finally, when $C_{\mu, jet} = 0.12 \cdot 10^{-3}$ (Figure 4.6e) the flow becomes fully attached and the reversed flow domain is completely eliminated (within resolution of the PIV measurements). The changes in the flow are accompanied by significant reduction in the thickness of the surface vorticity layer downstream of the apex, that is followed by gradual cross-flow thickening as a result of the adverse pressure gradient (the layer thickness at the downstream end of the insert model based on $U/U_0 = 0.99$ is $y/c \approx 0.16$). It is also remarkable that the thickness of the vorticity layer over the flat surface downstream of the insert model that scales with the thickness of the layer over the insert model, diminishes as the flow begins to accelerate when the adverse streamwise pressure gradient diminishes ($x/c > 5.91$) as is evidenced by the increase in the magnitude of the streamwise velocity near the surface and the cross-stream thickness of spanwise vorticity concentrations is about $y/c \approx 0.15$. It is noted that downstream ($x/c > 6.3$), the fully reattached flow (Figure 4.6e) shows a finite velocity in the cross-stream distributions of the velocity vectors near the surface, which is due to the meeting of the wake structure over the model merging with the re-forming boundary layer in the favorable pressure gradient which is shown to be small in magnitude near the surface at the end of the insert model ($x/c = 5.91$), and accelerates near the wall in the downstream direction as evidences by the increased magnitude in the near wall region. The accelerating flow leads to a thin boundary layer in this region, and the gross-flow representation of the velocity vectors does not capture the no-slip condition at the surface ($U = 0$ at $y/c = 0$) due to the PIV reflections near the surface, whereas in the base flow (Figure 4.6a), the reattached flow has yet to

develop a new, thin boundary layer and shows a smaller near-wall velocity magnitude for $x/c > 6.4$.

The time-averaged vorticity fields in Figure 4.6 show that fluidic actuation leads to streamwise reduction in the extent of the separation domain as manifested by streamwise upstream/downstream migration of the separation/reattachment locations. The variation of the streamwise extent of the separation domain with actuation strength C_μ is extracted from the time-averaged PIV measurements based on the presence of reverse flow along the surface and shown in Figure 4.7a. The corresponding separation and reattachment

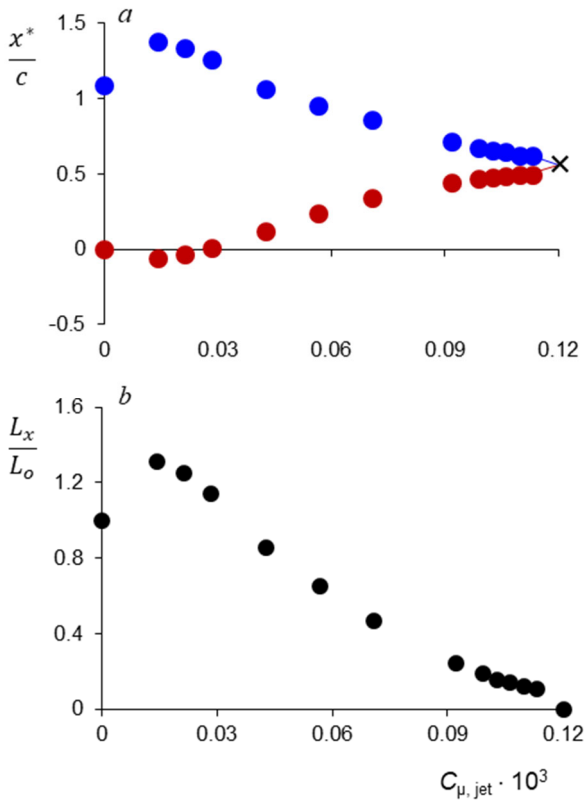

Figure 4.7. Variation with actuation momentum coefficient $C_{\mu,\,jet}$ of a) the location of the separation (●) and reattachment (●) along the model surface (x^*) relative to the base flow separation at $x/c = 5.22$ and b) the overall separation extent L_x (●).

locations are extracted along the surface and shown such that $x^* = 0$ where the base flow separation location is ($x/c = 5.22$). Note that since the actuation at $C_{\mu, jet} = 0.12 \cdot 10^{-3}$ fully reattaches the flow, the individual separation and reattachment locations cannot be extracted and the ensuing locations are depicted schematically and marked by the extensions and from the extracted points and the × in Figure 4.8a. The ensuing distance along the surface between the locations of separation and reattachment, L_x, and its ratio relative to the corresponding length in the base flow L_o is shown in Figure 4.7b. As noted in connection with Figure 4.6b, at the lowest actuation level ($C_{\mu, jet} < 0.03 \cdot 10^{-3}$) the extent of the reversed flow domain actually increases. It is conjectured that at low levels of actuation, the jets effect a blockage "bubble" that deflects the flow away from the surface and forces premature separation compared to the base flow while delaying reattachment downstream. With increasing actuation level ($0.03 \cdot 10^{-3} < C_{\mu, jet} < 0.09 \cdot 10^{-3}$), separation migrates downstream, while simultaneously reattachment moves upstream (Figure 4.7a), thereby decreasing the overall length of the separation domain (Figure 4.7b). It is noteworthy that the rate of change of the length of the separation domain varies nearly linearly with C_μ for $0.03 \cdot 10^{-3} < C_{\mu, jet} < 0.09 \cdot 10^{-3}$ as shown in Figure 4.7b. These data indicate further increases in the actuation strength ($C_{\mu, jet} < 0.09 \cdot 10^{-3}$) do not have as strong an influence on the separation and reattachment as they begin to asymptotically approach each other (Figure 4.8a), resulting in a decaying response (i.e. decreasing slope) of the overall separation length for $0.09 \cdot 10^{-3} < C_{\mu, jet} < 0.12 \cdot 10^{-3}$ in Figure 4.7b.

The changes in the structure of the flow near the onset of separation in the base flow (x/c = 5.2, M_0 = 0.25) in the presence of actuation can be observed using cross-stream distributions of the streamwise and cross-stream velocities in local wall-normal coordinates (U' and V', respectively), and of the spanwise vorticity as shown in Figure 4.8a-c,

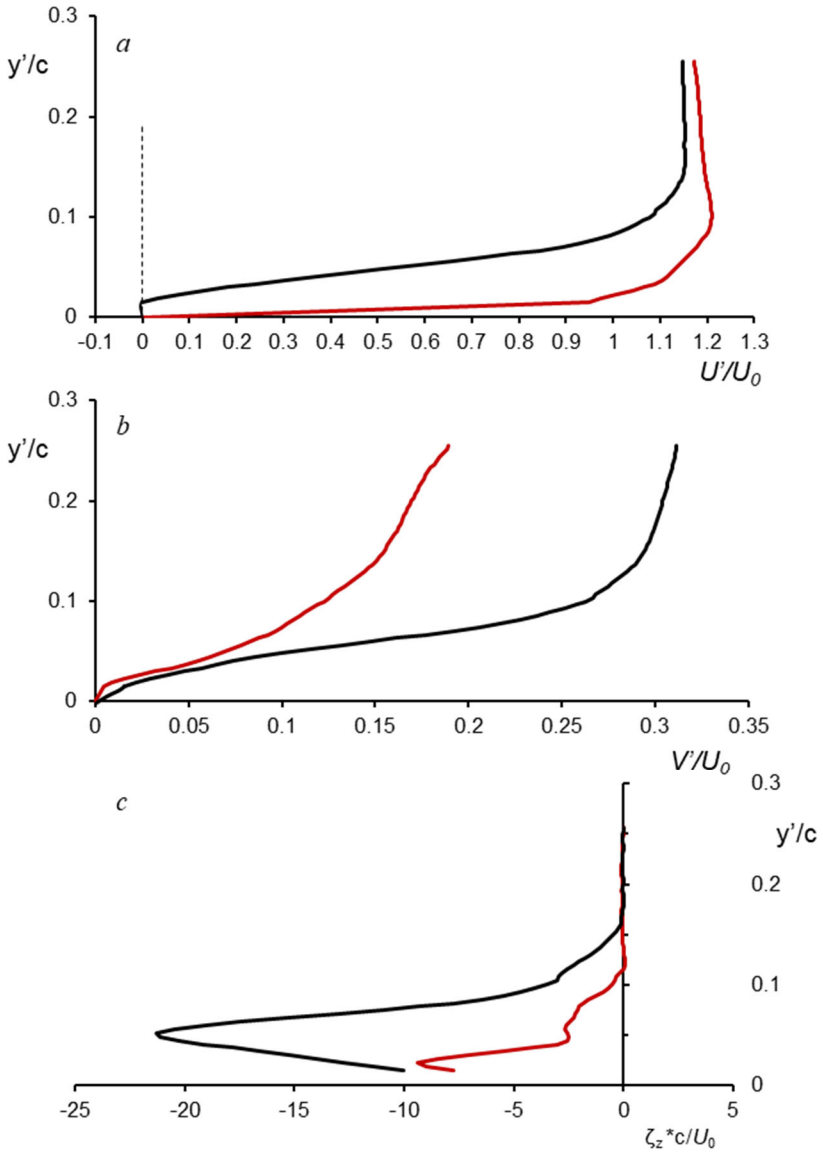

Figure 4.8. Cross-stream time-averaged distributions of the wall-tangential velocity U' (a), wall-normal velocity component V' (b), and spanwise vorticity (c) in the base (black line) and actuated flow (red line, $C_{\mu,\,jet}\cdot 10^3 = 0.12$) at the base flow separation location x/c = 5.22 and M_0 = 0.25.

respectively., in the absence and presence of actuation at a level that leads to the elimination of the reversed flow domain ($C_{\mu, jet} = 0.12 \cdot 10^{-3}$). The presence of the jets leads to significant increase in the wall-tangential streamwise velocity *U*' at *x/c* = 5.2 (the jet exit plane is at *x/c* = 5.10) for *y'/c* < 0.1 that overcomes the effect of the adverse pressure gradient. The wall-normal velocity *V*' (Figure 4.8b) in the presence and absence of actuation remains positive (away from the surface) throughout the cross-stream distributions owing to the decomposition of the flow into the local wall-normal coordinates. In the absence of actuation, the onset of separation is marked by an increase in the wall-normal velocity component *V*' as the local blockage of the reverse flow domain forces the near wall flow away from the surface and induces the separation. In the presence of actuation, the increase in the wall-tangential velocity *U*' (Figure 4.8a) is accompanied by reduction in the wall-normal velocity *V*' near the wall for 0.5 < *y'/c* < 0.1 as the outer flow (*y'/c* > 0.1) is entrained and re-directed along the surface. Furthermore, as shown in the cross-stream distribution of the time-averaged spanwise vorticity (Figure 4.8c), the onset of separation in the base flow is marked by an intense near-wall region (*y'c* < 0.1) of CW spanwise vorticity concentrations, as was shown in the PIV in Figure 4.6. The presence of the wall jets (Figure 4.8c) leads to a reduction in the intensity of the CW vorticity layer near the surface (*y'/c* < 0.1) and is also marked by the formation of a layer of CCW vorticity that marks the outer edge of these wall jets (0.1 < y'/c < 0.13) as the increased flow *U*' due to the jets is then reduced towards the outer flow for y'/c > 0/1 in Figure 4.8a.

The effects of the actuation level on the cross-stream distributions of the time-averaged wall-tangential velocity *U*' at the separation and reattachment at four actuation levels $C_{\mu, jet} = 0$, $0.02 \cdot 10^{-3}$, $0.05 \cdot 10^{-3}$, and $0.08 \cdot 10^{-3}$ are shown in Figure 4.9a and b. Note

that the cross-stream scale is doubled between separation and reattachment. At the lowest actuation level ($C_{\mu, jet} = 0.02 \cdot 10^{-3}$), the velocity distribution at the separation is nearly identical to the base flow except in the outer core flow velocity which increases slightly ($U'/U_0 = 1.15$ to 1.16) due to the contraction imposed by the upstream migration of separation. As the location of separation migrates downstream with $C_{\mu, jet}$ noted above ($x/c = 5.22$, 5.17, 5.43, and 5.61 for $C_{\mu, jet} = 0$, $0.02 \cdot 10^{-3}$, $0.05 \cdot 10^{-3}$, and $0.08 \cdot 10^{-3}$, respectively) dU'/dy increases the slope of the nearly-linear velocity distribution in the outer shear region (above the near-wall vanishing shear) indicating that the shear domain extends in the cross-stream direction as separation migrates downstream along the insert's surface while the magnitude of the free stream velocity (marked by the nearly invariant

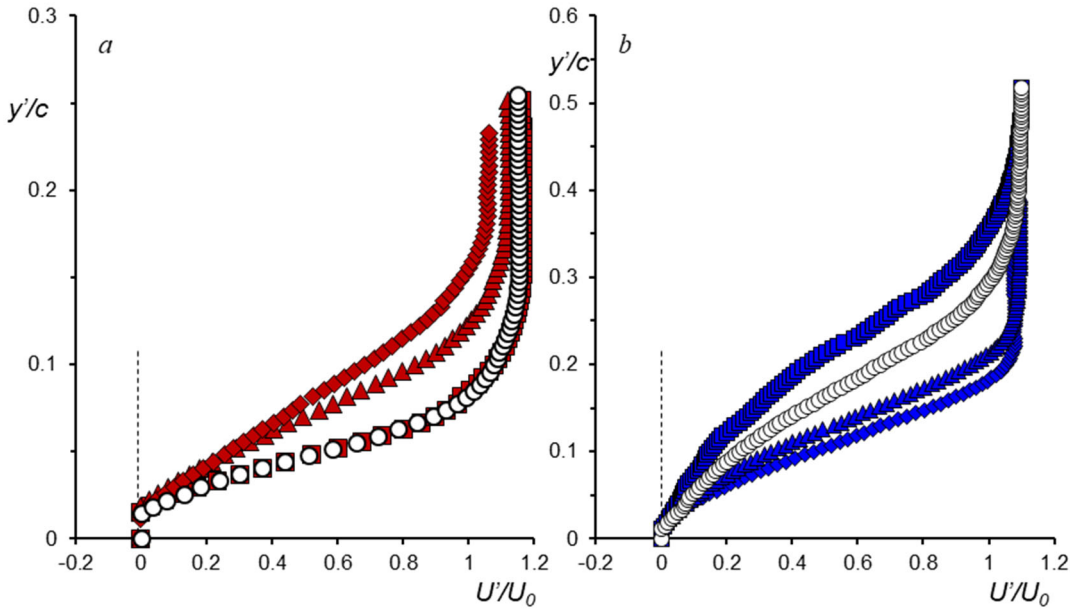

Figure 4.9. Cross-stream distributions of the wall-tangential velocity U' at local **separation** (a) and **reattachment** (b) for the base flow (○) and in the presence of actuation at $C_{\mu, jet} = 0.02 \cdot 10^{-3}$ (■), $0.05 \cdot 10^{-3}$ (▲), and $0.08 \cdot 10^{-3}$ (♦) ($M_0 = 0.25$). The corresponding points of **separation** at $x/c =$ (○) 5.22, (■) 5.17, (▲) 5.43, (♦) 5.61 and at **reattachment** $x/c =$ (○) 6.38, (■) 6.49, (▲) 6.10, (♦) 5.85.

outer flow) decreases as the core flow extends towards the surface due to the delay in separation. The increase in the slope of *U*' in the shear domain is clearly accompanied by a reduction in the nominal cross-stream magnitude of the spanwise vorticity concentrations since the circulation across the layer remains nearly unchanged.

The velocity distributions at the local reattachment (Figure 4.9b) show that the velocity of the core flow does not vary appreciably in the absence and presence of the actuation, indicating the effects of the displacement thickness of the surface boundary layer downstream of the insert model. Low actuation level ($C_{\mu,\,jet}\cdot 10^3 = 0.02$) delays reattachment and therefore results in a wider velocity distribution (Figure 4.9b) and velocity gradient in the shear region. However, increasing the actuation level migrates the reattachment upstream and therefore leads to a decrease in the slope of the streamwise velocity distribution within the domains $0.1 < y'/c < 0.2$ ($C_{\mu,\,jet} = 0.05\cdot 10^3$) and $0.1 < y'/c < 0.19$ ($C_{\mu,\,jet} = 0.08\cdot 10^3$), while moving the respective inflection points of the shear domains closer to the surface.

The effects of the actuation and flow attachment on the small-scale motions within the wake domain of the insert model are depicted in Figure 4.10 using color aster plots of the *TKE* in the presence of actuation where the *TKE* distribution in the base flow (cf. Figure 4.2) is included for reference (Figure 4.10a). As discussed in Chapter 2, the fluidically oscillating actuation jets operate at a frequency (≈ 12 kHz) that is selected to be significantly higher than the unstable characteristic frequencies of the wake shear layer so that it is decoupled from the natural frequency of the near wake of the model (estimated to be ≈ 800 Hz based on the universal Strouhal number $St_s^* = 0.17$ proposed by Yarusevych

and Boutilier (2011) and using the wake height at the base flow reattachment location x/c = 6.38 where the velocity distribution reaches U'/U_0 = 0.99 for the reference height d*). The actuation operates within the dissipative range of the spectral content of the base flow

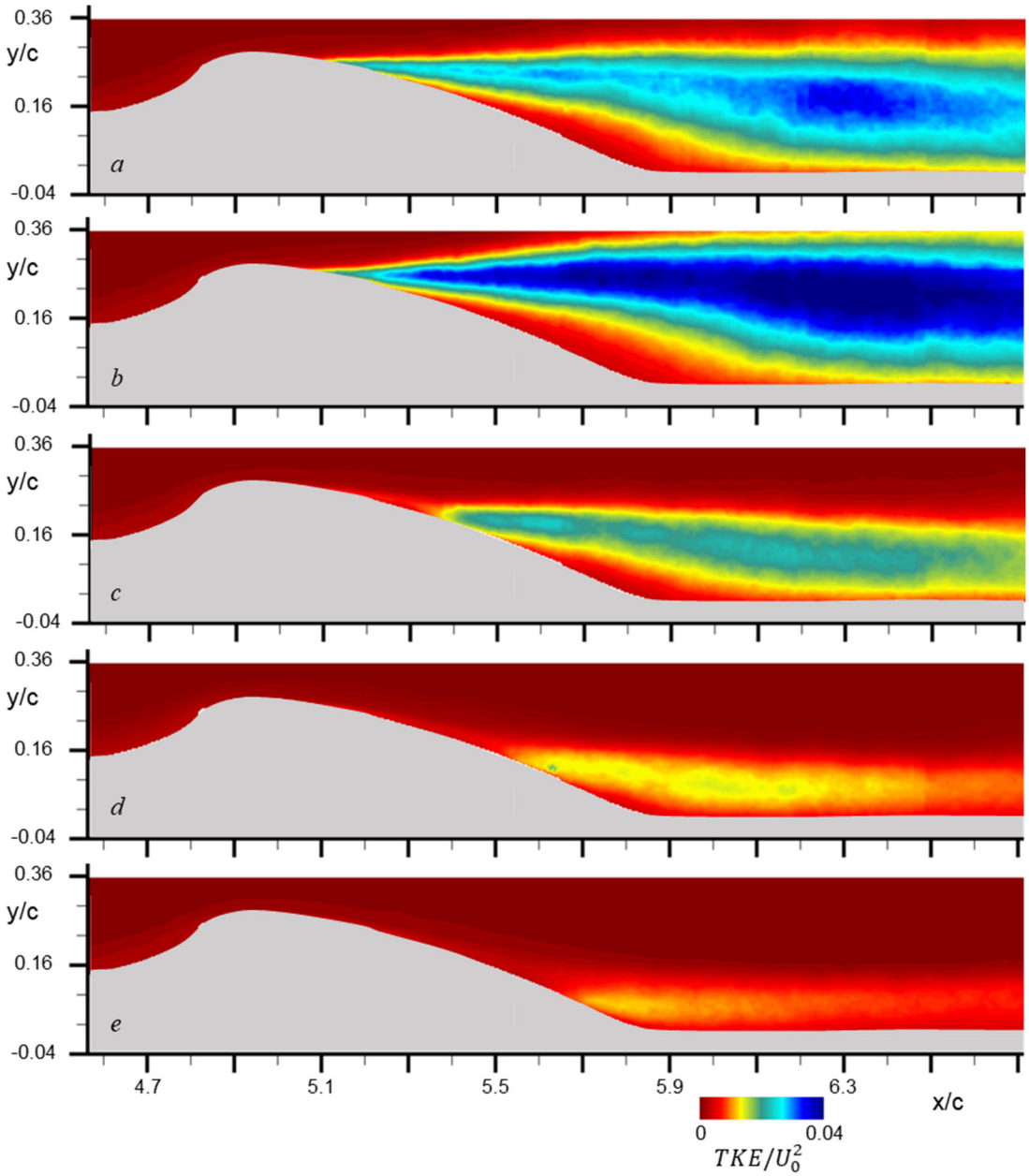

Figure 4.10. Color raster plot of the turbulent kinetic energy $\left(\overline{u'^2} + \overline{v'^2}\right)/2$ for $C_{\mu,\,jet}$ = 0 (*a*), 0.02·10^{-3} (*b*), 0.05·10^{-3} (*c*), 0.08·10^{-3} (*d*), and 0.12·10^{-3} (*e*) at M_0 = 0.25.

and therefore directly forces small-scale motions (Vukasinovic, Rusak et al., 2010). As was discussed in connection with Figure 4.2b, in the base flow the formation of the shear layer associated with the wake structure is accompanied by increasing levels of turbulent kinetic energy about the centerline of the shear layer that are indicative of cross-stream stretching of the flow over the surface and strong cross-stream mixing, with a peak that occurs well downstream of the insert about ($x/c \approx 6.3$) near the point of reattachment and closure of the reversed flow domain ($x/c = 6.4$, cf. Figure 4.2). As shown in Figure 4.10b, the low actuation level that led to an increase in the recirculation domain leads to a significant increase in the *TKE* within the shear layer domain as manifested by the increase in the cross-stream width near the reattachment ($x/c = 6.49$) from $y'/c \approx 0.3$ in the base flow to $y'/c \approx 0.35$ (Figure 4.9b). Further increases in the actuation level (e.g. $C_{\mu, jet} = 0.05 \cdot 10^{-3}$ and $0.08 \cdot 10^{-3}$, Figure 4.10c and d, respectively) are marked by significant reductions in the elevated levels and cross-stream extent of the *TKE* as the separation migrates downstream. These reductions indicate that the shear within the bounding shear layer of the wake domain is significantly reduced and with it, the rate of entrainment and mixing and the formation of small-scale motions. When the flow is fully attached ($C_{\mu, jet} = 0.12 \cdot 10^{-3}$, Figure 4.10e), the layer marked by elevated *TKE* levels originates at $x/c = 5.7$ on the surface of the model and indicates onset of the cross-stream spreading of the attached boundary layer as the flow over the curved surface transition to the flat surface at $x/c = 5.91$.

When comparing the velocity distribution at the local separation location (cf. Figure 4.9a), cross-stream integral scale associated with the effects of the actuation is obtained by using the vorticity flux across the wake domain and the total circulation within the

streamwise domain of recirculation (between separation and attachment) using Equations 4.1 and 4.2.

$$\Omega_{flux} = \sum_{\frac{y'}{c}=0}^{\frac{y'}{c}=0.99U'/U_0} \zeta_z U' \Delta y' \Big/ cU_0^2 \qquad 4.1$$

$$\Phi^* = \iint \zeta_z dxdy/cU_0 \qquad 4.2$$

The vorticity flux Ω_{flux}, is integrated in the cross-stream direction between $y = 0$ and $y = y^*$ where $U' = 0.99U_0$. The total circulation (Φ^*) is the area integral of the vorticity between the streamwise locations of the separation and reattachment, and the outer bound of the recirculation domain that is defined by the location of matched volume flow rate of the reverse flow and outer flow (cf. Figure 4.2). The variation of the net cross-stream vorticity flux with actuation momentum coefficient is computed across the streamwise positions of separation and reattachment (cf. Figure 4.9) of the forced flow at different actuation levels as shown in Figure 4.11a. The data in Figure 4.11a shows the flux of CW vorticity across the flow over the model at corresponding locations of separation and reattachment in the baseline flow and in the presence of actuation. As noted above, at $M_0 = 0.25$ the respective locations of separation and reattachment migrate downstream and upstream with increasing levels of actuation as noted in parenthesis for each value of $C_{\mu, jet}$: 0 (●, x/c = 5.22 and 6.38) $0.02 \cdot 10^{-3}$ (■, x/c = 5.17 and 6.49), $0.05 \cdot 10^{-3}$ (▲, x/c = 5.43 and 6.10), and $0.08 \cdot 10^{-3}$ (♦, x/c = 5.61 and 5.85), and for $C_{\mu, jet} = 0.12 \cdot 10^{-3}$ the flow becomes fully attached. The variation of Ω_{flux} with C_μ is analyzed using corresponding cross-stream distributions of the surface tangential velocity (U') and of the spanwise vorticity (ζ_z) that are identified in

Figure 4.11a by the symbols of the actuation levels at the locations of separation and reattachment. The vorticity flux in the base flow is effected by concentrations of high-level spanwise vorticity within a relatively narrow layer $y'/c < 0.15$ (ζ_z has a strong maximum at $y'/c = 0.05$). The corresponding Ω_{flux} at $C_{\mu,\,jet} = 0.02 \cdot 10^{-3}$ is slightly higher (3%) than in the base flow due to somewhat higher peak levels of ζ_z within a similar cross-stream layer as the base flow ($y'/c < 0.15$) owing to the increased free-stream velocity

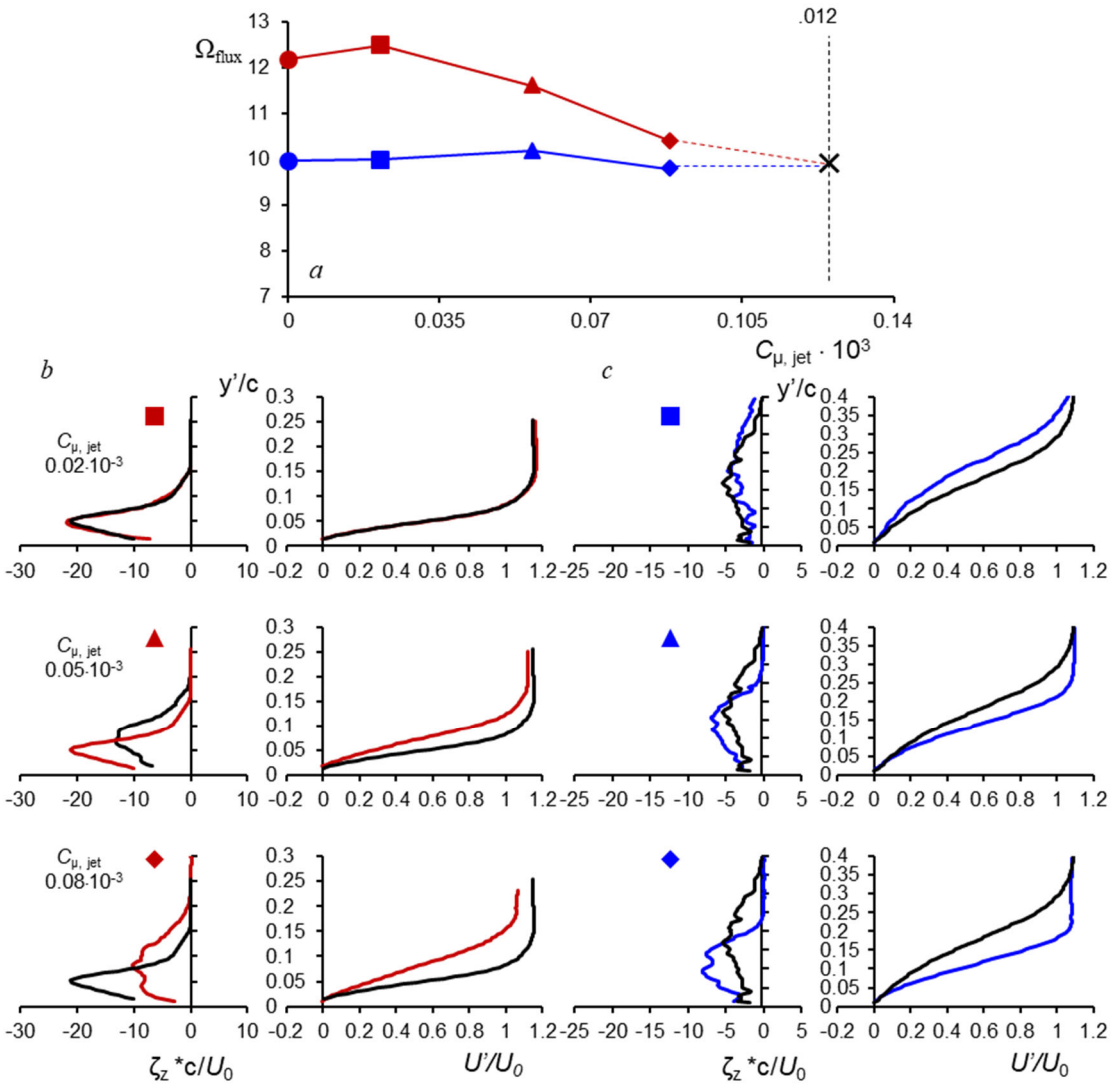

Caption on following page

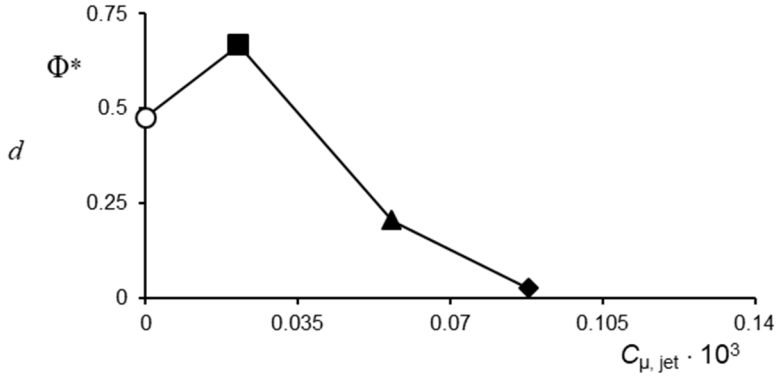

Figure 4.11. Evolution of the total vorticity flux (Ω_{flux}) of the base (●) and actuated flow ($C_{\mu,\,jet}$ = 0.02·10^{-3} (■), 0.05·10^{-3} (▲), and 0.08·10^{-3} (♦), M_0 = 0.25) at **separation** (x/c = (●) 5.22, (■) 5.17, (▲) 5.43, (♦) 5.61) and at **reattachment** (x/c = (●) 6.38, (■) 6.49, (▲) 6.10, (♦) 5.85) (a), cross-stream distributions of the wall-tangential velocity U'(solid lines) and spanwise vorticity (dashed lines) at separation for x/c = (-) 5.22, and 5.61(-) (b) and at reattachment x/c = (-) 6.38, and 5.85(-) for $C_{\mu,\,jet}$ = 0 and 0.08·10^{-3} (c), and the total circulation (Φ*) of the separated domain (d), with jet momentum coefficient $C_{\mu,\,jet}$= 0 (○), 0.02·10^{-3} (■), 0.05·10^{-3} (▲), 0.08·10^{-3} (♦) for M_0 = 0.25.

experienced as the separation moves upstream. Thereafter Ω decreases monotonically with increasing C_μ as manifested by cross-stream spreading of U' and reduction in the cross-stream gradient that are associated with diminution and spreading of ζ_z. These changes in vorticity distributions are related to changes in the streamwise pressure gradient. As shown in Figure 4.12, the pressure gradient is shown to become increasingly adverse throughout the separated domain ($5.2 < x/c < 6.4$) with increasing actuation as the flow experiences the diffuser effect along the aft of the insert model as well as forcing the flow to recover and match the favorable wind tunnel pressure gradient over a shorter streamwise distance owing to the reduction in the reverse flow domain. The increasingly adverse pressure gradient causes the vorticity to diffuse as well, resulting in a reduction in the vorticity flux along the insert model with increasing actuation. Remarkably, Ω at the locations of flow reattachment is significantly lower and its rate of change with C_μ is significantly lower than

through separation. The data in Figure 4.11a shows that for $C_{\mu, jet} = 0$ and $0.02 \cdot 10^{-3}$, the cross-stream vorticity layers nominally extend to $y'/c = 0.4$ and their cross-stream distributions are similar. However, when the flow recirculation domain diminishes with increasing actuation level, the cross-stream width of the vorticity layer and the velocity variation diminish compared to the base flow and the vorticity flux is apparently maintained by corresponding increases in ζ_z.and in the velocity gradient, or magnitude of U' within the layer. Figure 4.11a also shows an extrapolation of the measurements to the actuation level at which the recirculation domain vanishes ($C_{\mu, jet} = 0.12 \cdot 10^{-3}$), showing that Ω would reach a level of ≈ 9.5 in the absence of separation. The actual level of Ω at $x/c = 5.73$ is computed to be 8.8, which is lower than the extrapolated value and presumed to be due to the selected location remaining within the diffusing region (recall end of the insert model ends at $x/c = 5.91$) and would further diffuse the vorticity along the model.

Another integral measure of the effects of the actuation is the dimensionless circulation Φ^* across the wake domain within the streamwise domain of recirculation (between the separation and reattachment, Equation 4.2). As shown in Figure 4.2, cross-stream concentrations of the spanwise vorticity extend above the boundary that defines the recirculation domain (based on the vanishing cross-stream flow rate across the domain). The variation of Φ^* with C_μ is shown in Figure 4.11b, for the recirculation domain bounding the separation and reattachment locations based on the location of the matched volume flow rate of the reverse flow and outer flow defined in Figure 4.2. As the separated domain increases for low levels of actuation ($C_{\mu, jet} \cdot 10^3 = 0.02$, cf. Figure 4.7), unsurprisingly the circulation also increases (by 40%). Further increases in the actuation strength ($C_{\mu, jet} \cdot 10^3 > 0.02$), however, reduce the measured circulation within the separated

domain by 57% at $C_{\mu, jet} \cdot 10^3 = 0.05$ and 95% at $C_{\mu, jet} \cdot 10^3 = 0.08$ compared to the base flow, and when the flow is fully reattached for $C_{\mu, jet} = 0.12 \cdot 10^3$, the reverse flow domain ceases to exist and no longer has any associated circulation.

The effects of the actuation in Figure 4.6 on the streamwise variation of the static surface pressure along the centerline ($z/c = 0$) is assessed in conjunction with the PIV data in Figure 4.6, and is shown in Figure 4.12 (the static pressure in the base flow is shown using open symbols for reference, cf. Figure 4.4). These data show that C_p upstream ($x/c < 5$) and far downstream ($x/c > 8.5$) of the model's apex are not affected by the presence of the actuation, despite the reduction in the extent of the reversed flow and wake domains discussed in connection with Figure 4.6, suggesting that the effect of the actuation is primarily confined within the base flow separated domain ($5.2 < x/c < 6.4$). Despite the reduction in the separated domain, there is no indication of significant global losses (as was shown in the diffuser duct in Chapter 3), which suggests that the reduction of the blockage due to the separation is balanced by increased friction losses along the surface of the model due to the increased flow velocity near the surface in the reattached flow and the diffusive effect along the aft of the model which is improved due to the reduced blockage of the reversed flow domain. As was discussed in connection with the base flow (cf. Figure 4.4) the overall pressure "gradient" along the test section is clearly favorable, and is locally interrupted by domains of flow contraction and expansion upstream and downstream of the apex of the insert. As the flow accelerates over the model ($4.62 < x/c < 5.16$) C_p becomes more negative and reaches a local minimum at $x/c = 5.16$, just downstream of the model's apex ($x/c = 5$), and these data show that the magnitude of the suction peak increases with actuation level (from $C_p = -0.6$ in the base flow to -0.97 at $C_{\mu, jet} \cdot 10^3 = 0.12$), as the losses

due to the wake flow downstream of the apex diminish. It is noted that at the lowest actuation level ($C_{\mu, jet} \cdot 10^3 = 0.02$, Figure 4.12) the suction peak diminishes up to $C_p = -0.5$ compared to $C_p = -0.6$ in the base flow, owing to the increase in the wake domain and ensuing upstream migration of separation in Figure 4.6 which shifts the blockage by the wake further upstream and decreases local flow acceleration over the model. Throughout the reversed flow domain of the base flow ($5.2 < x/c < 6.4$) and the recovery (as marked by the changing sign of the slope of C_p back to negative to return to the favorable pressure gradient of the wind tunnel) downstream of the reattachment ($6.4 < x/c < 7.2$), however, C_p of the base flow and actuation at $C_{\mu, jet} = 0.02 \cdot 10^3$ are similar. The diminution in the extent of the wake domain when the actuation level increases to and above $C_{\mu, jet} \cdot 10^3 = 0.05$, is

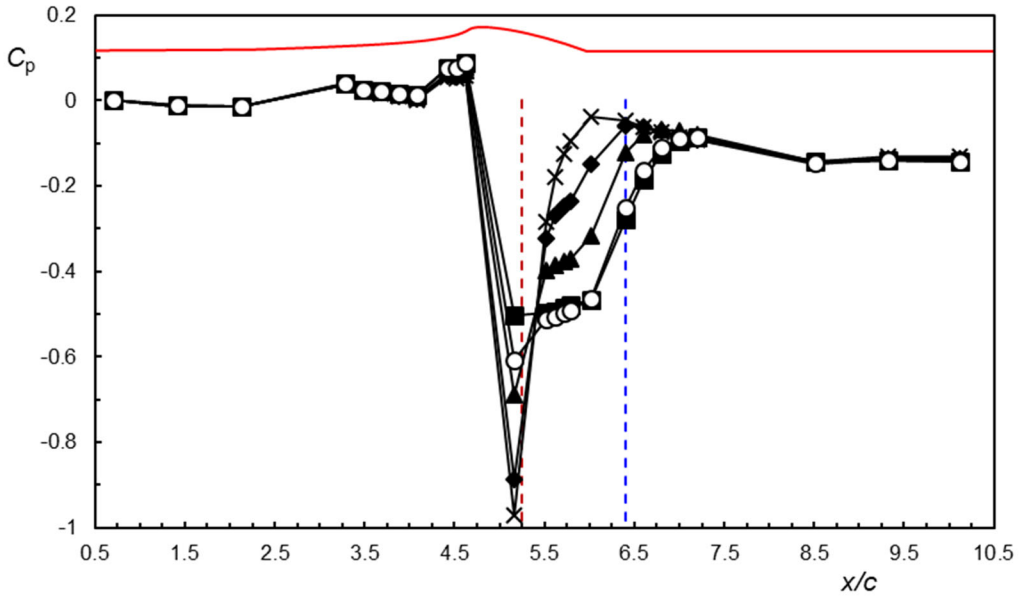

Figure 4.12. Streamwise distributions of the static pressure along the centerline of the base flow (○) and in the presence of actuation at $C_{\mu, jet} \cdot 10^3 = 0.02$ (■), 0.05 (▲), 0.08 (♦), and 0.12 (×) for $M_0 = 0.25$. The upstream separation ($x/c = 5.2$) and downstream reattachment ($x/c = 6.4$) points of the base flow are shown as red and blue dashed lines, respectively, for reference.

marked by an increase in the levels of C_p between $5.2 < x/c < 6.4$ compared to the base flow that are commensurate with the pressure level downstream of the insert model as the extent of the wake domain diminishes and the flow expands over the model towards the flat surface downstream. The reduction on the extent of the reversed flow domain with increasing actuation level is manifested by changes in C_p within and immediately downstream of the reversed flow domain. For example, for $C_{\mu, jet} = 0.05 \cdot 10^3$ within the reversed flow domain ($5.2 < x/c < 5.8$) C_p varies nearly linearly with x/c and $dC_p/d(x/c) \approx 0.094$, but immediately downstream of the reattachment ($6.01 < x/c < 6.6$) the flow recovers and shows a rapid increase in C_p with $dC_p/d(x/c) \approx 0.40$. At the highest actuation level ($C_{\mu, jet} = 0.12 \cdot 10^3$) in the absence of reversed flow, C_p transitions smoothly from the adverse to favorable pressure gradient with peak recovery values at $x/c = 6$, just downstream from the edge of the insert model at $x/c = 5.91$.

The time-averaged wall-tangential velocity distributions of the base flow and in the presence of the actuation in Figure 4.9a showed that at the locations of the downstream and upstream migration of separation and reattachment, the respective cross-stream gradient of the wall-tangent velocity distributions increase or decrease relative to the base flow, indicating a gradual decrease in the cross-stream extent of the wake flow downstream of the apex of the model that is accompanied by a reduction in the local velocity of the core flow. Finally, it is noted that the evolution of the boundary layer flow in the presence of an adverse pressure gradient can be analyzed using the scaling proposed by Schatzman and Thomas (2017, cf. Section 3.3.2, Figure 3.25). Cross-stream distributions of U' at the streamwise locations of separation and reattachment (cf. Figure 4.9) in the absence and

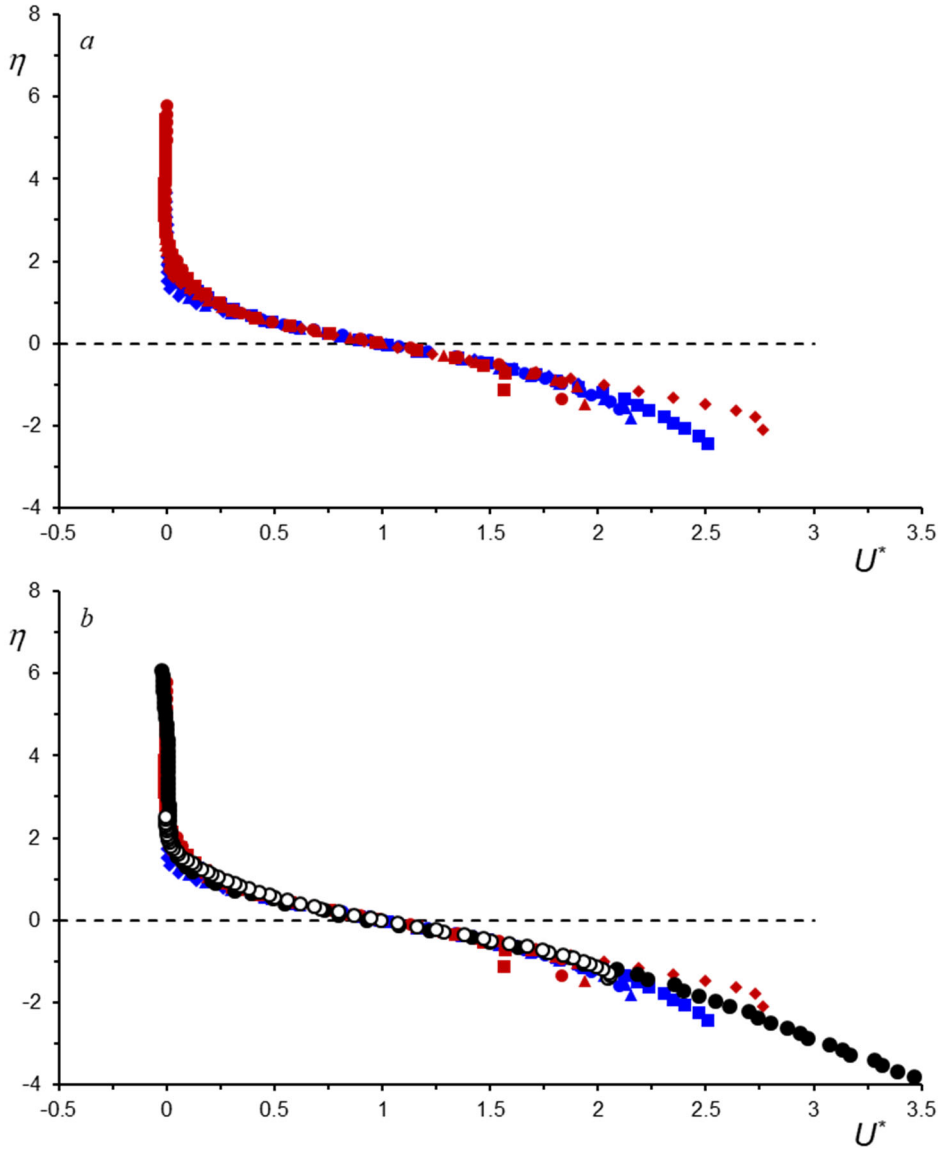

Figure 4.13. a) Cross-stream distributions of the scaled time-averaged wall-tangential streamwise velocity U^* with η based on the distributions shown in Figure 4.9 based on the scaling by Schatzman and Thomas (2017) (cf. Section 3.3.2, Figure 3.25) at separation x/c = (●) 5.22, (■) 5.17, (▲) 5.43, (♦) 5.61 and at reattachment x/c = (●) 6.38, (■) 6.49, (▲) 6.10 (♦) 5.85. b) The velocity distributions of (a) overlaid with the corresponding scaled velocity distributions in the diffusing duct discussed in Section 3.3.2 for $C_q = 0$ (open symbols) and 0.8% (closed symbols) at $M_0 = 0.4$.

presence of actuation are scaled by their characteristic outer parameters (shear layer thickness δ_ζ and the velocity deficit U_d' Equations 3.1 and 3.2, respectively) to convert

them to the non-dimensional velocity and length scale U^* and η, as shown previously in Figure 3.24. The scaled velocity distributions are plotted in Figure 4.13a and show a remarkable collapse of the flow domain away from the wall to the core flow ($-1 < \eta < 6$) considering the shape and cross-stream scale of the different velocity distributions in Figure 4.9. There is, however, an associated breakdown of the scaling close to the surface (typically $y'/c < 0.5$, Figure 4.9) as the scaling is based on the outer parameters and the near wall shear changes with the application of the flow control and migration of the separation, resulting in the individual data trends breaking away from the collapsed profile for $\eta < -1$. The collapse of these data show that the closed separation domain is governed both at separation and reattachment in the absence and presence of actuation by the same outer flow features presented by the growing shear domain with an outer inflection point (cf. Figure 3.24, Schatzman and Thomas, 2017) and associated CW vorticity, despite the near-wall application of the fluidic actuation and reverse flow domain spanning between the separation and reattachment. Furthermore, the collapse of the velocity distributions within the domain near the boundary of the core flow which is mapped onto $1.5 < \eta < 6$ shows that the scaling can accommodate the changes in the local speed of the expanding core flow as the actuation leads to deflection of the core flow towards the surface. This collapse lends credence to the notion that the flow downstream of the apex of the model resembles a wake flow and that the cross flow between the core and the surface is dominated by the shear layer that extends to the local core flow. Even though the actuation is applied at the surface, it affects the entire shear domain of the cross flow through separation and all the way to reattachment implying structural similarity in the presence and absences of actuation and is congruent with the embedded shear domain proposed by

Schatzman and Thomas (2017). Corresponding scaled velocity distributions at separation in the absence and presence of actuation ($C_q = 0$ and 0.8% at $M_0 = 0.4$) measured across the boundary layer of the diffuser described in Chapter 3 Section 3.3.2 (cf. Figure 3.25) are included along with the present data in Figure 4.13b. It is remarkable that the scaled velocity distributions collapse onto a single distribution in the outer flow regardless of differences in surface geometry and actuation details, indicating that the flow structure at separation is similar in the base flow and in the presence of actuation and delayed separation.

CHAPTER 5. THE 3-D STRUCTURE OF THE SEPARATION CELL IN THE PRESENCE AND ABSENCE OF FLUIDIC ACTUATION

5.1 Overview

The investigations in Chapter 4 of the structure of the 3-D separation cell that forms downstream of spanwise separation in the adverse pressure gradient of a diffuser flow focused on the evolution of the separated and reattached flow along the plane of symmetry. This chapter focuses on characterizing the three-dimensional structure of the separation cell that forms on the insert model between the sidewalls of the test section in the absence and presence of fluidic actuation. The topology of the flow is explored using surface oil flow visualization and stereoscopic particle image velocimetry (sPIV) in three streamwise-normal planes (x/c = 5.26, 5.54, and 5.72, cf. Figure 2.8). These streamwise locations are selected based on the evolution of the local separation in the spanwise-normal (centerline) plane of the base flow and in the presence of actuation as discussed in Chapter 4. The chapter commences with a discussion of the structure of the separation cell within the base flow, followed by a description of the effects of spanwise actuation using arrays of discrete, fluidically oscillating jets including a single isolated jet (at the centerline) and with multiple jets at different spanwise spacings. The structural changes in the reattaching flow are reviewed with emphasis on the changes in its turbulent characteristics.

5.2 The Base Flow

As shown in Chapter 4 (Figure 4.2), at $M_0 = 0.25$ the base flow separates at $x/c \approx 5.2$ and reattaches at $x/c \approx 6.4$. The topology of the separated domain is inferred from surface oil flow visualization within $5.1 < x/c < 7.4$ (from the exit plane of the spanwise jet array to downstream of reattachment) as shown schematically in Figure 5.1 (the flow direction is top to bottom). The positioning of the flow domain and oil streaks (left) is shown along with a schematic of a streamwise cross-section profile of the test surface (right). The location of three spanwise normal planes in which sPIV data were acquired are also shown for reference along with a section of the exit plane of the actuation jets. The oil-paint mixture is applied in two locations that span the entire test section: one thin spanwise strip immediately downstream of the exit plane of the jets ($x/c = 5.1$) and a larger rectangular spanwise patch downstream of the model mold line (streamwise centered approximately along F-G-H, Figure 5.1). The oil image in Figure 5.1 shows that the base flow forms a closed separation cell (cf. Section 1.1.1.2) that is characterized by a separation line upstream (marked A-B-C-D-E), reattachment line (marked F-G-H) and two surface-normal vortices (marked V_L and V_R) that each rotate towards the centerline (CW and CCW, respectively). As evidenced by the oil streaks, the flow upstream of the separation line (marked A-B-C-D-E) is attached downstream of the jet exit plane. Similarly, as shown by the uniform oil streaks, the flow reattaches downstream at the reattachment node (point G) beyond the end of the model curvature at $x/c = 5.91$. The central portion of the reattachment region shows nearly uniform reverse flow as the oil streaks are drawn directly upstream from the nodal line through G to the line through C, up to $x/c \approx 5.72$. Upstream of $x/c = 5.72$, the reverse flow is split into two regimes: a central region that spans

approximately the middle third of the test section from B to D, and the outer regions (A-B and D-E). Outside of the central region, the oil streaks no longer flow uniformly upstream and are curved and drawn into each of two surface-normal vortices (V_R and V_L). In the central region, the flow remains drawn uniformly upstream, however, this region is primarily void of oil as the streaks are drawn from the two original oil patches, and as shown by the streaks, the shear of the reverse flow region is not sufficient to pull the oil all the way to the upstream separation line (line B-C-D, Figure 5.1), and the streaks become stagnant along the surface. Similarly, as the oil patch applied near the jet exit plane moves downstream and meets the reverse flow region (along separation front A-B-C-D-E in Figure 5.1) the flow along the surface is slowed down and the oil begins to accumulate along the boundary (B-C-D in Figure 5.1). Outside of the central region, the oil streaks suggest the flow along the reattachment boundary flows laterally from the reattachment node (point G Figure 5.1) and forms two saddle points on the side walls (to the left from G to F and right from G to H in Figure 5.1). When this lateral flow reaches the sidewalls it is turned downstream and upstream, which results in reverse flow along the sidewalls as evidenced by the oil streaks reaching to the corners near the jet exit plane from the saddle points (from F to A and H to E on the left and right of Figure 5.1), while the flow at the saddle points that is turned downstream eventually merges with the central region to form uniform flow streaks in the reattached flow. As the reverse flow along the walls reaches the jet exit plane (points A and E, Figure 5.1) it meets the oncoming attached flow and is forced to turn to the central region along the separation line A-B-C-D-E in Figure 5.1, which results in shearing and induces the rotation of the surface-normal vortices. The

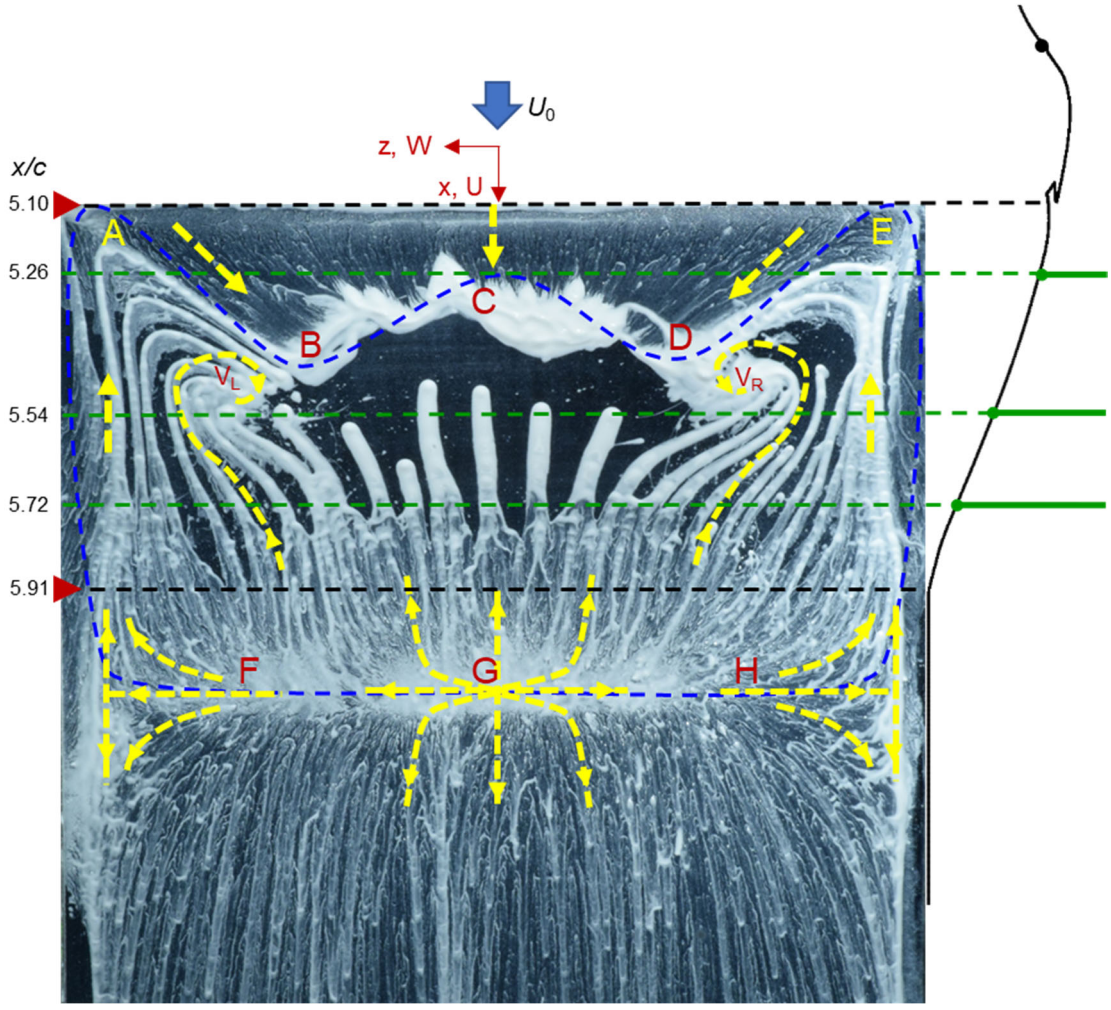

Figure 5.1. Oil flow visualization of the separation cell in the base flow (M_0 = 0.25, and the direction of the freestream is from top to bottom) aligned with a streamwise profile of the model insert section. The upper edge of the image is aligned with the exit plane of the actuation array at x/c = 5.10 (▶). The downstream edge of the model insert (cf. Chapter 2) is marked x/c = 5.91 (▶). The streamwise locations of the sPIV streamwise-normal planes are marked by the solid-dashed green lines at x/c = 5.26, 5.54, and 5.72.

turning of the corner flow at A inward towards the centerline (C) in Figure 5.1, forces the CW sense of the left vortex V_L, and similarly the opposite sense of the right vortex V_R. The resultant undulating separation line A-B-C-D-E, also shows the effects of the flow induced by the counter-rotating surface vortices that result in local extensions of the

attached flow at B and D approximately half way between the centerline C and the sidewalls at $z/c = \pm 0.51$.

While the oil visualization in Figure 5.1 indicates that the separated domain is reminiscent of the separation cells discussed in Section 1.1.1.2, it should be noted that the sense of the two surface-normal vortices is opposite of the sense of the vortices that are typical of stall cells that form in the absence of sidewalls over airfoils (e.g. Winkelmann, 1982, Schewe, 2001). The sense of rotation in the present separation domain appears to be effected by the presence of the sidewalls that direct reverse flow towards the separation line in Figure 5.1.

The surface flow topology of the base flow separation cell in Figure 5.1 guided the study of the separation cell using sPIV data acquired in three spanwise-normal planes marked in Figure 5.1 and described in Chapter 2. The evolution of the streamwise, cross-stream, and span-wise velocity components (U, V, W, respectively) over and within the separation cell is shown in Figure 5.2 at the three streamwise locations using composites of color raster plots extending from mid-span ($z/c = 0$) to the sidewall ($z/c = -1.02$). The vertical elevation in each measurement plane is measured relative to the surface of the insert model ($y/c = 0$) and the position of the sidewall is marked using black dashed lines. The superposed velocity vectors (V and W) are not displayed at the full resolution of the measurements and are used to highlight overall features of the flow. As shown in Figure 5.1, in the upstream plane (Figure 5.2, I-a), the flow is nominally attached for $-0.8 < z/c < 0$ and the streamwise velocity above the surface boundary layer is nearly spanwise uniform ($U = 0$ is marked by the white contour). Within the domain $-1.02 < z/c < -0.8$, the reversed flow along the sidewall and above the model surface turns toward the centerline and the

PIV data show evidence of this turning near the surface. Farther downstream, the corner region of reverse flow spreads radially outward from the sidewall corner (Figure 5.2 I-b and -c), and the thickness of the boundary layer over the surface increases downstream of the separation line in Figure 5.1. Despite the reverse flow domain beyond the separation line A-B-C-D-E in Figure 5.1, the measurement planes farther downstream (Figure 5.2 I-b and -c) show only a narrow band of reverse flow along the center domain ($-0.64 < z/c < 0$) as evidenced by the white contour $U = 0$ close to the surface, and in Figure 5.2 I-b the reverse flow is within the resolution of the sPIV near the surface. The data in Figure 5.2 I-b and I-c show evidence of the surface bound vortex in the oil flow visualization V_R in Figure 5.1 that is located at $z/c = -0.51$ which results from shear between the higher speed streamwise flow ($U > 0$) through the center region ($0 < z/c < -0.51$) and the region of reverse flow along the sidewall where $U < 0$ ($-1.02 < z/c < -0.51$, Figure 5.2 I-b and I-c). The opposing directions of the streamwise velocity induce the CCW orientation of the right surface vortex as shown in the oil visualization (V_R, Figure 5.1).

Corresponding distributions of the cross-stream velocity component V and spanwise component W are shown in Figure 5.2 II-a, b and c and Figure 5.2 III-a, b and c, respectively. The streamwise evolution of V (Figure 5.2 II-a, b and c) shows that in the free stream above the wall the flow is directed downward towards the surface as a result of turning over the apex of the model mold line. The streamwise evolution of the W (Figure 5.2 III-a, b and c) show that the flow includes a spanwise velocity component that is directed towards the model centerline ($z/c = 0$) whose magnitude diminishes as the flow progresses downstream. This coincides with the upstream separation front in the oil flow (cf. Figure 5.1) which shows that the attached flow has a significant spanwise motion (right

to left) due to the presence of the surface vortex V_R where the right to left motion in the measurement plane in in agreement with the plane at x/c = 5.26 and 5.54 in Figure 5.2III-a and III-b, while this motion reverses downstream on the opposite side of the same CCW vortex associated with spanwise left to right oil streaks in Figure 5.1, which is also evidenced in the measurements at x/c = 5.72 (Figure 5.2III-c). The evolution of the corner flow in the juncture between the sidewall and the surface of the model (Figure 5.2 II-a, b and c) is evidenced by the spreading of upward V in the corner region corresponding to the reverse flow region shown in Figure 5.2 I-a, b and c. The distribution of V exhibits counter-clockwise rotation (circles in Figure 5.2 II-c and III-c) where $V > 0$ on the right (near the sidewall) and $V < 0$ to the left, which is in agreement with the rotational sense of the surface bound vortex (V_R in Figure 5.1). Similarly, the distribution of W in the corner region shows a coupled layer of left and right spanwise velocity associated with CCW rotation in the outer flow (circle in Figure 5.2 III-c). It can be surmised from the evolution the corner flow, that this reverse flow region acts as a blockage to the nominally streamwise flow, which explains the higher U along the centerline compared to the flow near the sidewall, the direction of W towards the centerline, and the orientation of the surface-normal vortices V_R and V_L in Figure 5.1.

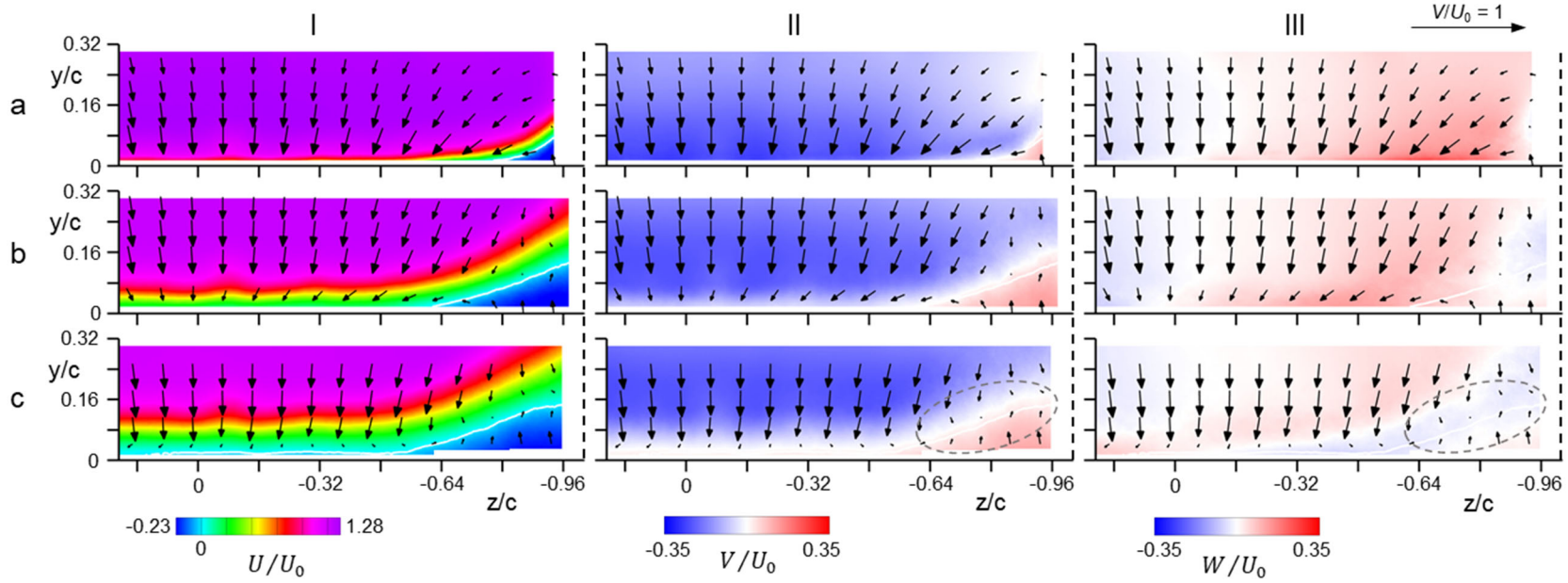

Figure 5.2. Color raster plots of the time-averaged streamwise, cross-stream, and spanwise velocity components, U (column I), V (column II), and W (column III), respectively in the streamwise-normal (y-z) plane of the base flow superposed with velocity vectors: x/c = 5.26 (row a), 5.54 (row b) and 5.72 (row c), M_0 = 0.25. (U = 0 is marked white, and the tunnel sidewalls are marked by black dashed lines).

Concentrations of the time-averaged streamwise vorticity ξ_x in the measurement planes at x/c = 5.26, 5.54, and 5.72 are shown in Figure 5.3 that is computed from the time-averaged flow fields of the V and W (cf. Figure 5.2 II and III). The attached flow at x/c = 5.26 (Figure 5.3a) shows vanishingly small vorticity concentrations within the flow over the surface boundary layer with a band of predominantly clockwise (CW) streamwise vorticity along the surface ($-0.80 < z/c < 0$) that intensifies towards the corner flow, which is characterized by a counterclockwise (CCW) vorticity concentration. These concentrations of CW vorticity appear to be associated with the weak turning of the flow over the surface towards the centerline (cf. Figure 5.2 III-a), whereas the corner regions of

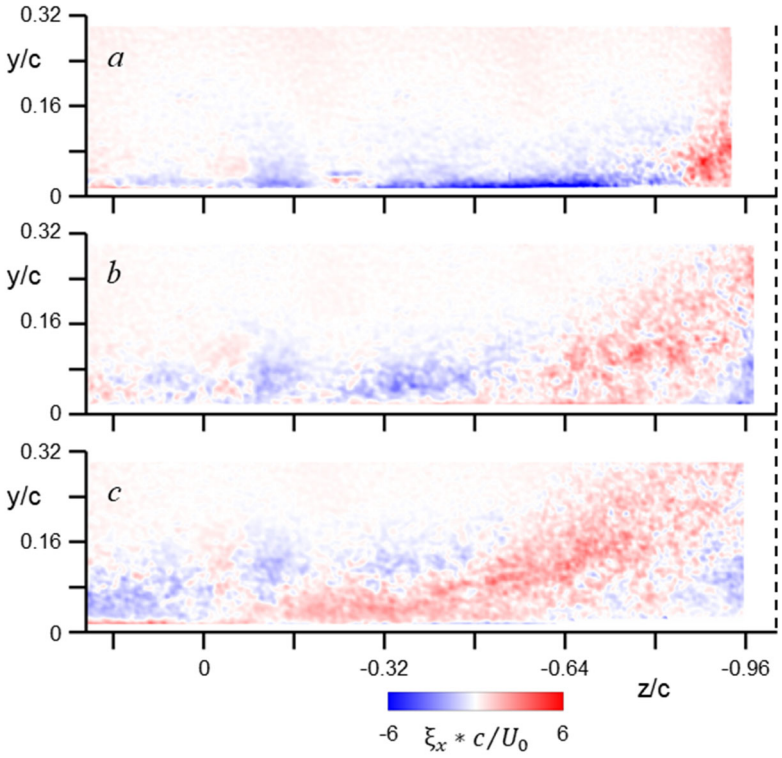

Figure 5.3. Color raster plot of concentrations of the time-averaged streamwise vorticity ξ_x in the base flow (M_0 = 0.25) at x/c = 5.26 (a), 5.54 (b) and 5.72 (c). Counter-clockwise (CCW) vorticity concentrations are marked by $\xi_x > 0$.

CCW vorticity are associated with growth of the reverse flow region and pairs of opposite concentrations of *V* and *W* as discussed in connection with Figure 5.2 II-a-c and III-a-c. As the flow is advected downstream, the CW band of surface bound vorticity weakens and migrates towards the outer flow. Simultaneously, the dominant CCW corner region spreads radially outward and encroaches towards the center underneath the former band of CW vorticity near the surface, which is attributed to the effect of the surface-normal CCW vortex V_R in Figure 5.1. As the CCW vorticity concentrations spread radially from the corner region when the flow is advected downstream, a small concentration of CW vorticity forms entirely within the reverse flow region in the corner as a result of upwards *V* near the sidewall within the reverse flow region in Figure 5.2 II-c.

Further insight into the characteristics of the separation cell are gleaned from concentrations of the time-averaged turbulent kinetic energy $TKE = (\frac{1}{2}(\overline{u'u'} + \overline{v'v'} + \overline{w'w'}))$ that are shown using color raster plots in Figure 5.4. Remarkably, the *TKE* levels associated with the streamwise CW vorticity band along the surface within the domain $-0.7 < z/c < 0$ in Figure 5.4a (cf. Figure 5.3a) are low ($TKE/U_0^2 < 0.07$) and appear to be associated with low streamwise velocity in the central domain of the separation cell in Figure 5.1, in which the flow near the surface is too low to transport the oil streaks upstream. As the flow is advected downstream, the central region shows an elevated band of *TKE* that forms away from the lower surface, which is attributed to the flow over the separated domain and the outer velocity gradient (Figure 5.2 I-a, b and c) over the central separated region. This outer *TKE* peak is also evident in the planar PIV measurements

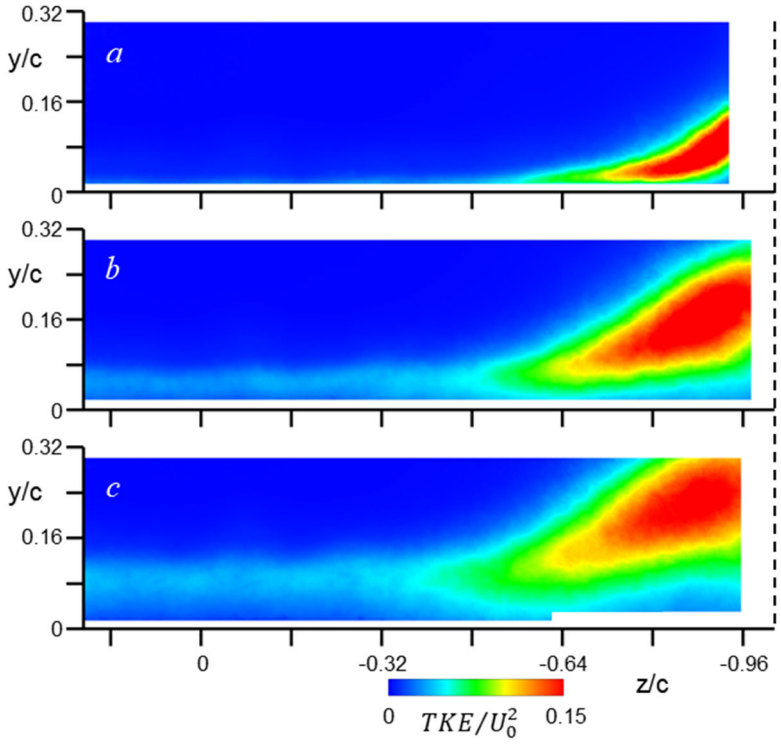

Figure 5.4. Color Raster plot of the time-averaged *TKE* in the base flow ($M_0 = 0.25$) at $x/c = 5.26$ (a), 5.54 (b) and 5.72 (c).

along the center plane ($z/c = 0$) of the separated domain in Figure 4.2. Near the sidewall ($-1.02 < z/c < -0.64$), however, the *TKE* is intensified in the region of reverse flow (Figure 5.2 I-a), and there is a significant peak in the outer flow. The intensified *TKE* levels in Figure 5.4a are coincident with the CCW vorticity concentrations in Figure 5.3a, and the peak is located within the center of this region, which is formed due to pairing of concentrations of *V* and *W* (Figure 5.2) of opposing sense. The peak *TKE* levels in the corner region, then, are the result of low momentum fluid that is pushed upward along the sidewall ($V > 0$, Figure 5.2 II-a), which then mixes with the higher momentum free stream, creating this domain of high intensity fluctuations. The *TKE* in the corner region reduces intensity, spreads radially, and migrates upwards by *V* in the corner at $z/c = -0.88$ in Figure

5.2 II-c. The central peak of the high intensity region is collocated with the CCW vorticity concentrations (Figure 5.3) and show the fluctuations that are associated with the instantaneous motions of the vortex. The region of high *TKE* is confined between the core of the surface vortex at *z/c* = -0.51 and the sidewall above the surface, commensurate with the oil flow in Figure 5.1 that shows evidence of lower momentum upstream flow along the surface and the sidewall.

The corresponding turbulent production at *x/c* = 5.72 (cf. Figure 5.4c) $\Pi = -\langle u_i u_j \rangle \overline{S_{ij}}$ and the dissipation $\varepsilon = 2\nu\langle s_{ij} s_{ij} \rangle$, respectively using the notation of Pope (2000) are shown in Figure 5.5a and b, respectively. It should be noted that these calculations do not account for the streamwise rate of change of the *V* and *W* but that $\partial u/\partial x$ is computed using the continuity equation. It is recognized, however, that the present PIV measurements (vector grid resolution $\Delta x/c = 4 \cdot 10^{-3}$) cannot resolve well flow scales down to the Kolmogorov scale (estimated to be about $x/c = 2 \cdot 10^{-5}$ in the present measurements) that are needed to estimate turbulent dissipation (Wang et al., 2021) and, as a result, the dissipation is significantly underestimated (its magnitude is about 30 times smaller than the production in the base flow in Figure 5.5). However, the computed dissipation is nevertheless included in the discussion of the base flow for reference and is omitted from further discussion of the results in Sections 5.3 and 5.4. In the base flow, the turbulent production (Figure 5.5a) occurs within a concentrated band away from the model

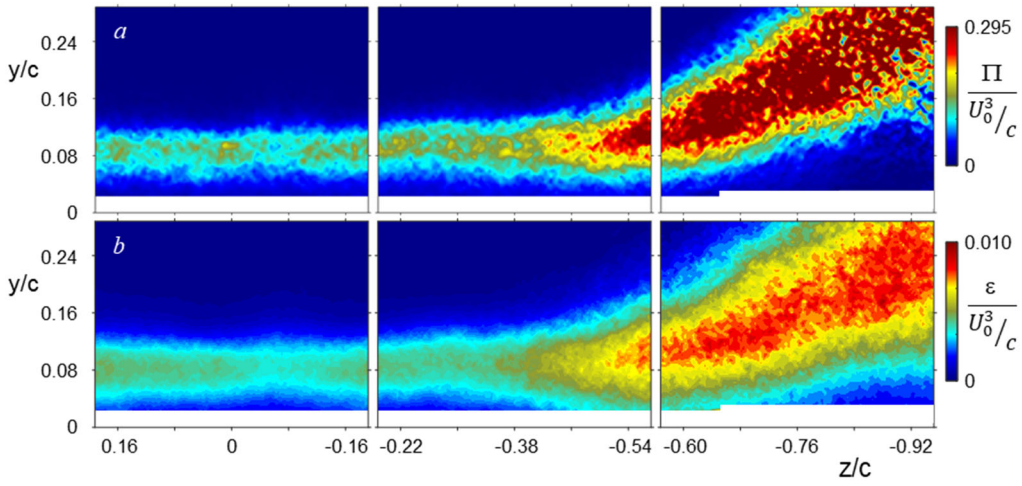

Figure 5.5. Turbulent Production (*a*) and Dissipation rate (*b*) for the base flow ($M_0 = 0.25$) at the streamwise plane $x/c = 5.72$ corresponding to Figure 5.4c.

surface through the majority of the central domain ($-0.54 < z/c < 0$), with peak levels around the center of the streamwise gradient of the time-averaged streamwise velocity outside of the reverse flow region (cf. Figure 5.2 I-c) and owing to the shear in this layer. Similarly, the estimate of the turbulent dissipation (Figure 5.5b) also is concentrated within a band away from the model surface in the same spanwise domain as the production. The band of elevated turbulent production levels intensifies laterally towards the sidewall and widens while also extending away from the lower surface ($-0.92 < z/c < -0.60$). The peak production levels occur within the region of predominantly CCW vorticity (cf. Figure 5.3c) and are attributed to the mixing of the reverse flow along the wall being turned back to the center in the surface foci as seen in the oil visualization (cf. Figure 5.1). The turbulent dissipation follows the same spatial trend as the production, at significantly lower levels.

The time-averaged *TKE* in Figure 5.4 shows the location of velocity fluctuations within the separation cell and represents instantaneous flow structures that are associated

with these fluctuations. Following the analysis of vortices formed in the turbulent wake of an airfoil by Ghaemi and Scarano (2011) and their later studies of a separating turbulent boundary layer (Elyasi and Ghaemi, 2019, Ma et al., 2020, and Ma, 2020), third order turbulence moments ($\langle u'u'u' \rangle, \langle u'u'v' \rangle, and\ \langle u'u'w' \rangle$) are used to assess how the turbulent kinetic energy associated with streamwise velocity fluctuations $\langle u'u' \rangle$ is transported, and since $\langle u'u' \rangle$ is positive its transport is determined by the third fluctuating velocity component. In this context, $u > 0$ and $v < 0$ are attributed to the presence of 'sweeping' motions, i.e., in the streamwise and surface directions, while the opposite directions $u < 0$ and $v > 0$ indicate the presence of 'ejection' motions, i.e., in the upstream and away from the surface direction. These 'sweeping' and ejection' motions that are tied to the formation and advection of turbulent structures in turbulent flow are discussed in a review of coherent motions within a turbulent boundary layer by Robinson (1991) and the study of hairpin vortices in wall turbulence by Adrian (2007). A sketch summarizing the turbulent ejection

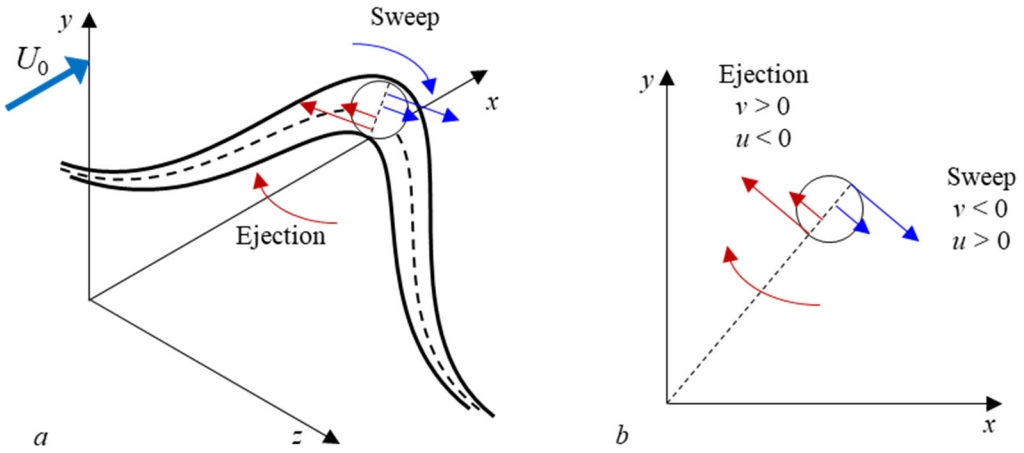

Figure 5.6. Schematic rendition of a hairpin vortex oriented in the streamwise direction with the head of the vortex centered along the *x*-axis (*a*) and a cross-section of the vortex indicating the direction of ejection and sweeping motions (*b*) (following Adrian, 2007).

and sweeping motions is provided in Figure 5.6. The resultant third order turbulence moments for the base flow are shown as color raster plots in Figure 5.7. Remarkably, the *v'* and *u'* fluctuations (Figure 5.7a and b) form two distinct layers through the central region ($0 < z/c < -0.54$) that increase laterally in intensity and lift up the sidewall ($-0.54 < z/c < -0.92$), but remain separate. The concentrations of these turbulent moments in Figure 5.7a and b show that the outer flow domain of upward cross-stream velocity fluctuations $v > 0$ (marked by the red in Figure 5.7a) pair with the outer flow domain of upwind streamwise velocity fluctuations $u < 0$ (marked by blue in Figure 5.7b) which show that $\langle u'u' \rangle$ in these regions is transported via ejection motions (cf. Figure 5.6). Similarly, the remaining concentrations show that the near wall region transports $\langle u'u' \rangle$ via sweeping motions. The

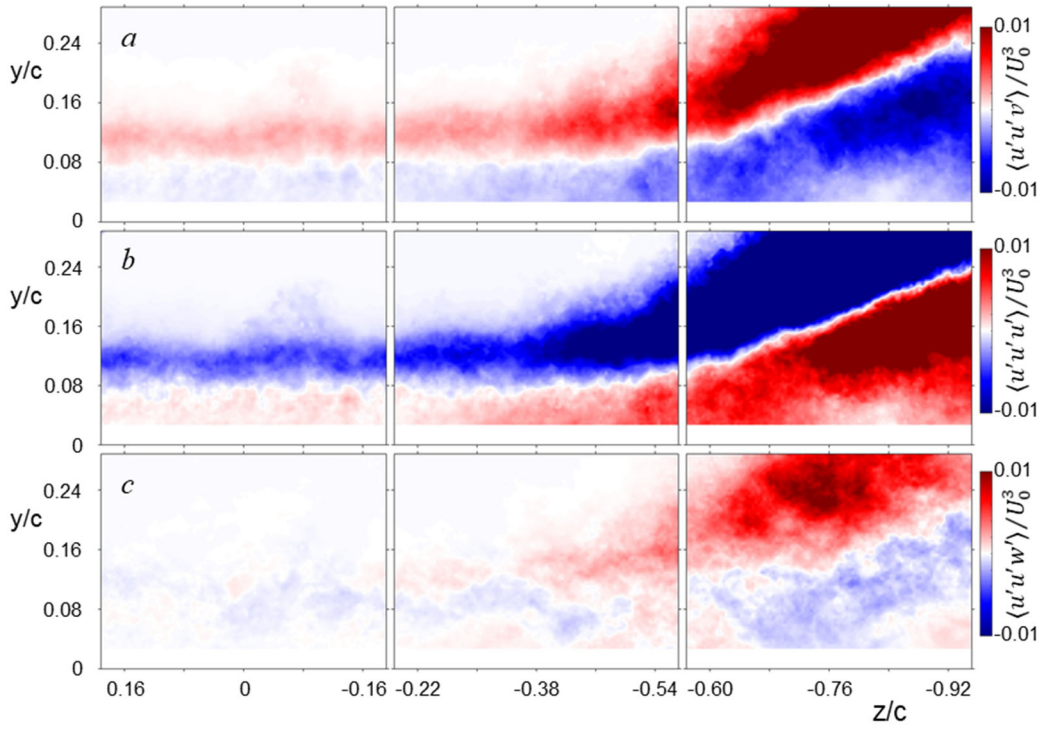

Figure 5.7. Third order turbulence moments $\langle u'u'v' \rangle / U_0^3$, $\langle u'u'u' \rangle / U_0^3$, and $\langle u'u'w' \rangle / U_0^3$ (a, b, and c, respectively) in the base flow ($M_0 = 0.25$) and the streamwise plane at $x/c = 5.72$.

dividing line between the ejection and sweeping motions is located away from the wall ($y/c = 0.8$, $0 < z/c < -0.54$) and suggests that these structures are forming in the midst of a shear layer that develops a time-averaged rolling motion centered on the dividing line at $y/c = 0.8$. This CW orientation of spanwise vorticity ξ_x was shown in Chapter 4, and is reminiscent of the analysis by Schatzman and Thomas (2017) who showed that the CW vorticity in the outer shear region of a turbulent boundary layer in an adverse pressure gradient gives rise to both sweeping and ejection motions centered about an outer inflection point within the embedded shear region. As was noted in Chapters 3 and 4, the evolution of this flow is mostly affected by the dynamics of the outer region shear flow rather than at the near wall domain.

The near-absence of fluctuations of the spanwise velocity component w in Figure 5.7c compared to the fluctuations of u and v throughout the central domain ($0 < z/c < -0.54$) show that $\langle u'u' \rangle$ is not transported by spanwise motions through the central domain. However, the flow near the sidewall ($-0.60 < z/c < -0.92$) shows that the outer flow transports $\langle u'u' \rangle$ via spanwise fluctuations from right to left (marked by red), whereas the flow near the surface indicates left to right fluctuations (marked by blue). The pairing of these spanwise fluctuations (left on top, and right on bottom, Figure 5.8c) indicate an underlying CCW sense of rotation near the sidewall, in accord with the time-averaged vorticity concentrations in this region (cf. Figure 5.3c).

5.3 Effects of Fluidic Actuation: Single Jet

The investigations of the interactions of the actuation jets with the separation cell of the base flow commence with the effect of a single jet placed at the centerline of the

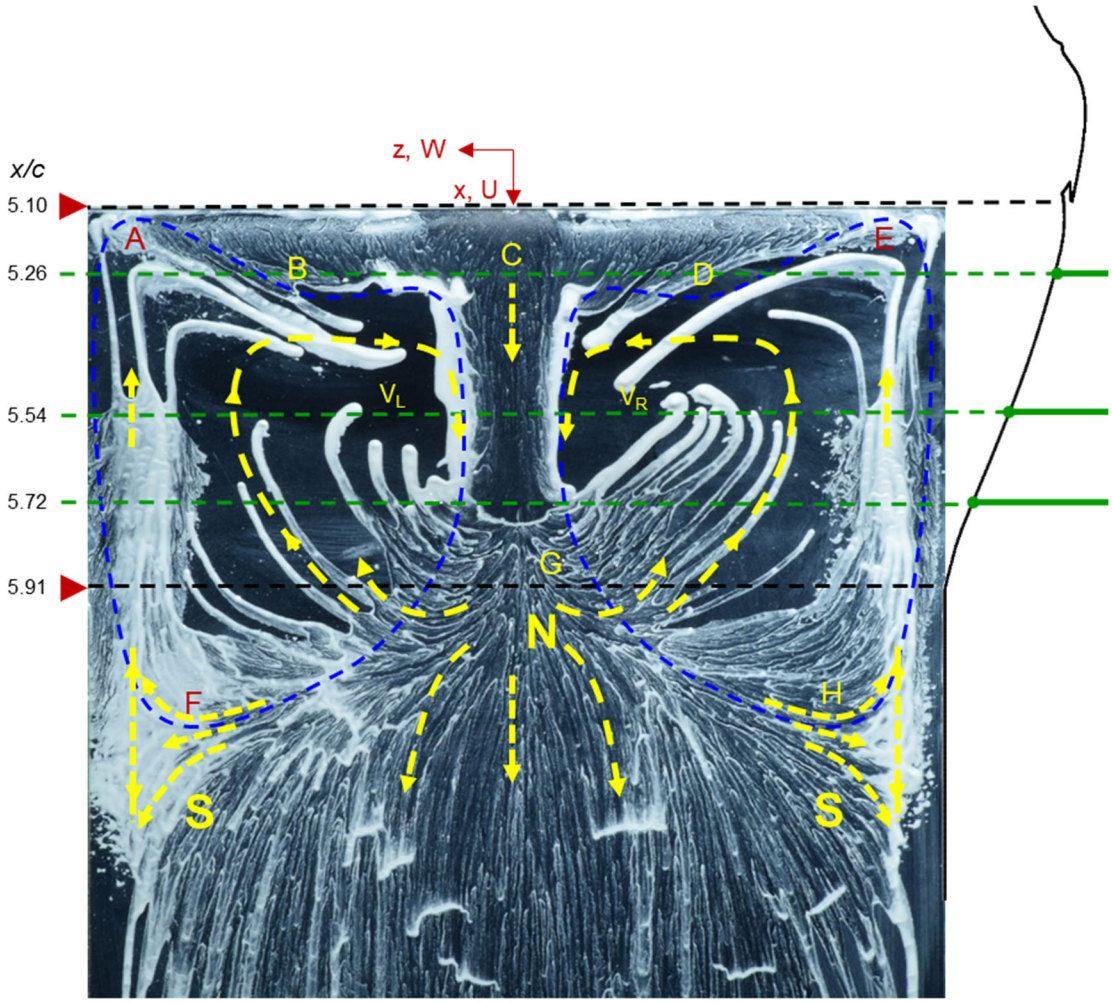

Figure 5.8. Oil flow visualization in the presence of actuation by the center jet at $C_{\mu,\,\text{per jet}} = 0.12{\cdot}10^{-3}$ ($M_0 = 0.25$). The image is aligned with a streamwise profile of the model insert section on the right. The upper edge of the image is aligned with the exit plane of the actuation jet array at $x/c = 5.10$ (marked by ▶). The downstream edge of the insert model is at $x/c = 5.91$ (marked by ▶). The streamwise locations of the sPIV streamwise-normal planes are marked by solid-dashed green lines at $x/c = 5.26$, 5.54, and 5.72.

separation cell ($z/c = 0$) at $C_{\mu,\,\text{per jet}} = 0.12{\cdot}10^{-3}$ that was sufficient to result in full reattachment on the flow's centerline (cf. Chapter 4). The effects of single jet actuation on the separation cell are shown using the oil flow visualization in Figure 5.8. In the presence of the jet, the separated flow becomes reattached along a narrow segment about the centerline of the cell as evidenced by the streamwise oil streaks between points C and G,

and splits the cell to two closed recirculating flow regions marked by lines A-B-F and D-E-H. Remarkably, despite the attached flow along the centerline between C and G, the topological features outside of this region remain similar to the base flow including the formation of the two counter-rotating surface vortices (V_L and V_R) that, compared to the base flow, are somewhat displaced downstream and are closer to the centerline ($z/c = 0$) The reverse flow along the sidewalls reaches to the corners at the jet exit plane (A and E) before it is turned towards the centerline. The presence of the streamwise flow of the jet interrupts the nearly stagnant flow downstream of the separation line A-B-D-E and is consistent with the direction of the flow induced by the surface-normal vortices. The presence of the center jet migrates separation around the plane of symmetry in the base flow farther downstream and the reattachment node G upstream, while the saddle points along the sidewalls H and F remain in nearly the same positions as in the base flow. As the center of the jet approaches the reattachment node G, the oil streaks are split and diverted left and right of the jet centerline and appear to be drawn towards V_R and V_L within the reverse flow regions of the separation cell. The flow visualization image in Figure 5.8 shows that the effect of the single actuation jet is highly localized and the separation cell relaxes back to its natural state outside of this domain.

The streamwise evolutions of the time-averaged velocity components U, V, W in the presence of the single jet actuation ($C_{\mu,\,\text{per jet}} = 0.12 \cdot 10^{-3}$) at three streamwise positions are shown in Figure 5.9 using composite color raster plots between the centerline and the sidewall ($0 < z/c < -1.02$). The upstream distribution of the U (Figure 5.9 I-a) is nearly unchanged compared to the base flow (cf. Figure 5.2 I-a) since, as is apparent from the respective oil visualization images, the flow is attached within the domain ($-0.8 < z/c < 0$)

and appears to be separated in the vicinity of the sidewall ($-1.02 < z/c < -0.8$) where U is reversed. The effects of the actuation become prominent at $x/c = 5.54$ (Figure 5.9 I-b), where the central domain is clearly bisected along the centerline with a region of increased U ($-0.08 < z/c < 0.08$), while the surrounding near-wall flow immediately to the left and right outside of this region demonstrates larger U velocity deficit compared to the outer flow. The increase in the magnitude of U near the surface is the result of flow attachment on both sides of the jet centerline (cf. Figure 5.8) while outside of the domain of the jet influence (e.g. $z/c < -0.08$) the velocity distribution near the surface is nearly the same as in the base flow (cf. Figure 5.2 I-b), including the reverse flow domain in the corner of the sidewall. Farther downstream ($x/c = 5.72$, Figure 5.9 I-c), the effect of the jet begins to diminish as is evidenced by the reduction in the spanwise width of the attached flow ($-0.04 < z/c < 0.04$), which is also apparent in the oil visualization (cf. Figure 5.8). The streamwise velocity distribution immediately to the right and left of the jet effect domain (marked by a dashed ellipse in Figure 5.9 I-b and c) exhibits a cross-stream protrusion towards the core flow which is indicative of the effects of a counter-rotating vortex pair (CCW on the right) that form at the spanwise edges of the actuation jet.

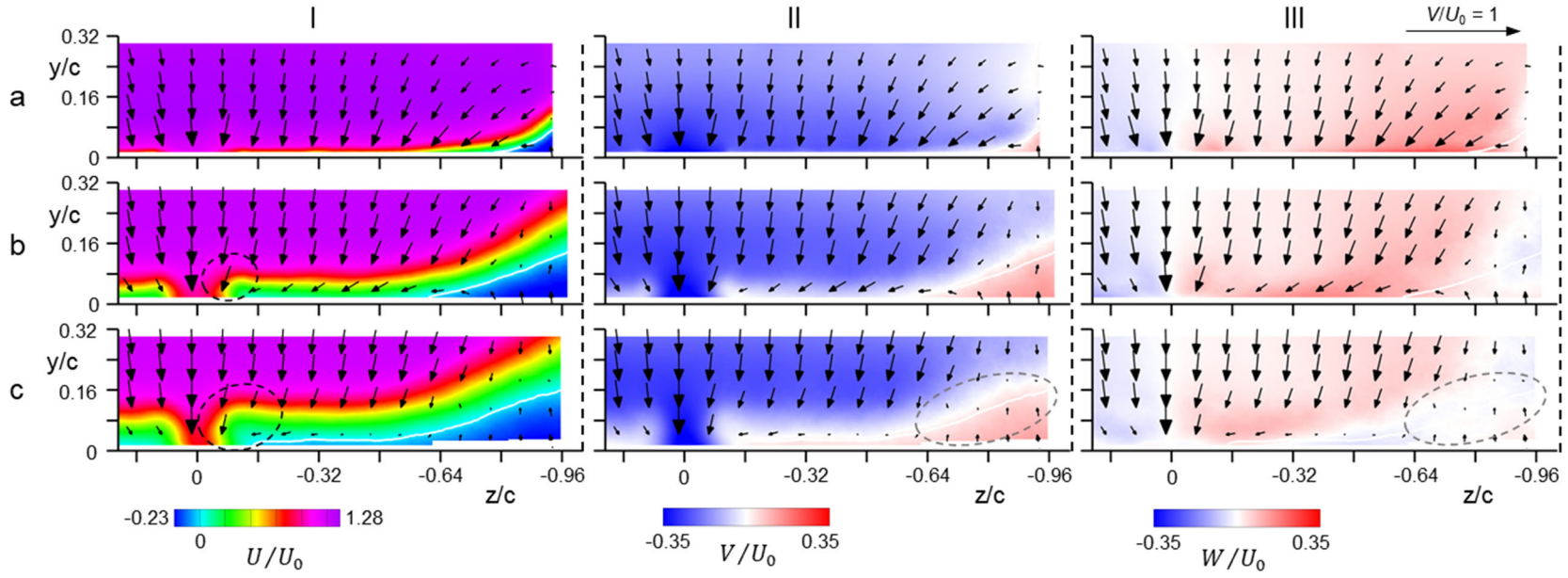

Figure 5.9. Color raster plots of the time-averaged U (column I), V (column II), and W (column III) velocity components, superposed with velocity vectors in the y-z plane at x/c = 5.26 (row a), 5.54 (row b) and 5.72 (row c) showing the effects of single jet actuation on the centreline of the cell (M_0 = 0.25, $C_{\mu,\text{ per jet}} = 0.12 \cdot 10^{-3}$). In these images $U = 0$ is marked using a white contour, and the tunnel sidewalls are marked by black dashed lines).

The corresponding distributions of V and W (cross-stream and spanwise velocity components) are shown in Figure 5.9 II and III a-c, respectively. The streamwise evolution of V (Figure 5.9 II-a, b, and c) shows that the region of reattached flow about the cell's centerline effected by the jet (cf. Figure 5.8) is accompanied by increased downward V that is associated with downwash of the core flow towards the surface as a result of entrainment by the jet (cf. Figure 5.2 II). These data also show that immediately to the right and left of the reattached flow domain there is slight upwash consistent with the presence of a CCW streamwise vortex on the right and CW on the left of the reattached flow as discussed above ($z/c \approx \pm 0.08$). The corresponding distributions of the spanwise velocity component show a small increase in the flow towards the centerline compared to the base flow (cf. Figure 5.2) as a result of entrainment by the jet.

Corresponding concentrations of the streamwise vorticity ξ_x are shown in Figure 5.10. As postulated in connection with Figure 5.9, the presence of the jet is marked by the formation of a pair of counter-rotating streamwise vorticity concentrations at the spanwise edges of the interaction domain of the jet with the adjacent flow that intensify as the flow is advected downstream. It is noteworthy that by $x/c = 5.72$ (Figure 5.10), the presence of the CCW vorticity concentrations at the right edge of the jet ($z/c \approx -0.08$) leads to accumulation of concentrations of CW vorticity sense above the layer of CCW vorticity over the surface that is indicative of spanwise flow towards the centerline. It also appears that the induced spanwise flow along the surface leads to intensification of the corner vortex next to the sidewall. The oil visualization image in Figure 5.8 indicates that the measurement plane $x/c = 5.72$ is located downstream of the wall-normal vortex center V_R and direction of the oil streaks indicates motion towards the sidewall creating a near-

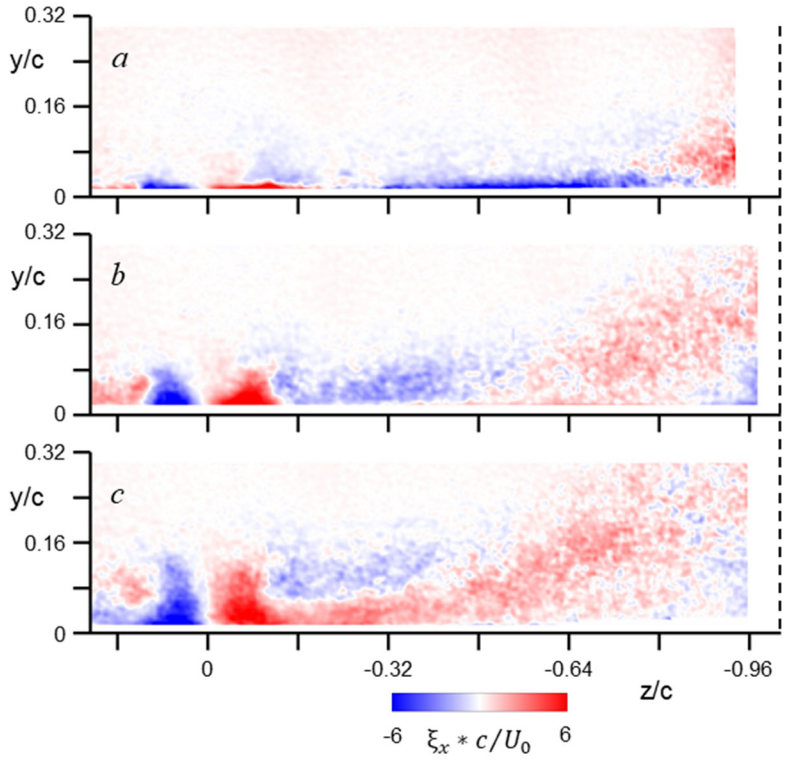

Figure 5.10. Color raster plot of concentrations of the time-averaged streamwise vorticity ξ_x in the presence of the center actuation jet ($M_0 = 0.25$, $C_{\mu,\text{per jet}} = 0.12 \cdot 10^{-3}$) at $x/c = 5.26$ (a), 5.54 (b) and 5.72 (c). Counter-clockwise (CCW) vorticity concentrations $\xi_x > 0$ are marked in red.

surface layer of CCW vorticity. The CCW vorticity layer along the surface connects to the radially spreading CCW concentration along the sidewall that is also present in the base flow (cf. Figure 5.3) and is connected to the to the surface-normal vortex V_R within the separation cell.

The data presented in the preceding figures show that the sense of time-averaged CW and CCW streamwise vorticity pairs that are induced by the actuation wall jets have the opposite sense compared to the streamwise vortices that are induced by jets in cross flow that lift off the surface. This difference is manifested by the direction of the flow that is induced between the vorticity pairs along the jet's centerline. While in off-wall jets in

cross flow the induced flow relative to the axes of the streamwise vortices is nominally an upwash flow (Fric and Roshko, 1994), the vorticity pairs formed by the actuation wall jet induce corresponding downwash relative to the surface (Matsuda, et. al., 1990). This is discussed further in connection with Figure 5.17. It is also noted that the velocity vectors in Figure 5.9 and Figure 5.15 are widely spaced to capture representative features of the flow and do not directly show the upwash flows, which are of significantly lower magnitude than the core flow and are determined from the color raster plots of the velocity components and the streamwise vorticity.

Corresponding distributions of the time-averaged *TKE* (Figure 5.11) show considerable difference relative to the base flow at x/c = 5.26 and 5.72 (Figure 5.11b and

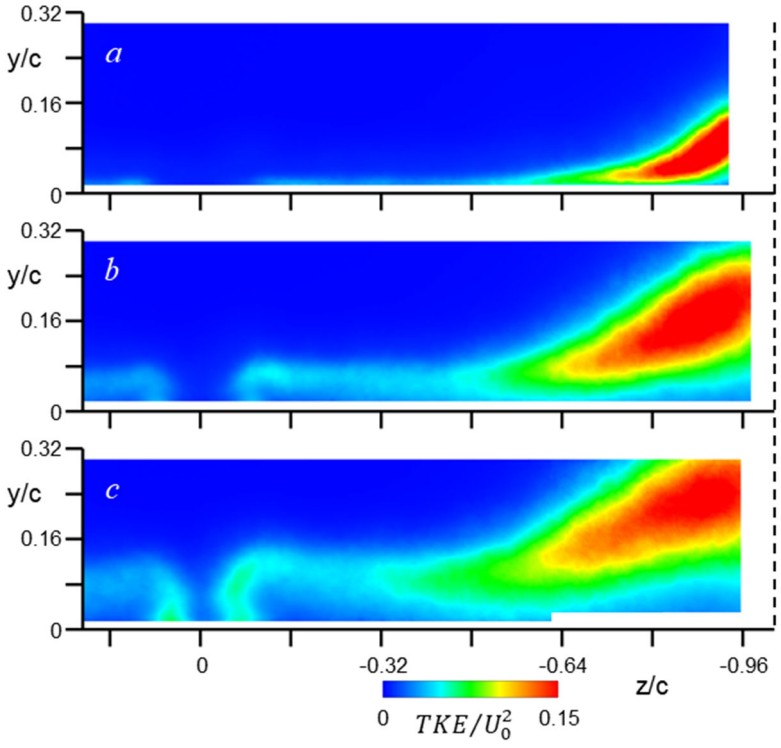

Figure 5.11. Color Raster plot of the time-averaged *TKE* in the actuated flow (single jet, M_0 = 0.25, $C_{\mu,\text{ per jet}} = 0.12 \cdot 10^{-3}$) at x/c = 5.26 (a), 5.54 (b) and 5.72 (c).

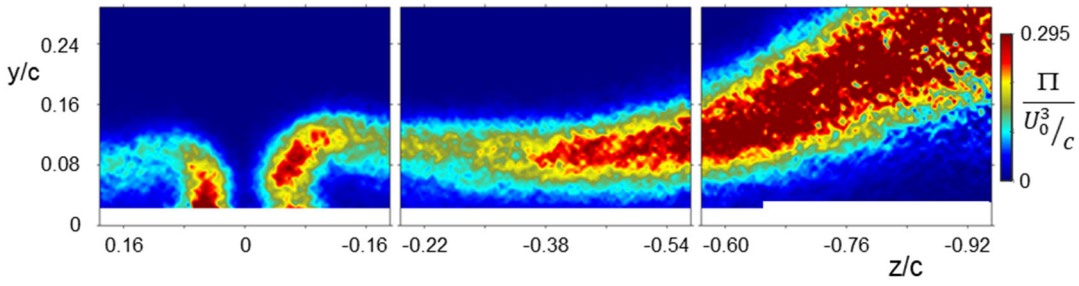

Figure 5.12. Turbulent production for the single jet actuated flow ($M_0 = 0.25$, $C_{\mu,\text{ per jet}} = 0.12 \cdot 10^{-3}$ at the streamwise plane $x/c = 5.72$.

c). The concentrated *TKE* band in the base flow (cf. Figure 5.4b) is severed such that the *TKE* appears to be "rolled" about the counter-rotating streamwise jet-induced vorticity and protrudes into the outer flow, while the *TKE* about the centerline where the flow is attached is significantly lower. The lowering of *TKE* levels along the jet implies that part of the reattachment process, despite the induced vorticity concentrations (cf. Figure 5.10) and increased U and V along the centerline (cf. Figure 5.9), is the suppression of turbulent fluctuations compared to the base flow separation cell. As shown in the oil flow (cf. Figure 5.8), the effective spanwise jet domain is lessened as the flow progresses downstream and the *TKE* levels are only lowered within the domain $-0.04 < z/c < 0.04$ at $x/c = 5.72$. Another slight difference compared to the base flow is that the *TKE* that is associated with the corner vortices is somewhat extended and protrudes farther towards the centerline, but outside of the local interaction region of the jet ($-0.16 < z/c < 0.16$), the distribution of the *TKE* still relaxes back to similar distributions as shown in the base flow. Similarly, the presence of the jet appears to diminish the turbulent production at $x/c = 5.72$ (Figure 5.12) within the attached flow and increase it around the pairs of counter-rotating streamwise vorticity concentrations at the edges of the jet and in the corner vortex.

Finally, the effects of the presence of the jet on the transport of the $u'u'$ at $x/c = 5.72$ is shown in Figure 5.13 using the third-order turbulence moments. These data show that the effect of the jet on the transport associated with the corner vortex is minimal and it is primarily felt near the centerline of the cell. The regions of ejection and sweeping motions are segmented and the outer layer of ejection-based motions is migrated towards the surface (Figure 5.13a and b). This is consistent with the entrainment of the outer flow as part of the reattachment process. Outside of the domain of influence of the jet, the fluctuating u and v form the two-layer structure of the base flow (cf. Figure 5.7 a and b). The fluctuating w (Figure 5.13c), which is featureless within the center domain in the base flow (cf. Figure 5.7c), are populated by four concentrations of alternating sign within the jet's domain of

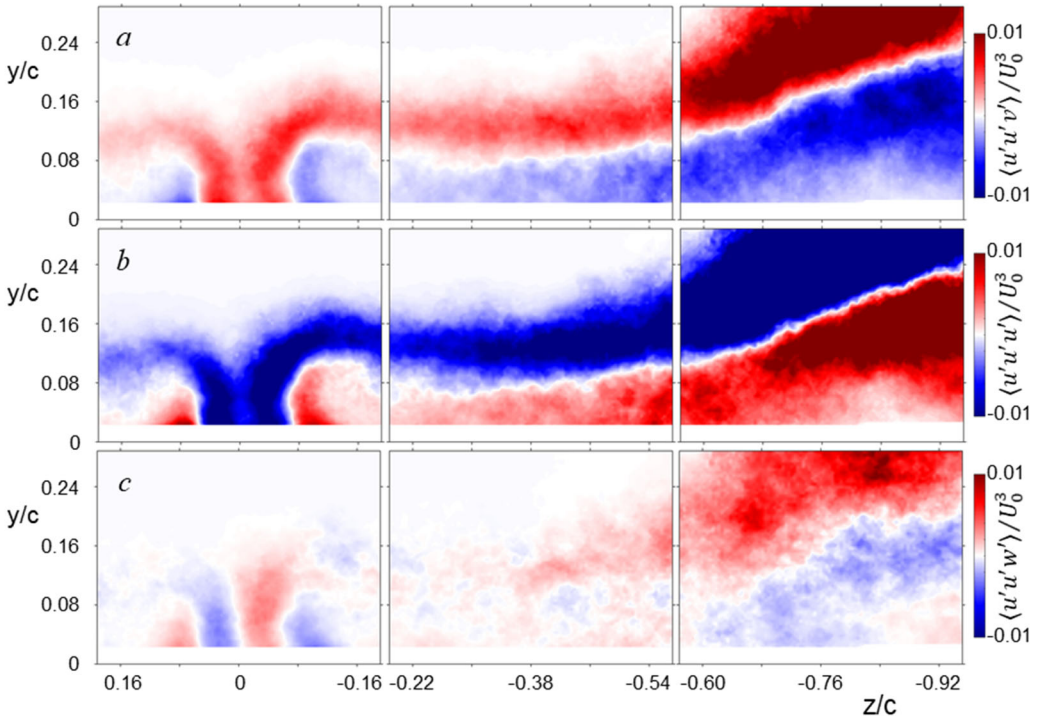

Figure 5.13. Third order turbulence moments $\langle u'u'v'\rangle/U_0^3$, $\langle u'u'u'\rangle/U_0^3$, and $\langle u'u'w'\rangle/U_0^3$ (a, b, and c, respectively) in the single jet actuated flow ($M_0 = 0.25$, $C_{\mu,\text{per jet}} = 0.12 \cdot 10^{-3}$) and the streamwise plane at $x/c = 5.72$.

interaction. The center ($-0.04 < z/c < 0.04$) pair suggest that the $u'u'$ is transported via w fluctuations towards the centerline of the jet, associated with entrainment. The outer pair, however, shows that the jet also produces spanwise fluctuations away from its centerline as is evidenced in the oil flow visualization (cf. Figure 5.8) by streaks that are turn from the center of the jet and wrap laterally into the surface-normal vortices. The two pairs on each side of the centerline of the jet, then, suggest the presence of cross-stream vorticity ξ_y as the flow splits towards and away from the centerline of the jet at these edge effects between opposing w fluctuations at $z/c = \pm 0.4$, which is further suggested as a factor in the enhanced *TKE* levels to the left and right of the jet influence domain shown in Figure 5.11.

5.4 Control of the Separation Cell using Arrays of Fluidic Oscillators with Varying Spanwise Actuation Wavelength

Following the discussion of the effects of an isolated single actuation jet on the topology of the separation cell in Section 5.3, this section focuses on the effects of arrays of jets with varying spanwise spacings $\Delta z/c = 0.11$, 0.22, and 0.33 where $\Delta z/c = 0.22$ corresponds approximately to the spanwise width of the domain of influence of the single jet at $x/c = 5.72$. These models are referred to as configurations '1λ', '2λ', and '3λ' and include 17, 7, and 5 jets, respectively. Since in these actuation configurations the momentum coefficient per jet is held constant ($C_{\mu,\,\text{per jet}} = 0.12 \cdot 10^{-3}$), the total actuation C_μ decreases ($2.04 \cdot 10^{-3}$, $0.84 \cdot 10^{-3}$, and $0.60 \cdot 10^{-3}$, respectively).

5.4.1 Segmented Reattachment Cells

The effects on the topology of the separation cell in the presence of actuation at each of the three spanwise wavelengths (1λ, 2λ, and 3λ) is first assessed using surface oil

flow visualization (Figure 5.14 a, b, and c, respectively, the position of the active jets are marked for reference). These images show that each of these arrays effects flow reattachment over a broad spanwise extent of the previously separated flow within the central region of the separation cell. The outboard jets are shown to couple to the reverse flow along the sidewalls (F-A and G-E, Figure 5.14a, b, and c) which intensifies the surface-normal vortices V_L and V_R. The interaction with the return flow along the side wall is strongest when the outboard jet is closest to the return flow in Configuration 1λ and weakens as the spanwise spacings increase. As a result of interactions with the actuation jet array, the surface-normal vortices V_L (CW) and V_R (CCW) migrate downstream and outboard towards the sidewalls compared to the base flow (cf. Figure 5.1), and the overall size of the surface-normal vortices diminishes with increasing spanwise spacing between the jets. Ultimately, with further increasing jet spacing, the vortices would return to the size shown in the base flow. Concomitantly, as the spacings between the jets increase, they begin to tilt towards the centerline of the cell close to their orifices. These effects appear to be connected to the interaction of the outboard jets with the return flow along the sidewalls, and the deflection of the outboard jets towards the centreline affects the neighboring inboard jets, which is more pronounced when the actuation is more sparse. However, farther downstream (about $5.54 \lesssim x/c \lesssim 5.72$ in Figure 5.14a, b, and c, respectively) the flow within the cell on each side of the centreline begins to turn towards the corresponding sidewall and wrap about the surface-normal vortex on the same side. These images also indicate that for a larger span when the side walls are located farther to the right and left of the centerline, the span of the reattached base flow between the surface-

normal vortices would be extended as the deflection of the outboard jets would be minimized as the vortices would be displaced farther outboard.

Similar to the evolution of the single jet (cf. Figure 5.8), the reattachment of the flow in each actuation configuration is brought about by shifting the reattachment node of the base flow upstream, that results in angled saddle points along each side wall, which are present in each of the actuation configurations (F and G Figure 5.14a, b, and c), where the outboard flow is diverted upstream and downstream along the side walls. The reattachment line (line A-B-C-D-E, Figure 5.14a, b, and c) shows that the downstream edge of the reattachment domain effected by the actuation jets migrates upstream relative to the base flow, and that the streamwise extent of the reattachment is nearly invariant with jet spacing. However, there are clear differences in the form and details of the reattachment owing to

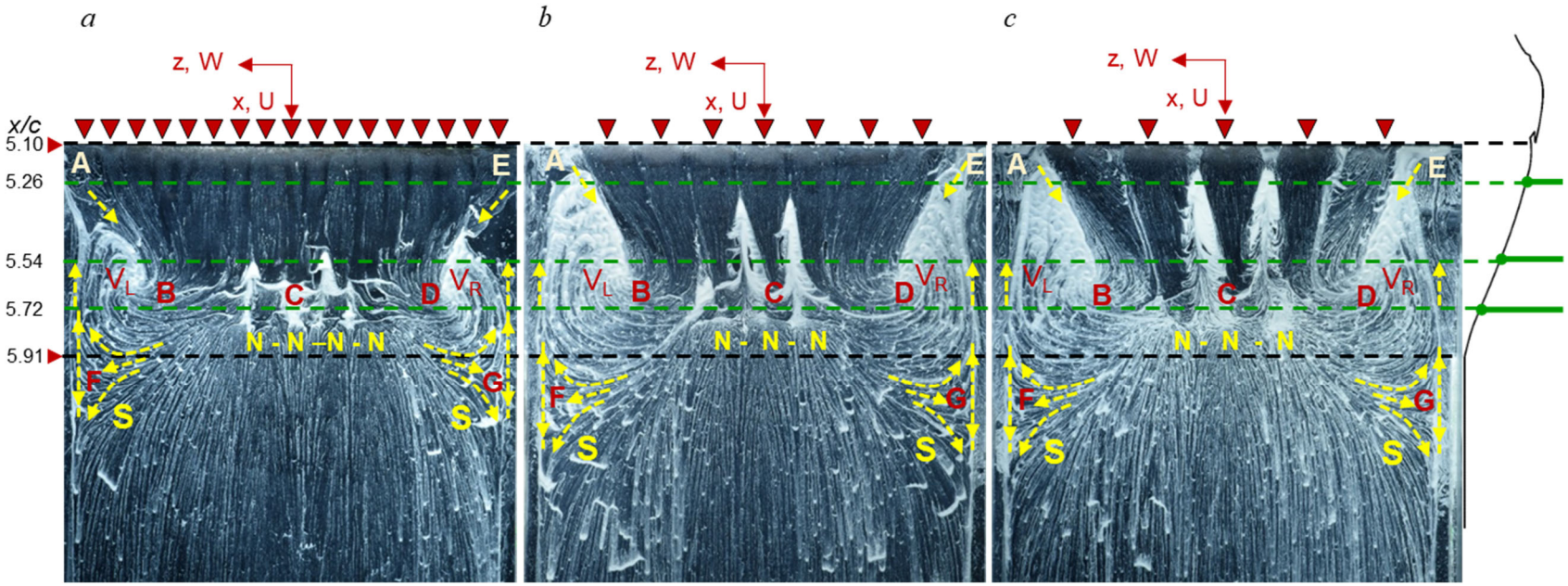

Figure 5.14. Oil flow visualization in the presence of actuation ($C_{\mu,\,\text{per jet}} = 0.12 \cdot 10^{-3}$, $M_0 = 0.25$, flow is top to bottom) along with the streamwise profile of the flow surface (on the right) for 1λ (a), 2λ (b), and 3λ (c) configurations (the spanwise positions of the active jets are marked by triangles). The upper edge of the image is aligned with the exit plane of the jet array at $x/c = 5.10$ (▶). The downstream edge of the model at $x/c = 5.91$ is marked by (▶). The streamwise positions of the streamwise-normal sPIV planes at $x/c = 5.26$, 5.54, and 5.72 are marked by dashed green lines.

the differences in the overall momentum coefficient of the actuation and the jet spacing. The extent to which the central reattachment region is affected by the topology of the flow along the side walls increases with the spanwise spacing of the actuation jets and the strength and location of the surface-normal vortices as is evident from the jets' deflection towards the centerline and the 3-D effects of the outboard jets.

Color raster plots of the time-averaged streamwise vorticity overlaid with velocity vectors for Configuration 2λ (Figure 5.15) show the streamwise evolution of the flow in three measurement planes (x/c = 5.25, 5.54, and 5.72) as the actuation strength is varied up to the level of the surface oil flow visualization in Figure 5.14b (base flow distributions are repeated in Figure 5.15a for reference). As the actuation is increased from $C_{\mu,\,\text{per jet}} = 0$ to $0.12 \cdot 10^{-3}$ (Figure 5.15 I-a to Figure 5.15 I-e) the predominantly CW vorticity band across the surface at x/c = 5.26 ($-0.80 < z/c < 0$) is segmented into pairs of vorticity concentrations of opposing sense that intensify with increasing actuation (Figure 5.15 I-b, -c, and -e). At this streamwise position, the spanwise base flow in the center domain ($0.64 < z/c < -0.64$) is still attached as shown in Figure 5.1. At the highest actuation level ($C_{\mu,\,\text{per jet}} = 0.12 \cdot 10^{-3,}$ Figure 5.15 I-e) the corresponding pairs begin to extend slightly away from the surface, but overall there are no significant changes in the outer flow. The corner flow ($-1.02 < z/c < -0.80$, Figure 5.15 I-a to I-e) is primarily characterized by a CCW vorticity concentration, that only slightly increases in intensity with increasing actuation. At the next measurement domain (x/c = 5.54, Figure 5.15 II-b to II-e) the pairs of counter-rotating streamwise vorticity concentrations extend further into the outer flow and are intensified with increasing actuation levels, but the outboard vortices ($-0.48 < z/c < -0.64$) appear to lose their coherence as a result of interactions of the actuation jets with the corner flow and

the surface-normal vortex for $C_{\mu,\,\text{per jet}} < 0.05 \cdot 10^{-3}$ (Figure 5.15II-c). As C_μ increases ($C_{\mu,\,\text{per jet}} > 0.08 \cdot 10^{-3}$, Figure 5.15II-d, -e) the outboard vorticity pairs formed by the outer jets become intensified and are somewhat distinct from the corner flow, but are still affected by the presence of the surface-normal vortex as the vorticity pairs are shown to be tilted towards the side wall (to the right). These data show that the corner vorticity at this streamwise position ($-1.02 < z/c < -0.64$) is somewhat intensified by the presence of the actuation due to the interaction between the outboard jets and the reverse flow along the side wall. It is noteworthy that as C_μ increases, a CW vorticity concentration forms in the boundary layer near the horizontal and vertical surfaces of the corner due to the surface-normal vortex angling the reverse flow along the side wall away from the wall at $x/c = 5.26$, shown in the oil visualization in Figure 5.14b. At $x/c = 5.72$ (Figure 5.15 III) at the low actuation level (Figure 5.15 III-b) the corner CCW vorticity migrates along the span towards the centerline of the separation cell and the induced vortex pairs are displaced in the cross-stream direction over this layer of the CCW streamwise vorticity ($0.08 < y/c < 0.16$). However, as the actuation level increases, these vortex pairs are intensified and migrate back towards the surface indicating that the strength of the actuation jets is sufficient to hold the spanwise spreading of the corner vortex which continued to wrap induced CW vorticity within the global CCW concentration (Figure 5.15 III-e). It is noteworthy that as the flow within the separation cell in the presence of actuation is advected downstream, the spanwise spreading of the vortex cores for a given actuation spacing is limited by the neighboring vortices (e.g. Figure 5.15 II-e) and they spread in the cross-stream direction.

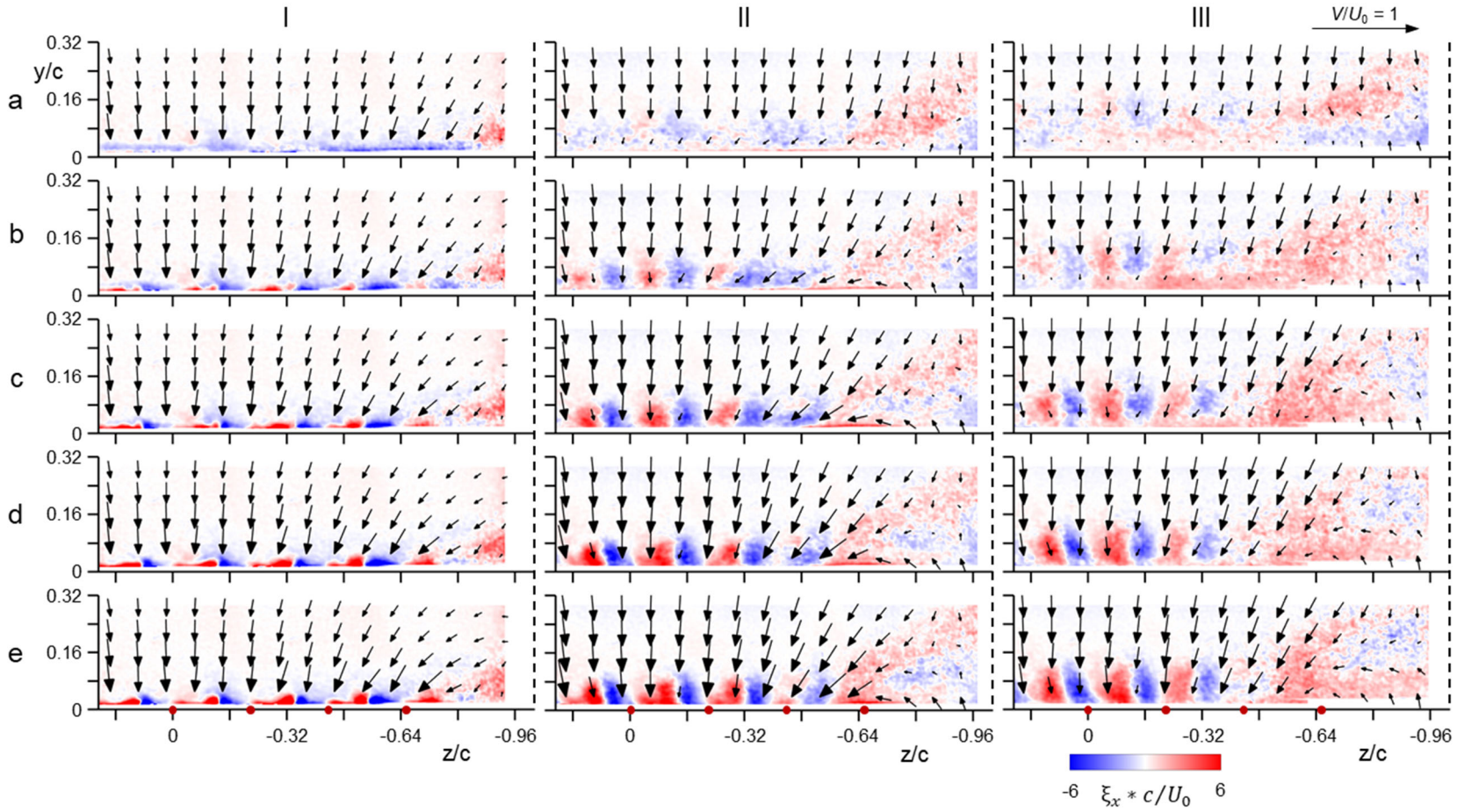

Figure 5.15. Color raster plots of concentrations of the time-averaged streamwise vorticity ξ_x superposed with velocity vectors in the actuated flow for Configuration 2λ (jet spacing $\Delta z/c = 0.22$, $M_0 = 0.25$) $C_{\mu,\text{ per jet}} = 0$ (a), 0.02 (b), 0.05 (c), 0.08 (d), and $0.12 \cdot 10^{-3}$ (e) at $x/c = 5.26$ (I), 5.54 (II) and 5.72 (III). CCW vorticity (in red) are $\xi_x > 0$. The spanwise locations of the jets are marked on the abscissas by •.

The streamwise evolution of the counter-rotating vorticity pairs induced by the actuation jets at varying spanwise spacings of Configurations 1λ and 3λ (at $C_{\mu,\,\text{per jet}}$ = 0.02, 0.05, 0.08, and 0.12 · 10^{-3}) are compared to Configuration 2λ at x/c = 5.72 in Figure 5.16. The evolution of the streamwise vorticity concentrations in the presence of actuation for Configurations 1λ and 3λ (Figure 5.16 I and III-a, b, c and d, respectively) is similar to Configuration 2λ. The number of vorticity pairings and their spanwise interactions scale with the jet spacing, and the proximity of the neighboring jets bounds the spanwise growth of the individual vorticity concentrations. Specifically, Configuration 1λ leads to a tighter grouping of the vorticity pairs (cf. Figure 5.16I-d), while the increased spacing in Configurations 2λ (Figure 5.16II-d) and 3λ (Figure 5.16III-d) allow the vorticity pairs to grow and fill the spacing between the jets. At the highest actuation level, the vorticity pairs within the central region of Configuration 1λ extend over a larger spanwise domain ($-0.64 < z/c < 0$, Figure 5.16I-d) than in Configurations 2λ and 3λ (Figure 5.16II- and III-d, respectively). This difference is the result of the interactions of the outboard jets with the return flow along the sidewall. The variation in the spanwise packing of the vorticity pairs is accompanied by small increases in their cross-stream scale for $y/c \approx 0.10$ (1λ), 0.12 (2λ) and 0.16 (3λ).

As was shown in the oil visualization images (cf. Figure 5.14a), Configuration 1λ results in the strongest confinement of the corner flow which intensifies with the actuation level ($-1.02 < z/c < -0.64$, Figure 5.16 I-a, b, c, and d) as the surface-normal vortices migrate towards the side walls. As the level of the actuation increases, a CW vorticity concentration appears in the corner as a result of the surface boundary layer on the side

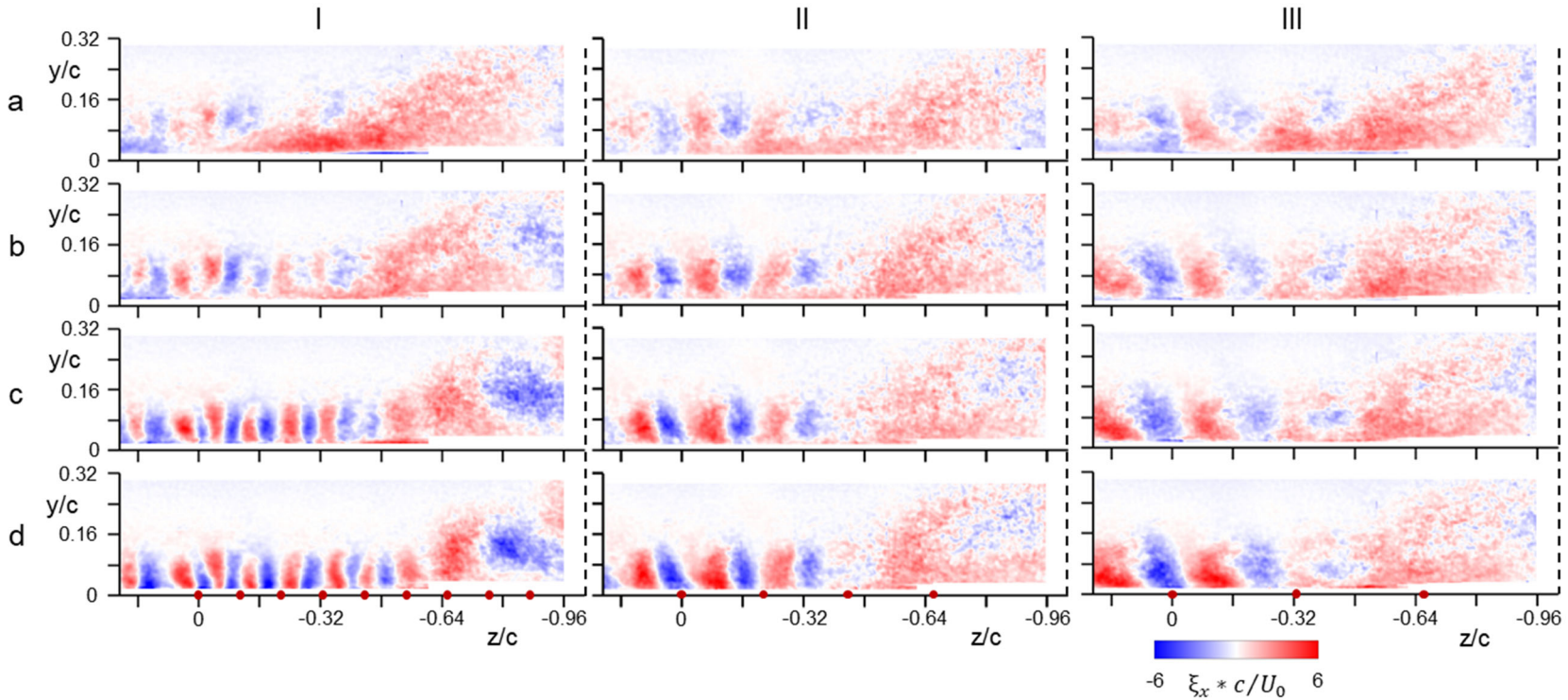

Figure 5.16. Color raster plots of concentrations of the time-averaged streamwise vorticity ξ_x at x/c = 5.72 (M_0 = 0.25) in the presence of actuation in Configurations 1λ (jet spacing $\Delta z/c$ = 0.11, I), 2λ (jet spacing $\Delta z/c$ = 0.22, II), and 3λ (jet spacing $\Delta z/c$ = 0.33, III) for $C_{\mu,\,\text{per jet}}$ = 0.02 (a), 0.05 (b), 0.08 (c), and 0.12 · 10^{-3} (d). CCW vorticity (in red) are $\xi_x > 0$. The spanwise jet locations are marked on the abscissa by •.

wall (-1.02 < z/c < -0.64). This effect diminishes for Configurations 2λ and 3λ (Figure 5.16II and III-d).

As discussed above, flow reattachment is associated with pairs of counter-rotating vorticity concentrations that are each effected by an actuation jet within the central domain of the separation cell where the individual jets are isolated from the effects of the outboard surface-normal vortices as shown schematically in Figure 5.17. These structures effectively lead to spanwise segmentation of the separated flow into individual cells. To highlight the breakdown of the separation cell in the presence of actuation, the topology of its central domain in the base flow is shown schematically in Figure 5.18a, which consists of an attached flow up to a separation front followed by reversed flow upstream of a reattachment node. Downstream of the reattachment node and the reattachment line connecting the two spanwise saddle points at the side walls, the flow remains attached. Remarkably, in the presence of actuation, this basic structure is replicated within the segmented cells that form by the actuation jets and is an essential ingredient of the reattachment mechanism. The surface oil visualization of Configuration 2λ (cf. Figure 5.14b) is repeated in Figure 5.18b using an earlier image during the oil flow and the

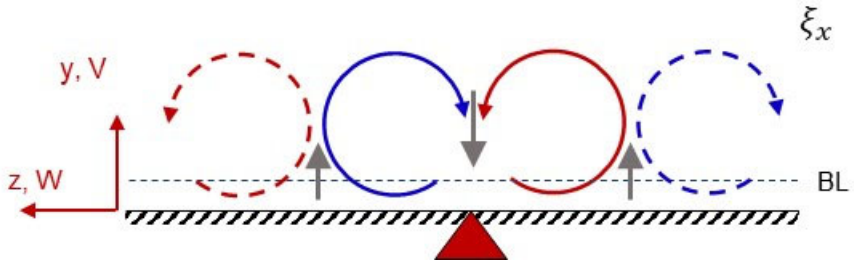

Figure 5.17. Schematic depicting formation of streamwise vorticity concentrations (CW and CCW) along the centerline of a single jet (▶) with associated induced upwash and downwash flows by neighboring vorticity pairs (→).

topology associated with the center jet is highlighted and labeled. This image shows that the reattachment is formed by spanwise segmentation of the base flow (cf. Figure 5.1) into a cellular structure along the centerline of each jet that is defined by a reattachment node

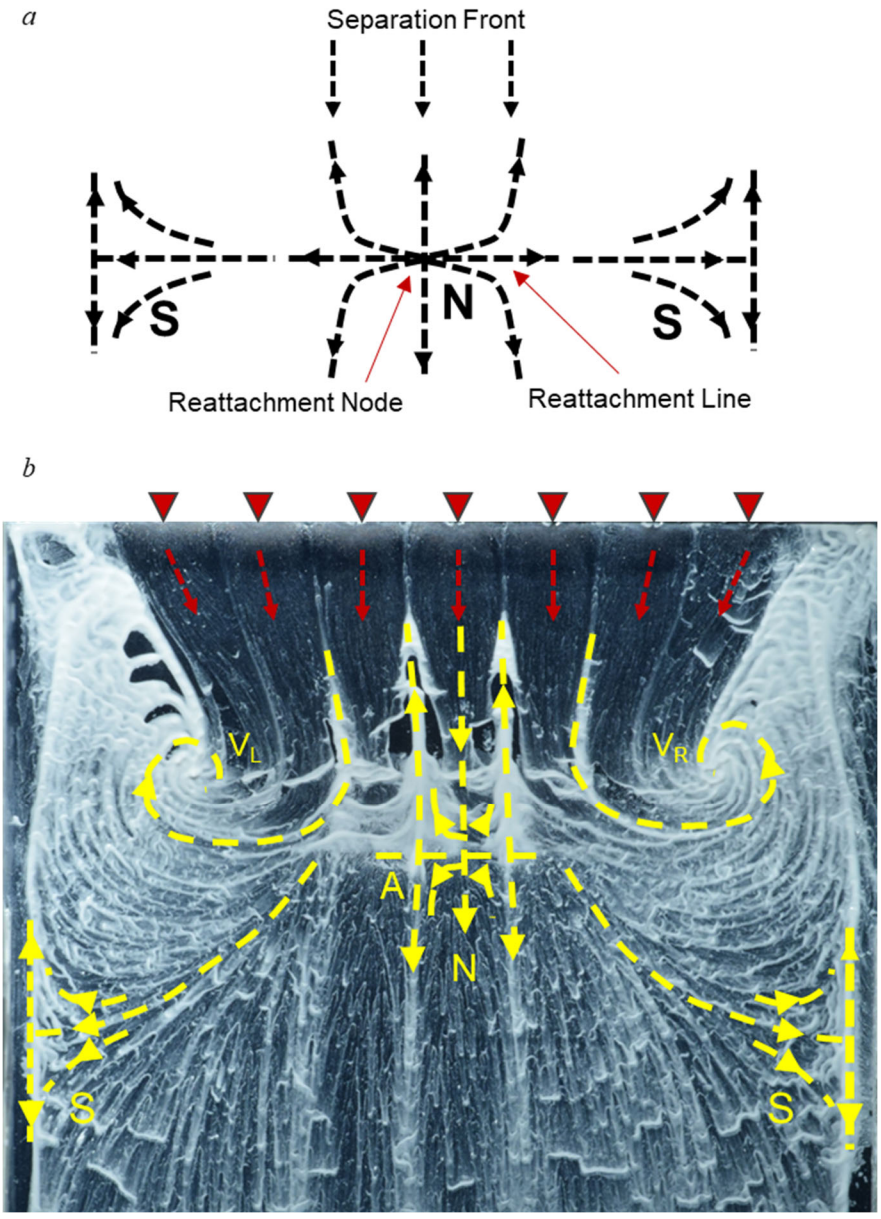

Figure 5.18. a) Schematic rendition of the base flow topology (cf. Figure 5.1) showing reattachment node and side saddle points and b) Surface oil visualization showing the cellular breakdown and flow topology in Configuration 2λ (cf. Figure 5.14b) with a center reattachment node and side saddle points. The direction of the flow is from top to bottom

(A in Figure 5.18b). These cellular structures form by the actuation jets within the central domain that is not influenced by the presence of the side walls and the formation of the surface-normal vortices on each side of the centerline. The cellular structure associated with the center jet is replicated along with the corresponding concentrations of the

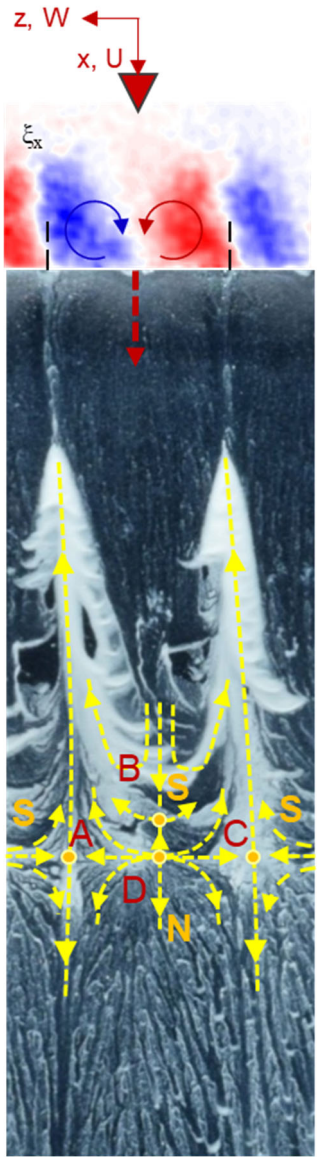

Figure 5.19. A segment of the surface oil visualization image showing the topology of the central reattachment cell in Configuration 2λ (cf. Figure 5.14b) superposed with corresponding CW and CCW vorticity concentrations. The image also includes the relevant critical points •.

streamwise vorticity in Figure 5.19. The flow along the jet centerline is reminiscent of the attached flow in the base separation cell as it reaches point B in Figure 5.19. The reattachment node point D in Figure 5.19 shows lateral oil streaks to two saddle points A and C in Figure 5.19 where the flow is bounded by the neighboring jets and is turned up and downstream, leading to uniformly attached flow. In the limit of high-density actuation jets, the reattachment process is effected segmentation of the separation cell in the base flow into smaller versions of the same topology. This corroborates the earlier observation that separation and reattachment locations are affected simultaneously as discussed in Chapter 4 (cf. Figure 4.7). Similar reattachment cells are present in each of the actuation configurations as evidenced by the oil streaks near the reattachment in Figure 5.14 (the spanwise scale of the reattachment cells is clearly dependent on the actuation wavelength) indicating the role of each jet as a building block of flow reattachment. A summary schematic of the reattachment cell process is shown in Figure 5.20, depicting the formation of the streamwise vorticity and the induced near-surface flows. The surface normal

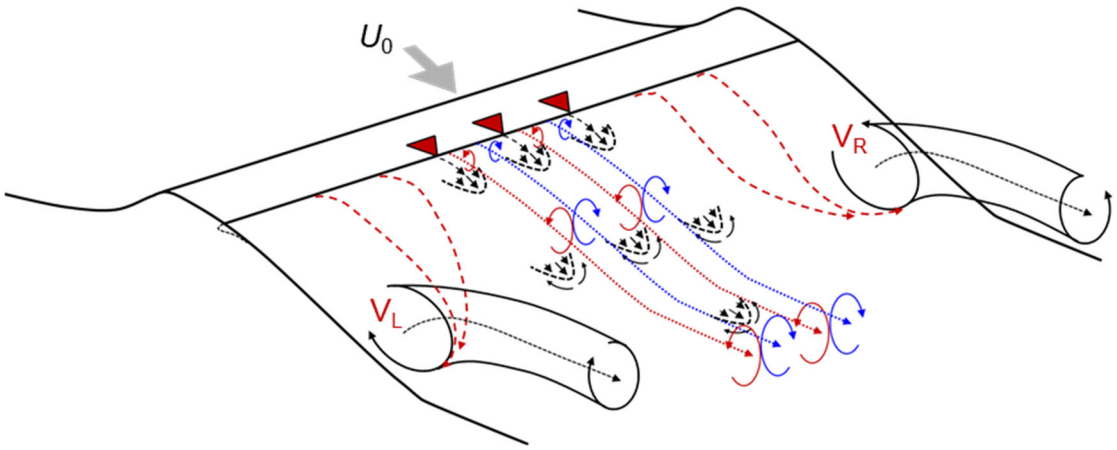

Figure 5.20. Notional cartoon depicting three-dimensional reattachment and the formation of CW and CCW streamwise vorticity concentrations by three central jets (marked by ▶) that segment the base separation cell into reattachment cells.

vortices V_L and V_R are also depicted showing notionally how the outboard jets are interacting with them and streamwise shedding of streamwise vorticity in the corners as shown in Figure 5.16.

5.4.2 Some Comments on the Instantaneous Flow within the Reattachment Cells

The discussion of flow attachment so far was based on the time-averaged data with little attention to the time-dependent velocity and vorticity distributions. A fundamental question is how is the time-averaged flow structure depicted in the previous section related to the actual instantaneous flow structure? To illustrate this point, the time-averaged streamwise vorticity concentrations about the center jet (i.e. center reattachment cell) for the base flow and in the presence of actuation at $C_{\mu,\,\text{per jet}} = 0.12 \cdot 10^{-3}$ for Configurations 1λ, 2λ, and 3λ are compared with corresponding (single) instantaneous concentrations of the streamwise vorticity in Figure 5.21. The distributions of the instantaneous vorticity are calculated from a 40 mode POD-reconstruction of the instantaneous velocity field. As previously discussed in connection with Figure 5.3, the central domain of the cell is characterized by nominally 2-D separation and void of any coherent streamwise vortical structures. The data in Figure 5.21 II-a shows that the *instantaneous* turbulent streamwise vorticity field within the shear layer between the core flow and the surface is characterized by intermingled strands of CW and CCW streamwise vorticity concentrations. The formation of coherent counter-rotating pairs of streamwise vorticity concentrations in the presence of actuation in Figure 5.21 II-b-d indicates that the interaction of the actuation jets with the cross flow can lead to both organization of the random vorticity strands within the separated base flow and to the formation of additional strands by the shear effected by the actuation wall jets. It is conjectured that the spanwise oscillations of the actuation jets

along the surface lead to alternate formation of strands of both CCW and CW streamwise vorticity concentrations that are advected downstream. However, considering the

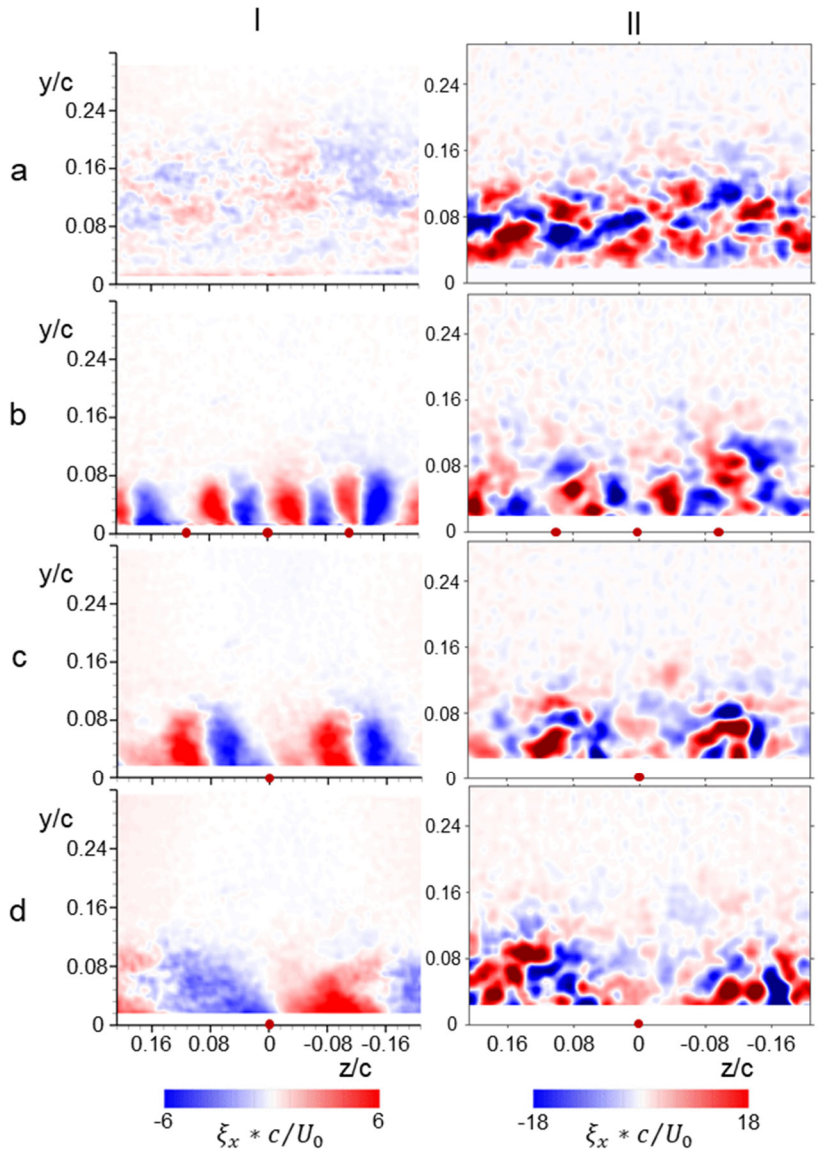

Figure 5.21. Color raster plots of concentrations of the time-averaged streamwise vorticity ξ_x (Column I) and corresponding instantaneous concentrations computed from 40 POD-mode reconstructions of the spanwise and cross-stream instantaneous velocity components in the base flow (a) and in the presence of actuation for Configurations 1λ ($\Delta z/c = 0.11$, b), 2λ ($\Delta z/c = 0.22$, c), and 3λ ($\Delta z/c = 0.33$, d) ($M_0 = 0.25$, $C_{\mu,\text{ per jet}} = 0.12 \cdot 10^{-3}$) at $x/c = 5.54$. CCW vorticity concentrations (in red) are $\xi_x > 0$. The spanwise locations of the jets are marked on the abscissas by •.

kinematics of the jet oscillations it can be argued that the cumulative effects lead to predominantly CW and CCW time-averaged vorticity concentrations as depicted by the time-averaged PIV data in Figure 5.16 (CW on the left and CCW on the right about the jet centreline). In fact, as shown in Figure 5.21 II-b, -c, and -d, respectively, instantaneous distributions of streamwise vorticity concentrations in the presence of actuation with Configurations 1λ, 2λ, and 3λ include intermingled strands of small-scale vorticity concentrations of opposing sense throughout the cross-stream shear layer. However, in the presence of the actuation jets the concentrations are biased by the jet induced shear that depicts higher concentrations of the dominant time-averaged vorticity orientation even in the instantaneous flow. Furthermore, these vorticity concentrations are advected towards the upwelling region between the jet-induced time-averaged vorticity concentrations, while in the downwash domains along the jet centerlines the corresponding concentrations are significantly weaker.

The fluctuating streamwise vorticity is assessed from calculations of the RMS of the instantaneous vorticity fields as:

$$\xi'_{RMS} = \sqrt{\frac{\sum_1^N \left(\xi'_x - \bar{\xi}_x\right)^2}{N}} \qquad 5.1$$

The distributions of the RMS streamwise vorticity for the base flow and in the presence of actuation with Configuration 2λ at $C_{\mu,\text{ per jet}}$ = 0.02 ·10^{-3}, 0.05 ·10^{-3}, 0.08 ·10^{-3} and 0.12 ·10^{-3} is shown in Figure 5.22. The base flow (Figure 5.22a) is characterized by significant vorticity RMS within the shear layer (y/c < 0.16) whose magnitude diminishes towards the core flow, even though the corresponding time-averaged vorticity concentrations are small (cf. Figure 5.3). In the presence of actuation (Figure 5.22) the RMS fluctuations are congregated about the dominant time-averaged vorticity concentrations showing local minima near the centerline of the actuation jet and cross-stream protrusions in the upwelling region *between* adjacent jets. These effects are clearly intensified with the magnitude of the actuation. The resultant RMS fluctuations are co-located within the time-averaged streamwise vorticity concentrations that form due to adjacent jets (cf. Figure 5.21c), but show that despite the finding that the time-averaged vorticity exhibits clear organized pairs of counter-rotating streamwise vorticity concentrations within the upwelling regions (i.e. CCW for -0.08 < z/c < 0 and CW for -0.16 < z/c < -0.08), there are intense fluctuations of vorticity concentrations in this region. This indicates that the instantaneous flow in the presence of actuation still includes multiple strands of both CW

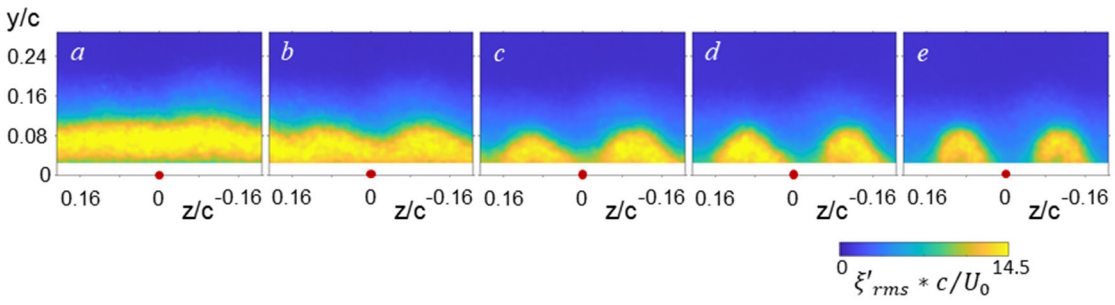

Figure 5.22. RMS of the streamwise vorticity for the base flow (a) and with Configuration 2λ at $C_{\mu,\text{ per jet}}$ = 0.02 (b), 0.05 (c), 0.08 (d), and 0.12 · 10^{-3} (e) (x/c = 5.54, M_0 = 0.25). The locations of the actuation jets are marked by •.

and CCW vorticity. Despite the fluctuations in the upwelling regions, the jets clearly organize the flow structure as is evident by the low levels of RMS fluctuations near their centerlines.

The organization of the instantaneous vorticity structure is depicted using color raster plots of the cumulative sum (computed using a threshold) of instantaneous CCW (positive) and CW (negative) streamwise vorticity concentrations in Figure 5.23Ia-c and Figure 5.23IIa-c, respectively, that are shown along with the corresponding time-averaged streamwise vorticity in Figure 5.23IIIa-c for the base flow and in the presence of actuation for Configuration 2λ. The streamwise vorticity in the base flow (Figure 5.23a) clearly shows that the entire separated domain within the shear layer between the surface and the core flow includes nearly equal concentrations of both CW and CCW streamwise vorticity and, as a result, the corresponding time-averaged distributions are nearly void of coherent structures. However, in the presence of actuation, the levels of streamwise vorticity along the actuation jet centerline are low when the flow becomes attached. Concomitantly, the jets organize the intermingled concentrations of streamwise vorticity into distinct concentrations between neighboring jets ($0 < z/c < 0.16$ and $-0.16 < z/c < 0$). At intermediate actuation strength ($C_{\mu,\,\text{per jet}} = 0.05 \cdot 10^{-3}$, Figure 5.23b), concentrations of both CW and CCW streamwise vorticity are interspersed between the jets, which results in relatively weak, but distinct, time-averaged streamwise vorticity concentrations that yield

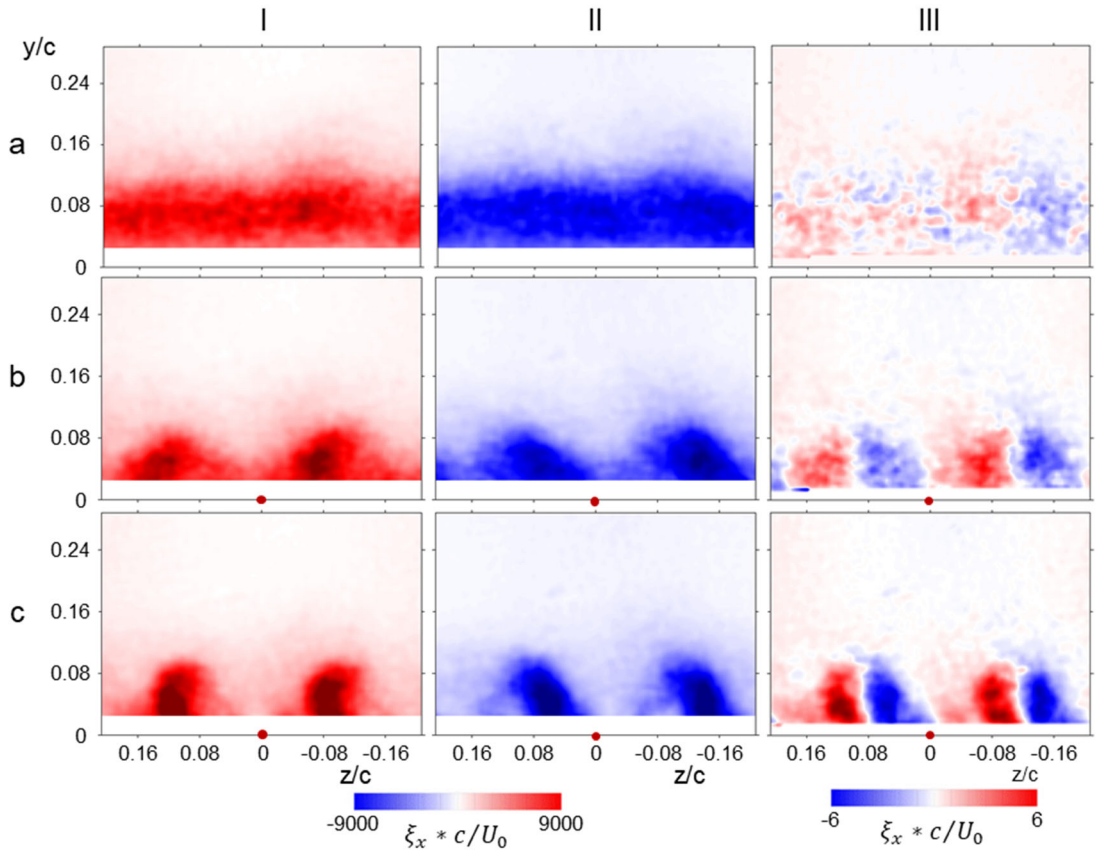

Figure 5.23. Cumulative summation of the instantaneous CCW (red, Column I) and CW (blue, Column II) streamwise vorticity concentrations computed using a threshold for Configuration 2λ ($x/c = 5.54$, $M_0 = 0.25$) at $C_{\mu,\text{ per jet}} = 0$ (a), $0.05 \cdot 10^{-3}$ (b), and $0.12 \cdot 10^{-3}$ (c). The corresponding time-averaged streamwise vorticity distributions of Column I and II are plotted in Column III. The locations of the actuation jets are marked by ●.

upwelling flow between the jets and downwash along their centerlines. As noted in connection with Figure 5.21, the presence of both senses of streamwise vorticity throughout the regions between the jets is a clear consequence of the spanwise sweeping motion of the fluidic-oscillations that leads to intermittent time-periodic formations of fragmented strands of streamwise CW and CCW vorticity. Further increase in the actuation level ($C_{\mu,\text{ per jet}} = 0.12 \cdot 10^{-3}$, Figure 5.23c) shows similar phenomena, and it is apparent that CCW concentrations are skewed to the left and CW concentrations to the

right within the regions between the jets ($0 < z/c < 0.16$ and $-0.16 < z/c < 0$). When the centers of the dominant peaks of the CCW concentrations ($0.08 < z/c < 0.16$ and $-0.12 < z/c < 0$) and the CW concentrations ($0 < z/c < 0.08$ and $-0.16 < z/c < -0.12$) are superposed they clearly match the centers of the corresponding time-averaged streamwise vorticity concentrations. The preferential orientation of the instantaneous CW and CCW streamwise vorticity on the left ($0 < z/c < 0.08$) and on the right ($-0.12 < z/c < 0$) of each jet's centerline indicate that the jets entrain higher-momentum fluid from the outer flow along their centerline and eject lower-momentum fluid between them that is associated with the accumulation of CW and CCW vorticity.

Streamwise development of the statistical characteristics of the induced flow fields at each actuation configuration ($C_{\mu,\,\text{per jet}} = 0.12 \cdot 10^{-3}$) is examined at three spanwise locations at the core of each of the time-averaged counter-rotating streamwise vorticity concentrations and at the same elevation on the centerline of the central jet at each of the three streamwise PIV measurement planes as shown for Configuration 2λ at at $x/c = 5.54$ and $C_{\mu,\,\text{per jet}} = 0.12 \cdot 10^{-3}$ in Figure 5.24a. Histograms of streamwise vorticity distributions (computed from POD-reconstructed velocity fields using 40 modes) are computed at each of these spanwise locations and are shown in Figure 5.24b-d. The histograms of vorticity concentrations centered about the CW and CCW time-averaged vorticity are skewed towards $\xi_x < 0$ in Figure 5.24b and $\xi_x > 0$ in Figure 5.24d (even though each includes both CW and CCW concentrations). This can be attributed to the spanwise oscillations of the

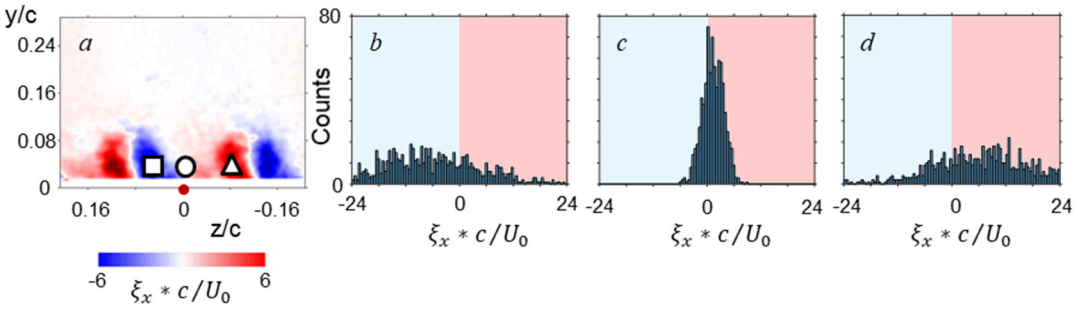

Figure 5.24. a) The time-averaged streamwise vorticity ξ_x (cf. Figure 5.21c) showing the three spanwise locations to the left (CW, □), center (○), and right (CCW, △) of the center jet ($z/c = 0$) for Configuration 2λ at $x/c = 5.54$, and histograms of the streamwise vorticity at each location □ (b), ○ (c), and △ (d) ($M_0 = 0.25$, $C_{\mu,\text{ per jet}} = 0.12 \cdot 10^{-3}$). The jet locations is marked by •, and the sense of vorticity in the histograms is highlighted CW (blue) and CCW (red).

jet that form preferential vorticity sense while the jet oscillates, while the histogram about the center of the jet (Figure 5.24c) is significantly narrower and shows nearly symmetric concentrations of CW and CCW vorticity. This narrow distribution of the streamwise vorticity about the central jet also demonstrates how the actuation jets redistribute the intermingled senses of streamwise vorticity in the base flow into the upwash regions between the jets, while entraining flow from above the shear layer which still contains both senses of streamwise vorticity, although at much lower intensity.

The variation with C_μ of the time-averaged streamwise vorticity and its associated standard deviation utilizing the histograms at the three spanwise locations discussed in connection with Figure 5.24a above, for the base flow and with actuation for Configurations 1λ, 2λ, and 3λ at $x/c = 5.26$, 5.54, and 5.72 are shown in Figure 5.25 (since the standard deviations on either side of the jet centerline are similar, Figure 5.25d-f show only the standard deviations on the center and left of the actuation jets). As expected, at

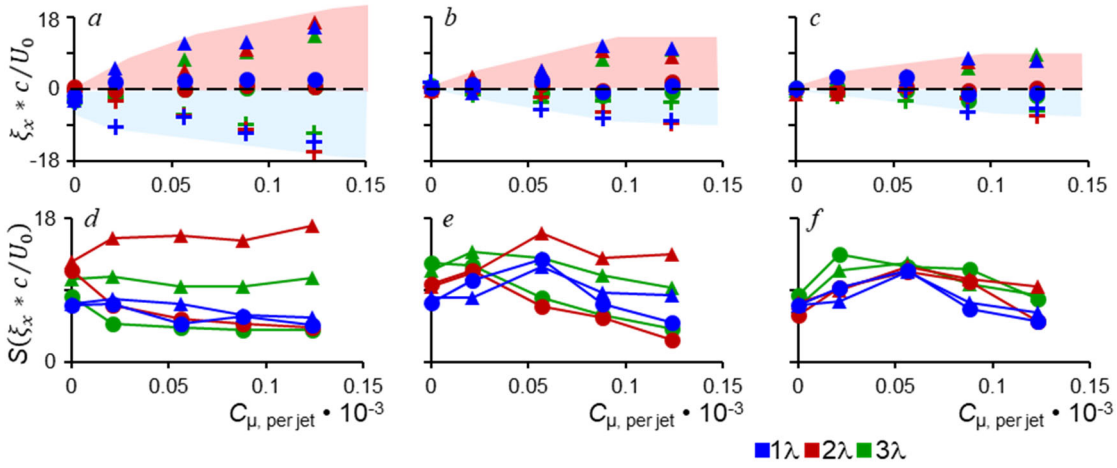

Figure 5.25. Variation with $C_{\mu,\ per\ jet}$ of ξ_x (a, b, and c) and the standard deviation (c, d, and e) at the locations identified in Figure 5.24a (+ left, ○ center, and △ right) for the base flow and with actuation for Configurations 1λ, 2λ, and 3λ at x/c = 5.26 (a, d), 5.54 (b, e), and 5.72 (c, f). The sense of the vorticity in figures a, b, and c is highlighted in the background (CW and CCW).

the center of the jet ξ_x nominally vanishes. The magnitudes of the time-averaged CW and CCW vorticity at the center of the streamwise vorticity concentrations show monotonic increase with C_μ where the rate of increase diminishes with streamwise distance from the jets owing to cross-stream and spanwise spreading. It is noteworthy that at each streamwise position the magnitude of ξ_x is nearly invariant with the spanwise spacing of the jets, which is attributed to the matched $C_{\mu,\ per\ jet}$. The standard deviation (Figure 5.25d-f) may be thought of as the measure of the time-dependent variation of the streamwise vorticity concentrations, and indicates the spread from the mean, or how "organized" the instantaneous flow becomes in the presence of actuation. The standard deviation measured at the centerline of the jets shows a monotonic decrease at the most upstream measurement location with C_μ. Farther downstream, however, the standard deviation initially increases with C_μ before decreasing, until the flow is reattached at $C_{\mu,\ per\ jet} = 0.12 \cdot 10^{-3}$ and shows a

reduction in the measured standard deviation compared to the base flow. The response in the standard deviation is attributed to the initial organization of the streamwise vorticity concentrations upstream, which then advect as the flow reseparates and causes further mixing downstream. When the flow is fully attached and the reattachment cells are formed, the centerline of the jets remains void of intense streamwise vorticity concentrations of either sense as the outer flow is entrained along the center of the jets and the reduction in the standard deviation reflects this improved "organization". Remarkably, despite the increased magnitude of the CW and CCW streamwise vorticity with C_μ, the standard deviation within these concentrations responds similarly to the centerline of the jet at $x/c = 5.72$, demonstrating how the actuation jets form a preferential sense of the vorticity to the right and left of the jet centerline and "organize" the instantaneous flow despite the spanwise oscillations forming strands of both CW and CCW vorticity in the region between the neighboring jets.

5.4.3 Turbulent Characteristics of the Reattachment Cells

Distributions of the time-averaged *TKE* ($x/c = 5.72$) for actuation Configurations 1λ, 2λ and 3λ are shown in Figure 5.26 for increasing actuation levels ($C_{\mu,\text{ per jet}} = 0.02 \cdot 10^{-3}$, $0.05 \cdot 10^{-3}$, $0.08 \cdot 10^{-3}$, and $0.12 \cdot 10^{-3}$). These data show two primary trends namely, within the center domain of the separation $-0.48 < z/c < 0.16$ and within the corner flow $z/c < -0.48$. Within the center domain, the time-averaged topology of the *TKE* distributions is rather similar to that of the RMS of the streamwise vorticity in Figure 5.22. The *TKE* is clearly affected by the respective upwash and downwash flows between opposite sense vorticity concentrations at the spanwise edges of adjacent jets and on both sides of the jet centerlines. As shown in Figure 5.26, the *TKE* forms bands that appear to cross through

the center of the time-averaged upwash regions between the jets. These bands nearly vanish between the vorticity concentrations about the jet centerline in concert with the downwash of nearly quiescent fluid from the core flow and are amplified and form a "halo" like structure at the peak of the upwash between the jets. Furthermore, as shown in Figure 5.26, the *TKE* bands are most intense when the actuation spacing is increased, albeit at the *same* $C_{\mu,\,\text{per jet}}$ as a result of the increased spacings between adjacent jets that enables intensification of the streamwise vortices (cf. Figure 5.16). It is noteworthy that the levels of *TKE* in the streamwise flow between adjacent jets is significantly lower when the global momentum coefficient is higher at lower spacing of the actuation jets as can be seen in Figure 5.26 I a-d compared to Figure 5.26 III a-d. Clearly, the resultant *TKE* levels between adjacent jets in the attached flow (Figure 5.26 I-III d) is dependent on the spanwise scale of the reattachment cells as the base flow is subdivided by the actuation. Furthermore, the *TKE* signatures of the outboard jets (which were also absent in the streamwise vorticity distributions in Figure 5.16) are indistinguishable from the corner flow for all actuation Configurations as the developed streamwise oriented 'halo' structures are wrapped into the adjacent surface-normal vortices. While the effects of actuation at Configurations 2λ and 3λ on the corner flow is negligible, the effect of the actuation at Configuration 1λ on the corner flow is significant. At this configuration, the outboard actuation jets are closest to the return flow along the side walls as discussed in connection with Figure 5.14 and the increase of the momentum coefficient leads to reduction in the spanwise extent of the corner flow and the width of the spanwise domain that is characterized by $TKE/U_0^2 > 8$ decreases from $\Delta z/c \approx 0.70$ to 0.42 as the total C_μ increases from $0.34 \cdot 10^{-3}$ to $2.04 \cdot 10^{-3}$. Furthermore, this configuration also distributes the *TKE* in the corner into a similar 'halo'

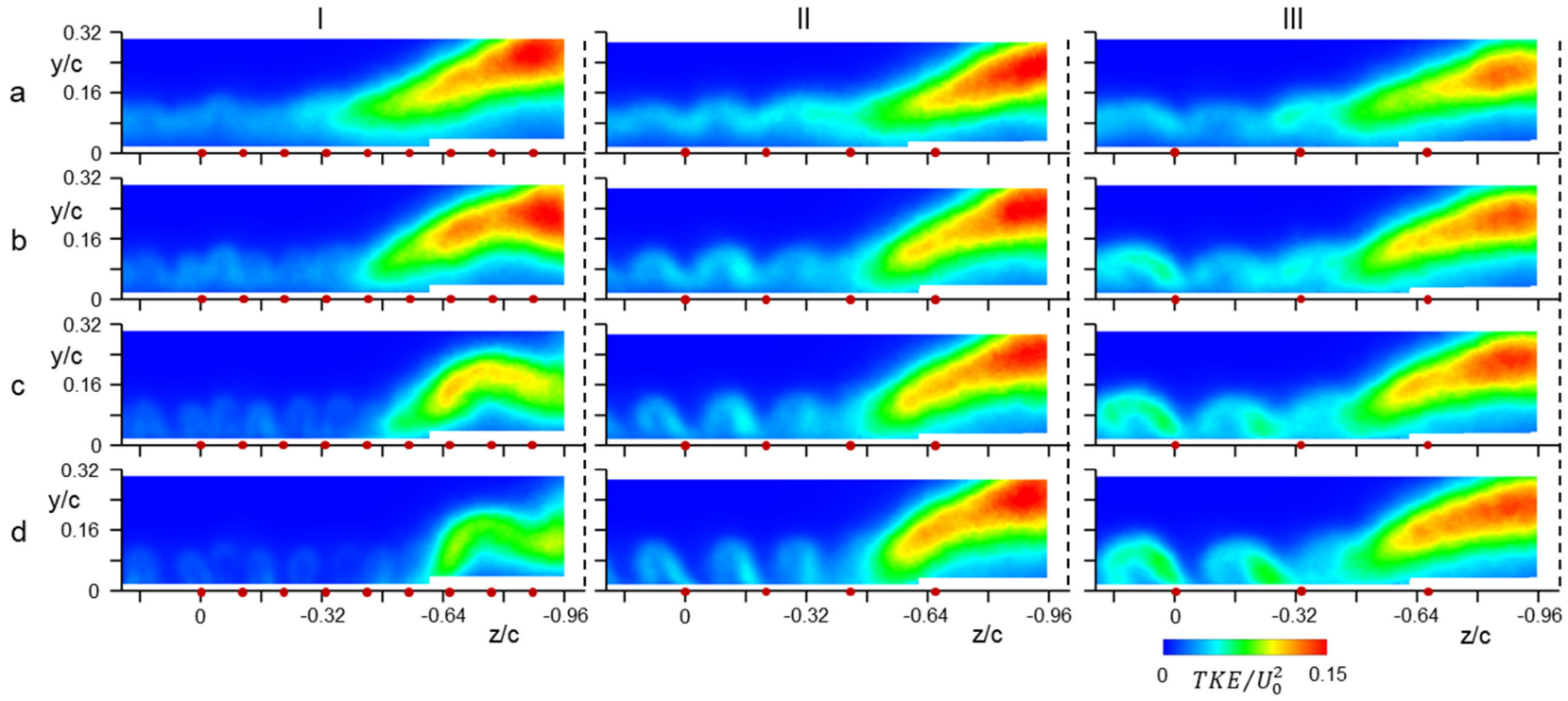

Figure 5.26. Color raster plots of the time-averaged *TKE* at $x/c = 5.72$ when the flow is actuated with Configurations 1λ (jet $\Delta z/c = 0.11$, Column I), 2λ (jet $\Delta z/c = 0.22$, Column II), and 3λ (jet $\Delta z/c = 0.33$, Column III) for $C_{\mu,\,\text{per jet}} = 0.02$ (a), 0.05 (b), 0.08 (c), and $0.12 \cdot 10^{-3}$ (d). The tunnel sidewall is marked by the dashed lines and the locations of the actuation jets are marked by •.

structure shown throughout the central domain, which is indicative of the intensification of the surface-normal vortex with associated CCW orientation and the associated pairing of CW and CCW streamwise vorticity developed in the corner shown in Figure 5.16I-d.

The corresponding color raster plots of the turbulent production at $x/c = 5.72$ for actuation Configurations 1λ, 2λ, and 3λ at $C_{\mu,\,\text{per jet}} = 0.12 \cdot 10^{-3}$ are shown in Figure 5.27. Similar to the time averaged *TKE,* the interaction of the actuation jet and the core flow results in elevated turbulent production within bands that pass through the spanwise centers

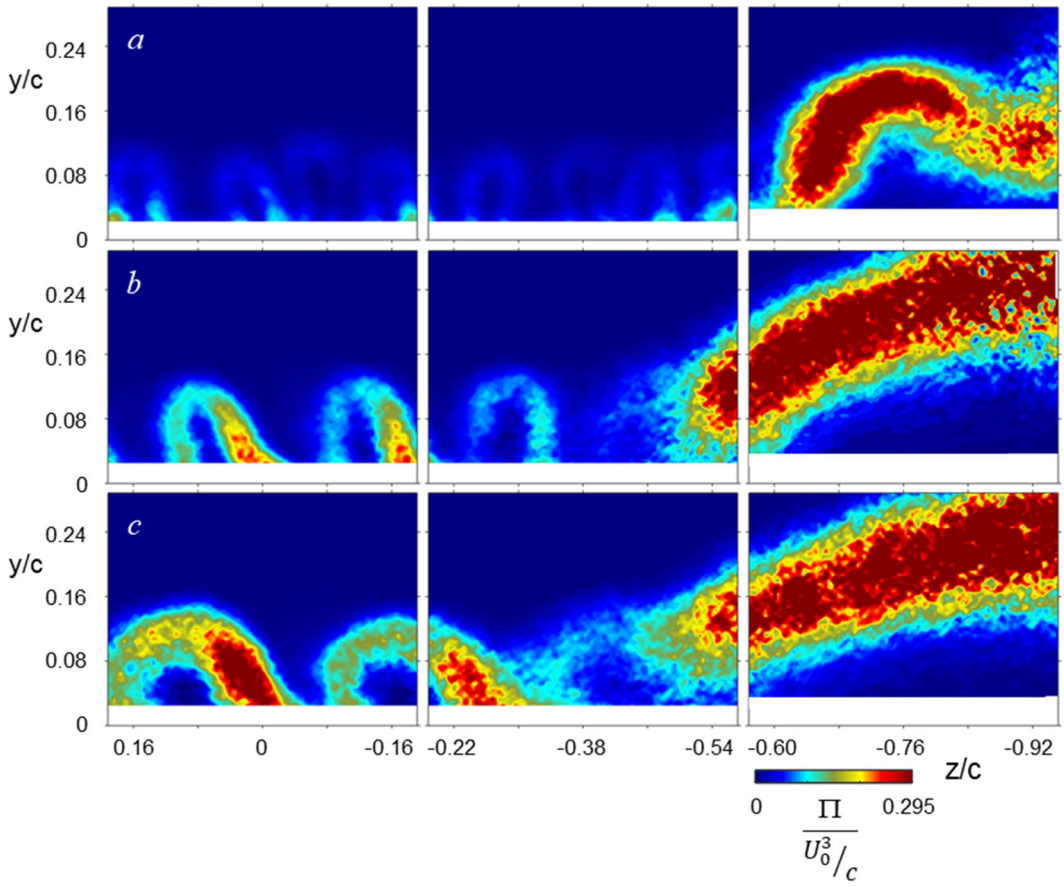

Figure 5.27. Color raster plots of distributions of the turbulent production at $x/c = 5.72$ for actuation Configurations 1λ (jet $\Delta z/c = 0.11$, a), 2λ (jet $\Delta z/c = 0.22$, b), and 3λ (jet $\Delta z/c = 0.33$, c) ($M_0 = 0.25$, $C_{\mu,\,\text{per jet}} = 0.12 \cdot 10^{-3}$).

of the induced time-averaged streamwise vorticity concentrations and form 'haloes' above the upwash regions between the jets in all three spacing models (Figure 5.27 a, b, and c). These data show that the peak production occurs within the bands near the cores of the CCW vorticity concentrations (cf. Figure 5.16). It is conjectured that this skewness may be related to the proximity to the side wall on the right-hand side ostensibly due to the effect of the corner vortex. Again, the peak turbulent production levels within the segmented bands are clearly dependent on the actuation spacing. Furthermore, the 'halo' structures of the outboard jets are shown to be angled and absorbed into the turbulent production signature of the corner flow for each actuation Configuration. Unlike the time-averaged *TKE* (cf. Figure 5.26), the corner flow is marked by similar peak turbulent production levels between the actuation Configurations.

Similar to the analysis in connection with Figure 5.7 the transport of *u'u'* at $x/c = 5.72$ for Configuration 2λ is shown in Figure 5.28 using third-order turbulence moments. As discussed in connection with Figure 5.13, a single actuation jet segments the distinct layers of ejection and sweeping motions of the base flow separation cell and draws the region of ejection motions to the surface. Similar to the time-averaged *TKE* in Figure 5.26, the third-order moments (Figure 5.28a and b, respectively) form arch-like structures throughout the central region of the cell $-0.46 < z/c < 0$. In each arch structure, the outer band contains regions of ejection motions ($v > 0$, $u < 0$), while the self-contained "pockets" underneath the arch contain the inner layers of the sweeping motions ($v < 0$, $u > 0$) that transport *u'u'*. The outer ejection motions are brought to the surface as part of entrainment within the reattachment cells the reattachment cells along the centerline of the jets ($\Delta z/c = 0.22$), similar to actuation with a single jet (cf. Figure 5.13), and the arch structures

are formed due to the neighboring jets (or neighboring reattachment cells). Outside of the arch structures throughout the central region ($-0.46 < z/c < 0$), the corner flow ($-0.92 < z/c < -0.46$) retains the original separate inner and outer layers of *v'* and *u'* as in the base flow (cf. Figure 5.7), although the inner edge of these layers is drawn to the surface as part of the reattachment process ($-0.60 < z/c < -0.46$).

As discussed in connection with Figure 5.13, the central region of flow actuated by a single jet showed that *u'u'* is transported by *w*' concentrations that are situated along the lateral edges of the jet interaction domain and entrain flow towards the center of the jet as well as laterally towards the side walls. In the presence of actuation with configuration 2λ

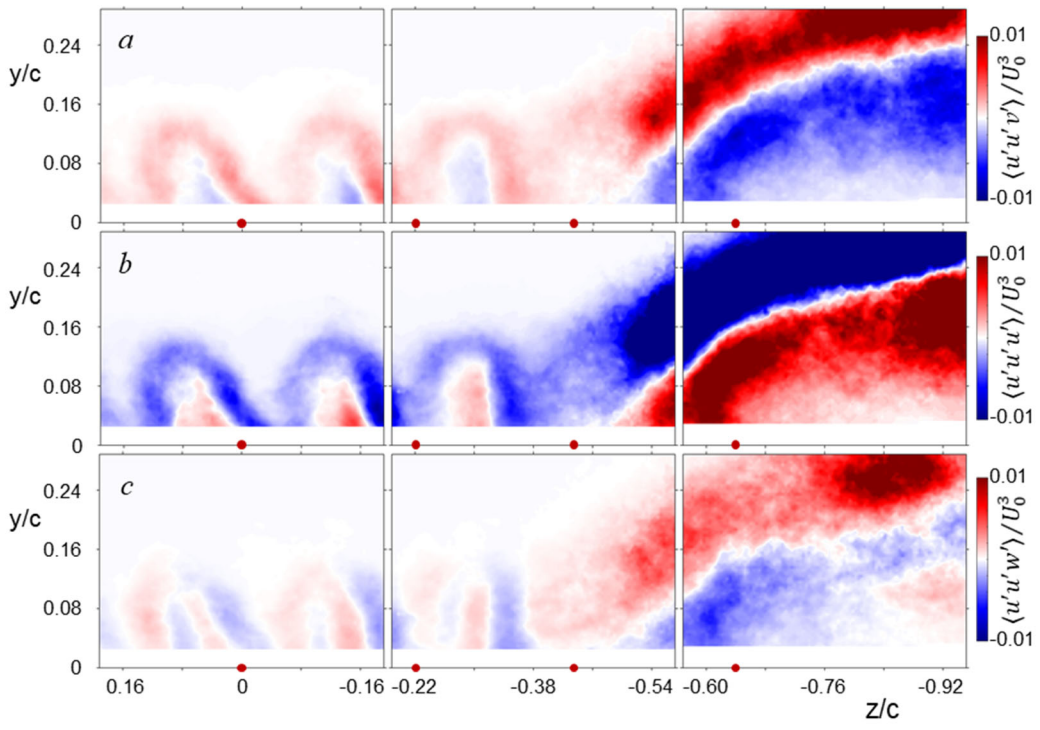

Figure 5.28. Third order turbulence moments $\langle u'u'v'\rangle/U_0^3$, $\langle u'u'u'\rangle/U_0^3$, and $\langle u'u'w'\rangle/U_0^3$ (a, b, and c, respectively) in the presence of actuation for the '2λ' model (jet spacing $\Delta z/c = 0.22$, $M_0 = 0.25$, $C_{\mu,\text{ per jet}} = 0.12 \cdot 10^{-3}$) at $x/c = 5.72$. Jet locations marked ●.

(cf. Figure 5.28c), the central domain $-0.46 < z/c < 0$ forms multiple concentrations of *w'* that are formed due to the reattachment nodes at the center of each segmented reattachment cell (cf. Figure 5.19). The concentrations are situated such that the lateral flow is split along the spanwise edge of each reattachment cell and is directed towards the centerlines of the jets or towards the upwash regions between the jets. This explains the origin of lateral fluctuations on the outboard edges of each jet. The corner region $-0.92 < z/c < -0.46$ (Figure 5.28c) shows that *w'* form an associated CCW motion as the upper layer (red) is directed towards the center (left) and the lower layer (blue) is directed towards the side wall (right). The corner region transports streamwise *u'u'* within the CCW oriented fluctuations induced by the surface-normal vortex.

Spanwise distributions of the cross-stream aggregate of the time-averaged *TKE* in the base flow and in the presence of actuation for Configurations 1λ, 2λ and 3λ ($C_{\mu,\,\text{per jet}} = 0.12 \cdot 10^{-3}$) are shown in Figure 5.29. At $x/c = 5.26$ (Figure 5.29a) the *TKE* within the central domain $-0.64 < z/c < 0$ is rather low in the presence and absence of actuation ostensibly because in the base flow the separation front is located beyond the jet overhang and the flow is essentially attached there in the presence of the jets. However, in the corner region ($-1.02 < z/c < -0.64$) the *TKE* of the base flow is matched or slightly exceeded ($-0.80 < z/c < -0.64$) by Configurations 2λ and 3λ indicating the effect of the coupling of their outboard jets with the surface-normal vortices. Remarkably, the mismatch between the outboard jets of Configurations 1λ and 3λ as shown in Figure 5.14 results in significantly lower levels of *TKE*. At $x/c = 5.54$ and 5.72 (Figure 5.29b and c) upwash and downwash flows associated with the formation of the reattachment cells are apparent and marked by respective higher and lower levels of *TKE* within the domain -

$0.48 < z/c < 0$. The *TKE* levels are locally lower than in the base flow except for the upwash regions for Configuration 3λ. Despite the formation of the reattachment cells, the

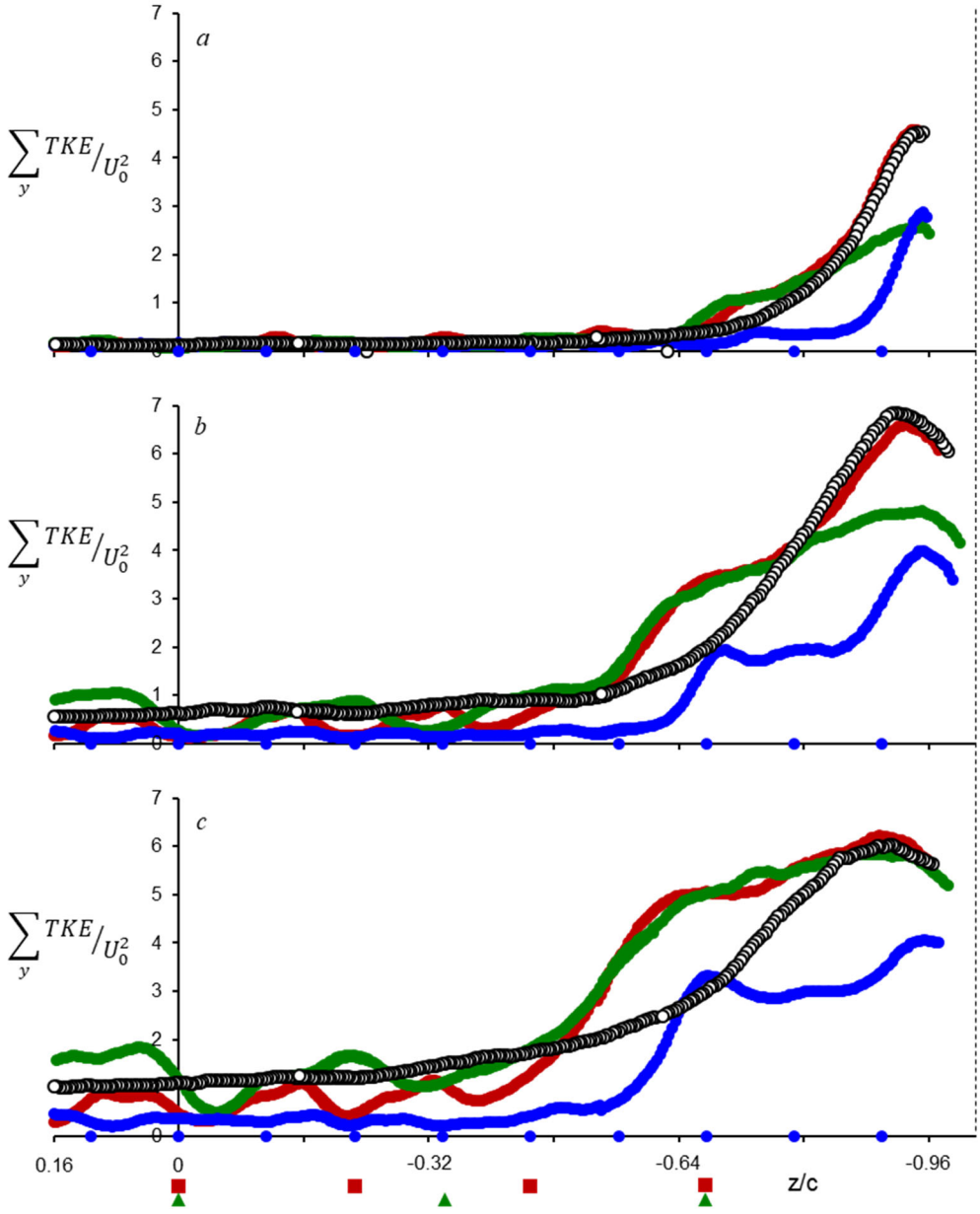

Figure 5.29. Spanwise distributions of the cross-stream aggregate of the time-averaged *TKE* in the base flow (○) and in the presence of actuation with Configurations 1λ, 2λ and 3λ ($C_{\mu,\text{ per jet}} = 0.12 \cdot 10^{-3}$) at $x/c = 5.26$ (a), 5.54 (b), and 5.72 (c). Spanwise jet locations are marked along the abscissa: 1λ ●, 2λ ■, and 3λ ▲. The tunnel side wall ($z/c = -1.02$) is marked by a dashed line.

central region in Configuration 1λ shows a relatively uniform distribution of lowered *TKE* levels compared to the base flow, whereas Configurations 2λ and 3λ show a large variation across the span due to the induced upwash and downwash regions. These data suggest that decreasing the spacing between the individual jets suppresses overall turbulence levels due to the bounding of the neighboring jets, despite the formation of the upwash and downwash flows. Near the side wall ($-1.02 < z/c < -0.48$), the *TKE* levels for Configurations 2λ and 3λ increase significantly compared to the base flow. The most notable change from the upstream condition is in Configuration 1λ ostensibly due to the formation of the opposite (CW) vortex next to the right side wall (cf. Figure 5.16).

The streamwise variation of the time-averaged *TKE* within the central reattachment cell (TKE_{cell}) integrated in the cross-stream and over the spanwise domain of the actuation spacing $z/c = + \Delta z/c$ and $- 0.5\Delta z/c$ is shown in Figure 5.30 where $\Delta z/c = 0.11$, 0.22, and 0.33 for Configurations 1λ, 2λ and 3λ, respectively. In the base flow TKE_{cell} is simply computed over the same domain in the absence of actuation for each Configuration and shown for reference at $C_{\mu,\,per\,jet} = 0$. While at $x/c = 5.26$ (Figure 5.30a) there is little difference between the configurations, there are measurable changes in TKE_{cell} between the configurations at $x/c = 5.54$ and 5.72 (Figure 5.30 b and c). In the presence of actuation ($C_{\mu,\,per\,jet} = 0.02 \cdot 10^{-3}$), the three configurations show a slight decrease in TKE_{cell} compared to the background flow as the central jet entrains the core flow. As the actuation level increases ($C_{\mu,\,per\,jet} > 0.02 \cdot 10^{-3}$), TKE_{cell} in Configurations 1λ and 2λ decreases

monotonically, while Configuration 3λ exhibits a monotonic increase, and at the highest actuation level ($C_{\mu,\text{ per jet}} = 0.12 \cdot 10^{-3}$, Figure 5.30) TKE_{cell} scales with the spacing of the jets at both x/c = 5.54 and 5.72. These data show that there is a clear tradeoff in the turbulence

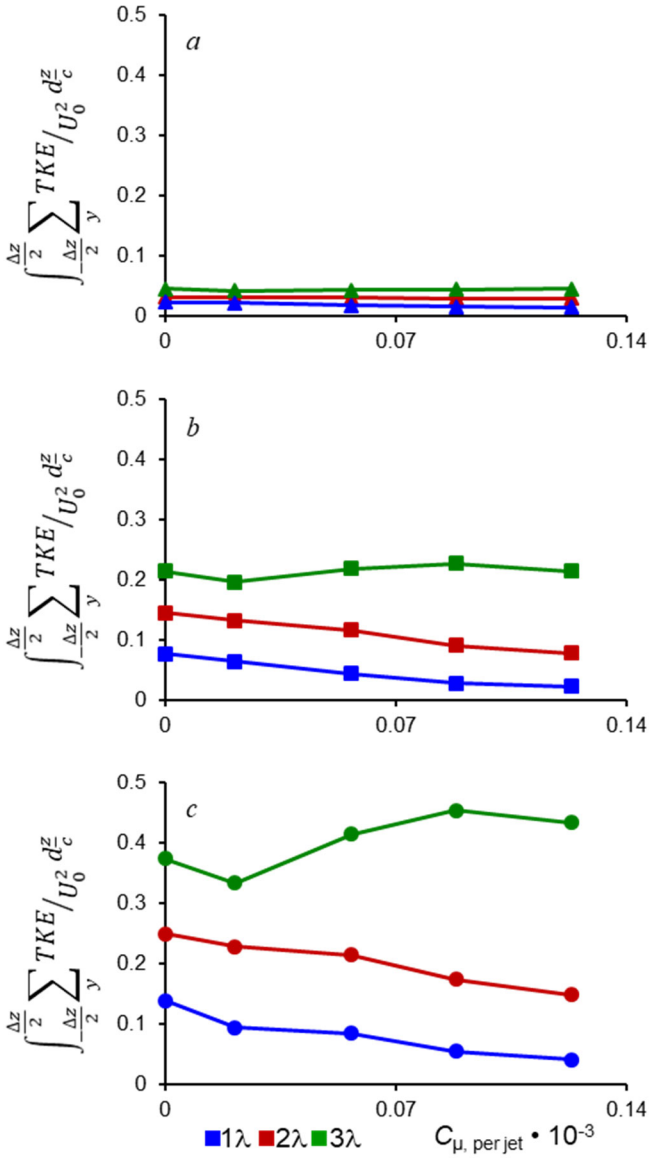

Figure 5.30. Variation with C_μ of the time-averaged *TKE* within the central reattachment cell in the cross-stream and over the spanwise domain of the actuation spacing between z/c = + and – 0.5 $\Delta z/c$ integrated at x/c = 5.26 (a), 5.54 (b), and 5.72 (c) for actuation Configurations 1λ, 2λ , and 3λ for $C_{\mu,\text{ per jet}}$ = 0, 0.02, 0.05, 0.08, and $0.12 \cdot 10^{-3}$ for each spacing model.

levels between the three configurations. Smaller spacings of the jets (1λ and 2λ, Figure 5.30c) reduce the overall turbulence levels throughout the reattachment process by limiting the scale of the growth into the upwelling regions between the jets. With larger spacing of the actuation jets (3λ) the streamwise vorticity evolves into a larger domain between the jets (cf. Figure 5.16) and contributes to the increase in TKE_{cell}. Since the individual reattachment cells are the building blocks of the reattachment process, the turbulence levels present a trade-off parameter when the flow is attached over a large spanwise extent when larger spanwise spacings between the actuation jets is desirable.

CHAPTER 6. CONCLUSIONS

6.1 Summary of the Work

The present investigations focus on the interactions between a separated boundary layer within a separation cell that forms in an adverse pressure gradient over an inner surface of a diffuser duct and a spanwise array of fluidically oscillating jets. A central objective of the present research is understanding the changes in the flow structure and dynamics of the base flow in the presence of actuation and the mechanisms that delay separation. These effects are investigated in two flow diffuser configurations having significant differences in their inlet conditions namely, a branching, open-end diffuser duct and a curved surface insert within a channel. The equally-spaced actuation jet modules are integrated within the surface and issue from under a surface-offset overhang that directs the jet tangentially to the surface as each jet oscillates in the spanwise direction (at frequencies up to 12 kHz)

The primary diagnostic tools used for characterization of the separation cell in the absence and presence of fluidic actuation are planar and stereo particle image velocimetry, where images are acquired at 200 and 15 fps, respectively. The planar PIV measurements are acquired along the center plane of each of the two diffuser configurations and stereo measurements are acquired in several streamwise-normal planes within the separation cell. These PIV data form composite distributions of velocity data that are assembled from multiple high spatial resolution views throughout the measurement domain and allow for detailed assessment of the flow structure. Complementary high -resolution planar fields are taken centered at the streamwise locations of flow separation and reattachment in the

base flow and in the presence of actuation to investigate the streamwise flow structure. Some planar PIV data sets acquired at 5 kHz capture the spectral content of the flow at separation. In addition to the PIV data, streamwise distributions of static surface pressure are utilized to assess the effects of the actuation on the time-averaged pressure upstream and downstream of separation in the base flow, the local pressure gradients within the separated domain, and the effects of flow losses. Total pressure measurements at the exit plane of the primary channel that feeds the branching diffuser allow for assessment of the mass flow rate fraction that is diverted into the diffuser. The three-dimensional flow topology of the separation cell in the base flow and in the presence of actuation is inferred from images of detailed surface oil visualization over the channel insert model.

In the first part of the present investigations, the effects of fluidic actuation on the structure of the separated base flow that forms in an adverse pressure gradient within a straight wall diverter diffuser downstream of its curved convex branching inlet are characterized. Once the flow separates, in the absence and presence of actuation, the flow does not experience reattachment upstream of the free end of the diffuser, and can be considered an 'open' separation cell. Measurements of the velocity show that the boundary layer of the separating flow over the lower surface of the diffuser forms a partial wake-like structure that is characterized by a thick shear layer (with nominal clockwise spanwise vorticity ξ_x) between a reversed flow layer next to the surface and the core flow above. The shear layer forms with similar structure over a range of inlet Mach numbers $M_0 < 0.4$. As the flow is advected along the diffuser's inlet section, the shear layer spreads in the cross-stream direction and the reversed flow along the surface occupies nearly 50% of the local duct's cross-stream height, while the core flow accelerates to maintain the cross-

sectional mass flow rate. The blockage associated with this spreading leads to streamwise losses within the diffuser that are assessed using measurements of the static pressure along the diffuser. In the presence of actuation at varying mass flow rate C_q (e.g. C_q up to 0.019 at $M_0 = 0.2$), the streamwise onset of separation is delayed and the shear layer is drawn towards the lower surface.

Measurements of the flow at separation are conducted using high-resolution PIV fields of view that are anchored to the time-averaged streamwise location of separation in the base flow and with separation migrating downstream in the presence of actuation. The flow dynamics of the time-averaged flow are assessed using distributions of the turbulent kinetic energy (*TKE*), analysis of the near-wall velocity distributions, and proper orthogonal decomposition (POD) of the vorticity fields. Scaling arguments of adverse pressure gradient flows by Schatzman and Thomas (2017), utilizing the outer vorticity thickness and velocity deficit inherent to the formation of an outer shear layer, are further used to assess the structure of the flow at separation in the absence and presence of actuation.

Investigations of the structure of separation are extended to the closed separation domain of a separation cell that forms in an adverse pressure gradient over a curved surface insert within a constant cross-section straight duct with specific emphasis on the flow topology in the absence and presence of actuation. The 3-D structure of the time-averaged separation cell is inferred from surface oil visualization across the entire span of the test section, and is comprised of two surface-normal vortices of opposing sense (CW on the left and CCW on the right) that bound a central, nominally 2-D, reverse flow region with reattachment occurring downstream of the insert's transition surface. The closed

separation domain formed by the cell is markedly different than that present in the diffuser, which did not reattach upstream of its free exit. Composite PIV images of the base flow ($M_0 = 0.25$) along the cell's plane of symmetry showed similar features to the branching diffuser flow namely, the formation of a shear layer between the core flow and the separated flow layer over the surface. Downstream of the curved insert surface where the channel returns to a constant cross-section, the separated flow becomes reattached. Similar to the flow within the branching diffuser, the flow along the separation cell's plane of symmetry over the insert model is assessed using time-averaged composites of distributions of the streamwise velocity and concentrations of spanwise vorticity and *TKE*. In addition to the actuation mass flow rate, the actuation is also characterized using its momentum coefficient C_μ (for reference $C_q = 0.001$ and 0.008 at $M_0 = 0.4$ translate to $C_{\mu, jet} = 0.04 \cdot 10^{-3}$ and $0.36 \cdot 10^{-3}$, respectively at $M_0 = 0.25$). In addition to the effects of the actuation on separation, these measurements also allowed for assessing effects on the reattachment. Despite variations in the cross-stream scale, velocity distributions at separation and reattachment are similarly characterized by the presence of an outer shear layer owing to the wake-like structure that forms in the adverse pressure gradient, similar to the velocity distributions at separation in the diffuser. The scaling arguments of Schatzman and Thomas (2017) are revisited and shown to collapse the velocity distributions of the separation cell at separation and reattachment in the absence and presence of actuation, and remarkably also collapse with the velocity distributions of the diffuser flow in the absence and presence of actuation.

The spanwise structure of the flow within the separation cell in the base flow and in the presence of actuation is inferred from stereo PIV in three streamwise-normal planes

spanning from the plane of symmetry to the channel's sidewalls. The spanwise spacing of the actuator jet arrays was determined based on the interaction domain of a single jet at the center of the separation cell. Based on this evolution, three spacings were investigated at, below, and above the width of the interaction domain of a single jet, while matching the jets' momentum coefficient C_μ per jet ($C_{\mu,\,jet} < 0.12 \cdot 10^{-3}$). The actuation forms spanwise-periodic concentrations of streamwise vorticity of opposing sense that in the time-averaged sense, when paired, form downwash regions along the individual jet centerlines with associated upwash between the bounding neighboring jets. Flow attachment across the span is effected by the actuation subdividing the original base flow separation cell into smaller spanwise-periodic 'reattachment' cells, comprised of the same topological structure that are scaled by the actuator spacing.

Separation cells formed in an adverse pressure gradient are shown to be receptive to spanwise actuation via tangentially-issued fluidically oscillating jets, which manipulate the flow dynamics in the vicinity of separation and develop concentrations of streamwise vorticity to incrementally delay separation along the surface bounded by the reverse flow region with increasing actuation strength. The base flow separation cell is subdivided into smaller reattachment cells due to the actuation, which mitigate the adverse effects of reverse flow along the surface. Through demonstration of the efficacy to delay separation and highlighting the structural basis for flow reattachment, these active flow control technologies could be implemented in multiple applications that are susceptible to and suffer from the losses induced by the adverse effects of internal flow separation, such as diffusers, ducts, and engine inlets, in order to increase their efficiency and/or produce future advanced designs without their current limitations.

Potential future work related to the present investigations could explore further the evolution of the small-scale motion within the time-averaged reattachment cells. The insight into the structure and mechanisms of reattachment in the present investigations should be compared with control of separation in other configurations with potential effects on improved efficacy and control authority.

6.2 New Findings and Insights

The present investigations have led to a number of new findings on and insights into the evolution of a separated flow domain (or separation cell) in an adverse pressure gradient within a diffuser, and specifically into the effects of flow actuation on the changes in the flow structure within the separation domain.

1. **Structure of the Separating Flow Layer:** The present investigations showed that the flow in the plane of symmetry of a separation cell that forms in the adverse pressure gradient within each diffuser configuration is characterized by a wake-like structure in which a shear layer buffers between the core flow from above and a reversed flow layer over the surface. The formation of the reversed flow domain forces the streamwise flow in the diffuser to constrict by displacement due to the reversed flow layer and velocity reduction through the shear layer. The fluidic actuation leads to a streamwise delay of separation that is accompanied by an increase in the characteristic cross-stream scale of the spanwise vorticity concentrations within the shear layer while it is deflected towards the surface. The passage of the vortices into the domain of the onset of reversed flow is associated with an increase in the local *TKE* in the vicinity of the migrated separation that is

accompanied by enhanced energy cascade to small-scale, dissipative motions within the flow.

2. **Scaling of the Velocity Distributions at Separation and Reattachment in the Separation Cell:** Perhaps one of the most salient findings of the present investigations is an extension of studies of boundary layers in adverse pressure gradient and their scalability based on local vorticity thickness and velocity deficit in the outer embedded shear layer as suggested by Schatzman and Thomas (2017). Despite clear differences in surface geometries, inlet conditions, adverse pressure gradient, cross-stream velocity scales, and spectral content, distributions of the time-averaged streamwise velocity along the center plane of the separation cell at separation and reattachment in the absence and presence of actuation within both diffuser configurations show remarkable collapse when scaled by the local velocity deficit and vorticity thickness of the respective outer flows. This scaling implies that the evolution of separation and reversed flow near the surface is dominated by the characteristics of the shear that buffers between the core flow and the reversed flow layer over the surface regardless of details of the surface geometry and the absence or presence of actuation. Furthermore, the remarkable collapse of these mean velocity distributions implies that the scaling can be applied to a large variety of boundary layer flows with varying surface configurations and adverse pressure gradients and suggests that the time-averaged flow is similarly governed by and scales with the buffer shear layer. Perhaps not surprisingly, proper orthogonal decomposition of the spanwise vorticity fluctuations at separation in the diffuser in the absence and presence of actuation shows that the underlying modes are

remarkably similar, lending credence to the similarity of the flows shown by the scaled velocity distributions. These findings also indicate an underlying structural similarity between the separating base flow and the separating flow when the separation is delayed in the presence of actuation.

3. **Reduction in Diffuser Flow Losses:** The present investigations showed that the cross-stream blockage effected by the formation of the separation's reversed flow domain over the surface diminishes with streamwise migration of the separation as the intensity of the fluidic actuation increases. The present measurements showed that this reduction in blockage is accompanied by significant reduction in pressure losses within the diffuser and therefore can enable regulation of the mass flow rate that is diverted into the diffuser from the main flow channel. Increasing levels of actuation was manifested by an increase in the Mach number at the inlet of the main flow channel at a fixed blower power. This increase in the inlet Mach number reached an upper limit when the diffuser flow became attached along most of its length.
4. **The 3-D Structure of the Separation Cell:** The evolution and topology of a separation cell in the adverse pressure gradient of a diffuser flow was investigated over the surface of an insert model. The separation cell is characterized by two counter-rotating surface-normal vortices, that bound a central, nominally two-dimensional reverse flow domain. Each of the test section sidewalls couples to the formation of the cell by directing reverse flow along the wall which is turned toward the center plane and creates the orientations of the surface-normal vortices. This separation cell is reminiscent of stall cells that are formed over airfoils, but the

presence of the sidewalls forces an opposite sense of the surface-normal vortices. In the presence of actuation at several spanwise spacings ($C_{\mu, jet} \leq 0.12 \cdot 10^{-3}$), the surface-normal vortices are shifted downstream and towards the sidewalls due to flow attachment in the center segment of the cell. The fluidic actuation does not affect the sense of the vortices, but can lead to their intensification by coupling with the reverse flow along the sidewalls. The outboard migration of the vortices suggests that in the absence of the test section sidewalls the vortices would continue to migrate laterally, allowing for spanwise spreading of flow attachment over a larger spanwise extent between them.

5. **Spanwise Interactions of the Fluidic Actuation with the Separation Cell:** The interactions of a spanwise-periodic array of fluidically oscillating jets with the separation cell builds on spanwise replication of the flow mechanisms of single jet actuation. It was shown that the core flow of a single actuator jet flowing into a separated flow domain forms a pair of counter-rotating streamwise vorticity concentrations at its spanwise edges that induce downwash flow along the jet's centerline (similar to the flow induced by conventional wall-jets) and thereby effect flow attachment. It is noted, that the sense of the counter-rotating vortex pairs that are induced by the actuation wall jet in the presence of the cross flow have an opposite sense from the vortices that are formed by a jet in cross-flow that is detached from the surface from which the jet issues. Unlike a free jet in cross-flow, the vortices that are formed by a wall-bounded jet induce a downwash flow and entrainment along the jet centerline and upwash of low-momentum fluid between adjacent actuation jets. When a spanwise array of jets is assembled, the downwash

regions along their centerlines extend spanwise attachment along with the upwelling flow between adjacent jets. It is shown that the spanwise spacing of adjacent actuation jets of a given momentum coefficient can be adjusted and perhaps optimized based on the momentum coefficient and the scaling of the streamwise vorticity concentrations so that attachment is not impeded if this spacing is too large. Surface oil flow visualization coupled with time-averaged measurements of the streamwise vorticity structure showed that reattachment is effected by segmentation of the base flow separation cell into multiple spanwise reattachment cells centered along each jet. The topology of these segmented cells that scale with the jet spacing has elements of the topology of the base flow cell including a separation front, reattachment node, and saddle points. The presence of these cells is consistent with the downstream/upstream migration of separation and reattachment indicating that the mechanism of flow attachment lies with the segmentations of the base flow separation cell that can withstand the core flow adverse pressure gradient.

6. **Turbulent Characteristics of the Separation Cell:** As noted in §6.2 1-5, the time-averaged spanwise array of adjacent counter-rotating vorticity concentrations that are induced by the actuation jets lead to segmentation and attachment within the base flow separation cell. The present measurements showed that these time-averaged counter-rotating vorticity concentrations develop through organization of instantaneous concentrations of streamwise vorticity strands of opposite sense that are intermingled throughout the separated flow region of the base flow. The stress field effected by the presence of the actuation jets leads to a preferred spatial

orientation of these vortex strands that resemble the structure of the time-averaged vorticity concentrations. These concentrations become more organized with increasing actuation strength C_μ. The effects of the spanwise actuation on the organization of the instantaneous structure of the flow also alter the inherent turbulent fluctuations within the separation cell. The spanwise distributions of the *TKE* form arch-like concentrations within the upwelling domain of the individual reattachment cells while the *TKE* is lower in the downwash along the jet centerlines (similar to the effect of single jet actuation). Consequently, as the reattachment cells induce larger upwelling regions between the jets, the overall turbulence intensity increases with actuation spacing. While reattachment can be effected over a range of actuator spacings, *TKE* levels should be assessed as a tradeoff parameter for actuator spacing.

APPENDIX A. DECOMPOSITION METHODS

A.1 Proper Orthogonal Decomposition (POD)

The underlying flow structure of the flow approaching separation in a diverting diffuser in Chapter 3 is investigated using the proper orthogonal decomposition (POD) method (Berkooz, Holmes et al., 1993 and Sirovich, 1987), which can also be used as a basis for a low pass filter for reconstructing flow fields on varying ordered energy levels. Instantaneous velocity (or vorticity) fields are used to calculate the averaged fields to extract the POD modes of the flow field as:

$$\vec{X}(t) = <\vec{X}> + \sum_{n=1}^{N} A_n(t) \cdot \vec{\varphi}_n \qquad \text{A.1}$$

where $\vec{X}(t)$ is an instantaneous state vector (of either velocity, vorticity, or any general input) of a data set to be reconstructed using the POD modes, $<\vec{X}>$ is the ensemble (or time) averaged value of the input, $\vec{\varphi}_n$ is the *n*th POD mode, $A_n(t)$ is the weighted time coefficient of the *n*th POD mode, and *N* is the rank (or length) or the data set. The analysis for extraction of the POD modes is such that the *N* number of modes is calculated by creating the state vector of $\vec{X}(t)$ chosen to be a column vector of the input (e.g. velocity, or vorticity) concatenated vertically with a total of *N*+1 realizations. Such that the state matrix is then $\overrightarrow{X_{state}} = \left[\vec{X}(1), \vec{X}(2), \ldots \vec{X}(N)\right]$. Once the state matrix is created, the POD modes are solved as follows: solve the eigenvalue problem: $\left(\overrightarrow{X_{state}}^{T} \overrightarrow{X_{state}}\right) A^i = \lambda^i A^i$,

then arrange the solutions by eigenvalues as $\lambda_1 > \lambda_2 \ldots > \lambda_N = 0$. The POD modes ($\vec{\varphi}_n$) are essentially eigenvalues of $\overrightarrow{X^*_{state}} \cdot \overrightarrow{X^*_{state}}^T$, but can be found as the following:

$$\vec{\varphi}_n = \frac{\sum_{n=1}^{N} A_n^i \vec{X}_n}{\left\| \sum_{n=1}^{N} A_n^i \vec{X}_n \right\|} \quad \text{A.2}$$

The resulting POD modes are ordered by the corresponding modal energy contributions, and the energy contribution of each mode $\vec{\varphi}_n$ is quantified in terms of its ordered eigenvalue λ_n as:

$$E_n = |\lambda_n|^2 \Big/ \sum_{i=1}^{N} |\lambda_i|^2 \quad \text{A.3}$$

REFERENCES

Adrian, R. J., "Hairpin vortex organization in wall turbulence," *Physics of fluids*, vol. **19**, no. 4, pp. 041301, 2007.

Amitay, M., Pitt, D. and Glezer, A., "Separation control in duct flows," *Journal of Aircraft*, vol. **39**, no. 4, pp. 616-620, 2002.

Amitay, M. and Glezer, A. (2006). Aerodynamic flow control using synthetic jet actuators. Control of Fluid Flow, Springer**:** 45-73.

Balantrapu, N. A., Hickling, C., Alexander, W. N. and Devenport, W., "The structure of a highly decelerated axisymmetric turbulent boundary layer," *Journal of Fluid Mechanics*, vol. **929**, no., 2021.

Berkooz, G., Holmes, P. and Lumley, J. L., "The proper orthogonal decomposition in the analysis of turbulent flows," *Annual review of fluid mechanics*, vol. **25**, no. 1, pp. 539-575, 1993.

Blanckaert, K., "Flow separation at convex banks in open channels," *Journal of Fluid Mechanics*, vol. **779**, no., pp. 432-467, 2015.

Burrows, T. J., Vukasinovic, B., Glezer, A., Lakebrink, M. T. and Mani, M., "Experimental and numerical investigation of active flow control of a serpentine diffuser," *AIAA Journal*, vol. **59**, no. 2, pp. 607-620, 2021.

Castillo, L. and George, W. K., "Similarity analysis for turbulent boundary layer with pressure gradient: outer flow," *AIAA journal*, vol. **39**, no. 1, pp. 41-47, 2001.

Cattafesta III, L. N. and Sheplak, M., "Actuators for active flow control," *Annual Review of Fluid Mechanics*, vol. **43**, no., pp. 247-272, 2011.

Dandois, J., Garnier, E. and Sagaut, P., "Numerical simulation of active separation control by a synthetic jet," *Journal of Fluid Mechanics*, vol. **574**, no., pp. 25-58, 2007.

Dell'Orso, H. and Amitay, M., "Parametric Investigation of Stall Cell Formation on a NACA 0015 Airfoil," *AIAA Journal*, vol. **56**, no. 8, pp. 3216-3228, 2018. 10.2514/1.J056850.

Dengel, P. and Fernholz, H., "An experimental investigation of an incompressible turbulent boundary layer in the vicinity of separation," *Journal of Fluid Mechanics*, vol. **212**, no., pp. 615-636, 1990.

Elsberry, K., Loeffler, J., Zhou, M. and Wygnanski, I., "An experimental study of a boundary layer that is maintained on the verge of separation," *Journal of Fluid Mechanics*, vol. **423**, no., pp. 227-261, 2000.

Elyasi, M. and Ghaemi, S., "Experimental investigation of coherent structures of a three-dimensional separated turbulent boundary layer," *Journal of Fluid Mechanics*, vol. **859**, no., pp. 1-32, 2019. doi:10.1017/jfm.2018.788.

Esfahani, A., Webb, N. and Samimy, M., "Stall cell formation over a post-stall airfoil: effects of active perturbations using plasma actuators," *Experiments in Fluids*, vol. **59**, no. 9, pp. 1-16, 2018.

Ethier, C. R., Prakash, S., Steinman, D. A., Leask, R. L., Couch, G. G. and Ojha, M., "Steady flow separation patterns in a 45 degree junction," *Journal of Fluid Mechanics*, vol. **411**, no., pp. 1-38, 2000.

Fearn, R. and Weston, R. P., "Vorticity associated with a jet in a cross flow," *AIAA Journal*, vol. **12**, no. 12, pp. 1666-1671, 1974.

Fric, T. and Roshko, A., "Vortical structure in the wake of a transverse jet," *Journal of Fluid Mechanics*, vol. **279**, no., pp. 1-47, 1994.

Gartner, J. and Amitay, M. (2015). Flow Control in a Diffuser at Transonic Conditions. 45th AIAA Fluid Dynamics Conference.

Ghaemi, S. and Scarano, F., "Counter-hairpin vortices in the turbulent wake of a sharp trailing edge," *Journal of Fluid Mechanics*, vol. **689**, no., pp. 317-356, 2011.

Glezer, A., Kadioglu, Z. and Pearlstein, A. J., "Development of an extended proper orthogonal decomposition and its application to a time periodically forced plane mixing layer," *Physics of Fluids A: Fluid Dynamics*, vol. **1**, no. 8, pp. 1363-1373, 1989.

Glezer, A. and Amitay, M., "Synthetic jets," *Annual review of fluid mechanics*, vol. **34**, no. 1, pp. 503-529, 2002.

Glezer, A., "Some aspects of aerodynamic flow control using synthetic-jet actuation," *Philosophical Transactions of the Royal Society A: Mathematical, Physical and Engineering Sciences*, vol. **369**, no. 1940, pp. 1476-1494, 2011.

Graftieaux, L., Michard, M. and Grosjean, N., "Combining PIV, POD and vortex identification algorithms for the study of unsteady turbulent swirling flows," *Measurement Science and technology*, vol. **12**, no. 9, pp. 1422, 2001.

Gregory, J. and Tomac, M. N. (2013). A review of fluidic oscillator development and application for flow control. 43rd AIAA fluid dynamics conference.

Ho, C.-M. and Huerre, P., "Perturbed free shear layers," *Annual review of fluid mechanics*, vol. **16**, no. 1, pp. 365-422, 1984.

Huang, Y. and Green, M. A., "Detection and tracking of vortex phenomena using Lagrangian coherent structures," *Experiments in Fluids*, vol. **56**, no. 7, pp. 1-12, 2015.

Jhaveri, V., DeSalvo, M., Glezer, A. and Colton, J., "Effects of manufacturing parameters on performance of fluidic oscillators for aerodynamic flow control," *Proceedings of the Institution of Mechanical Engineers, Part G: Journal of Aerospace Engineering*, vol. **233**, no. 10, pp. 3603-3611, 2019. https://doi.org/10.1177/0954410018803715.

Johnston, J. P. and Nishi, M., "Vortex generator jets-means for flow separation control," *AIAA journal*, vol. **28**, no. 6, pp. 989-994, 1990.

Joslin, R. D. and Miller, D. N., Fundamentals and applications of modern flow control, American Institute of Aeronautics and Astronautics, 2009.

Kamotani, Y. and Greber, I., "Experiments on a turbulent jet in a cross flow," *AIAA journal*, vol. **10**, no. 11, pp. 1425-1429, 1972.

Kim, S.-H. and Kim, K.-Y., "Effects of installation conditions of fluidic oscillators on control of flow separation," *AIAA Journal*, vol. **57**, no. 12, pp. 5208-5219, 2019.

Kiya, M. and Sasaki, K., "Structure of a turbulent separation bubble," *Journal of Fluid Mechanics*, vol. **137**, no., pp. 83-113, 1983.

Kiya, M. and Sasaki, K., "Structure of large-scale vortices and unsteady reverse flow in the reattaching zone of a turbulent separation bubble," *Journal of Fluid Mechanics*, vol. **154**, no., pp. 463-491, 1985.

Koklu, M., "Effect of a Coanda Extension on the Performance of a Sweeping-Jet Actuator," *AIAA Journal*, vol. **54**, no. 3, pp. 1131-1134, 2016. 10.2514/1.J054448.

Koklu, M., "Performance Assessment of Fluidic Oscillators Tested on the NASA Hump Model," *Fluids*, vol. **6**, no. 2, pp. 74, 2021.

Koukpaizan, N. K. K., Improved Techniques for Aerodynamic Flow Control Simulation with Fluidic Oscillators, Georgia Institute of Technology, 2020.

Lin, J. C., "Review of research on low-profile vortex generators to control boundary-layer separation," *Progress in Aerospace Sciences*, vol. **38**, no. 4-5, pp. 389-420, 2002.

Ma, A., Unsteady Topology and Control of a Turbulent Boundary Layer Separation over an Airfoil. Master of Science, University of Alberta, 2020.

Ma, A., Gibeau, B. and Ghaemi, S., "Time-resolved topology of turbulent boundary layer separation over the trailing edge of an airfoil," *Journal of Fluid Mechanics*, vol. **891**, no., 2020.

Mahesh, K., "The interaction of jets with crossflow," *Annual review of fluid mechanics*, vol. **45**, no., pp. 379-407, 2013.

Manolesos, M. and Voutsinas, S. G., "Study of a stall cell using stereo particle image velocimetry," *Physics of Fluids*, vol. **26**, no. 4, pp. 045101, 2014.

Marušić, I. and Perry, A., "A wall-wake model for the turbulence structure of boundary layers. Part 2. Further experimental support," *Journal of Fluid Mechanics*, vol. **298**, no., pp. 389-407, 1995.

Matsuda, H., Iida, S.-i. and Hayakawa, M., "Coherent structures in a three-dimensional wall jet," vol. no., 1990.

Mehta, R. and Bradshaw, P., "Longitudinal vortices imbedded in turbulent boundary layers Part 2. Vortex pair with 'common flow'upwards," *Journal of Fluid Mechanics*, vol. **188**, no., pp. 529-546, 1988.

Namgyal, L. and Hall, J., "Reynolds stress distribution and turbulence generated secondary flow in the turbulent three-dimensional wall jet," *Journal of Fluid Mechanics*, vol. **800**, no., pp. 613-644, 2016.

Nishi, M., Yoshida, K. and Morimitsu, K., "Control of separation in a conical diffuser by vortex generator jets," *JSME International Journal Series B Fluids and Thermal Engineering*, vol. **41**, no. 1, pp. 233-238, 1998.

Ostermann, F., Woszidlo, R., Nayeri, C. and Paschereit, C. O. (2019). Interaction between a Jet emitted by a Fluidic Oscillator and a Crossflow at a Skew Angle. AIAA Scitech 2019 Forum.

Ostermann, F., Woszidlo, R., Nayeri, C. N. and Paschereit, C. O., "The interaction between a spatially oscillating jet emitted by a fluidic oscillator and a cross-flow," *Journal of Fluid Mechanics*, vol. **863**, no., pp. 215-241, 2019.

Otto, C., Tewes, P., Little, J. C. and Woszidlo, R. (2018). Comparison of Fluidic Oscillators and Steady Jets for Separation Control on a Wall-Mounted Hump. 2018 AIAA Aerospace Sciences Meeting.

Otto, C., Tewes, P., Little, J. C. and Woszidlo, R. (2019). Comparison of Various Fluidic Oscillators for Separation Control on a Wall-Mounted Hump. AIAA SciTech 2019 Forum.

Papadopoulos, G. and Otugen, M., "Separating and reattaching flow structure in a suddenly expanding rectangular duct," *Journal of Fluids Engineering*, vol. no. 117, pp. 17-23, 1995.

Pauley, L. L., Moin, P. and Reynolds, W. C., "The structure of two-dimensional separation," *Journal of fluid Mechanics*, vol. **220**, no., pp. 397-411, 1990.

Pauley, W. R. and Eaton, J. K., "Experimental study of the development of longitudinal vortex pairs embedded in a turbulent boundary layer," *AIAA journal*, vol. **26**, no. 7, pp. 816-823, 1988.

Perry, A. and Marušić, I., "A wall-wake model for the turbulence structure of boundary layers. Part 1. Extension of the attached eddy hypothesis," *Journal of Fluid Mechanics*, vol. **298**, no., pp. 361-388, 1995.

Peterson, C. J., Vukasinovic, B. and Glezer, A., "Laser pulse separation measurements for spectral flow analysis using particle image velocimetry," *FME Transactions*, vol. **48**, no. 1, pp. 1-6, 2020. doi:10.5937/fmet2001001P.

Pope, S. B., Turbulent Flows. Cambridge, UK, Cambridge Univesity Press, 2000.

Raghu, S., "Fluidic oscillators for flow control," *Experiments in Fluids*, vol. **54**, no. 2, pp. 1-11, 2013.

Robinson, S. K., "Coherent motions in the turbulent boundary layer," *Annual review of fluid mechanics*, vol. **23**, no. 1, pp. 601-639, 1991.

Rodríguez, D. and Theofilis, V., "On the birth of stall cells on airfoils," *Theoretical and Computational Fluid Dynamics*, vol. **25**, no. 1, pp. 105-117, 2011.

Schatzman, D. and Thomas, F., "An experimental investigation of an unsteady adverse pressure gradient turbulent boundary layer: embedded shear layer scaling," *Journal of Fluid Mechanics*, vol. **815**, no., pp. 592-642, 2017.

Schewe, G., "Reynolds-number effects in flow around more-or-less bluff bodies," *Journal of Wind Engineering and Industrial Aerodynamics*, vol. **89**, no. 14-15, pp. 1267-1289, 2001.

Simmons, D., Thomas, F. O. and Corke, T. C., "Smooth Body Flow Separation Experiments and Their Surface Flow Topology Characterization," AIAA Aviation 2019 Forum, 2019. doi: 10.2514/6.2019-3085.

Simmons, D., Thomas, F. O. and Corke, T. C. (2019). Evidence of Surface Curvature Effects in Smooth Body Flow Separation Experiments. AIAA Aviation 2019 Forum.

Simmons, D. J., Thomas, F. O. and Corke, T. C. (2018). A Smooth Body, Large-Scale Flow Separation Experiment. 2018 AIAA Aerospace Sciences Meeting.

Simpson, R. L., Strickland, J. and Barr, P., "Features of a separating turbulent boundary layer in the vicinity of separation," *Journal of Fluid Mechanics*, vol. **79**, no. 3, pp. 553-594, 1977.

Simpson, R. L., Chew, Y.-T. and Shivaprasad, B., "The structure of a separating turbulent boundary layer. Part 1. Mean flow and Reynolds stresses," *Journal of Fluid Mechanics*, vol. **113**, no., pp. 23-51, 1981.

Simpson, R. L., Chew, Y.-T. and Shivaprasad, B., "The structure of a separating turbulent boundary layer. Part 2. Higher-order turbulence results," *Journal of Fluid Mechanics*, vol. **113**, no., pp. 53-73, 1981.

Simpson, R. L., "Turbulent boundary-layer separation," *Annual Review of Fluid Mechanics*, vol. **21**, no. 1, pp. 205-232, 1989.

Sirovich, L., "Turbulence and the dynamics of coherent structures. I. Coherent structures," *Quarterly of applied mathematics*, vol. **45**, no. 3, pp. 561-571, 1987.

Suzuki, T., Colonius, T. and Pirozzoli, S., "Vortex shedding in a two-dimensional diffuser: theory and simulation of separation control by periodic mass injection," *Journal of Fluid Mechanics*, vol. **520**, no., pp. 187-213, 2004.

Vaccaro, J. C., Elimelech, Y., Chen, Y., Sahni, O., Jansen, K. E. and Amitay, M., "Experimental and numerical investigation on steady blowing flow control within a compact inlet duct," *International Journal of Heat and Fluid Flow*, vol. **54**, no., pp. 143-152, 2015.

Van Buren, T., Beyar, M., Leong, C. M. and Amitay, M., "Three-dimensional interaction of a finite-span synthetic jet in a crossflow," *Physics of Fluids*, vol. **28**, no. 3, pp. 037105, 2016.

Vukasinovic, B., Rusak, Z. and Glezer, A., "Dissipative small-scale actuation of a turbulent shear layer," *Journal of Fluid Mechanics*, vol. **656**, no., pp. 51-81, 2010.

Wang, G., Yang, F., Wu, K., Ma, Y., Peng, C., Liu, T. and Wang, L.-P., "Estimation of the dissipation rate of turbulent kinetic energy: A review," *Chemical Engineering Science*, vol. **229**, no., pp. 116133, 2021.

Weihs, D. and Katz, J., "Cellular patterns in poststall flow over unswept wings," *AIAA Journal*, vol. **21**, no. 12, pp. 1757-1759, 1983.

Wieneke, B., "PIV uncertainty quantification from correlation statistics," *Measurement Science and Technology*, vol. **26**, no. 7, pp. 074002, 2015.

Winkelmann, A. (1981). An experimental study of separated flow on a finite wing. 7th Atmospheric Flight Mechanics Conference.

Winkelmann, A. (1982). An experimental study of mushroom shaped stall cells. 3rd Joint Thermophysics, Fluids, Plasma and Heat Transfer Conference.

Woszidlo, R., Ostermann, F. and Schmidt, H.-J., "Fundamental properties of fluidic oscillators for flow control applications," *AIAA Journal*, vol. **57**, no. 3, pp. 978-992, 2019.

Yang, W. and Kuan, B., "Experimental investigation of dilute turbulent particulate flow inside a curved 90 bend," *Chemical Engineering Science*, vol. **61**, no. 11, pp. 3593-3601, 2006.

Yarusevych, S. and Boutilier, M. S., "Vortex shedding of an airfoil at low Reynolds numbers," *AIAA journal*, vol. **49**, no. 10, pp. 2221-2227, 2011.

Yon, S. A. and Katz, J., "Study of the unsteady flow features on a stalled wing," *AIAA journal*, vol. **36**, no. 3, pp. 305-312, 1998.